

# **Polymer Degradation and Performance**

ACS SYMPOSIUM SERIES **1004**

# Polymer Degradation and Performance

**Mathew C. Celina**, Editor  
*Sandia National Laboratories*

**Jeffrey S. Wiggins**, Editor  
*The University of Southern Mississippi*

**Norman C. Billingham**, Editor  
*The University of Sussex*

Sponsored by the  
**Division of Polymer Chemistry, Inc.**



American Chemical Society, Washington, DC



The paper used in this publication meets the minimum requirements of American National Standard for Information Sciences—Permanence of Paper for Printed Library Materials, ANSI Z39.48–1984.

ISBN: 978-0-8412-6978-1

Copyright © 2009 American Chemical Society

Distributed by Oxford University Press

All Rights Reserved. Reprographic copying beyond that permitted by Sections 107 or 108 of the U.S. Copyright Act is allowed for internal use only, provided that a per-chapter fee of \$40.25 plus \$0.75 per page is paid to the Copyright Clearance Center, Inc., 222 Rosewood Drive, Danvers, MA 01923, USA. Republication or reproduction for sale of pages in this book is permitted only under license from ACS. Direct these and other permission requests to ACS Copyright Office, Publications Division, 1155 16th Street, N.W., Washington, DC 20036.

The citation of trade names and/or names of manufacturers in this publication is not to be construed as an endorsement or as approval by ACS of the commercial products or services referenced herein; nor should the mere reference herein to any drawing, specification, chemical process, or other data be regarded as a license or as a conveyance of any right or permission to the holder, reader, or any other person or corporation, to manufacture, reproduce, use, or sell any patented invention or copyrighted work that may in any way be related thereto. Registered names, trademarks, etc., used in this publication, even without specific indication thereof, are not to be considered unprotected by law.

PRINTED IN THE UNITED STATES OF AMERICA

# Foreword

The ACS Symposium Series was first published in 1974 to provide a mechanism for publishing symposia quickly in book form. The purpose of the series is to publish timely, comprehensive books developed from ACS sponsored symposia based on current scientific research. Occasionally, books are developed from symposia sponsored by other organizations when the topic is of keen interest to the chemistry audience.

Before agreeing to publish a book, the proposed table of contents is reviewed for appropriate and comprehensive coverage and for interest to the audience. Some papers may be excluded to better focus the book; others may be added to provide comprehensiveness. When appropriate, overview or introductory chapters are added. Drafts of chapters are peer-reviewed prior to final acceptance or rejection, and manuscripts are prepared in camera-ready format.

As a rule, only original research papers and original review papers are included in the volumes. Verbatim reproductions of previously published papers are not accepted.

**ACS Books Department**

# Preface

The performance of polymeric materials and the science of polymer degradation and materials reliability are of ever increasing importance for sustainable global economic development. Many of the challenges we face require better performing, cheaper and more specialized polymers ranging from composites and thermosets to thermoplastics and elastomers, and increasingly originating from biomass rather than fossil resources. Whether polymers find their way into consumer products, energy applications, microelectronics, defense areas, or space exploration, there is one commonality: a requirement for improved reliability and the ability to predict material behavior in a variety of environmental conditions. Polymer performance is governed by the polymer's ability to resist chemical and physical degradation processes under thermal, photo, radiation, hydrolytic, and biological conditions. The emerging high performance material needs in the near future will undoubtedly be related to energy and biomedical applications and will have to address concerns about sustainability and environmental impact.

The 24 chapters in this symposium series volume provide an overview of current research and development trends related to the performance, degradation, reliability, and optimization of novel polymeric materials. This book was developed from the 53 excellent papers (including four tutorials) presented at the symposium on *Polymer Performance Degradation and Materials Selection* at the American Chemical Society (ACS) spring meeting held in March 2007 in Chicago, Illinois. We discussed the progress in this interdisciplinary research field that relies on an exchange of creative ideas where the commonality is in analysis methods, characterization techniques, synthetic routes, processing improvements, similar degradation mechanisms, and the philosophy of what affects performance. The ongoing challenge remains to better understand materials performance under complex environmental exposures rather than idealistic single stress conditions. We have met about every seven years as part of the ACS conferences (Chicago 1993,

San Diego 2001, and Chicago 2007) and have witnessed well-attended and stimulating symposia. It is with great satisfaction that we continue to attract contributions from new talents entering this field. In fact, as this book demonstrates, our field is more complex and broader-ranging than ever before. Considering the success of the symposium, many presenters inquired about the possibility of contributing a chapter to a conference proceedings book. We hope that we were able to present here a selection and overview of the many research activities that were being addressed. Many of the contributing authors are recognized as experts in their respective fields and have contributed innovative concepts.

The authors and the editors sincerely hope that this overview will provide guidance and an improved understanding of the various issues connected with polymer materials performance and will assist our fellow scientists in their research and development of improved materials.

**Mathew C. Celina**

R&D, Organic Materials Department  
Sandia National Laboratories  
Albuquerque, NM 87185

**Jeffrey S. Wiggins**

Polymer Science and Engineering  
The University of Southern Mississippi  
Hattiesburg, MS 39406-0001

**Norman C. Billingham**

Department of Chemistry and Biochemistry  
University of Sussex  
Brighton BN1 9QJ  
United Kingdom

# Author Index

- Allred, Ronald E., 180  
Anchordoquy, T. J., 195  
Assink, Roger A., 26  
Balazs, Bryan, 2  
Black, Steve, 16  
Blinco, James, 59  
Bottle, Steven, 59  
Brunsvold, Amy L., 140  
Celina, Mathew C., 26, 37, 153  
Chaleat, Celine, 287  
Chinn, Sarah, 2  
Chirila, Traian V., 301  
Clarke, Stephen, 261  
Clough, Roger L., 37, 153  
Dargaville, Tim R., 153  
Dhevi, D. Manjula, 103  
Elliott, Julie M., 26  
Gee, Rid, 2  
George, Graeme, 59  
Gijnsman, Pieter, 48  
Ginic-Markovic, Milena, 261  
Gjersing, Erica, 2  
Guenthner, Andrew J., 140  
Halley, Peter J., 287  
Hama, Yoshimasa, 131  
Hamskog, Mikael, 48  
Han, Song-Hee, 232  
Harrah, Larry A., 180  
Herberg, Julie, 2  
Hill, David J. T., 116, 301  
Hong, John Hee, 103  
Hoyt Haight, Andrea E., 180  
Itani, Toshiro, 253  
Ito, Kenji, 131  
Ito, Masayuki, 70  
Iwata, Minoru, 131  
Jones, Gary D., 37  
Kaise, Motoaki, 277  
Katsumura, Yosuke, 131, 166  
Kawabata, Shuichi, 277  
Kawaue, Akiya, 317  
Kemp, Anne, 301  
Kempner, E. S., 195  
Kim, Jae Yong, 232  
Kim, Kap Jin, 103  
King, Saskia H., 328  
Kobayashi, Yoshinori, 131  
Kondo, Mitsuaki, 131  
Kudo, Hisaaki, 131, 166  
Kuzviwanza, Pfumai, 92  
Lacevic, Naida, 2  
Lee, Chong Oh, 232  
Lee, Jong Soon, 103  
Lee, Takhee, 232  
Lenhart, Joseph L., 328  
Lou, Jianzhong, 92  
Mabry, Joseph M., 140  
MacDonald, Ian, 261  
Marchant, Darrell, 140  
Markotsis, Martin G., 287  
Matisons, Janis, 261  
Matsui, Yoshinori, 253  
Matsumoto, Toshihiko, 277  
Maxwell, Robert, 2  
McGrath, Laura M., 328  
Micallef, Aaron, 59  
Minton, Timothy K., 140  
Molina, M. D. C., 195

- Murakami, Takeshi, 131  
Muroya, Yusa, 166  
Murphy, Julian, 16  
Nagasawa, Naotsugu, 166  
Najafi, Ebrahim, 232  
Oka, Toshitaka, 131  
Okamura, Haruyuki, 317  
Oshima, Akihiro, 131, 204  
Parnas, Richard S., 328  
Patel, Mogon, 2, 16  
Petteys, Brian J., 140  
Russo, Melissa, 287  
Saiki, Seiichi, 166  
Sargent, Anna Lisa, 287  
Schimmel, Keith, 92  
Seki, Shu, 220, 253  
Shin, Kwanwoo, 232  
Shirai, Masamitsu, 317  
Sopade, Peter A., 287  
Sugimoto, Masaki, 220  
Tagawa, Seiichi, 220, 253  
Takahashi, Risa, 277  
Tan, Ihwa, 287  
Tomczak, Sandra J., 140  
Truss, Rowan W., 287  
Tsuji, Shou, 253  
Tsukuda, Satoshi, 220  
Vij, Vandana, 140  
Warren, Dana, 92  
Washio, Masakazu, 131, 204  
Wheeler, Hilary, 2  
Whittaker, Andrew K., 301  
Wilson, Thomas W., III, 83  
Wilson, Mark, 2  
Wright, Michael E., 140  
Wu, Dong Yang, 261  
Yan, Jizhong, 92  
Yandek, Gregory R., 140  
Yoshii, Fumio, 166  
Zainuddin, 301



# Subject Index

## A

- Acrylated epoxidized soybean oil (AESO)  
 modification, 73*f*  
 soybean oil resin, 71  
*See also* Soy polymers
- Addition polymers,  
 degradation/biodegradation, 5, 6*f*
- Agricultural mulching by landcover,  
 polyethylene with pro-oxidant additive, 14, 15*f*
- Aircraft, need for new structures, 199
- Aliphatic polyesters. *See*  
 Hyperbranched aliphatic polyesters
- Anionic polymerization, ethyl glyoxylate, 41
- Anticancer agents  
 polymer formulations containing, 65–66
- Armor, body. *See* Poly(p-phenylene benzobisoxazole) (PBO) fibers

## B

- Backbiting reactions,  
 poly(dimethylsiloxane) (PDMS), 252, 253*f*
- Bimolecular combination, non-terminating, 123, 125
- Biodegradability, commercial polymers, 18
- Biodegradation  
 addition and condensation polymers, 5, 6*f*  
 hyperbranched aliphatic polyesters, 22–24  
 measuring rate, 5  
 oxidized films, 10, 12  
 process, 4*f*
- Biodegradation testing, respirometer, 9
- Biomedical polymers, fatty acids in development, 60
- Biometer, measuring carbon dioxide evolution, 9
- Biopolymers  
 "cradle to gate, grave and cradle" diagram, 32, 34*f*  
 U.S. market, 32
- Bisphenol A, di(cyanate ester) of. *See* Cyanate esters
- Bisphenol A polycarbonate. *See* Polycarbonate (PC)
- Body armor. *See* Poly(p-phenylene benzobisoxazole) (PBO) fibers
- Boltorn™ polyesters  
 schematics, 20*f*  
*See also* Hyperbranched aliphatic polyesters
- Broadband dielectric spectroscopy (BDS)  
 method, 241–242  
 nanocomposite systems, 245–246, 247*f*  
 spectra of 2% Cloisite polysiloxane system aged under dry N<sub>2</sub>, 246, 247*f*  
 spectra of 2% Cloisite polysiloxane system aged under moist air, 246, 247*f*  
 unfilled elastomer, 245, 245*f*  
*See also* Polysiloxane nanocomposites

## C

- Carbon dioxide, respirometer biodegradation testing, 9
- Carbon dioxide photo-generation absorbance during UV illumination for polyethylene (PE) and polypropylene (PP), 155*f*
- carbonyl group development in PE and PP, 150, 153–154
- carbonyl group development monitoring, 150
- CO<sub>2</sub> absorbance at 2360 vs. 1713 cm<sup>-1</sup> for PE and PP films, 157*f*
- CO<sub>2</sub> monitoring, 149–150
- correlation between, and carbonyl group development, 154, 156
- experimental, 148–150
- infrared transmission spectra of unpigmented exposed PP, 153*f*
- mechanistic implications of, from polyalkene films, 156–157
- PE and PP, 150, 151*f*
- poly(ethylene terephthalate) (PET), 154, 156*f*
- polyester studies, 157
- possible induction phenomenon for PP, 150, 152*f*
- purpose built cell, 149*f*
- Carbon nano fiber (CNF)
- poly(dimethylsiloxane) (PDMS) with, 262, 265*f*
- scanning electron microscopy of, showing fibrous nature, 262, 266*f*
- stress-strain curves for PDMS modified with silica nano fiber, CNF and single- and multi-walled nano fiber, 262, 267*f*
- Carbonyl groups
- build-up in air, 137, 138*f*
- correlation with CO<sub>2</sub> generation, 154, 156
- development in PE and PP, 150, 153–154
- Carbonyl insertion, chain insertion reactions, 7
- Carborane modified materials
- filled poly(dimethylsiloxane) (PDMS) samples, 257–258, 259*f*
- schematic of, PDMS system, 259*f*
- Castor oil
- incorporation into poly(lactic acid), 67, 68*f*
- See also* Fatty acids
- Cell structure, physical properties of foam, 256
- Chain insertion reactions, environmentally degradable polyolefins, 7
- Chain scission
- number of, vs. time of exposure, 140*f*
- number of moles of, per mass unit, 137
- oxidation induced embrittlement, 136*f*
- poly(vinyl chloride) (PVC), 222–223, 224*f*
- purely random, 139
- Chlorinated water, exposure of polyolefin pipes, 163–164
- Chlorosulfonated polyethylene cables
- lifetime prediction, 164, 166
- lifetime vs. temperature for Hypalon core insulation, 168*f*
- master curve of indenter modulus of jacketing, 166*f*
- Cis-platin, polymer formulation containing, 65–66
- Compost, oxidized films, 10, 12
- Composting
- biodegradation of poly(lactide) (PLA) bottles exposed to commercial, 37*f*
- commercial, 33, 35, 37*f*
- compostability of plastic material, 32–33, 38

cumulative measurement  
   respirometric system (CMR),  
   36*f*  
 experimental, 33, 35  
 hydrolytic chain scission of PLA,  
   39*f*  
 molecular weight variation under  
   commercial, 39*f*  
 packaging, 32  
 preparation of commercial compost  
   pile, 35*f*  
 simulated, 33, 35, 38, 39*f*  
 waste disposal, 32  
 Condensation polymers,  
   degradation/biodegradation, 5,  
   6*f*  
 Cone calorimetry, poly(ethylene) and  
   nanocomposites, 215–217  
 Controlled oxidation, environmentally  
   degradable polyolefins, 7  
 Cross-linking, natural oils with styrene  
   and divinylbenzene, 72*f*  
 Cumulative measurement  
   respirometric system (CMR),  
   simulated composting, 33, 35, 36*f*  
 Cyanate esters  
   di(cyanate ester) of bisphenol A  
   (BADCy), 199–200  
   di(cyanate ester) of dimethylbis(p-  
   phenol)silane (SiMCy), 199–  
   200  
   experimental, 199–201  
   methods of analysis, 201  
   SiMCy vs. BADCy, 203  
   structures of BADCy and SiMCy,  
   200*f*  
   thermogravimetric analysis of  
   BADCy and SiMCy under  
   nitrogen and air, 201, 202*f*  
   weight gain of castings of BADCy  
   and SiMCy, 201, 203*f*  
   *See also* Poly-p-phenylene resins  
 Cyclohexane dicarboxylic anhydride,  
   modifying acrylated epoxidized  
   soybean oil (AESO), 73*f*

## D

Degradation  
   addition and condensation  
   polymers, 5, 6*f*  
   plastics, 4  
   poly(ethyl glyoxylate), 46, 48, 50  
   unsaturated polyester in sub-critical  
   water with additives, 91, 93, 94*t*  
   unsaturated polyester in sub-critical  
   water without additives, 91, 92  
 Dehydration, unsaturated polyester in  
   sub-critical water, 91, 92  
 Dendritic macromolecules  
   tailoring properties, 18  
   *See also* Hyperbranched aliphatic  
   polyesters  
 Desiccative aging,  
   poly(dimethylsiloxane) network,  
   176, 177*f*  
 Di(cyanate ester)s. *See* Cyanate esters  
 Differential thermal analysis (DTA),  
   poly(ethylene) and  
   nanocomposites, 214–215  
 Diffusion coefficient, equation, 21  
 Dimethylbis(p-phenol)silane,  
   di(cyanate ester) of. *See* Cyanate  
   esters  
 Disintegration, degradation, 4  
 2,6-Di-t-butyl-4-methylphenol,  
   thermo-oxidative degradation of  
   poly(vinyl chloride) (PVC), 223,  
   225*t*  
 Divinylbenzene, cross-linking with  
   natural oils, 72*f*  
 Drug delivery systems  
   administration routes, 62  
   microspheres for controlled, 60–61  
   nicotine load and release, 54–55  
   polyanhydrides, 61  
   polyesters for, 61  
   *See also* Poly( $\epsilon$ -caprolactone)  
   (PCL); Poly(ester-anhydrides)  
 Drug release, classic diffusion model,  
   55

Dynamic mechanical thermal analyzer (DMTA), pigmented epoxy coatings, 279, 280–281, 283f

## E

Embrittlement in oxidative aging  
 carbonyl build-up in air, 138f  
 ductile-brittle transition, 145f  
 extending model to predicting, 135, 136f  
 molar mass embrittlement criterion, 139, 142  
 moles of chain scissions per mass unit, 137  
 morphological embrittlement criterion, 142–143  
 number of chain scissions vs. time of exposure, 140f  
 possible causal chains for, 136f  
 presumed shape of thermal aging point trajectories, 145f  
 radical chemistry to molar mass validation, 136–137, 139  
 random chain scission, 139  
 strain at break vs. amorphous layer thickness for PE of differing molar mass, 144f  
 strain at break vs. weight average molar mass, 142f  
 weight average molar mass changes vs. time of exposure, 141f  
 Engineering silicones. *See* Silicon based polymer systems  
 Environmental degradation, processes, 4f  
 Environmentally degradable plastics approaches to, polyolefins, 6–8  
 definition, 5  
 history of development, 7  
 Enzymatic attack, environmentally degradable polyolefins, 7  
 Enzymes, promoting biodegradability, 18

Epoxidized soybean oil (ESBO), ring-opening reactions, 74

Epoxy coatings. *See* Pigmented epoxy coatings

Estane® 5703

chemical structure, 182f, 229f  
 composition, 182, 228

*See also* Plastic-bonded explosive PBX 9501; Poly(ester urethane) binder, plasticized

Ester group hydrolysis, poly(ethyl glyoxylate) degradation, 50, 51f

Ester linkages, chain insertion reactions, 7

Ethyl glyoxylate

anionic polymerization, 41

*See also* Poly(ethyl glyoxylate) (PETG)

Extrapolation methods, lifetime prediction, 160

## F

Failure criteria, lifetime prediction, 160

Fatty acids

castor incorporation in polyesters, 67, 68f

influencing properties of polymers, 61

poly(ester-anhydrides), 61–66

poly(lactic acid-co-castor oil)

polyesters, 67, 68f

poly(lactic-co-ricinoleic acid) ester, 67

polyesters with, 66–67

polymer development, 60

ricinoleic acid incorporation in polyesters, 67

*See also* Poly(ester-anhydrides)

Film surface changes, oxidation, 10

Film weight gain, oxidation, 9–10, 11f

Fire properties, poly(ethylene)/zinc copper hydroxy stearate nanocomposites, 217

Fluoropolymers. *See* Piezoelectric fluoropolymers

Foamed polysiloxanes with nanoparticles

2D slices of foam structure during deformation, 271, 274*f*

3D X-ray computer tomography (3DCT), 271, 273*f*

carborane modified materials, 257–258

cell structure and physical properties, 256

compressive strain plots for modified PDMS materials, 260*f*

development and characterization of foams, 268–269, 271

elastomers of poly(dimethylsiloxane) (PDMS), 257

experimental, 257

finite element (FE) mesh overlaid onto 3DCT, 271, 273*f*

foam structure, 269

force decay curves for, with varying closed cell contents, 268*f*

picture of elliptically deformed foam cell structures, 269*f*

pictures of foam structure before and after removal of pore former, 272*f*

polyhedral oligomeric silsesquioxane (POSS) modified materials, 258, 262

scanning electron microscopy (SEM) of PDMS modified with silica nano fibers, 262, 263*f*

schematic of carborane modified PDMS system, 259*f*

schematic of POSS, 260*f*

SEM pictures of PDMS with CNF, 262, 265*f*

SEM showing discrete fibrous nature of CNF, 262, 266*f*

silica and carbon nano fiber (CNF) modified systems, 262

stress-strain curves for foamed and unfoamed PDMS systems, 270*f*

stress-strain curves for PDMS with fumed silica, 262, 263*f*

stress-strain curves for PDMS with silica nano fiber, CNF and single- and multi-walled nano fiber, 262, 267*f*

stress-strain curves for PDMS with silica nano fibers, 262, 264*f*

stress-strain hysteresis of silica and POSS filled PDMS composites, 261*f*

T<sub>2</sub> relaxation time changes for silica filled PDMS vs. gamma radiation doses, 258*f*, 259*f*

Foams

2D slices of structure during deformation, 271, 274*f*

3D X-ray computer tomography (3DCT), 271, 273*f*

desirable properties, 268

development and characterization, 268–269, 271

pictures of structures before and after pore former, 272*f*

stress strain curves for foamed and unfoamed PDMS, 270*f*

structure, 269

Forest soil, biodegradation of polyethylene with pro-oxidant additive, 12

Fragmentation, degradation, 4

Fungal growth and degradation, enzymatic attack, 7

**G**

Gamma radiation, carborane modified poly(dimethylsiloxane) (PDMS) samples, 257–258, 259*f*

Gas product analysis, plastic-bonded explosive PBX 9501, 230–231, 232*f*

Gel permeation chromatography (GPC)

degradation measurement, 44

plasticized poly(ester urethane)

binder with and without

stabilizer, 188, 190*f*

poly(ethyl glyoxylate) degradation, 48, 49*f*

soy polymers, 76, 77, 80*f*

Glass transition temperature, cured

and uncured poly-p-phenylene

resins, 205, 206

Green processing. *See* Soy polymers

## H

Heat release rate curves,

poly(ethylene) and

nanocomposites, 215–216

Hot water exposure, poly(ethylene)

pipes, 161, 163

Hydrolytic degradation

aging mechanism, 183

Estane® binder with

nitroplasticizer (NP), 188, 191–193

experimental, 183–184

hydrolyzed Estane® sample with

NMR Mobile Universal

Explorer (NMR MOUSE), 193

molecular weight and relative

amount of alcohol end groups,

193, 194*f*

predicting hydrolysis products with

alcohol end-groups, 191–192

proton spin-spin relaxation decay

curve of hydrolyzed Estane®,

193, 195*f*

*See also* Poly(ester urethane)

binder, plasticized

Hydroxy double salts (HDSs)

enhancing thermal stability, 210

*See also* Nanodimensional layered metal hydroxides

Hyperbranched aliphatic polyesters

biodegradation behavior, 22–24

characteristics, 19

dendritic macromolecules, 18

diffusion coefficient, 21

equation for flux, 21

experimental, 19, 21–22

glass transition behavior of

different networks, 25*f*

hydrolytic degradation at surface or

bulk, 23

marine biodegradation behavior of

2nd and 4th generations of pure

Boltorn™, 23*f*

materials, 19, 21–22

mineralization calculation, 22

oxygen barrier behavior, 26–28

oxygen barrier characteristics of

pure, and networks, 27*t*

oxygen permeability, diffusivity

and solubility of, networks,

29*f*

permeability, 21

schematics of Boltorn™, 20*f*

sea biodegradation, 23–24

stress-strain behavior of, networks,

26*f*

techniques, 21–22

thermal and stress-strain behavior,

25–26

water uptake behavior, 24*f*

## I

Incineration, waste disposal, 32

International Space Station (ISS). *See*

Materials International Space

Station Experiment (MISSE-6)

Irradiation

bisphenol A polycarbonate, 299,

303

*See also* Polycarbonate (PC)

**K****Kinetic models**

KINOXAM, 121

*See also* Embrittlement in oxidative aging**Kinetics**

Estane® oxidation without oxygen, 236

oxidation of plasticized poly(ester urethane) binder, 186, 187*f*rates for evolution of product gases from Constituent Aging Study (CAS) samples and HMX explosive crystals, 231, 232*f***KINOXAM**

kinetic model, 121

*See also* Predictions for polymers in oxidative environments**L**Landcover for agricultural mulching, polyethylene with pro-oxidant additive, 14, 15*f*Landfill cover, polyethylene with pro-oxidant additive, 14, 15*f*

Land filling, alternative recovery methods, 32

Laser scanning confocal microscopy (LSCM)

epoxy coatings with and without dispersant after outdoor exposure, 281, 284*f*, 285*f*, 286pigmented epoxy coatings, 279, 280, 282*f*

Layered double hydroxides (LDHs)

enhancing thermal stability, 210

*See also* Nanodimensional layered metal hydroxides

Lead stearate, thermo-oxidative degradation of poly(vinyl chloride) (PVC), 220–223

**Lifetime prediction**

chlorosulfonated polyethylene (PE) cables, 164, 166

extrapolation, 160

failure criteria, 160

kinetic model, 130, 132–133

lifetime vs. temperature for

Hypalon core insulation aged in nitrogen, 168*f*

master curve of indenter modulus of jacketing based on

chlorosulfonated PE, 166*f*method for pipes, from oxidation induction time (OIT) data, 162*f*OIT vs. exposure time, 165*f*PE in air vs. dose rate, 132*f*

PE hot water pipes, 161, 163

poly(vinyl chloride) (PVC) cables, 167

polymeric products, 160

polyolefin pipes exposes to

chlorinated water, 163–164

Light-induced degradation,

mechanisms, 288

Litter control, polyethylene with pro-oxidant additive, 12, 13*f*

Lubricants, vegetable oils, 75

**M**Maleic anhydride, modifying acrylated epoxidized soybean oil (AESO), 73*f*

Mass loss

polysiloxane nanocomposite systems, 249

rate curves for poly(ethylene) and nanocomposites, 216

Materials International Space Station Experiment (MISSE-6)

bimorph position vs. 24h excitation cycling, 109*f*bimorph position vs. excitation time and temperature, 109*f*

- electronics for driving and sensing  
bimorphs, 108, 110  
experimental details, 105, 107–110  
Long Duration Exposure Facility  
(LDEF) Experiment, 103  
Passive Experiment Container  
(PEC), 103, 104*f*, 105  
Photo-sensor signal intensity vs.  
absolute film position, 107*f*  
position sensors, 110  
sample arrangements, 106*f*  
self-sufficiency of experiments,  
108  
*See also* Piezoelectric  
fluoropolymers
- Michigan State University,  
composting pile, 33, 35*f*
- Mineralization  
calculation, 22  
simulated composting, 38, 39*f*
- Models  
classic diffusion, of drug release,  
55  
*See also* Embrittlement in oxidative  
aging; Predictions for polymers  
in oxidative environments
- Moisture uptake, cured and uncured  
poly-*p*-phenylene resins, 205,  
206*t*
- Molar mass changes  
embrittlement criterion, 139, 142  
oxidation, 139  
oxidation induced embrittlement,  
136*f*  
strain at break vs., 142*f*  
weight average, vs. time of  
exposure, 141*f*
- Molecular weight analysis  
plastic-bonded explosive PBX  
9501, 231, 233–234  
*See also* Gel permeation  
chromatography (GPC)
- Morphological changes  
Ductile-brittle transition, 145*f*  
embrittlement criterion, 142–143  
oxidation induced embrittlement,  
136*f*  
presumed shape of thermal aging  
point trajectories, 145*f*  
strain at break, 144*f*
- Multiple Quantum nuclear magnetic  
resonance (MQ NMR)  
elastomer network structure and  
heterogeneities, 171  
pulse, 172*f*  
*See also* Silicon based polymer  
systems
- Municipal solid waste, containers and  
packaging, 32
- N**
- Nanocomposites  
polymer, with layered metal  
hydroxides, 210  
*See also* Polysiloxane  
nanocomposites
- Nanodimensional layered metal  
hydroxides  
anion exchange, 211  
basal spacing for ZCA, 212  
compatibility improvements with  
zinc copper acetate (ZCA), 211  
composite preparation of  
poly(ethylene)/zinc copper  
hydroxy stearate (PE/ZCHS),  
211  
cone calorimetry, 215–217  
differential thermal analysis  
(DTA), 211  
DTA for pure PE, PE-ZCHS-5 and  
PE-ZCHS-10, 214–215  
enhancing thermal stability of  
polymers, 210  
experimental, 210–211  
fire properties of PE-ZCHS  
nanocomposites, 217  
heat release rate curves, 215–216  
mass loss rate curves vs. time, 216*f*



TGA analysis, 213–214  
 thermogravimetric analysis (TGA), 211  
 time to ignition, 216, 217*t*  
 wide-angle x-ray scattering method, 211  
 XRD data for ZCA and partially exchanged ZCHS revealing new phases, 212*f*  
 ZCA and ZCHS peaks, 212–213  
 Nanoparticles. *See* Foamed polysiloxanes with nanoparticles  
 Network reformation, nanocomposite systems, 252, 253*f*  
 Nicotine  
 drug load and rate release, 54–55  
 mass of, released from poly(caprolactone) vs. time, 55, 56*f*  
 proposed mechanism for release from degradable polymer, 57, 58*f*  
*See also* Poly( $\epsilon$ -caprolactone) (PCL)  
 Nitroplasticizer (NP)  
 chemical structure, 182*f*, 229*f*  
 composition, 182, 228  
*See also* Plastic-bonded explosive PBX 9501; Poly(ester urethane) binder, plasticized  
 Non-empirical kinetic model. *See* Predictions for polymers in oxidative environments  
 Norrish I and II reactions  
 polyamides and polyesters, 288, 289, 290  
 possible Norrish I reactions in poly(butylene terephthalate) (PBT), 293, 296  
 Nuclear magnetic resonance (NMR)  
 aged and unaged plasticized poly(ester urethane) binder, 188, 191  
 chemical speciation changes, 171  
 degradation measurement, 43

multiple quantum (MQ) NMR, 171  
 oxidation of plasticized poly(ester urethane) binder, 185–186  
 plastic-bonded explosive PBX 9501, 234–235  
 poly(ethyl glyoxylate), 44, 45*f*  
 poly(ethyl glyoxylate) spectra vs. degradation time, 50, 51*f*  
 soy polymers, 76, 79, 81*f*, 82*f*, 84*f*, 85*f*  
*See also* Silicon based polymer systems  
 Nuclear magnetic resonance Mobile Universal Surface Explorer (NMR MOUSE), hydrolsis of plasticized poly(ester urethane) binder, 193

## O

Optical scattering, pigmented epoxy coatings, 279, 281, 284*f*, 285*f*, 286  
 Oxidation  
 apparent termination rate constant for poly(ethylene) (PE), 128*f*  
 film degradation, 9–10  
 induction time for PE in oxygen excess, 127*f*  
 maximum, rate for PE in oxygen excess, 127*f*  
 normalized, profiles into thick PE, 130*f*  
 spatial distribution of, products for PE after exposure in air, 131*f*  
 thickness of, layer for PE in air vs. dose rate, 131*f*  
*See also* Embrittlement in oxidative aging  
 Oxidation induction time (OIT)  
 exposure of polyolefin pipes to chlorinated water, 163–164  
 OIT vs. exposure time, 165*f*  
 predicting lifetime of poly(ethylene) (PE) pipes, 162*f*, 163

- Oxidative chain scission, poly-(vinyl chloride) (PVC), 222–223, 224*f*
- Oxidative degradation  
aging mechanism, 183  
Estane® binder with  
nitroplasticizer (NP), 185–186, 188, 193  
experimental, 183–184  
first order kinetics fitting NMR data, 186, 187*f*  
tensile properties of aged Estane®/NP samples, 186, 188, 189*f*  
*See also* Poly(ester urethane) binder, plasticized
- Oxidative environments. *See* Predictions for polymers in oxidative environments
- Oxygen absorption  
poly(ethylene) (PE) in oxygen excess, 124*f*  
typical shape of kinetic curves, 122*f*  
*See also* Predictions for polymers in oxidative environments
- Oxygen barrier behavior, hyperbranched aliphatic polyesters, 26–28
- Oxygen diffusion/reaction coupling, kinetic model, 126, 129–130
- Oxygen diffusivity, hyperbranched aliphatic polyesters, 27–28, 29*f*
- P**
- Packaging materials, recycling or recovery, 32
- Paclitaxel, polymer formulation containing, 65–66
- PBO. *See* Poly(p-phenylene benzobisoxazole) (PBO) fibers
- Permeability  
equation, 21  
hyperbranched aliphatic polyesters, 26–27, 29*f*
- Photodegradation  
measuring photo-generated CO<sub>2</sub>, 148  
*See also* Carbon dioxide photo-generation
- Photo-Fries reaction, bisphenol A polycarbonate, 290, 291
- Photolysis  
light-induced degradation, 288  
weathering of polymers, 288
- Photo-oxidation  
light-induced degradation, 288  
weathering of polymers, 288
- Piezoelectric fluoropolymers  
adaptive optics mirrors for low earth orbit (LEO) telescopes, 101  
bimorph position vs. 24h excitation cycling, 109*f*  
bimorph position vs. excitation time and temperature, 109*f*  
electronics for driving and sensing bimorphs, 108, 110  
examining poly(vinylidene fluoride) (PVDF) and copolymers, 101  
experimental, 102–103  
LEO materials exposure to atomic oxygen (AO), 102  
Materials International Space Station Experiment (MISSE-6), 103, 105  
MISSE-6 experimental details, 105, 107–110  
MISSE Passive Experiment Container (PEC), 103, 104*f*  
photo-sensor signal intensity vs. absolute film position, 107*f*  
position sensors, 110  
sample arrangements for VUV side and VUV + AO, 106*f*  
self-sufficiency of experiments, 108

- VUV radiation, 101–102
- Pigmented epoxy coatings
- characterization methods for
    - microstructure and dispersion, 277, 278
  - experimental, 277–279
  - glass transition temperature, storage modulus, and 20° gloss retention for, without and without dispersant, 283*f*
  - laser scanning confocal microscopy (LSCM) images for, with and without dispersants after outdoor exposure, 281, 284*f*, 285*f*
  - material properties measurements, 279
  - materials, 277
  - optical properties measurements, 279
  - outdoor UV exposure method, 278
  - pigment dispersion and UV degradation, 281–282, 283*f*
  - sample preparation, 278
  - structure and pigment dispersion
    - characterization by ultra small angle neutron scattering (USANS), 280, 281*f*
  - surface morphology and optical properties of, with and without dispersant, 280, 282*f*
  - surface morphology
    - characterization, 279
  - surface morphology of coatings
    - after exposure, 281, 286
- Plant oils
- polymers based on, 71
  - raw materials, 70
  - See also* Soy polymers
- Plastic-bonded explosive PBX 9501
- aging study findings, 230
  - change in Estane® molecular weight distribution vs. aging time, 233, 234*f*
  - combinations of constituents of PBX 9501, 230*t*
  - composition, 228
  - Estane® 5703 and nitroplasticizer (NP), 228, 229*f*
  - future work, 237
  - gas product analysis, 230–231
  - kinetic results normalized by initial NP, 236*t*
  - kinetics for rate of product gases
    - from degradation of Constituent Aging Study (CAS) samples and neat HMX, 231, 232*f*
  - kinetics of Estane® oxidation
    - without oxygen, 236
  - molecular weight analysis, 231, 233–234
  - NP normalized crosslinking rate for CAS samples, 237*f*
  - nuclear magnetic resonance (NMR) studies, 234–235
  - proposed mechanism for
    - decomposition of model similar to NP, 229*f*
- Plasticized poly(ester urethane) binder. *See* Poly(ester urethane) binder, plasticized
- Plasticizer migration, poly(vinyl chloride) (PVC), 167
- Plastics
- compostability, 32–33, 38
  - environmentally degradable, 3–8
  - landfill degradation of films, 14, 15*f*
- Polyamides
- CO and CO<sub>2</sub> formation during weathering, 292, 295*f*
  - CO and CO<sub>2</sub> formation vs. drop in elongation at break, 297, 299*f*
  - CO formation vs. oxygen uptake, 292, 294*f*
  - CO<sub>2</sub> formation vs. oxygen uptake, 292, 295*f*
  - drop of elongation at break of polyamide 6 (PA6) weathered in borosilicate, 293, 298*f*
  - experimental, 290, 292

- Norrish I and II reactions, 288, 289, 290
- oxygen uptake, 292, 294*f*
- photolysis and photo-oxidation, 288
- UV absorption spectrum of PA6, 289*f*
- weathering tests, 290, 292
- Poly(butylene terephthalate) (PBT)
- CO and CO<sub>2</sub> formation during weathering, 292, 295*f*
- CO and CO<sub>2</sub> formation vs. drop in elongation at break, 297, 299*f*
- CO formation vs. oxygen uptake, 292, 294*f*
- CO<sub>2</sub> formation vs. oxygen uptake, 292, 295*f*
- drop of elongation at break of, weathered in borosilicate, 293, 298*f*
- experimental, 290, 292
- oxygen uptake, 292, 294*f*
- PBT and its polytetrahydrofuran (PECO-1) and poly(propylene glycol) (PECO-2) copolymer, 297, 299, 300*f*, 301*f*, 302*f*
- photolysis and photo-oxidation, 288
- possible Norrish I reactions, 293, 296
- UV absorption spectrum, 289*f*
- weathering tests, 290, 292
- Poly( $\epsilon$ -caprolactone) (PCL)
- biodegradable, non-toxic polymer, 53
- calculating mass of water in particle, 56–57
- calibration curve, 54
- classic diffusion model of drug release, 55
- degree of matrix swelling, 55, 56
- drug delivery systems, 53
- investigating drug load on release rate from, 54–55
- in vitro assay, 54
- mass of nicotine released from PCL pellets vs. time, 55, 56*f*
- materials and methods, 53–54
- melt mixing and pellet formation, 53–54
- proposed mechanism for nicotine release, 57, 58*f*
- time dependent diffusion coefficient for drug, 56
- water content, 55
- Polycarbonate (PC)
- absorbance at 320 nm vs. irradiation time in weathering tests CPS and XXL+, 303, 304*f*
- absorbance at 1713 cm<sup>-1</sup> vs. irradiation time in CPS and XXL+, 303, 305*f*
- bisphenol A PC, 299, 303
- experimental, 290, 292
- fluorescence emission at 480 nm vs. irradiation time in CPS and XXL+, 303, 304*f*
- fluorescence spectra method, 292
- photo-Fries reaction, 290, 291
- photolysis and photo-oxidation, 288
- UV absorption spectrum, 289*f*
- Poly(dimethylsiloxane) (PDMS)
- backbiting reactions, 252, 253*f*
- compressive strain plots for variety of PDMS materials, 260*f*
- desiccative aging of highly filled PDMS sample, 176, 177*f*
- distributions of residual dipolar couplings in thermally degraded PDMS composites, 174*f*
- growth curve for pristine sample, 173*f*
- inclusion of filler phase, 256
- producing foamed systems, 257
- radiation degraded PDMS networks, 175, 176*f*
- thermally degraded PDMS, 172–175

- See also* Foamed polysiloxanes with nanoparticles; Polysiloxane nanocomposites; Silicon based polymer systems
- Poly(ester-anhydrides)  
 administration routes, 62  
 appearance after exposure to aqueous media, 64  
 bifunctional fatty acid ricinoleic acid, 62–63  
 drug delivery, 61  
 fatty acid incorporation into polyanhydride chain, 62  
 fatty acid terminated, 62*f*  
 formulations containing anticancer agents, 65–66  
 in-situ gelation mechanism, 64–65  
 lithocholic acid containing polyanhydrides, 63*f*  
 paclitaxel incorporation into polymer matrix, 65–66  
 physicochemical properties and ricinoleic acid content, 63–64  
 preparation, 61–62  
 structure of poly(sebacic-*co*-ricinoleic acid) anhydride, 63*f*  
*See also* Fatty acids
- Poly(ester urethane) binder, plasticized  
 accelerated aging, 182  
 aging mechanisms, 183  
 binder sample preparation, 183  
 chemical structure of Estane® 5703 and nitroplasticizer NP (BDNPA/F), 182*f*, 229*f*  
 comparing experimental data with hydrolysis model, 192*f*  
 evaluation of mechanical properties, 186, 188, 189*f*  
 experimental, 183–184  
 first order kinetics fitting NMR data, 186, 187*f*  
 gel permeation chromatography (GPC), 184  
 GPC of, with and without Irganox 1010, 188, 190*f*  
<sup>1</sup>H NMR of aged and unaged Estane®/NP/Irganox 1010, 188, 191  
<sup>1</sup>H NMR spectra of Estane®/NP binder aged at 85°C, 186*f*  
<sup>1</sup>H nuclear magnetic resonance (NMR), 184  
 hydrolysis with NMR Mobile Universal Surface Explorer (NMR MOUSE), 193  
 hydrolysis without stabilizer, 188  
 hydrolytic binder degradation study, 188, 191–193  
 instrumentation, 184  
 molecular weight vs. relative alcohol end-groups for hydrolyzed Estane® and Estane®/NP/Irganox, 193, 194*f*  
 NMR and GPC validating predictive models for hydrolysis, 191–192  
 oxidative binder and hydrolytic binder degradation aging studies, 184  
 oxidative binder degradation study, 185–186, 188  
 percentage oxidation of Estane® based on NMR, 187*t*  
 predicting relative hydrolysis products with alcohol end-groups, 192, 194*f*  
 proton spin-spin relaxation decay curve of hydrolyzed Estane®, 193, 195*f*  
 stress-strain curves for tensile data of Estane®/NP, 189*f*  
 tensile property testing, 184  
 tensile stress at 400% strain for samples with oxidation of methylene carbon of Estane, 189*f*  
*See also* Plastic-bonded explosive PBX 9501

## Polyesters

- biodegradable, 66–67
- CO<sub>2</sub> evolution during photodegradation, 157
- Norrish I and II reactions, 288, 289, 290
- photolysis and photo-oxidation, 288
- weathering tests, 290, 292

*See also* Hyperbranched aliphatic polyesters; Unsaturated polyesters (UPs)

## Poly(ethylene) (PE)

- Arrhenius plot of apparent termination rate constant, 128*f*
- Arrhenius plot of maximum oxidation rate, 127*f*
- Arrhenius plot of oxidation induction time, 127*f*
- carbonyl group development, 150, 153–154
- chlorosulfonated PE cables, 164, 166
- lifetime prediction, 130, 132–133
- lifetime prediction of PE hot water pipes, 161, 163
- normalized oxidation profiles into thick PE, 130*f*
- O<sub>2</sub> absorption curves in oxygen excess, 124*f*
- photogeneration of CO<sub>2</sub>, 150, 151*f*, 152*f*
- possible causal chains for oxidation induced embrittlement in PE, 136*f*
- spatial distribution of oxidation products for, after exposure in air, 131*f*
- thermally degradable PE films, 8–9
- thermal oxidation, 135
- thickness of oxidized layer for PE in air vs. dose rate, 131*f*
- TiO<sub>2</sub> pigments and photo-oxidation of PE, 148

*See also* Carbon dioxide photo-generation; Embrittlement in oxidative aging; Polyolefins; Predictions for polymers in oxidative environments

## Poly(ethylene terephthalate) (PET)

photogeneration of CO<sub>2</sub>, 154, 156*f*

*See also* Carbon dioxide photo-generation

## Poly(ethyl glyoxylate) (PEtG)

- anionic polymerization, 41
- chromatography, 48, 49*f*
- chromatography studies, 44
- degradation, 46, 48, 50
- degradation assumptions, 42
- ester group hydrolysis, 50, 51*f*
- evolution of pH during degradation, 47*f*
- experimental, 42–44
- gel permeation chromatography (GPC) during degradation, 48*t*
- <sup>1</sup>H nuclear magnetic resonance (NMR), 44, 45*f*
- mechanism of degradation, 50, 51*f*
- molar mass determination, 42–43
- NMR studies, 42–43, 50
- potentiometry, 43, 46, 47*f*
- synthesis, 42, 44, 46
- thermal analysis, 43
- thermogravimetric analysis, 46, 47*f*
- weight loss, 43, 46, 48

## Polyhedral oligomeric silsesquioxane (POSS)

- modified poly(dimethylsiloxane) (PDMS) samples, 258, 262
- schematic, 260*f*
- stress-strain hysteresis of silica and POSS filled PDMS composites, 261*f*

## Poly(lactic acid-co-castor oil)

- polyesters, fatty acid incorporation, 67, 68*f*

## Poly(lactic-co-ricinoleic acid) ester,

- fatty acid incorporation, 67

- Poly(lactide) (PLA)  
 biodegradation of PLA bottles in commercial composting, 35, 37*f*  
 hydrolytic chain scission of PLA, 38, 39*f*  
 renewable resources, 32
- Polymer blends, environmentally degradable polyolefins, 7
- Polymer matrix resin, undesirable properties, 199
- Polymer radiolysis  
 kinetic model, 125–126  
 radiochemical yields in oxygen excess, 128*t*
- Polymers in oxidative environments. *See* Predictions for polymers in oxidative environments
- Polymer systems, predictive aging models, 256
- Poly(methyl methacrylate) (PMMA), layered hydroxy salts, 210
- Polyolefins  
 additive Totally Degradable Plastic Additive (TDPA™), 3, 10, 12  
 analytical measurements, 8  
 applications of environmental degradation of PE/TDPA™ films, 12–14  
 approaches to environmentally degradable, 6–8  
 behavior of TDPA film in landfill, 14*t*  
 biodegradation of oxidized films, 10, 12  
 compost, 10, 12  
 elemental analysis, 8  
 environmentally degradable, 3  
 experimental for environmentally degradable, 8–9  
 film surface changes, 10  
 film weight gain, 9–10  
 forest soil, 12  
 landcover for agricultural mulching, 14, 15*f*  
 landfill cover, 14, 15*f*  
 litter, 12, 13*f*  
 outdoor exposure of PE with TDPA™ prodegradant, 12, 13*f*  
 oxidation, 9–10  
 pro-oxidant additives, 3  
 properties, 3  
 respirometer biodegradation testing, 9  
 size exclusion chromatography (SEC), 8  
 spectroscopic characterization, 8  
 thermally degradable polyethylene (PE) films, 8–9  
 weight gain by films in air, 11*f*
- Poly(*p*-phenylene benzobisoxazole) (PBO) fibers  
 applications, 114  
 difference spectra of officer's new and archive vest yards vs. spectrum of virgin yarn, 115–116  
 difference spectra vs. exposure time for aged vests, 117, 119*f*  
 experimental, 114–115  
 Fourier transform infrared spectroscopy (FTIR), 115  
 laboratory aging, 114–115  
 negative peaks in infrared difference spectra, 117  
 proposed intermediate products in PBO synthesis, 118*f*  
 tensile properties of vest yarns, 115, 116*t*  
 tensile properties of vest yarns during environmental chamber exposure, 117, 119*t*  
 tensile testing, 115
- Poly-*p*-phenylene resins  
 experimental, 199–201  
 glass transition temperature of cured and uncured Navy P3-2300-PE, 205, 206  
 methods of analysis, 201

- moisture uptake of cured and uncured Navy P3-2300-PE, 204, 206*t*
- rheometry data, 204, 205*f*
- structure of Navy P3-2300-PE, 200*f*
- synthesis, 200
- thermogravimetric analysis (TGA) for Navy P3-2300-PE, 204, 205*f*
- See also* Cyanate esters
- Poly(propylene) (PP)
- carbonyl group development, 150, 153–154
- photogeneration of CO<sub>2</sub>, 150, 151*f*, 152*f*
- See also* Carbon dioxide photogeneration
- Poly(propylene glycol)/poly(butylene terephthalate) copolymer
- CO formation vs. aging time of, and PBT, 297, 301*f*
- CO<sub>2</sub> formation vs. aging time of, and PBT, 297, 301*f*
- drop of elongation at break of, aged in borosilicate, 297, 300*f*
- formation rate of CO and CO<sub>2</sub> in air, 297, 302*f*
- oxygen uptake of, and PBT, 297, 299, 300*f*
- Polysiloxane nanocomposites
- accelerated aging methodology, 243
- aging of filled polysiloxanes, 240
- aging of polysiloxane elastomers, 241
- BDS (broadband dielectric spectroscopy) method, 241–242
- BDS analysis, 245–246
- BDS spectra of 2% Cloisite system aged under dry N<sub>2</sub>, 246, 247*f*
- BDS spectra of 2% Cloisite system aged under moist air, 246, 247*f*
- BDS spectra of nanocomposite systems, 246*f*
- BDS spectra of unfilled elastomer, 245*f*
- composite differential distillation profiles for virgin, N<sub>2</sub>-aged, and air-aged 2% Cloisite filled systems, 251*f*
- experimental, 241–243
- GC/MS chromatogram of collected cold-ring fraction from virgin unfilled elastomer, 251*f*
- intramolecular chain backbiting mechanisms, 253*f*
- micron scale silica filler, 240
- model of network reformation, 252
- onset degradation temperature vs. age time for systems aged under moist air, 249*f*
- onset degradation temperature vs. age time for systems aged under N<sub>2</sub>, 248*f*
- percentage mass loss vs. sample age, 250*f*
- preparation of siloxane-montmorillonite nanocomposites, 243
- sample mass analysis, 249
- thermal volatilization analysis (TVA) method, 242–243
- thermogravimetric analysis (TGA), 248
- TVA characterizing volatile species, 249–250, 251*f*, 252
- TVA system diagram, 244*f*
- Polysiloxanes. *See* Foamed polysiloxanes with nanoparticles
- Polytetrahydrofuran/poly(butylene terephthalate) copolymer
- CO formation vs. aging time of, and PBT, 297, 301*f*
- CO<sub>2</sub> formation vs. aging time of, and PBT, 297, 301*f*
- drop of elongation at break of, aged in borosilicate, 297, 300*f*



- formation rate of CO and CO<sub>2</sub> in air, 297, 302*f*
- oxygen uptake of, and PBT, 297, 299, 300*f*
- Poly(vinyl chloride) (PVC)
- antioxidant 2,6-di-*t*-butyl-4-methylphenol (BHT) and thermo-oxidative degradation of, 223, 225*t*
  - chain scission per monomer units vs. time, 223, 224*f*
  - FTIR spectra of starting and oxidized PVC, 223, 225*f*
  - importance of recycling, 220
  - lead stearate and thermo-oxidative degradation of, 220–223
  - lifetime prediction of PVC cables, 167
  - major reactions of thermo-oxidative degradation, 221
  - molecular weight distributions (MWDs) of, with oxygen with and without lead stearate, 220, 221*f*, 222*f*
  - oxidative chain scission, 222, 224*f*
  - reversible blocking mechanism, 220
  - thermal degradation, 219
- Poly(vinyl ester) (PVE), layered hydroxy salts, 210
- Potentiometry
- degradation measurement, 43
  - poly(ethyl glyoxylate) degradation, 46, 47*f*
- Prediction models
- hydrolysis of plasticized poly(ester urethane) binder, 191–192
  - polymer systems, 256
  - See also* Lifetime prediction
- Predictions for polymers in oxidative environments
- Arrhenius plot of apparent termination rate constant for polyethylene (PE), 128*f*
  - Arrhenius plot of maximum oxidation rate for PE in oxygen excess, 127*f*
  - Arrhenius plot of oxidation induction time for PE in oxygen excess, 127*f*
  - "closed-loop" mechanistic scheme (CLM), 122–123
  - core of model, 122–123
  - kinetic model KINOXAM, 121
  - lifetime prediction, 130, 132–133
  - non-terminating bimolecular combination, 123, 125
  - O<sub>2</sub> absorption curves for PE in excess oxygen, 124*f*
  - oxygen diffusion/reaction coupling, 126, 129–130
  - parameters for kinetic modeling, 124*t*, 126*t*
  - plot of lifetime for PE in air vs. dose rate, 132*f*
  - plot of thickness of oxidized layer for PE in air vs. dose rate, 131*f*
  - polymer radiolysis, 125–126
  - radiochemical yields in oxygen excess, 128*t*
  - spatial distribution of oxidation products for PE after exposure, 131*f*
  - typical shape of normalized oxidation profiles into thick PE, 130*f*
  - typical shapes of kinetic curves of O<sub>2</sub> absorption, 122*f*
  - See also* Lifetime prediction
- Pressure, molecular weight of soy polymers, 83, 86*t*
- Pro-oxidant additives, degradation of polyolefins, 3
- Prostate cancer, polymer-paclitaxel formulation, 66

## R

- Radiation degradation,  
poly(dimethylsiloxane) network,  
175, 176*f*
- Radical chain oxidation, oxidation  
induced embrittlement, 136*f*
- Radical chemistry, from, to molar  
mass validation, 136–137, 139
- Recycling  
poly(vinyl chloride) (PVC), 220  
waste disposal, 32
- Renewable resources  
biopolymers, 32  
"cradle to gate, grave and cradle"  
diagram of biopolymers from,  
32, 34*f*
- Reversible blocking mechanism,  
thermo-oxidative degradation of  
poly(vinyl chloride) (PVC), 220
- Rheometry, poly-p-phenylene resin vs.  
temperature, 204, 205*f*
- Ricinoleic acid  
bifunctional fatty acid, 62–63  
incorporation into poly(ester-  
anhydride), 63–64  
incorporation into poly(lactic acid),  
67  
*See also* Fatty acids

## S

- Shear viscosity, poly-p-phenylene  
resin vs. temperature, 204, 205*f*
- Silica nano fibers  
poly(dimethylsiloxane) (PDMS)  
modified with, 262, 263*f*  
stress-strain curves for PDMS  
modified with, carbon nano fiber  
and single- and multi-walled  
nano fiber, 262, 267*f*  
stress strain curves for PDMS with,  
262, 264*f*
- Silicon based polymer systems

- applications, 171  
characterization of desiccatively  
aged materials, 176, 177*f*  
characterization of radiation  
degraded materials, 175, 176*f*  
characterization of thermally  
degraded materials, 172–175  
dynamic order parameter  $S_b$ , 171  
experimental, 171–172  
growth curve for pristine sample,  
173*f*
- MQ NMR (multiple quantum  
nuclear magnetic resonance),  
171
- MQ NMR analysis of highly filled  
PDMS in desiccating  
environment for 4 years, 177*f*
- MQ NMR analysis of radiatively  
degraded PDMS networks, 176*f*
- MQ NMR pulse, 172*f*
- network structure of typical  
engineering silicone, 173*f*
- NMR and chemical speciation  
changes, 171
- residual dipolar couplings from  
MQ NMR of thermally  
degraded PDMS composites,  
174*f*
- simultaneous cross-linking and  
chain scission consistent with  
MQ NMR data, 175
- speciation changes at polymer-filler  
interface, 177*f*
- Thikonov regularization  
(FTIKREG) algorithm, 172
- Solubility, hyperbranched aliphatic  
polyesters, 27–28, 29*f*
- Soybeans  
composition, 71  
conversion of, oil to polymers, 71  
crop plant, 70  
*See also* Soy polymers
- Soy polymers  
acrylated epoxidized soybean oil  
(AESO) based resin, 71

- analysis, 76–77
- brominated polyol, 71–72
- $^{13}\text{C}$  NMR of polymers of soybean oil (PSBO) using different catalyst amounts, 85*f*
- $^{13}\text{C}$  NMR spectra of soybean oil (SBO) and PSBO, 79, 82*f*
- effect of catalyst amount, 77, 79, 83
- experimental, 75–77
- experimental reactor set-up, 78*f*
- formation of dimers and trimers, 79
- gel permeation chromatography (GPC), 76
- GPC profile of SBO and PSBO, 80*f*
- $^1\text{H}$  NMR of PSBO using different catalyst amounts, 84*f*
- $^1\text{H}$  NMR spectra of SBO and PSBO, 79, 81*f*
- levels of unsaturation in natural oils, 72
- modification of AESO using cyclohexane dicarboxylic anhydride or maleic anhydride, 73
- nuclear magnetic resonance (NMR), 76
- plant oil-based polymers, 71
- polymerization procedure in supercritical carbon dioxide ( $\text{scCO}_2$ ), 77
- polymerization temperature effect, 83
- pressure effect, 83, 86*t*
- proposed cross-linking of natural oils with styrene and divinylbenzene, 72*f*
- reaction temperature effect on molecular weight of PSBO, 80*t*
- ring-opening reactions of epoxidized SBO (ESBO) with reactants, 74
- $\text{scCO}_2$  as solvent, 75
- soybean composition, 71
- soybean crop plant, 70
- viscosity, 76–77
- Space environments. *See* Materials International Space Station Experiment (MISSE-6); Piezoelectric fluoropolymers
- Spin-spin relaxation decay, hydrolysis of plasticized poly(ester urethane) binder, 193, 195*f*
- Starches, polymer blends, 7
- Stresses, plastics degradation, 4
- Stress-strain behavior
- foamed and unfoamed poly(dimethylsiloxane) (PDMS) systems, 269, 270*f*
  - hyperbranched aliphatic polyesters, 25–26
  - PDMS formulated with fumed silica, 262, 263*f*
  - PDMS formulated with silica nano fibers, 262, 264*f*
  - PDMS with silica nano fiber, carbon nano fiber, single- and multi-walled nano fibers, 262, 267*f*
  - silica and polyhedral oligomeric silsesquioxane (POSS) filled PDMS composites, 258, 261*f*
- Styrene
- cross-linking with natural oils, 72*f*
  - See also* Unsaturated polyesters (UPs)
- Sub-critical water (SCW)
- advantages, 89
  - treatment, 90
  - See also* Unsaturated polyesters (UPs)
- Supercritical carbon dioxide
- alternative solvent, 75
  - soy polymer polymerization procedure, 77
  - See also* Soy polymers
- Surface changes, environmentally degradable polyolefins, 7

## T

Temperature, molecular weight of soy polymers, 80*t*, 83

Thermal analysis, degradation measurement, 43

Thermal behavior, hyperbranched aliphatic polyesters, 25–26

Thermal degradation  
poly(dimethylsiloxane) composite, 172–175

poly(vinyl chloride) (PVC), 219  
*See also* Polysiloxane nanocomposites

Thermal stability, polymer nanocomposites with layered metal hydroxides, 210

Thermal volatilization analysis (TVA)  
gas analysis technique, 242–243  
polysiloxane nanocomposite systems, 249–250, 251*f*, 252  
schematic diagram, 244*f*

Thermogravimetric analysis (TGA)  
cured poly-*p*-phenylene resins, 204, 205*f*

cyanate ester resins, 201, 202*f*  
nanocomposite systems as function of age time, 248, 248*f*, 249*f*  
poly(ethylene) and nanocomposites, 213–214  
poly(ethyl glyoxylate), 46, 47*f*

Thermo-oxidative degradation, reactions of poly(vinyl chloride) (PVC), 221

Thermosetting polymeric resins, new types, 199

Thikonov regularization algorithm, multiple quantum nuclear magnetic resonance, 172

Time, biodegradation in environment, 5

Time to ignition, poly(ethylene) and nanocomposites, 216, 217*t*

Titanium dioxide  
pigment dispersion, 277

*See also* Pigmented epoxy coatings

Totally Degradable Plastic Additive (TDPA™)

pro-oxidant additive, 3, 16

*See also* Polyolefins

Transition metals, controlled oxidation, 7

## U

Ultra small angle neutron scattering (USANS), microstructure and pigment dispersion, 278, 280, 281*f*

Unsaturated oils, polymer blends, 7

Unsaturated polyesters (UPs)  
advantages of sub-critical water (SCW), 89

crosslinked with styrene, 89

degradation of UP2 by SCW-treatment with additives, 94*t*

experimental, 89–91

infrared (IR) spectra of UP2 before and after SCW treatment, 96*f*

plausible reactions of UP2 in SCW with additives, 95

preparation of crosslinked UP, 90

re-crosslinking of polystyrene derivative, 91

SCW treatment, 90

SCW treatment of UP2 with additives, 91, 93

SCW treatment of UP2 without additive, 91, 92

separation of reaction mixture, 91

## V

Vegetable oils, lubricant substitutes, 75

Vest yarns. *See* Poly(*p*-phenylene benzobisoxazole) (PBO) fibers

Viscosity, soy polymers, 76–77

**W****Water content**

calculating mass of water in  
particle, 56–57

poly( $\epsilon$ -caprolactone) (PCL), 55

**Weapon systems**

need for new structures, 199

*See also* Cyanate esters; Poly-p-  
phenylene resins

**Weathering of polymers**

photolysis and photo-oxidation,  
288

*See also* Polycarbonate (PC)

**Weight gain**

cured cyanate ester resins, 201,  
203*f*

film oxidation, 9–10, 11*f*

**Weight loss**

degradation measurement, 43

poly(ethyl glyoxylate) degradation,  
46, 48

**Z****Zinc copper acetate (ZCA)**

basal spacing, 212

improving compatibility of  
polyethylene and  
inorganic/organic additive, 210,  
211

x-ray diffraction, 212*f*

**Zinc copper hydroxy stearate (ZCHS)**

poly(ethylene)/ZCHS  
nanocomposites, 211

*See also* Nanodimensional layered  
metal hydroxides

## Chapter 1

# Environmentally Degradable Polyolefins

Graham Swift<sup>1</sup>, Radu Baciu<sup>2</sup>, and Emo Chiellini<sup>3</sup>

<sup>1</sup>GS Polymer Consultants, 10378 East Church, Chapel Hill, NC 27517

<sup>2</sup>EPI, Environmental Products, Inc., 802–1788 West Broadway, Vancouver, British Columbia V6J 141, Canada

<sup>3</sup>Department of Chemistry, University of Pisa, Via Risorgimento 35, 56126 Pisa, Italy

Environmentally degradable polymers are the focus of a great deal of research around the world, which began over half a century ago with the recognition that plastics, particularly in packaging, were becoming a problem with regards to disposal. Two major approaches to replacement plastics were taken to alleviate the prospect of overflowing landfill sites and a litter tarnished environment. The search for modified extant plastics made good sense as the base technologies were commercial successes and available; the other approach was to develop new alternative plastics with desirable properties but with environmentally degradability on disposal or use. This paper is an overview of the development of environmentally degradable polyolefins, which appeared promising initially and were then long disregarded as an undesirable option due to flaws exposed in the early technology developments. In reality, later efforts indicate that there are real opportunities for modified polyolefins and they offer good cost/performance options for many packaging and other applications where environmental degradation is required (1,2).

Polyolefins, such as polyethylene, polypropylene, and polystyrene, for example, were developed as packaging plastics because of their exceptional properties such as resistance to degradation, decomposition, toughness, printability, low density, etc. They have become the predominant plastics in the world and enjoy a huge success because of these properties and their low cost. One of the major flaws of these plastics that had to be overcome in their early development phase was their proclivity towards oxidative degradation. This was overcome by the introduction of antioxidants into their formulations. The addition of such materials proved very successful and polyolefins rapidly dominated the packaging markets. However, the use of antioxidants for stabilization can be considered an inherent weakness and a point of attack if it is desired to develop polyolefins that are unstable in the disposal environments (most) where oxidation can occur. Indeed, this has been a very exploited approach with many attempts to over-ride the formulated antioxidants in a controlled manner by the addition of various oxidation promoters, so-called pro-oxidants, the goal being controlled, environmentally degradable polyolefins through oxidation to small organic fragments and subsequent biodegradation of these polyolefin fragments (1). The efforts and experimental approaches to demonstrating the validity of this approach have not always been consistent in the development and publication of precise information and supportable conclusions that are essential for wide acceptance and commercial success.

However, building on the work of the pioneers, several commercial pro-oxidant additives, are emerging that do indeed offer controlled oxidative degradation of polyolefins. The Totally Degradable Plastic Additive (TDPA™) developed by EPI Environmental Products is a good example of such additives. These have demonstrated, particularly with polyethylene, the ability to produce low molecular weight organic compounds which are biodegradable. This has allowed and will continue to allow the development of environmentally degradable and biodegradable plastics from polyolefins for disposal after use and for designed use in many application sites such as landfill and soil, and will certainly alleviate, if not solve, litter problems.

These environmentally degradable polyolefins, because of their cost/performance profiles are very competitive for the growing markets for such plastics. They will be strong competition for the polyester types such as poly(lactic acid) and polyhydroxyalkanoates so frequently publicized as the innovative solution to plastic waste management.

### **Environmentally Degradable Plastics**

Environmentally degradable plastics have been much promoted, much misunderstood and much misrepresented over the years in spite of sterling work by various standards organizations, ASTM, DIN, CEN, etc., to clarify the

meaning and intent of these plastics through standards for definitions, testing protocols and specifications. Environmental degradation processes that act on plastics when they are disposed of, or even during use in such applications as soil coverage films in agriculture can be represented diagrammatically as shown in Figure 1 which indicates just what is and is not acceptable for safety in the environment.

## ENVIRONMENTAL DEGRADATION PROCESSES

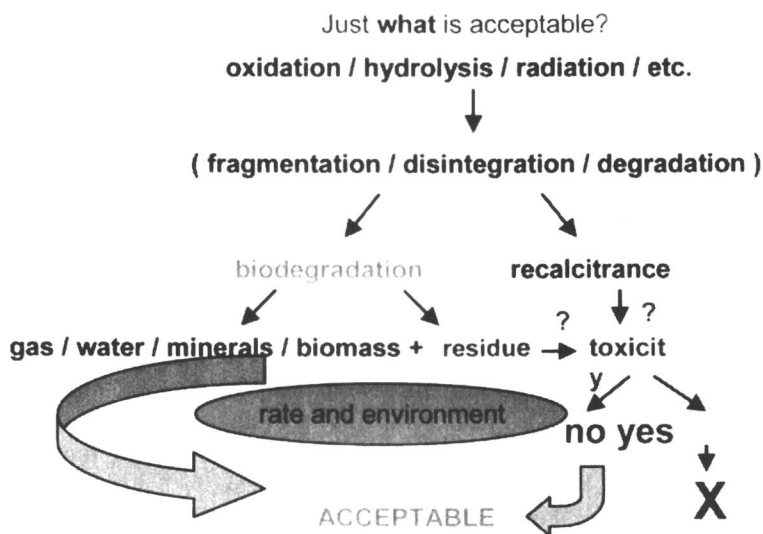


Figure 1. Environmental Degradation and Biodegradation.

Plastics may be subjected to stresses such as oxidation, hydrolysis, radiation, mechanical etc. on exposure in an environment. The first stage of "degradation" is referred to variously as fragmentation, disintegration and degradation, as well as other terms. The low molecular products of this first stage of degradation result in loss of the plastic properties, usually molecular weight loss and chemical changes to form simpler organic molecules such as acids, alcohols, ketones, aldehydes, etc. These lower molecular weight organic compounds may then biodegrade within weeks to months or remain as recalcitrants (these are usually materials that biodegrade very slowly) in the environment depending on their chemical characteristics.



If biodegradation occurs, the rate may be measured by following the volume of gas evolution over time; carbon dioxide is produced in an aerobic environment and methane and carbon dioxide in an anaerobic environment. Any residue may or may not be an issue depending on its toxicity characteristics. If it can be established that complete biodegradation occurs, no residue is left and all organic carbon is accounted for in the gas/mass balance, the original plastic may be considered to present no harmful influence to the environment under consideration. However, if residues remain due to incomplete biodegradation, these must be evaluated, as with recalcitrants (these are often slow biodegraders) for potential toxicity in the environment. If no toxicity is apparent, then one may conclude that all is well and no environmental contamination or harm will occur. The plastics are safe for disposal. If toxicity is established, the plastic should not be disposed of in the environment.

For each of the steps in the flow diagram, Figure 1, standards organizations worldwide have developed very similar and entirely appropriate laboratory simulation methods for testing plastics for use in various environments such as compost, soil, water, etc. Developing plastics may, therefore, be tested and approved as environmentally degradable in a particular environment, such as soil, compost, seawater and freshwater. Based on these methods, specifications have been established for what is and what is not disposable in such sites or use environments.

On a simple level, environmentally degradable plastics can be defined as plastics that degrade in the (an) environment to produce no harmful or toxic products. However, further classification into biodegradable and non-biodegradable is extremely desirable. The former leads to complete removal from the environment; the latter to a concentration build of recalcitrants and residues which, even though not harmful in laboratory tests, need to be recorded and monitored because negative tests, for toxicity or anything else, are never conclusive. Hence the benefit of developing totally biodegradable plastics.

A major issue still to be resolved, even though there is much current agreement on testing, is the time for a plastic to biodegrade in an environment, which is taken as the time from introduction of a plastic into the environment to the time of complete biodegradation as measured in standard tests, which generally stipulate a limit of a few months. This often has a major impact on the acceptability of a plastic, since condensation polymers (polyesters) and addition polymers (polyolefins) differ greatly in the rate and mechanism of degradation to low molecular weight species. Condensation polymers hydrolyze rapidly relative to the oxidative degradation of addition polymers. The degradation species from either degradation pathways are similar, as seen in Figure 2, and once at that stage biodegradation rates are similar. The disparity in first stage degradation rates grossly penalizes addition plastics and most cannot meet current specification for biodegradation. However, addition plastics, such as activated polyolefins, may be classed as environmentally degradable because

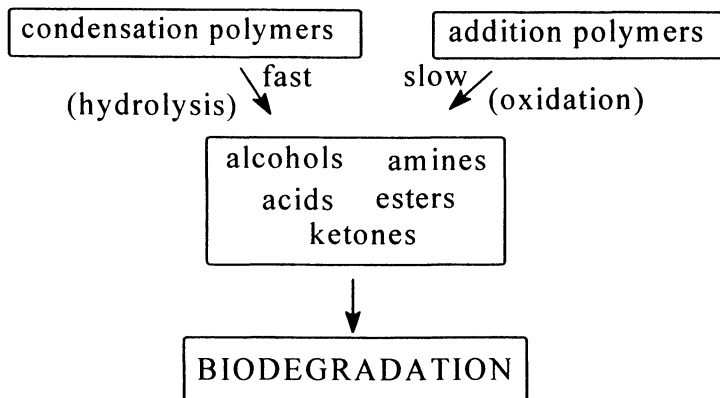


Figure 2. Degradation/Biodegradation of Addition and Condensation Polymers.

they do oxidatively degrade and then biodegrade, albeit at overall rates that are outside the current specifications of most standards.

Given the wide variation in biodegradation rates of natural materials, cf. cellulose v. lignin, it can be reasonably argued that time for and extent of biodegradation, as long as toxicity is not an issue, is irrelevant and certainly far too short as imposed by current testing methodology. This will certainly be a point of contention as products are developed and it is hoped that the standards organizations will reach a resolution. Indications are that resolution is near.

### Approaches to Environmentally Degradable Polyolefins

As mentioned above, there have been numerous and very elegant approaches to convert polyolefins into environmentally degradable plastics to replace a large segment of the dominant commodity plastics that currently are global in their usefulness. Nature generally degrades and biodegrades condensation polymers (polyesters, polyamides, polysaccharides, etc.) faster than addition polymers (polyolefins) as the evolved nature of the environment is such that condensation polymers are prevalent and are susceptible to hydrolysis as a first degradation stage. Conversely, addition polymers are similar to carbon chain polymers such as rubber and lignin found in nature which requires longer times to degrade. This difference in the combined degradation and biodegradation rates between the two plastic types has resulted in a larger effort in developing condensation polymers as they can be measured readily for biodegradation in simple laboratory tests. Addition plastics require more complicated tests methods and their emergence as environmentally degradable

plastics has been hampered by this, as well as by ill-founded claims without experimental substantiation in both earlier and recent developments. These have negatively impacted the technology and will continue to do so if they persist.

The history of the development of environmentally degradable polyolefins reveals some interesting technologies and innovation. Unfortunately most were without much commercial success. A few of these are shown below:

- Chain insertion reactions:
  - Ester linkages by several techniques such as vinyl ketals copolymerized with olefins to enhance the hydrolysis rate during environmental degradation
  - Carbonyl insertion into polyolefins by copolymerization of carbon monoxide to enhance radiation degradation (used in six pack holders for beverages and highly successful commercially)
- Surface changes:
  - Surface tension changes to allow wetting and enzyme adherence indicate enhanced degradation and biodegradation.
- Enzymatic attack:
  - Fungal growth and degradation using peroxidases indicated that degradation and biodegradation were achievable by natural organisms.
- Polymer blends:
  - Starches, and other condensation polymers, blended with polyolefins led to wild claims of biodegradation without substantiation. Degradation, due to leaching of additives from the polyolefin blend, occurs but the polyolefin component is left unchanged.
  - Unsaturated oils and oxidation facilitating materials added to polyolefins enhanced degradation, but little work was done on biodegradation in a quantitative manner.
- Controlled oxidation:
  - Transition metals either as salts or complexes added to polyolefins have been shown to promote degradation (3) and also biodegradation (4).

Collectively, these technical approaches indicate the potential of polyolefins to environmentally degrade and subsequently biodegrade; individually they do not always have enough substantiated evidence and data to be unequivocal. It is the approach using transition metals as oxidation catalysts that has become the predominant technology in the environmental degradation of polyolefins. The

use of transition metals for the oxidative degradation of polyolefins was elegantly demonstrated by Siponen and Rutherford of 3M Corporation (3). They clearly established a ranking order of metals for effectiveness in this oxidative chemistry. This has been taken a step further by EPI Environmental Products and others (4) and the biodegradation of the oxidative degradation products established. Most of the work to date, and that which is reported here is based on polyethylene; future papers from EPI's ongoing research will include results for polystyrene and polypropylene with similar catalysis at the oxidation stage.

## **Analytical Measurements**

### *Spectroscopic characterization*

Polyethylene film samples as well as relevant extraction fractions were characterized by  $^1\text{H}$  NMR and FT-IR using a Varian Gemini 200MHz instrument and a Jasco FT-IR model 410, respectively

### *Size Exclusion Chromatography (SEC)*

Molecular weight and polydispersity of the acetone extracted fractions from thermally degraded samples were determined by SEC with a Jasco PU-1580 HPLC pump equipped with two Pigel mixed D columns (Polymer Laboratories UK) connected in series, and a Jasco 830RI refractive index detector. Sample elution was with THF at 1 ml/minute flow rate. The instrument was calibrated with standard polystyrene samples.

### *Elemental Analysis*

Carbon content of each test sample was determined by elemental analysis using a Carlo Erba model 1106 elemental analyzer.

## **Experimental**

### **Thermally Degradable Polyethylene Films**

Polyethylene film samples containing pro-oxidant metal additives, LDPE-DCP540, FCB-ZSK15, and FCB-ZSK10 were provided by EPI Environmental

Plastics Inc. (Vancouver, Canada), weight average molecular weights were 147,000, 157,000, and 157,000, respectively.

All thermal degradation conditions and solvent extraction procedures are reported in earlier papers (4).

### Respirometer Biodegradation Testing

Biodegradation testing was done in the biometer described in Figure 3. The environments of choice were mixed with the plastic or degradation products and the rate and degree of carbon dioxide evolution measured by capture in the reservoir of caustic soda solution.

## Results and Discussion

### Oxidation

#### *Film Weight Gain*

Oxidation of the three films in air at 50°C and 70°C indicated a formulation sensitive weight gain in all instances, with the weight gains more rapid at the

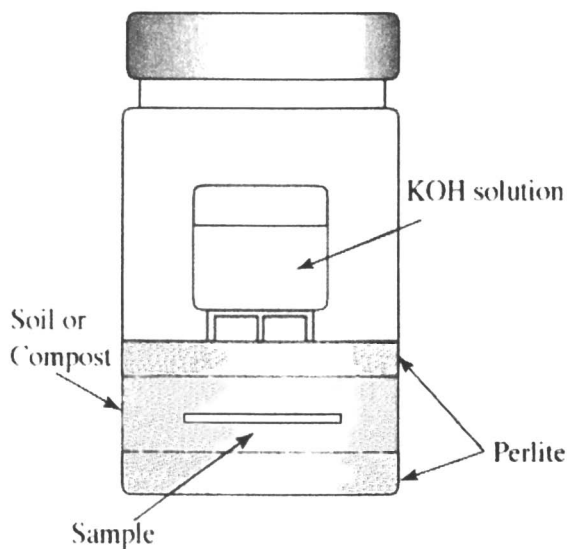


*Figure 3. Biometer for Measuring Carbon Dioxide Evolution in Biodegradation Testing.*

higher temperature. A peak weight increase of about 5% was observed regardless of formulation or temperature. These changes are clearly seen in Figures 4 and 5.

The film surface characteristics were also dramatically changed due to oxygen addition as was seen in the change in contact angle with water, at the peak weight increase at 70°C, films all showed water contact angle reduction of about 20 to 30 percent indicating a drastic reduction of hydrophobicity with the surface formation of carbonyl functionality (see below) which enhanced hydrophilicity.

The weight pick up is also indicated by the change in film density. Prior to oxidation, films float on water and after oxidation they rapidly wet and sink.

### *Film Surface Changes*

Infra red analysis of oxidized films over a period of exposure shows a build of carbonyl intensity which corresponds to a decrease in molecular weight of the plastic. Extraction of the films at their peak weight increase indicates that the carbonyl absorption in the infra-red reaches a maximum intensity and is consistent with dramatic molecular weight decrease. Oxidation lowers molecular weight to well below 10,000 from over 100,000. A moist atmosphere during the thermal treatment does not change the extent of weight pick up by the films but does slow the oxidation slightly as seen by the weight gain rate being slower than in dry conditions.

### **Biodegradation of Oxidized Films**

Biodegradation experiments were carried out in compost and soil environments using the biometer shown in Figure 3 to follow and measure the rate and extent of degradation through monitoring carbon dioxide evolution.

### *Compost*

The original film as supplied required approximately 600 days to reach 60% biodegradation in compost as measured by carbon dioxide evolution. This is well beyond the 180 days specified by ASTM Standard D6400 as acceptable for disposal by composting. However, the time is comparable with the rate of biodegradation of an oak leaf (OWS information) in a compost facility which suggests that specifications need to be revisited by standard organizations.

In a full-scale composting plant facility in Vienna, Austria, polyethylene with TDPA<sup>TM</sup> prodegradant showed no discernable plastic residue after normal

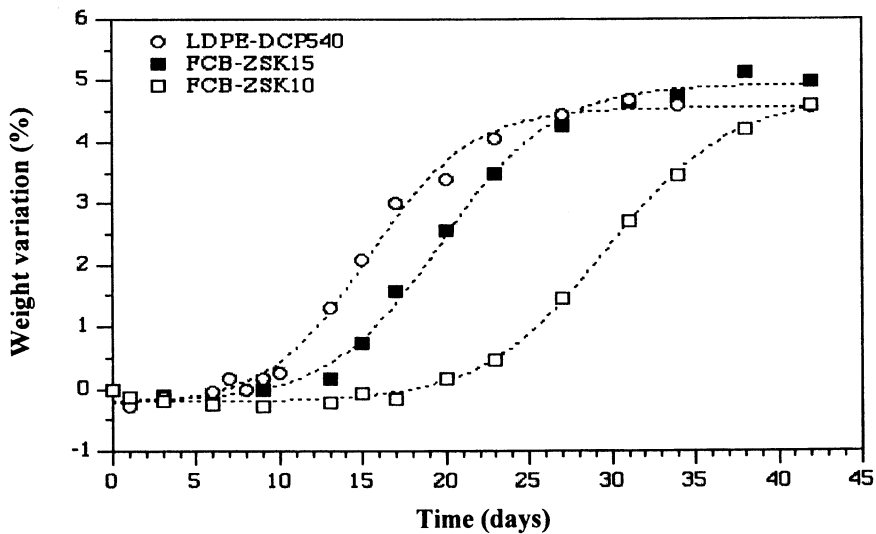


Figure 4. Weight Gain by Films in Air at 55°C.

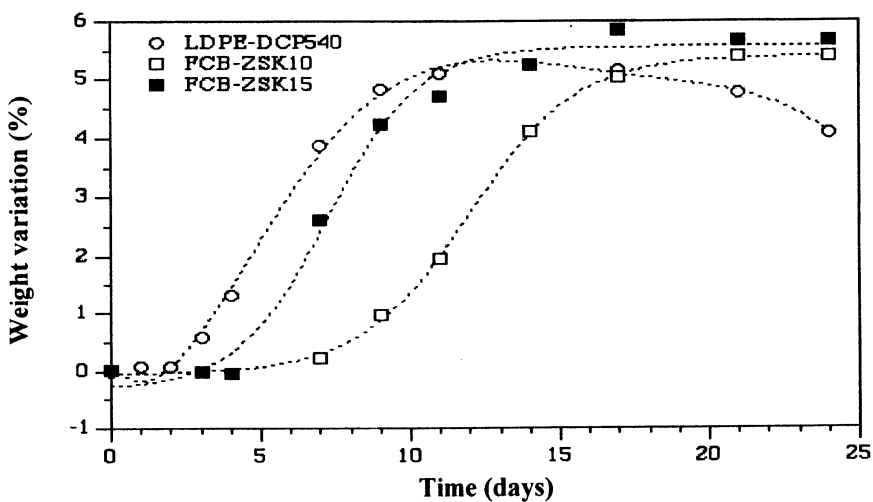


Figure 5. Weight Gain by Films in Air at 70°C.

composting. Compost toxicity testing (DIN V549900-3) showed no adverse effects on plant growth; results were the same as control com[posting in the absence of plastic.

Clearly, from the above information, polyethylene with TDPA™ additive is environmentally degradable and biodegradable, though not yet meeting current ASTM or other standards for compostability. It is non toxic on degradation and biodegrades over a longer period of time than that specified in the standard.

### *Forest Soil*

Soil biodegradation of polyethylene containing TDPA™ additive prior to oxidation is similar to that in composting, reaching 60% biodegradation in 720+ days, well beyond acceptable rates of current standards. However, extracted fractions of the polyethylene/TDPA™ oxidation/degradation products with lower molecular weights indicates that oxidation does produce a biodegradable fraction that biodegrades comparably to cellulose in 60 to 100 days in the biometer tests. Interestingly, soil biodegradation is slow for low molecular weight hydrophobic organic materials such as squalane, docosane, and docosandioic acid again indicating a complexity in the interpretation of test that needs renewed and attention and addressing by all involved. This likely relates to the hydrophile/hydrophobe balance of the molecules, which, of course, is the basic change made by the oxidation of hydrophobic polyolefins to promote biodegradation. Nature seems to use such a balance in controlling environmental degradation of natural materials.

It seems that oxidized polyethylene *will* biodegrade; the first oxidation stage is the limiting step. Hence, time is the limiting factor. This can be addressed.

### **Applications of Environmental Degradation of Polyethylene/TDPA™ Films**

Applications currently promoted for oxidatively biodegradable plastics include, landfill covers and bags for landfill disposal, agricultural film and a route to alleviate litter. They do not currently meet compost bag use.

### *Litter*

Litter control potential is indicated in Figure 6, which shows the slow degradation and disintegration of bags made from polyethylene and TDPA™ over a number of days. Although this is not a recommendation for litter as a disposal option, it does support the notion that as long as people are lazy and incorrigible on litter there is a way to limit its accumulation.



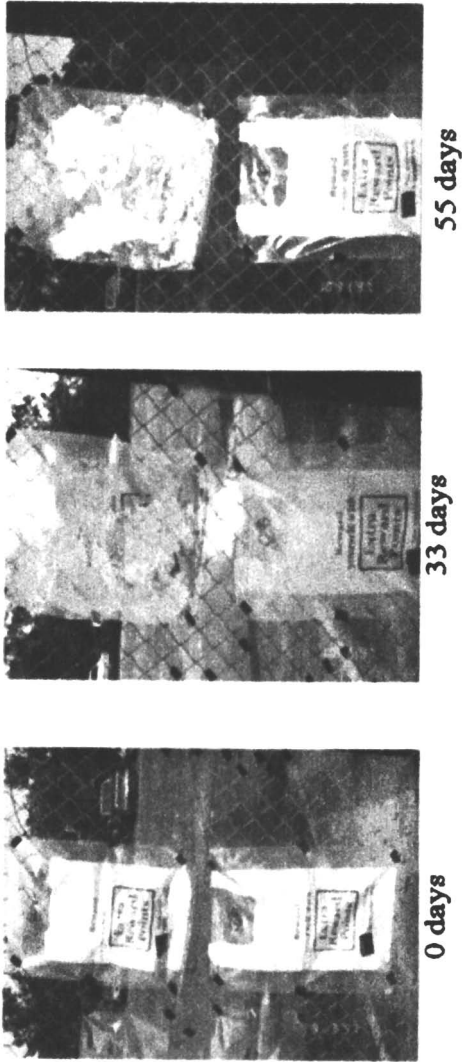


*Figure 6. Outdoor Exposure of Polyethylene with TDP<sup>TM</sup> Prodegradant (sample on lower row is control plastic without additive).*

*Landcover for Agricultural Mulching*

Landcover has many advantages for the farmer, it promotes crop growth, water retention by soil, and limits weed proliferation. Once the growing season is over, the plastic can be collected and disposed of or, better yet, tilled into the soil to degrade and biodegrade. Polyethylene films with a TDPA<sup>TM</sup> prodegradant additive containing an oxidation catalyst, promotes degradation and biodegradation and hence a better way to farm. The use is shown in Figure 7.

*Landfill cover*

Landfill covers allow operators to cover landfills at the end of each filling session (daily) to prevent wind blown debris from escaping and littering the neighborhood. They also offer an increase in volume availability relative to the conventional method of covering daily fills with several inches of soil. The polyethylene/TDPA<sup>TM</sup> landfill covers oxidize and degrade as the landfill is completed, and do not interfere with normal operations. This use of EPI technology has been expanded to develop landfill degradable bags that will degrade to low molecular weight products and disintegrate over time thus compacting landfill and allowing more use volume. This degradation was demonstrated in an operating landfill in Solihull, UK with the results in Table 1, which show no change in the molecular weight of the control polyethylene over 12 months at a depth of 2 meters in the landfill with household waste, but a dramatic change in the recovered experimental film, whose molecular weight fell to 4250 from 115,000, the film becoming too brittle to handle. The films are shown in Figure 8.

**Table 1. Behavior of TDPA film in landfill**

Sample	MFI g/10 min	Mw
Control Initial	0.75	114,000
Control Recovered	1.11	107,000
Experimental Initial	0.76	115,000
Experimental Recovered	13.3	4250

These results clearly show that landfills are not tombs, as some would indicate, but are actually active with enough oxygen at the depth evaluated to promote oxidative degradation of suitably formulated polyethylene.

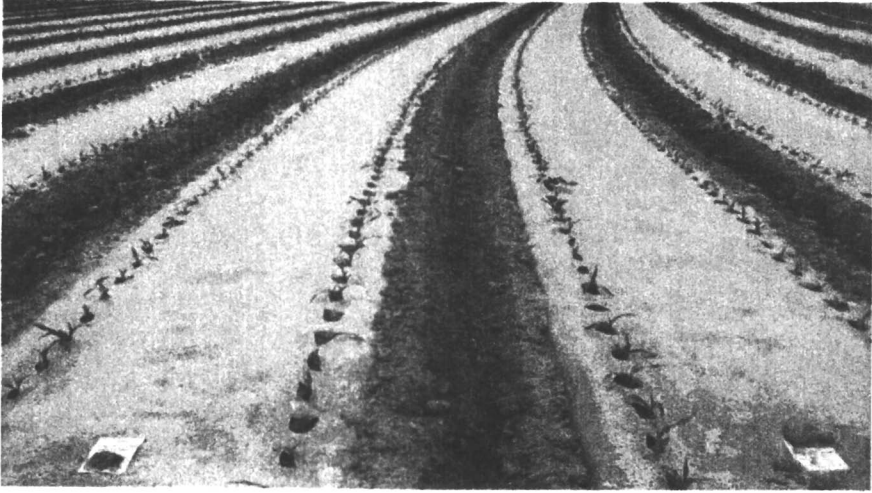


*Figure 7. Soil land cover for mulching.*

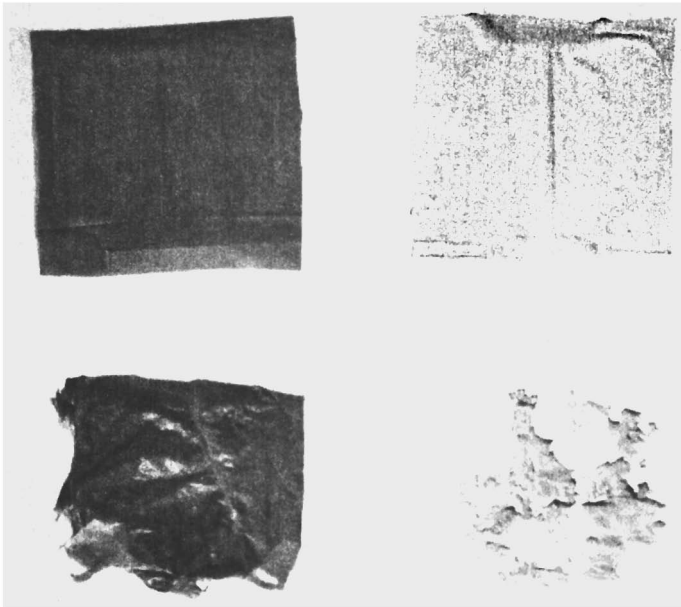


*Figure 8. Landfill Degradation of Plastic Films. Control samples on left, experimental samples on right, before (top) and after (bottom 10 months in a UK landfill at 2 meters depth.*

## Conclusions

TDPA™ additives for polyolefins, as described here for polyethylene:

- Promote oxidation to lower molecular weight products which subsequently biodegrade.
- Are a commercially viable approach to developing environmentally degradable polyolefins.
- Promote polyolefins as complementary to and competitive with current plastics which are available for the environmental degradation market.
- Require wider general acceptance in the field; further standard testing methods and specifications development will facilitate this.

## References

1. Chiellini, E.; Corti, A.; D'Antone, S. *Polym. Degrad. Stab.*, **2007**, *92*(7), 1378.
2. Swift, G; Baci, R. *Degradable Polymers and Materials: Principles and Practice*; K. Khemani and C. Schilz; Eds, *ACS Symp. Ser.* 939, **2006**, 398.
3. Sipinen, A. J.; Rutherford, D. R. *J. Environ. Polym. Degrad.* **1993**, *1*(3), 193.
4. Jakubowicz, I. *Polym. Degrad. Stab.* **2003**, *80*(1), 39.

## Chapter 2

# High-Oxygen Barrier Materials Based on Hyperbranched Aliphatic Polyesters

**Jason D. Pratt<sup>1</sup>, Brian G. Olson<sup>1</sup>, Justin P. Brandt<sup>1</sup>,  
Mohammad K. Hassan<sup>1</sup>, Jo Ann Ratto<sup>2</sup>, Jeffrey S. Wiggins<sup>1</sup>,  
James W. Rawlins<sup>1</sup>, and Sergei Nazarenko<sup>1</sup>**

<sup>1</sup>School of Polymers and High Performance Materials, Department of Polymer Science, The University of Southern Mississippi, Box 10076, Hattiesburg, MS 39406

<sup>2</sup>U.S. Army Natick Research, Development and Engineering Center, Combat Feeding Directorate, Kansas Street, Natick, MA 01760

This work explored commercially available Boltorn™ dendritic hydroxylated aliphatic esters to provide a new material platform for development of high oxygen barrier biodegradable films and coatings. Improved mechanical behavior was achieved via covalent linking of dendritic molecules using 1,6-hexamethylene diisocyanate. This report encompasses the information on structure, thermal, mechanical, oxygen barrier, and biodegradation behavior of pure and network systems.

## Introduction

The recognized lack of biodegradability of most commercial polymers, in particular those used for food packaging, focused public attention on the potential global environmental problem associated with plastic waste build-up in the countryside and on the seashore. Therefore, there is a growing demand for sea-biodegradable polymers.

Biodegradability is promoted by enzymes and it is generally accepted that only some hetero-chain polymers, i.e., aliphatic polyesters are truly biodegradable, although in practice the bio-assimilation step normally proceeds first via abiotic hydrolysis which results in monomeric and oligomeric products that are more readily consumed by microorganisms in the environment (1-3). While most commercially available biodegradable synthetic polyesters used for food packaging applications today, for instance poly(lactic acid) (PLA), polycaprolactone (PCL), poly(3-hydroxybutyrate-co-3-hydroxyvalerate) (PHBV) etc., have reasonably good water barrier, they unfortunately exhibit a mediocre oxygen barrier which is not high enough to satisfy the current market for packaging of oxygen-sensitive food (4, 5). The oxygen permeability of these biodegradable polyesters is somewhat comparable or in most instances higher than that exhibited by poly(ethylene terephthalate) (PET). A search for new biodegradable aliphatic esters with more advanced properties, in particular oxygen barrier, is ongoing.

Dendritic macromolecules exhibit compact globular structures which lead to their low viscosity in the melt or in solution. Furthermore, dendritic macromolecules are characterized by a very large number of available functional groups, which lead to unprecedented freedom for changing/tuning/tailoring the properties of these multivalent scaffolds via complete or partial derivatization with other chemical moieties. All these features have contributed to multi-disciplinary applications of these unique macromolecular structures in recent years (6, 7). The development of efficient synthetic routes in recent years has given rise to a virtually unlimited supply of commercially available dendritic polymers, at very affordable price. The transport properties of hyperbranched and dendritic polymers have recently attracted attention as potentially new barrier and membrane materials (8-9).

Commercially available hyperbranched aliphatic polyesters (Boltorn<sup>TM</sup> polyols) attracted our attention as potentially very interesting candidates for the aforementioned applications because of their degradable aliphatic ester nature and the presence in the structure of multiple hydroxyl groups which is an important attribute for the polymer to exhibit high oxygen barrier due to hydrogen bonding. The pseudo-one-step, divergent synthesis of these aliphatic-ester dendritic polymers, first described by Malmström *et al.* in 1995, involves sequential addition of monomer during synthesis; each addition corresponds to the stoichiometric amount of the next generation (10).

Although characterized by imperfect branching and significant polydispersity, these polymeric structures preserve the essential features of dendrimers, namely, high end-group functionality and a globular architecture. An imperfect dendrimer structure (4<sup>th</sup> generation) of hydroxylated polyester based on 2,2-bis-methylpropionic acid (bis-MPA) with an ethoxylated pentaerytriol (PP50) core is shown in Figure 1. Fourth generation Boltorn<sup>TM</sup> polyols contain 64 hydroxyl groups per molecule. Imperfect branching, which leads to incorporation of linear bis-MPA units, naturally introduces hydroxyl groups not only in the periphery as can be expected in the case of ideal dendrimers but also within the dendritic shell structure.

In contrast to linear polymers, the lack of chain entanglements between dendritic units and the overall globular architecture make dendrimers fairly weak when in the bulk. Thus to make materials based on dendrimers flexible and mechanically strong, the dendritic units must be covalently linked to form a network as shown in the insert in Figure 1. Considering the polyol nature of Boltorn<sup>TM</sup> polyesters, using diisocyanates for linking dendritic molecules together was a natural step, as it is well known that isocyanates undergo rapid reactions with compounds containing active hydrogen.

## Experimental

### Materials

Hydroxyl-functional dendritic (hyperbranched) polyesters of 2<sup>nd</sup> and 4<sup>th</sup> generation, Boltorn<sup>®</sup> H40 were obtained from Perstorp Specialty Chemicals AB, Sweden, in the form of pellets. About 100  $\mu\text{m}$  thick films were prepared via compression molding at 130°C in a Carver press followed by cooling under pressure by flowing water through the press platens. Prior to molding, as received pellets were dried in vacuum at 55°C for at least 24 hrs.

Boltorn<sup>TM</sup> H40 dendritic molecules were covalently linked in this work to make a network with aliphatic 1,6-hexamethylene diisocyanate (HDI). The molar NCO/OH ratio was varied for the reactants from 10 to 50% to prepare networks with different degrees of connectivity of dendritic units. The network samples are designated as H40/Z where Z stands for NCO/OH ratio expressed as a percentage. The network formation reaction of H40 with HDI was carried out in N,N-dimethylformamide (DMF) of 99.8% purity at 90°C. No catalyst was added. Isocyanates react readily with moisture to form urea linkages, therefore special precautionary measures were implemented to prevent moisture uptake either by HDI or DMF. Observation of the reaction vessel was maintained over the course of the reaction to monitor the viscosity of the solution. As viscosity of the solution increased to the desired level, suggesting that the gelation point was near, the solution was cast onto a glass plate which was immediately placed

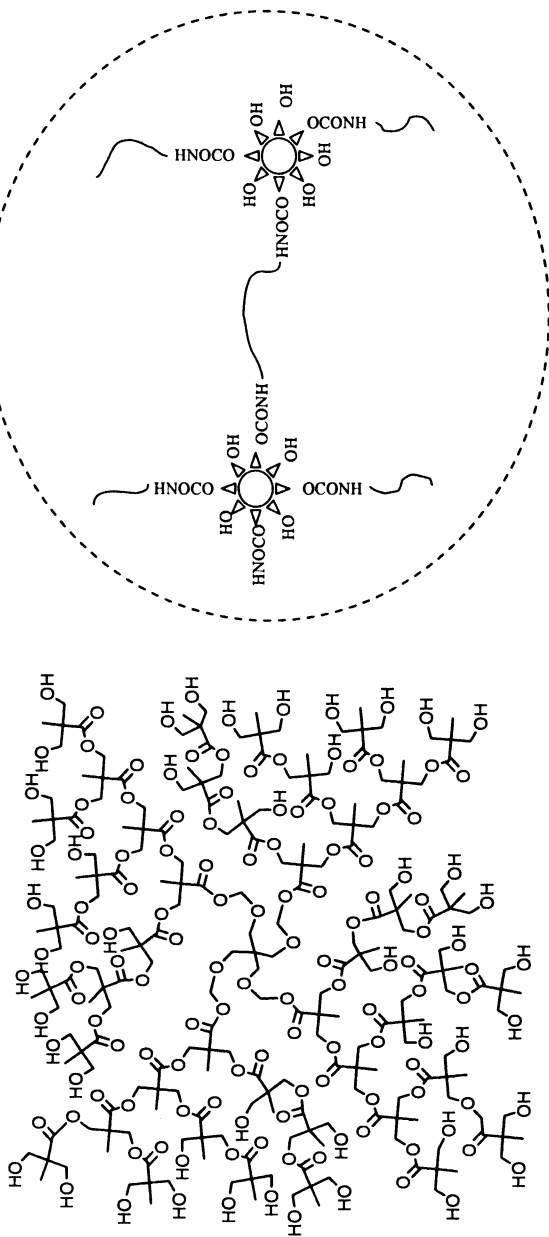


Figure 1. Schematics of Boltorn™ hyperbranched aliphatic esters. Insert shows the network formed by covalent linking of hyperbranched molecules with diisocyanate.



into an environmental chamber purged with dry nitrogen, and left at room temperature for 12 hr to complete the reaction and evaporate most of the residual DMF. The resulting film (~0.1 mm thick) was then peeled and further dried in vacuum first for 72 hr at 55°C and then annealed in vacuum at 155°C for one hour in order to remove even small traces of DMF solvent as the boiling temperature of DMF at 1 atm. pressure is 153°C. TGA, DSC and FTIR analysis confirmed that the amount of DMF left in the system after this drying procedure was negligibly small, i.e. well below the detection limit.

## Techniques

Thermal analysis was conducted using TA Instruments DSC Q-100. The calibration was carried out using indium and sapphire standards. Heating and cooling rates of 10°C min<sup>-1</sup> were used over the studied temperature range.

The density was measured at room temperature using a density gradient column constructed from toluene and carbon tetrachloride. The column was prepared according to ASTM-D 1505 Method B. The column was calibrated with glass floats of known density. The accuracy of density measurements was estimated to be ± 0.001 g/cm<sup>3</sup>. Small pieces (~ 25 mm<sup>2</sup>) were placed in the column and allowed to equilibrate before the measurements were taken.

Oxygen transport measurements were conducted at 25°C, 0% and 50% relative humidity RH, 1 atm partial oxygen pressure difference using the commercially manufactured diffusion apparatus OX-TRAN<sup>®</sup> 2/20 (Modern Control Inc.). This apparatus employs a continuous-flow method (ASTM-D 3985-81) to measure oxygen flux,  $J(t)$ , through polymer films or thin sheets. In order to obtain the diffusion coefficient and to accurately determine the permeability coefficient, the data, flux,  $J(t)$ , were fitted to the solution of Fick's second law:

$$\frac{\partial c}{\partial t} = D \frac{\partial^2 c}{\partial x^2} \quad (1)$$

with boundary conditions for the permeant concentration  $c(x = 0, t) = Sp$ ;  $c(x = l, t) = 0$ , where  $S$  is the solubility coefficient,  $p$  is the gas pressure,  $l$  is the sample thickness and initial conditions  $c(x, t = 0) = 0$ :

$$J(t) = \frac{Pp}{l} \left[ 1 + 2 \sum_{n=1}^{\infty} (-1)^n \exp(-D\pi^2 n^2 t/l^2) \right] \quad (2)$$

Permeability,  $P$ , and diffusion coefficient,  $D$ , were obtained by performing a two-parameter least squares fit of the experimental flux data to equation (2). The solubility,  $S$ , was obtained from the relationship  $P = D.S$ . The methodology of these oxygen barrier measurements, data analysis, and the sources of experimental error were previously described in detail elsewhere (11).

Standard marine biodegradation measurements were performed using ASTM 6691. In this test, powdered samples of dendritic polyols were placed into a bottle containing an inoculum that was consistent with microorganisms and minerals commonly present in the ocean. Biodegradation testing was carried out at 30°C, and involved measurements of gaseous CO<sub>2</sub> released as a final product of enzymatic degradation. From the amount of CO<sub>2</sub> released the amount of degraded (mineralized) polymer carbon atoms can be directly determined and expressed as a % Mineralization which is calculated as follows:

$$\% \text{Mineralization} = \frac{C_{\text{Test}} - C_{\text{Blank}}}{C_{\text{Initial}}} \cdot \% \quad (3)$$

where  $C_{\text{Test}}$  is the number of biogas carbon atoms produced in the test reactor in the presence of a polymer,  $C_{\text{Blank}}$  is the number of biogas carbon atoms produced in the reactor without a sample and associated with the bacterial activity present in incubator alone without a polymer, and  $C_{\text{Initial}}$  is the total number of carbons in polymer sample before degradation.

## Results and Discussion

### Biodegradation Behavior

Figure 2 shows preliminary sea biodegradation data conducted on pure 4<sup>th</sup> and 2<sup>nd</sup> generations of Boltorm™ dendritic polyols. The figure shows % of mineralization versus time for 4<sup>th</sup> (curve 1) and 2<sup>nd</sup> (curve 2) pseudo-generations of pure Boltorm™ dendritic polyols. The marine biodegradation test was conducted for 70 days and by the end of this experiment 14% of H40 carbon and 9% of H20 carbon were converted into CO<sub>2</sub> biogas. This level of mineralization is below that for which Boltorm polyols can be considered truly marine biodegradable, according to ASTM 7081. Both H40 and H20, except for a fairly short induction time, displayed fairly constant rates of biodegradation at about 0.20%/day and 0.13%/day, respectively. The larger degradation rate of H40 as compared to H20, by about 1.6 times, was attributed to a larger weight concentration of ester groups for this generation (1.5 times that of H20). The corresponding weight concentrations of ester groups were calculated based on the experimentally determined molecular weights  $M_w$ , as reported by Perstorp, for 2<sup>nd</sup> and 4<sup>th</sup> generations, 1800 and 5900 g/mol, and ester groups per molecule, 12 and 60, correspondingly.

Polymers do not normally biodegrade until they are broken down into fairly low molecular weight chemical species that can be assimilated by microorganisms. Aliphatic polyesters degrade in the presence of water by sequential hydrolytic cleavage of the backbone ester bonds leading to production of monomeric hydroxyl carboxylic acids which in turn can be metabolized by bacteria (3).

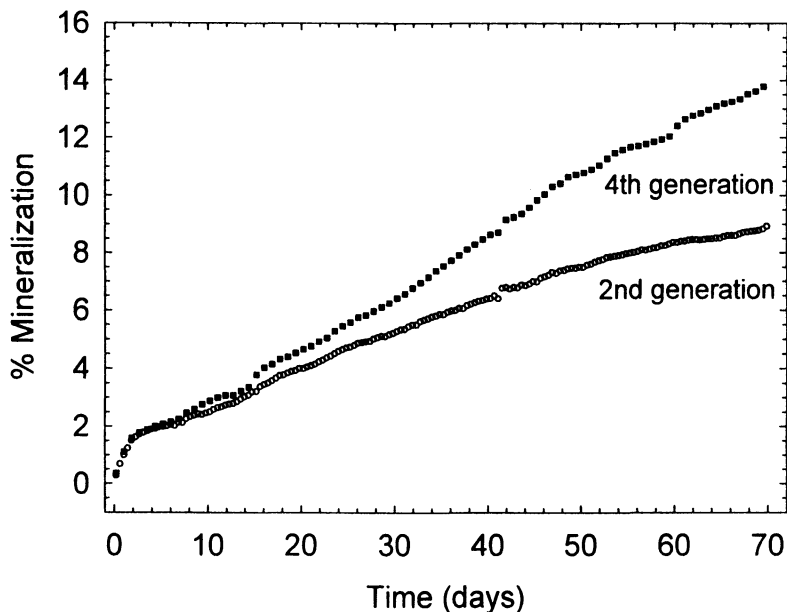


Figure 2. Marine biodegradation behavior of 2<sup>nd</sup> and 4<sup>th</sup> generations of pure Boltorn™ hyperbranched aliphatic esters.

The hydrolytic degradation proceeds either at the surface (homogeneous) or within the bulk (heterogeneous). The observed zero-order degradation kinetics for H40 and H20 samples suggested homogeneous (surface) mechanism of hydrolysis of pure Boltorn™ dendritic polyols followed by biotic assimilation of water soluble low molecular products of the hydrolysis. It is widely accepted that the surface abiotic degradation is considerably slower than the bulk one. A question can be posed; why surface hydrolysis dominated over bulk degradation in the case of pure dendritic polyols? One of the factors, experimentally confirmed in this work by DSC, was that the absorbed water in pure Boltorn™ polyols is formed predominantly in the unbound state, capable of freezing upon cooling. The unbound water seems to be much less hydrolytically reactive as compared to bound water, as the later is typically bonded to polar groups, in particular to the hydrolytically unstable ester groups. In turn, we determined that the absorbed water in crosslinked dendritic polyols formed predominantly in the bound state associated with the urethane networks, especially for NCO/OH concentration above 20%. Therefore, we anticipated that the networks may exhibit a different abiotic degradation behavior as compared to pure polyols.

As sea biodegradation investigation of cross-linked dendritic polyols is under scrutiny at Natick, tests were conducted to compare abiotic (hydrolysis) degradation of pure H40 Boltorn® and H40 cross-linked with HDI

(NCO/OH=35%). The film samples under comparison were placed in the buffer aqueous solution at 37°C. The wet weight was periodically measured. The mass uptake kinetics of the cross-linked sample are shown in Figure 3, with the cross indicating the point at which the sample disintegrated completely, only a few tiny particles were present in the solution.

The interesting observed feature of cross-linked samples is that they easily formed a hydrogel in the buffer solution while H40 remained essentially unswelled. The wet weight of swelled cross-linked samples increased exponentially with time, indicative of the decreased cross-linking density due to the hydrolysis reaction in the bulk. Eventually, the highly swelled cross-link sample completely disintegrated, practically overnight, (“exploded”) after being exposed to the aqueous environment for about 6 months. At about the point of rupture, “explosion”, the dry weight was found to be 28% of the original, so 72% percent of the polymer has been hydrolyzed to small monomer or oligomer products and dissolved in water. Interestingly, in the same experiment the sample of pure H40 degraded in the aqueous environment much slower as compared to the cross-linked one. Large pieces of H40 were still present in aqueous solution after the cross-linked sample completely disintegrated. The difference in the rate of abiotic degradation between pure and cross-linked H40 was attributed to the fact that first degraded via a surface, and the second via a bulk degradation mechanism.

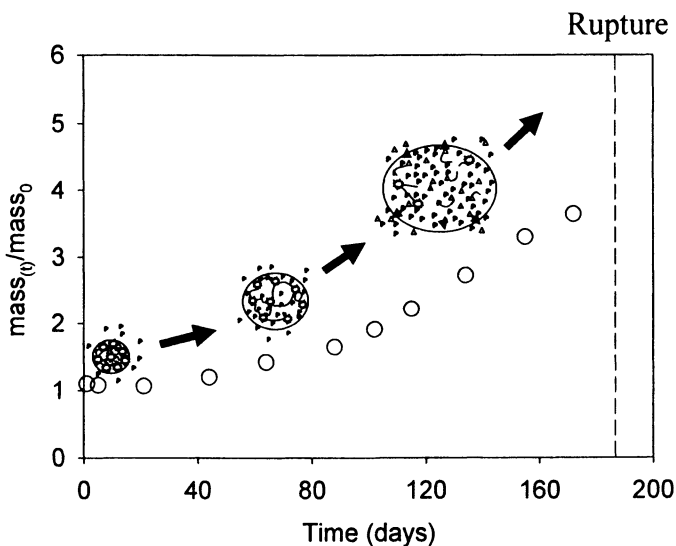


Figure 3. Water uptake behavior associated with abiotic degradation of Boltorn™ H40/HDI (NCO/OH=50%) network.

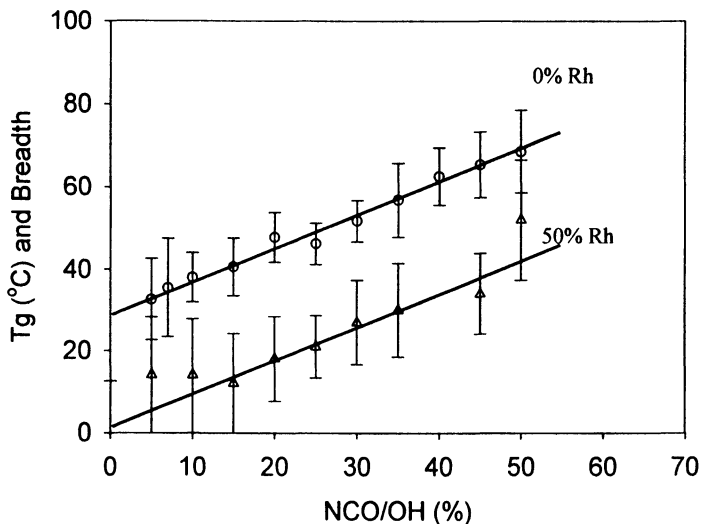


Figure 4.  $T_g$  behavior of different Boltorn™ H40/HDI networks at 0% and 50%RH.

### Thermal and Stress-Strain Behavior

Dendritic polymers are multivalent scaffolds, so the possibility that one HDI molecule reacts with two hydroxyl groups of the same dendritic unit can not be completely ruled out. Intra-molecular cross-links, associated with formation of loops, are not as efficient as inter-molecular cross-links, and typically lead to leveling off the glass transition temperature. To explore this behavior the dependence of  $T_g$  versus NCO/OH ratio was measured at 0 and 50% RH by DSC. Figure 4 displays  $T_g$ 's as a function of NCO/OH ratio with the breadth of the transition shown as error bars.  $T_g$ 's at 0%RH were determined using the second scans, while first scans were used to determine  $T_g$  at 50% RH for samples specifically conditioned at these levels of relative humidity prior to testing.  $T_g$  gradually increased from about 20°C to 70°C upon changing NCO/OH ratio from 0 to 50%. This result is in clear support of the predominant formation of intermolecular cross-links. Humidity played a pivotal role in lowering  $T_g$  due to breaking of the existing hydrogen bonding network and plasticizing the network structure. At 50% RH,  $T_g$ 's increased from about 0°C for pure H40 to about 50°C for cross-linked samples with NCO/OH = 50%. Two  $T_g$  trends at 0 and 50% RH are almost shifted in parallel fashion relative to each other, with a shift factor of about 20 degrees.

Engineering stress-strain curves of cross-linked samples are shown in Figure 5. All cross-linking materials showed dramatic improvement of

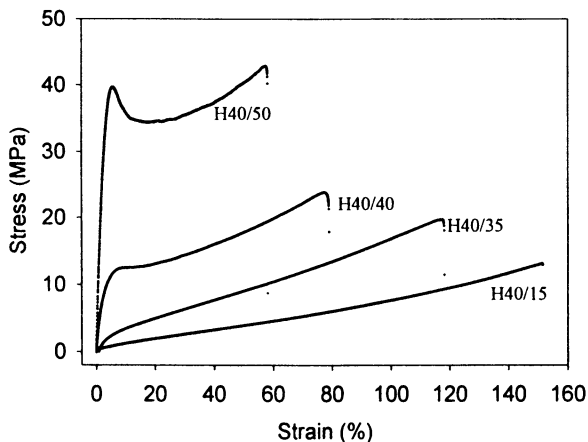


Figure 5. Stress-strain behavior of Boltorn™ H40/HDI networks.

mechanical properties at ambient conditions (RT and 50%RH) as compared to films made of pure H40 which were very brittle. Stress-strain behavior for samples with NCO/OH up to 35% was similar to that typically reported for the rubbery state, while beyond 35% a clear transition to the glassy state stress-strain behavior characterized by a much higher Young's modulus, yield point and a strain softening was apparent. Naturally, samples in the rubbery state exhibited larger elongation at break. Sample with NCO/OH=15%, for instance, exhibited elongation at break  $\epsilon_b = 150\%$  and sample with NCO/OH =35% the elongation at break was  $\epsilon_b = 110\%$ . The residual deformation of these samples recovered completely within a few minutes after unloading for these samples. Samples in the glassy state exhibited smaller elongation at break, however, it was still quite impressive; e.g. a sample with NCO/OH ratio 50% had  $\epsilon_b = 55\%$ .

### Oxygen Barrier Behavior

Oxygen barrier data for pure H40 systems and H40 network systems measured at RT and 0 and 50%RH are summarized in Table 1 which also reports  $T_g$ 's and densities in the dry state. Due to the high concentration of hydroxyl functional groups in the periphery, excellent gas barrier characteristics for pure H40 are predicted. As seen in Table 1, the pure H40 at 0%RH displayed considerably better oxygen barrier characteristics than PET and comparable to those for EVOH with 48% (mol/mol) of ethylene. EVOH copolymers with low and moderate ethylene content are considered benchmark materials for packaging applications. When exposed to ambient humidity (50% RH) the barrier properties were reduced, but still better than PET. Figure 6 (a), (b), and

**Table I. Oxygen barrier characteristics of pure Boltorn™ H40 and H40/HDMI networks at 0% and 50% RH.**

Materials	T <sub>g</sub> (°C)	Density (g/cm <sup>3</sup> )	RH (%)	P	D	S
H40/0	23.3	1.2832	0	0.91	2.7	3.9
	-1.0	-	50	7.70	35.8	2.5
H40/10	38.1	1.2813	0	1.60	6.9	2.7
	14.0	-	50	6.30	36.0	2.1
H40/20	47.7	1.2703	0	1.30	9.4	1.6
	18.0	-	50	5.63	33.9	1.9
H40/35	56.8	1.2609	0	3.06	8.8	4.0
	30.0	-	50	2.60	14.3	2.2
H40/50	68.6	1.2449	0	6.40	13.0	7.7
	52.0	-	50	5.60	18.7	3.5
*PET	76	1.3370	0	39.30	56.0	9.8
*EVOH48	48.0	1.1200	0	0.97	4.16	2.1

\*Measurements performed in authors lab. P – [10<sup>-2</sup> cc(STP) cm m<sup>-2</sup> day<sup>-1</sup> atm<sup>-1</sup>], D – [10<sup>-10</sup> cm<sup>2</sup> s<sup>-1</sup>], S – [10<sup>-2</sup> cc(STP) cm<sup>-3</sup> atm<sup>-1</sup>].

(c) also shows the corresponding graphs of permeability, diffusivity and solubility as a function of NCO/OH ratio determined at 0 and 50%RH. Because  $P = D \cdot S$ , an understanding of  $D$  and  $S$  trends beside  $P$  was essential to draw a complete picture of transport behavior. At 0%RH oxygen permeability exhibited a gradual increase from  $P = 0.009$  cc-cm/m<sup>2</sup>-day-atm for pure H40 to  $P = 0.064$  cc-cm/m<sup>2</sup>-day-atm for H40 with NCO/OH = 50%. In the case of NCO/OH = 35%  $P = 0.031$  cc-cm/m<sup>2</sup>-day-atm. Therefore practically speaking, oxygen barrier of dry cross-linked films was not that different from that displayed by pure H40. Both oxygen diffusivity and solubility exhibited a gradual increase with cross-linking as free volume increased (density decreased) with T<sub>g</sub> as can be seen from Table 1. The effect of T<sub>g</sub> on development of excess hole free volume and increase of gas transport characteristics has been described in details elsewhere (12, 13). Changes in diffusivity controlled the permeability predominantly at smaller NCO/OH ratios and changes in solubility controlled it at larger NCO/OH ratios. At 50% RH, oxygen gas barrier properties exhibited a more complex trend. This trend was due to the transition from the rubbery to glassy state, exhibited by cross-linked polyols at RT and 50%RH. This effect is somewhat similar to that discussed in the previous section with regards to stress-strain behavior, also determined at 50% RH. At 50%RH pure H40 displayed the largest oxygen permeability (worst barrier)  $P = 0.077$  cc-cm/m<sup>2</sup>-day-atm which was 8.5 times larger than that displayed by dry H40. With an increasing ratio of

NCO/OH, oxygen permeability gradually decreased to  $P = 0.026$  cc-cm/m<sup>2</sup>-day-atm, reaching this minimum at NCO/OH ratio of about 35%, then permeability increased again. For a sample with NCO/OH = 50%  $P = 0.056$  cc-cm/m<sup>2</sup>-day-atm. Therefore cross-linked polyols with NCO/OH ratio in the range of 30-40% in addition to excellent mechanical properties exhibited reasonably high oxygen barrier at 50%RH, although not as good as pure H40 at 0%RH. Oxygen permeability of the system with NCO/OH =35% at 50% RH was almost 3 times smaller than that for pure H40 at the same RH. Therefore, oxygen barrier of pure H40 at 50%RH was improved via cross-linking with HDI. At lower NCO/OH ratios, oxygen permeability for cross-linked systems was controlled by solubility, which decreased more gradually. Oxygen diffusivity changed very little, until about NCO/OH =20%. Then diffusivity, in contrast to solubility, upon transition from rubbery to the glassy state decreased by almost a factor of 4 predominantly determining oxygen permeability trends in the range NCO/OH 20-35%. Above NCO/OH= 35%, again oxygen solubility was determining oxygen permeability behavior as in this range of cross-linking oxygen diffusivity exhibited relatively small change.

## Conclusions

This work explored the potential of commercially available Boltorn<sup>TM</sup> dendritic hydroxylated esters as high oxygen barrier biodegradable films and coatings. Improved mechanical performance was achieved via covalent linking of dendritic molecules with 1,6-hexamethylene diisocyanate.

Oxygen transport for both the pure and cross-linked dry (0%RH) polymer films exhibited excellent oxygen barrier properties, considerably better than PET and comparable to that for EVOH with 48% (mol/mol) of ethylene. At 50% RH, the oxygen barrier of pure dendritic polyols was reduced. Hydrogen bonding was found to play a major role in determining the oxygen barrier and water sensitivity of these polymers. Cross-linked materials at 0% RH exhibited a gradual increase in oxygen permeability (reduction of barrier) as compared to dendritic polyols. This behavior was attributed to the increase of  $T_g$  and free volume of the films with the degree of cross-linking. A more complex trend developed when the oxygen permeability was examined at 50% RH due to the transition from the rubbery to glassy state, exhibited by cross-linked polyols at RT and 50%RH. The benefit of this transition is the improvement of oxygen barrier of cross-linked systems over the pure polymer. Biodegradation measurements of pure Boltorn dendritic hydroxylated polyesters showed that they degrade, however, at a rate too slow for them to be considered truly marine biodegradable. Also, cross-linking with HDI resulted in a peculiar acceleration of abiotic degradation in the aqueous environment, as compared to the much slower degradation of pure polymer. The improvement of abiotic degradation



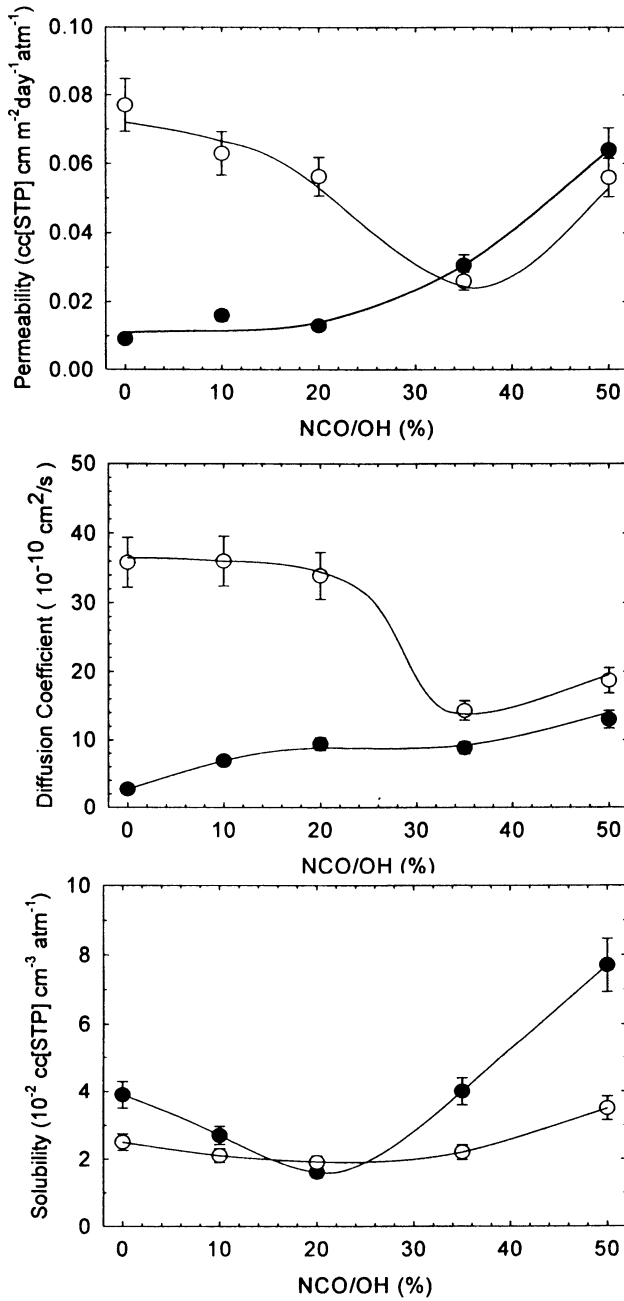


Figure 6. Oxygen Permeability, Diffusivity and Solubility of H40/HDI networks. Filled symbols are data 0%RH and open symbols are data at 50%RH.

was attributed to a change from a slower surface erosion mechanism, to the faster bulk degradation.

## Acknowledgements

This research was primarily funded by the Office of Naval Research, Grant No N00014-04-1-0703. The authors are also grateful to the National Science Foundation (MRSEC Award DMR 02138830). The authors would like to thank Perstorp Perstorp Specialty Chemicals AB for providing Boltorn™ hyperbranched polyols. The authors thank Dr. Robert Stote for biodegradation measurements at Natick. In addition the authors thank the Polymer Performance, Degradation and Material Selection ACS Symposium Series organizers for the opportunity to present our work and for the preparation of this book.

## References

1. Hammond, T.; Liggat, J. J. *Degradable Plastics*; Scott, G.; Gilead, D. (Eds.) Chapman and Hall: NY, **1995**, pp 88-101.
2. Tokiwa, Y.; Ando, T.; Suzuki, T.; Takeda, K. " *Biodegradation of Synthetic Polymers Containing Ester Bonds*," in *Agricultural and Synthetic Polymers, Biodegradability and Utilization*; Glass, J. E.; Swift, G. (Eds.) ACS Symposium Series 433; ACS: Washington, DC **1990**.
3. *Degradable Aliphatic Polyesters*; Albertson, A-C., Ed.; *Advances in Polymer Science* 157; Springer-Verlag, Berlin, **2001**.
4. *Bio-based Packaging Materials for the Food Industry: Status and Perspectives*; Weber, C. J., Ed.; Department of Dairy and Food Science, The Royal Veterinary and Agricultural University: Denmark, **2000**.
5. Cava, C.; Gimenez, E.; Gavara, R.; Lagaon, J. M. *J. Plastic Film Sheeting* **2006**, 22, 265-273.
6. Bosman, A. W.; Janssen, H. M.; Meijer, E. W. *Chem. Rev.* **1999**, 99, 1665.
7. Seiler, M. *Chem. Eng. Tech.* **2002**, 25, 237.
8. Hedenqvist, M. S.; Yousefi, R.; Malmström, E.; Johansson, M.; Hult, A.; Gedde, U. W.; Trollsas, M.; Hedrick, J. L. H. *Polymer* **2000**, 41, 1827.
9. Lange, J.; Stenroos, E.; Johansson, M.; Malmström, E. *Polymer*, **2001**, 42, 7403.
10. Malmström, E.; Johansson, M.; Hult, A. *Macromolecules* **1995**, 28, 1698.
11. Sekelik, D. J.; Stepanov, E. V.; Nazarenko, S.; Schiraldi, D.; Hiltner, A.; Baer, E. *J. Polym. Sci. Part B: Polym. Phys.* **1999**, 37, 847.
12. Vrentas J. S.; Duda, J. L. *J. Appl. Poly. Sci.* **1978**, 22, 2325.
13. Petropoulos, J. H. *J. Membr. Sci.* **1990**, 53, 229.

## Chapter 3

# Degradation of Biodegradable Polymers in Real and Simulated Composting Conditions

**Thitisilp Kijchavengkul, Gaurav Kale, and Rafael Auras\***

**140 School of Packaging, Michigan State University,  
East Lansing, MI 48824-1223**

**\*Corresponding author: telephone: (517) 432-3254; fax: (517) 353-8999;  
email: aurasraf@msu.edu**

Biodegradation of polylactide (PLA) under real composting conditions was investigated, and the results were compared with biodegradation values obtained in three simulated laboratory conditions (i.e., cumulative (CMR), gravimetric (GMR) and direct (DMR) methods). Laboratory conditions under-represent the biodegradation that takes place in real composting conditions. PLA bottles completely biodegraded in 30 days in real composting while 60% mineralization was reached at 38 days in the CMR method, 45 days in the GMR method, and 55 days in the DMR method.

## Introduction

The prevailing method of packaging waste disposal in the U.S. is land filling, followed by recycling, incineration, and composting. In the U.S., containers and packaging represent 32% of the total municipal solid waste (MSW). Most of the common materials used in packaging (i.e., steel, aluminum, glass, paper, paperboard, plastics and wood) can be efficiently recovered by recycling. For example, corrugated boxes are highly recoverable (71%). However, if packaging materials such as polymers and paper are used in food and medical packaging applications and are soiled with foods or other biological substances, physical recycling or recovery of these materials may be impractical (1). Therefore, they generally end up in landfills. Since landfills occupy valuable space and result in generation of greenhouse gases, nuisances and contaminants, recovery methods such as reuse, recycling and/or composting are encouraged as a way of reducing packaging waste disposal (1). Use of biopolymers opens up a new waste disposal option for packaging, composting, and a promising way to reduce MSW.

In 2005, the U.S. market for biopolymers was 173 million pounds and is expected to grow nearly 20% annually and to reach 420 million pounds in 2010 (2), with packaging being one of the main areas of application (2, 3). Cushioning, composting bags, paper coatings and food packaging such as disposable cutlery, cups and trays are some of the main application products. The main selling points of the new biopolymers, such as poly(lactide) (PLA) from NatureWorks®, poly(butylene adipate-co-terephthalate) (PBAT) or Ecoflex™ from BASF, and poly(hydroxybutyrate-co-valerate) (PHBV) or Mirel™ from Metabolix, are that they are obtained from renewable resources and that they can be biodegraded in biological environments such as soil and compost. Although recycling could be energetically more favorable than composting for these materials, it may not be practical due to excessive sorting and cleaning requirements. Therefore, the central goal is to dispose of them by composting. Figure 1 shows a “*cradle to gate, grave and cradle*” diagram of the use of these biobased materials obtained from renewable resources, such as PLA and PHBV.

So far, there is no extended formal agreement between companies, governments and consumers as to how this packaging composting will take place. In fact, the drive for the use of biodegradable packaging materials has been green and environmental marketing. However, packaging compostability could be an alternative for disposal of biobased materials as long as society as a whole is willing to formally address the challenges of the full cradle-to-grave life of a compostable package, and to include these new compostable polymers in industrial composting facilities.

Most of the relevant standards developed so far address the compostability of a plastic material from a package in laboratory simulated conditions which

differ from actual or commercial composting conditions. This paper addresses the differences between compostability under commercial and simulated laboratory conditions of biodegradable polymeric packages, and compares the results obtained from commercial composting and laboratory simulated techniques. The comparison of these results provides needed information for setting up reliable laboratory tests.

## Experimental

### Materials

PLA bottles (500 mL) were provided from NatureWorks® LLC (Blair, NE) with 96% L-lactide and bluetone colorant. The bottles were composted in a commercial compost pile and in laboratory simulated conditions.

### Commercial Composting

A composting pile was built at Michigan State University (East Lansing, MI) made up of cow manure and wood shavings with a carbon to nitrogen (C:N) ratio of 30:1. Temperature, relative humidity and pH of the compost pile were continuously monitored for the entire duration of the study (30 days) (4, 5). A general procedure of compost pile preparation and compost production is shown in Figure 2. A novel method was used for tracking and analyzing the PLA bottle samples from the compost pile. Further details of the methodology can be found in references (4,5). The biodegradability of the PLA bottles was assessed through visual inspection and analyses of variation in physical properties such as molecular weight, glass transition temperature and decomposition temperature.

### Simulated Composting

A laboratory scale cumulative measurement respirometric system (CMR) was built according to ISO 14855-1 (6) and ASTM D5338 (7). The system consists of 3 major components: (1) an air supply, (2) an air-tight closed vessel called the “bioreactor”, which contains the living test organisms, and (3) a measuring device to quantify the amount of O<sub>2</sub> uptake or CO<sub>2</sub> release (8). A picture of the CMR is shown in Figure 3. Nine bioreactors filled with mature manure compost obtained from the MSU composting facility were tested (i.e., three for the blanks; three positive controls and three PLA bottle samples (0.01m x 0.01m)). Humidified CO<sub>2</sub> free air was passed through the 3.78 liter bio-

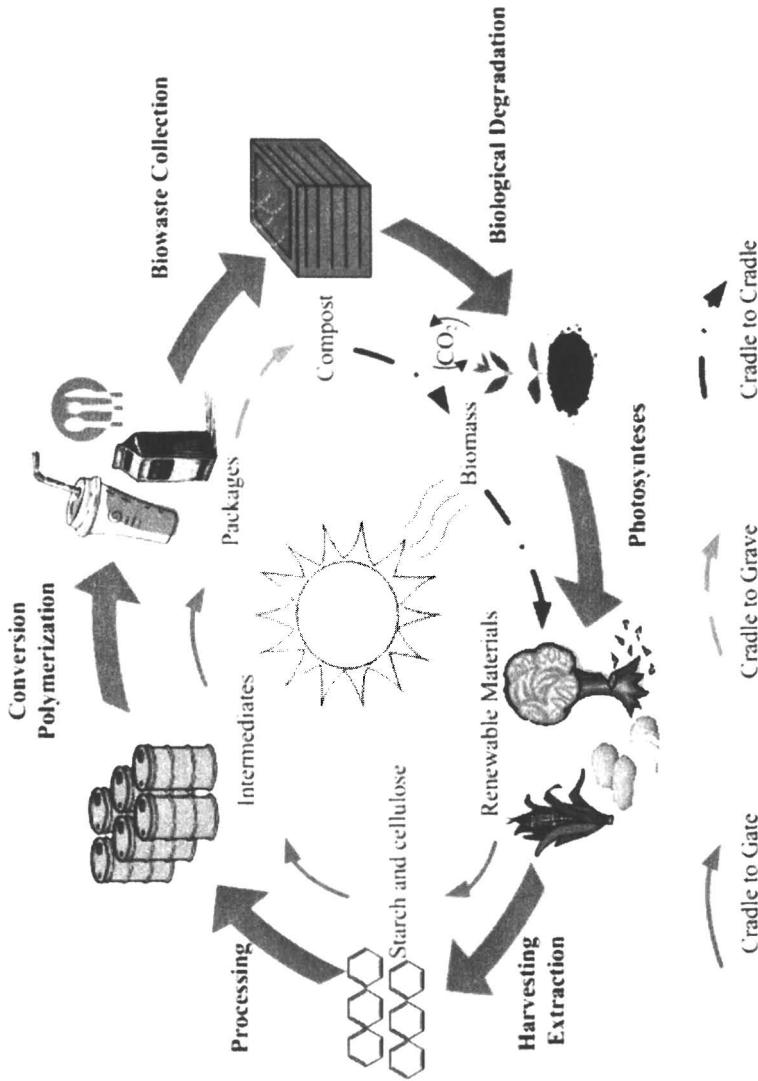
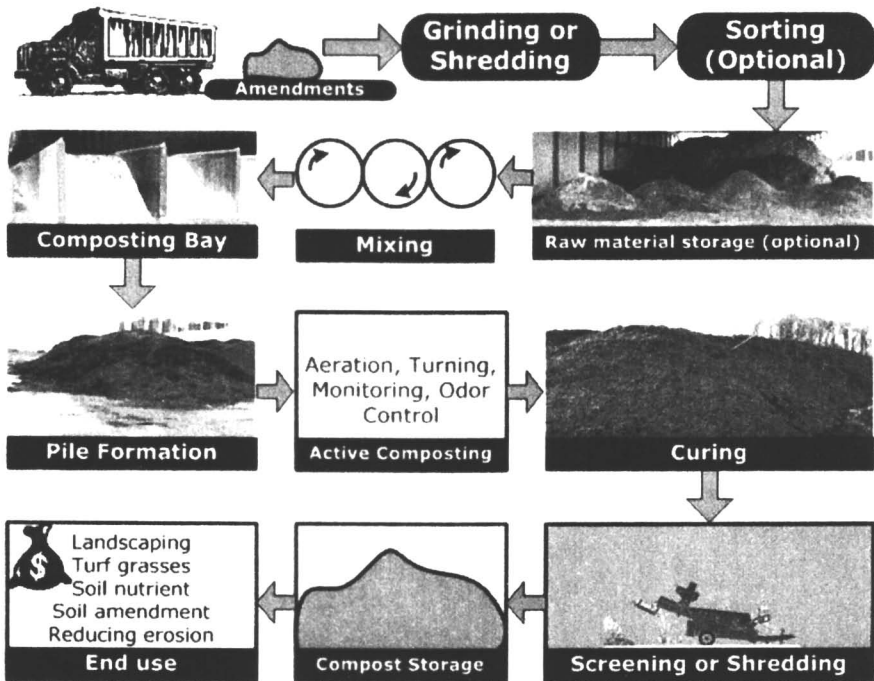


Figure 1. Cradle to gate, grave and cradle system of the implementation of biobased polymers obtained from renewable resources (Adapted with permission from reference 3. Copyright 2004).



*Figure 2. Preparation of a commercial compost pile (Reproduced with permission from reference 1. Copyright 2007 WILEY-VCH Verlag GmbH & Co. KGaA).*

reactors, and  $\text{CO}_2$  was trapped in 200 mL 0.5 N NaOH solution which was titrated using 0.186 N HCl solution to calculate the amount of  $\text{CO}_2$  evolution. Sigmacell cellulose powder from Sigma Aldrich (St. Louis, MO) was used as positive control.

## Results and Discussion

### Commercial Composting

The PLA bottles subjected to commercial composting were visually inspected for changes in color, dimensions, shape and texture and later analyzed for changes in their physical properties such as molecular weight,  $T_g$  and decomposition temperature. The average temperature of the compost pile was  $58 \pm 5^\circ\text{C}$  and the average relative humidity was  $60 \pm 5\%$ . Figure 4 shows the biodegradation trend observed in PLA bottles for a period of 30 days.

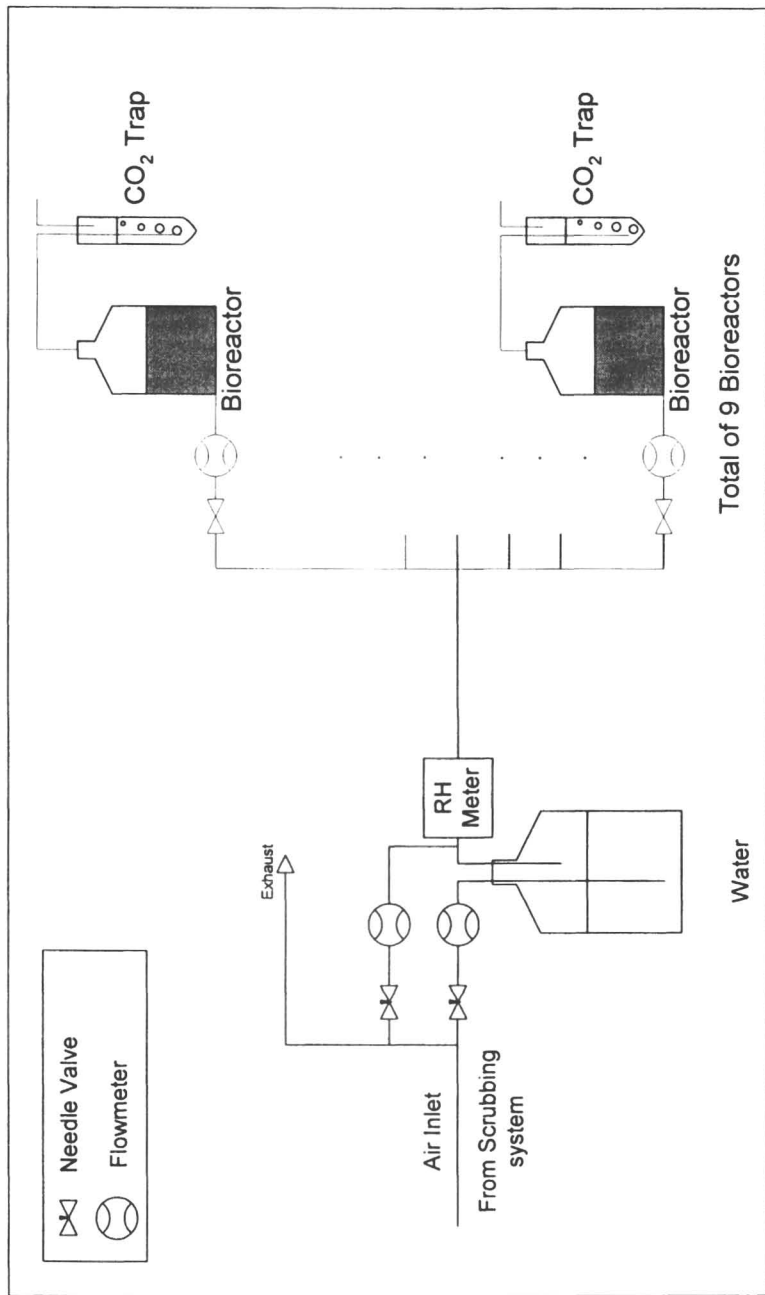
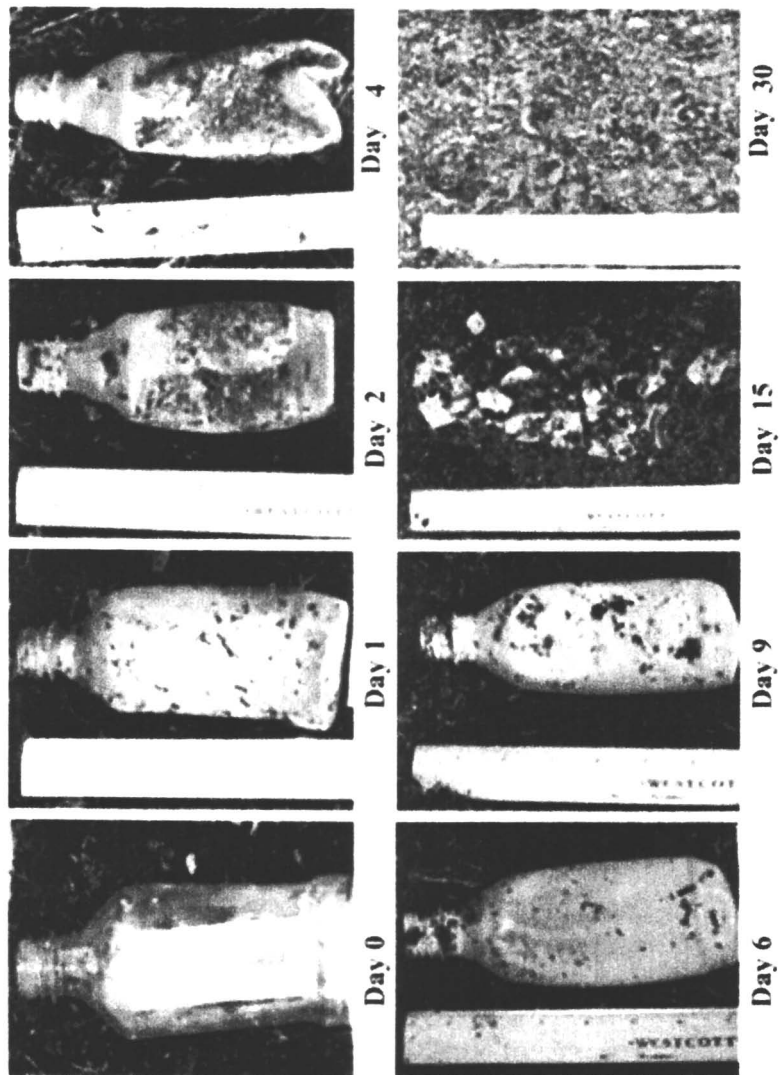


Figure 3. Cumulative measurement respirometric system (CMR) (Adapted with permission from reference 1. Copyright 2007 WILEY-VCH Verlag GmbH & Co. KGaA).





*Figure 4. Biodegradation of PLA bottles exposed to commercial composting (Reproduced with permission from reference 1. Copyright 2007 WILEY-VCH Verlag GmbH & Co. KGaA). (See page 1 of color insert.)*

## Simulated Composting

The mineralization curve based on CO<sub>2</sub> trapped in NaOH solution in the CMR system is shown in Figure 5. On the 15<sup>th</sup> day, around 10% of the total organic carbon was converted to CO<sub>2</sub>, and 60% mineralization was obtained on the 38<sup>th</sup> day. The variation in molecular weight of the bottles subjected to real compost conditions shows that the M<sub>w</sub> was reduced to 4.0 kDa on the 30<sup>th</sup> day from 210 kDa on day zero (Figure 5). Faster reduction of the molecular weight of the PLA bottles can be observed in commercial composting.

A similar study with PLA bottles and yard waste compost at 58°C and 60% RH using an automatic direct measurement respirometric system (DMR) where CO<sub>2</sub> concentration was measured with an in-line infrared detector was conducted by Kijchavengkul et.al. (8). In this study 10% mineralization was obtained on day 10, and 60% mineralization was obtained at day 55 (Figure 5). A similar biodegradation trend was observed through a study done in a gravimetric measurement respirometric system (GMR) where CO<sub>2</sub> quantification was based on the changes in weight of the CO<sub>2</sub> absorbing columns at an exhaust port (9). Sixty percent mineralization was obtained on the 45<sup>th</sup> day.

The main degradation process of PLA is hydrolysis where hydrolytic chain scission occurs prior to the beginning of biodegradation. This process is mainly described as a two-stage biodegradation mechanism (3,10). In the first stage, the PLA polymer undergoes hydrolytic degradation, which is mainly a non-enzymatic chain scission of the ester bonds in the polymer backbone, causing a decrease of the polymer molecular weight (see Figure 6). In the second stage, portions of the polymer chains are broken down into small fractions (or oligomers) with low molecular weight (3, 10) and are further consumed by contacting microorganisms. Hydrolysis of PLA requires temperature higher than the glass transition temperature to occur in a reasonable time frame, and classify PLA as compostable. Therefore, packages made of PLA will compost in commercial facilities where temperatures are higher than 50°C, but they may be difficult to completely compost in backyard composting were temperatures are much lower.

A polymer's compostability is a function of many factors such as pH, temperature, humidity, microorganisms' population, and osmotic pressure. Simulated laboratory conditions as described by ASTM D6400 (11), D5338 (7) and ISO 14855 (6) may be an oversimplification of commercial composting systems which do not completely reflect the conditions in the commercial composting facilities. Therefore, further studies are necessary to assure that laboratory studies can duplicate commercial systems.

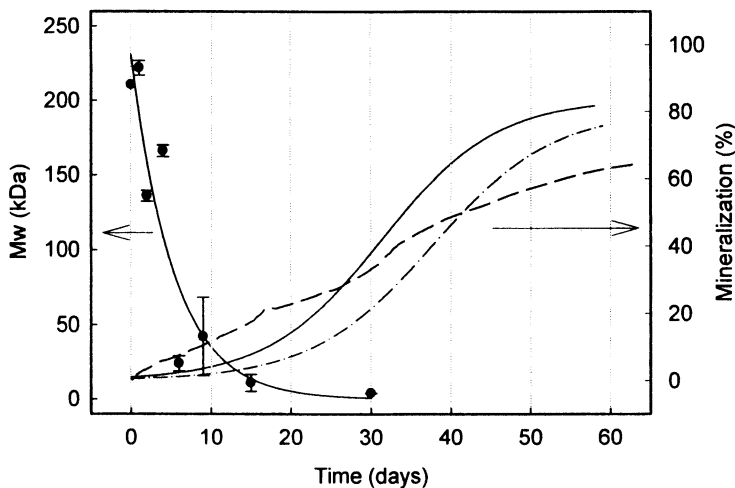


Figure 5. Molecular weight variation measured under commercial composting conditions and average percent mineralization measured with the CMR(—), DMR(---) data obtained from reference 8, and GMR (- · -) data obtained from reference 9.

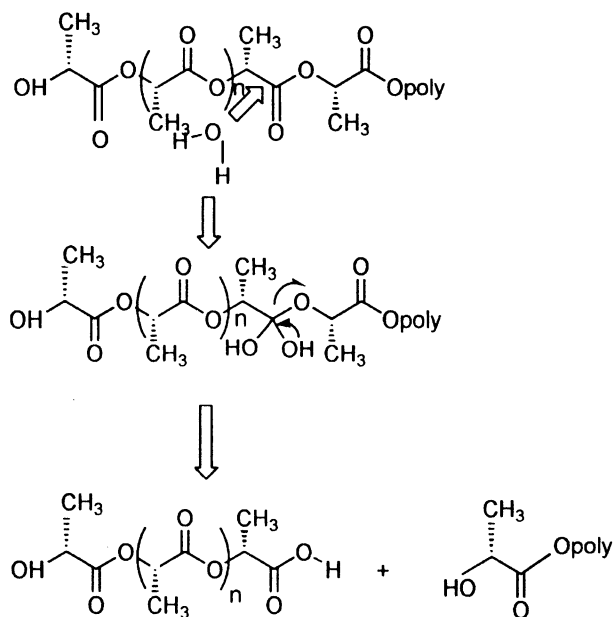


Figure 6. Hydrolytic chain scission of PLA (Reproduced with permission from reference 3. Copyright 2004 WILEY-VCH Verlag GmbH & Co. KGaA).

## References

1. Kale, G.; Kijchavengkul, T.; Auras, R.; Rubino, M.; Selke, S. E.; Singh, S. P. *Macromol. Biosci.* **2007**, *7*, 255-277.
2. *US Industry Study with Forecasts to 2010 & 2015*; Degradable Plastics; Freedonia Group: Cleveland, OH, 2006.
3. Auras, R.; Harte, B.; Selke, S. *Macromol. Biosci.* **2004**, *4*, 835-864.
4. Kale, G.; Auras, R.; Singh, S. P. *J. Polym. Environ.* **2006**, *14*, 317-334.
5. Kale, G.; Auras, R.; Singh, S. P. *Packag. Technol. Sci.* **2007**, *20*, 49-70.
6. *International Standards*; Standard ISO 14855-1; International Organization for Standardization: Geneva, Switzerland, 2005.
7. *Annual Book of ASTM Standards*; Standard D5338-98(2003); ASTM International: West Conshohocken, PA, 2006; Vol. 08.03, pp 115-119.
8. Kijchavengkul, T.; Auras, R.; Rubino, M.; Ngouajio, M.; Fernandez, R. T. *Polym. Test.* **2006**, *25*, 1006-1016.
9. Kale, G.; Auras, R.; Singh, S. P.; Narayan, R. *Polym. Test.* **2007**, *26*, 1049-1061.
10. Snook, J. B. M.S. thesis, Michigan State University, East Lansing, MI, 1994.
11. *Annual Book of ASTM Standards*; Standard D6400-04; ASTM International: West Conshohocken, PA, 2006; Vol. 08.03, pp 598-600.

## Chapter 4

# Synthesis and Degradation of Poly(ethyl glyoxylate)

Benjamine Belloncle, Fabrice Burel<sup>\*</sup>, and Claude Bunel

PBM, UMR 6522–Laboratoire de Matériaux Macromoléculaires–INSA  
de Rouen, B.P. 08 Place Emile Blondel,  
76131 Mont-Saint-Aignan Cedex, France

Poly(ethyl glyoxylate) (PEtG) is a new biodegradable polyacetal obtained by anionic polymerization of ethyl glyoxylate (EtG). End-capping PEtG with an adequate agent, as phenyl isocyanate, is necessary because of its low ceiling temperature. Degradation of PEtG was evaluated by *in vitro* hydrolysis using various techniques such as potentiometry, weight loss, gel permeation chromatography (GPC) and <sup>1</sup>H nuclear magnetic resonance (NMR). Whatever the pH of the medium, the degradation mechanism involved ester hydrolysis and chain scissions leading to ethanol and glyoxylic acid hydrate (GAH) release. Glyoxylic acid is a Krebs metabolite that confers a potential biodegradable character to PEtG.

Though the interest for synthetic biodegradable polymers is still increasing, few of them are currently available. The best known products are polyhydroxybutyrate, poly( $\epsilon$ -caprolactone), poly(glycolic acid), poly(lactic acid) and their copolymer.

We focused our attention on poly(methyl glyoxylate) (PMG) which is a polyacetal obtained by anionic polymerization of methyl glyoxylate (MG). This previous work (1) has shown that PMG has very interesting properties in terms of degradation and toxicity. The ultimate state of its degradation is glyoxylic acid, which is a metabolite of plant Krebs cycle. However, PMG degradation also releases methanol which is prohibited in pharmaceutical or medical applications. To overcome this problem we investigated the anionic polymerization of ethyl glyoxylate (EtG) (2).

Assuming similar degradation as in the case of PMG, poly(ethyl glyoxylate) (PEtG) hydrolysis should lead to glyoxylic acid and ethanol (3), which are both innocuous. Moreover, as in the case of PMG, PEtG has a low ceiling temperature. Thus, the hydroxyl ends have to be reacted with a capping agent under mild conditions. For the polymer concerned in this study, phenyl isocyanate was used.

This paper deals with the synthesis and the *in vitro* degradation study of PEtG. Various techniques including weighing, potentiometry, gel permeation chromatography (GPC) and nuclear magnetic resonance (NMR) were used to determine the hydrolysis mechanism.

## Experimental

### Materials

Dibutyl tin dilaurate (DBTL, Aldrich, 95%) and phenyl isocyanate (PhNCO, Acros, 99%) were used as received.

Ethyl glyoxylate (EtG) (M=102), in toluene solution (50% w/w) was kindly supplied by Clariant.

Triethylamine (NEt<sub>3</sub>, Acros) was distilled over potassium hydroxide (88°C) and dichloromethane (Acros) over sodium (40°C) before use.

### Synthesis

EtG was distilled under vacuum over phosphorus pentoxide (P<sub>2</sub>O<sub>5</sub>). A clear yellow liquid was obtained (100°C/50 mbar). A solution of Et<sub>3</sub>N (initiator) in dichloromethane (2 μL/mL) was added to the monomer (50% v/v) and the solution was stirred one hour at -20°C. A transparent viscous medium was obtained. An excess of phenyl isocyanate was then added to end-cap the polymer in the presence of DBTL as catalyst. The solution was stirred overnight at room temperature. Purification by precipitation into methanol was realized and the polymer was dried under vacuum at 50°C for 5 hours.

<sup>1</sup>H NMR : chemical shifts (CDCl<sub>3</sub>) : PEtG : 1.2 ppm (3H, CH<sub>3</sub>), 4.2 ppm (2H, CH<sub>2</sub>), 5.5 ppm (1H, CH), 7.3 ppm (10H, phenyl) ; EtG : 1.4 ppm (3H, t, CH<sub>3</sub>), 4.4 ppm (2H, q, CH<sub>2</sub>), 9.3 ppm (1H, s, CH).

### *NMR Studies*

NMR spectra were recorded on Bruker spectrometers 300 MHz. Molar masses were determined as follows (Equ. 1), using the integrations of ethyl ester group protons ( $I_{CH_2}$ ) and phenyl protons ( $I_{Ph}$ ).

$$M_n = \frac{I_{CH_2}/2}{I_{Ph}/10} \times 102 + 256 \quad (1)$$

Thin films of polymer were placed into four sterilized NMR tubes containing  $D_2O$  and  $D_2O$  buffered at pH=4, pH=7 and pH=9. NMR tubes were immediately sealed and placed in a drying oven at 37°C and analyzed at different degradation times.

### *Thermal Analysis*

The thermal stability of PETG was obtained using a Perkin Elmer thermogravimetric analyzer (TGA7) at the heating flow of 10°C/min and under  $N_2$ .

### *Potentiometry*

Film samples were placed directly in freshly distilled water thermostated at 37°C. For each degradation time, two samples were recovered. Sodium azide ( $NaN_3$ ) was added as a biocide to be sure that the decrease of pH was not due to bacteria growth.

### *Weight Loss*

Polymer thin films were placed in aluminum pans. Samples were weighed initially ( $m_0$ ) and placed in an oven at 37°C in water-saturated conditions. At selected times, two samples were dried under vacuum (0.1mbar, 50°C) for 48 h and weighed to obtain dry weights ( $m_d$ ). Weight loss was determined by comparing the remaining dry weight  $m_d$  with the initial weight  $m_0$ , (Equ. 2).

$$\% \text{ Weight Loss} = \frac{m_0 - m_d}{m_0} \times 100 \quad (2)$$

*Chromatography Studies*

Thin films of polymer were placed in a drying oven at 37°C in a saturated water atmosphere. At different times during degradation, samples were dried under vacuum for 48 h and analyzed.

Molecular weights were obtained by GPC in dichloromethane (1 mL/min) using a Waters pump model 6000, an injector (Rheodyne) and a refractive index detector (RID-6A Shimadzu), equipped with a PL gel 5 $\mu$ m mixed-C linear column. The system was calibrated using polystyrene standards with low polydispersity.

## Results and Discussion

### Synthesis

Ethyl glyoxylate (EtG) spontaneously polymerizes at room temperature. A distillation step on P<sub>2</sub>O<sub>5</sub> is first necessary to break the oligomers and obtain pure EtG. A previous study on the polymerization of EtG (2) showed that the optimum conditions are to work in CH<sub>2</sub>Cl<sub>2</sub> at -20°C, with triethylamine as an initiator. A lot of transfer reactions occur in the medium leading to low molar masses and to a hydroxyl ended PEtG.

Because of its low ceiling temperature, depolymerization of PEtG occurs at room temperature. That is why a termination step using an adequate agent is necessary.

The addition polymerization has not a living character and leads to hydroxyl ended PEtG chains which have to be end-capped similarly to other polyaldehydes (4). As recommended by the literature, we used phenyl isocyanate (2) as an end-capping agent.

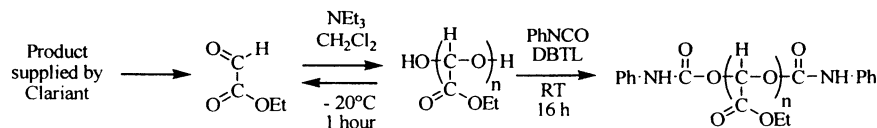


Figure 1. Synthesis of Poly(ethyl glyoxylate).

<sup>1</sup>H NMR in DMSO-*d*<sub>6</sub> was achieved on the end-capped polymer. Three main peaks were observed corresponding to the ethyl ester group (CH<sub>3</sub> : 1.20 ppm and CH<sub>2</sub> : 4.2 ppm) and to the acetalic one (CH : 5.3 ppm). The integration values are close to our expectations (3/2/1). The signal of the phenyl moieties is



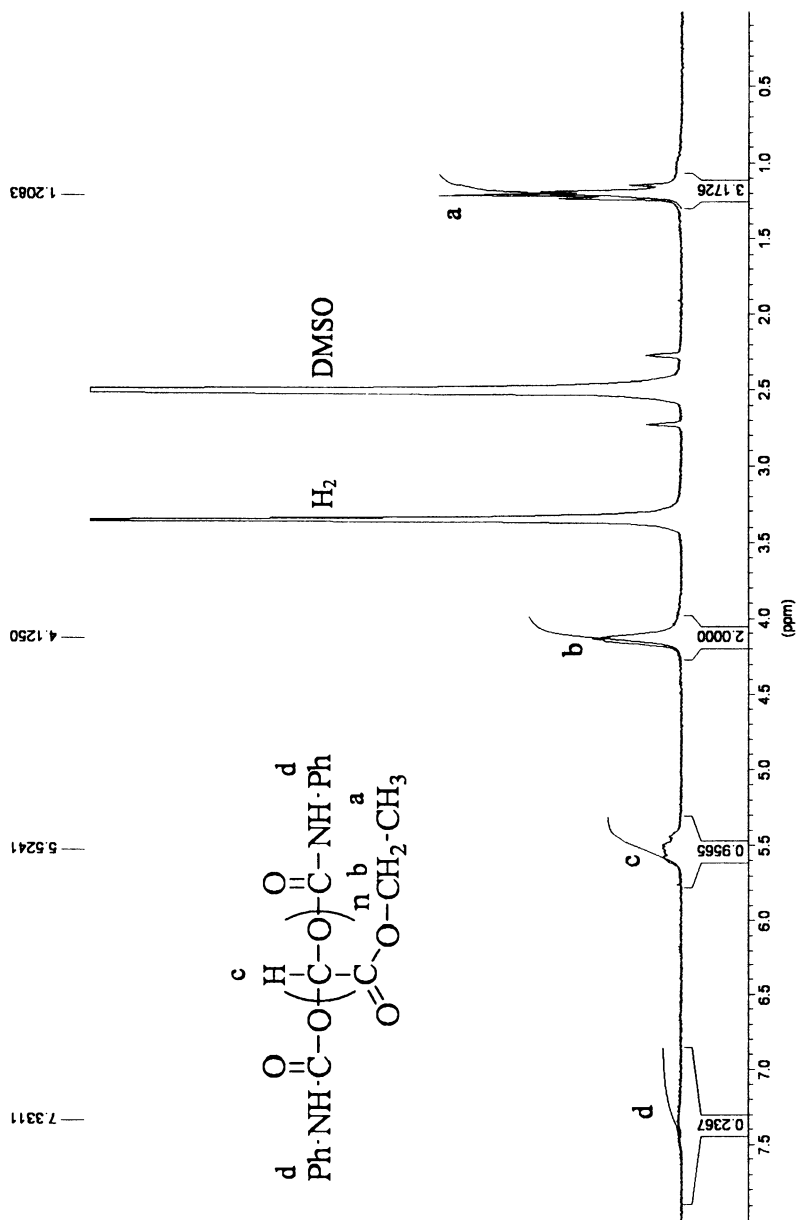


Figure 2.  $^1\text{H}$  NMR (300 MHz) of Poly(ethyl glyoxylate) in  $\text{DMSO-}d_6$ .

observed at 7,3 ppm. Assuming that PEtG is a linear chain, two phenyl groups are present in each chain and molecular weights can be determined from Equation 1. Moreover no signal corresponding to EtG can be detected thus proving that end-capping of PEtG was effective.

Thermogravimetric analysis is another way to determine whether PEtG is well end-capped or not. Indeed, a PEtG which is not end-capped or not properly end-capped will not be stable even at 50°C since chain depolymerization could occur, while end-capped PEtG is stable up to 200°C.

All experiments were conducted on the same PEtG whose end-capping was checked prior to the degradation study.

## Degradation

PEtG hydrolysis is a heterogeneous reaction since PEtG is non soluble in water, contrary to its hydrosoluble byproducts. Thus, to limit any possible surface dependence degradation, the samples used were all 3mm thick films.

### Potentiometry

Experiments were conducted at 37°C for potential medical application purposes. According to the results obtained for the *in vitro* hydrolysis of PMG (3), ester cleavage of PEtG is expected leading to carboxylic function, and that is why a drop in pH is expected. Results are presented in Figure 4.

During the first five days, no relevant pH variation was observed. From day six on, a pH drop was observed and attributed to an auto acceleration due to the presence of carboxylic groups coming from glyoxylic acid hydrate (GAH) and/or poly(glyoxylic acid) segments. From day eight on, a plateau was observed at pH = 2.30 which corresponds to the pH of glyoxylic acid monohydrate (GAH) in the same conditions.

### Weight Loss

PEtG was placed in an oven at 37°C in saturated humidity atmosphere. At selected times, two samples were taken, dried under vacuum (0.1 mbar/50°C) for 48 hours and then weighed. Any weight loss was attributed to the degradation of PEtG, (Figure 5).

During the first nine days, less than 1% of weight loss could be detected. Within fifteen days only 5% of weigh loss was observed. Then, up to thirty days, a significant weight decrease was observed leading to 27.5% weight loss. Over thirty days, the polymer turned to a sticky viscous liquid but no further weight loss was observed. Thus according to the plateau at 72.5%, only ethanol

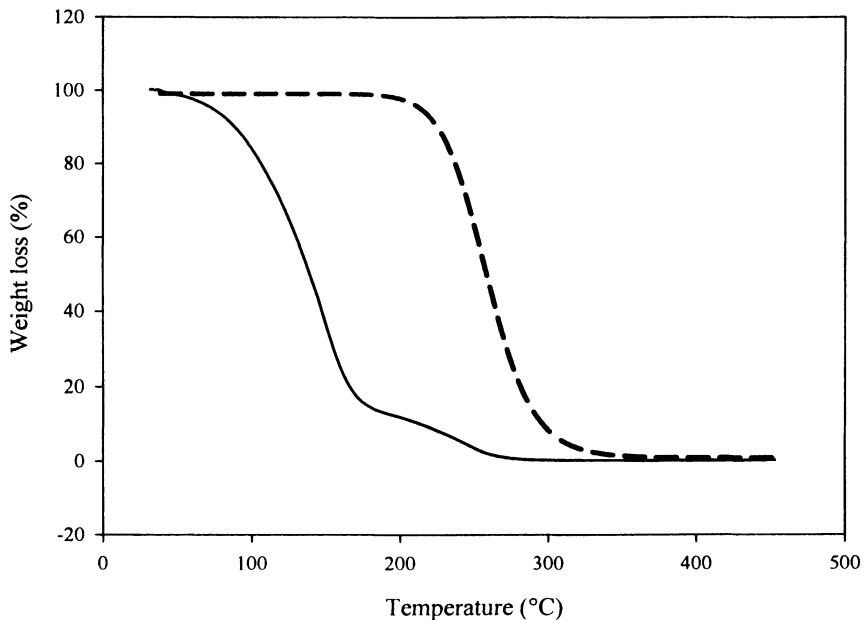


Figure 3. Thermogravimetric analysis of PEtG not end-capped (-) and end-capped (--) under N<sub>2</sub>.

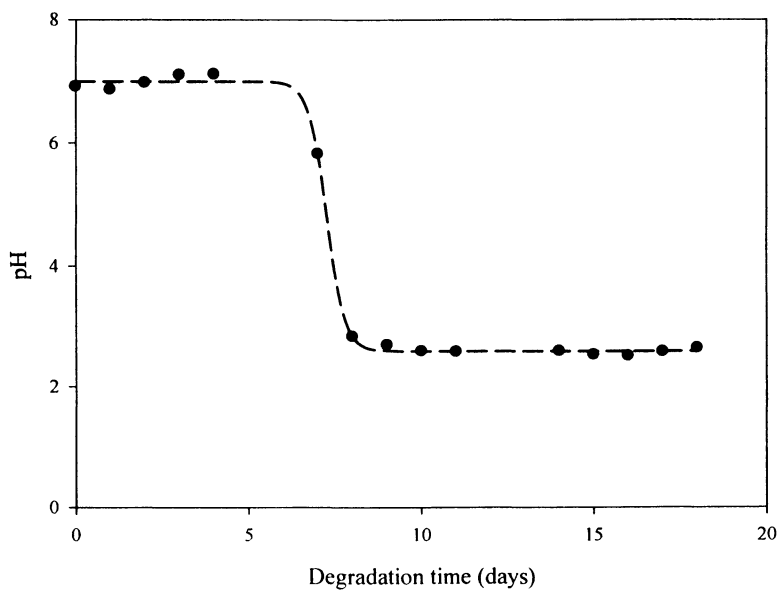


Figure 4. Evolution of pH during PEtG degradation. (Reproduced with permission from reference 5. Copyright 2008 Elsevier.)

elimination was observed, the remaining product being glyoxylic acid and hydrolyzed oligomers.

### Chromatography

PEtG molecular weights were measured at different degradation times to demonstrate chain scissions.

A shift of chromatograms to lower molecular weight and a widening of the peak are observed from the 4<sup>th</sup> day until the 18<sup>th</sup> day. After 18 days, no peak can be detected on the chromatogram. SEC results showed that chain scissions are present from the beginning of PEtG hydrolysis, (Figure 6). GPC data are resumed Table 1.

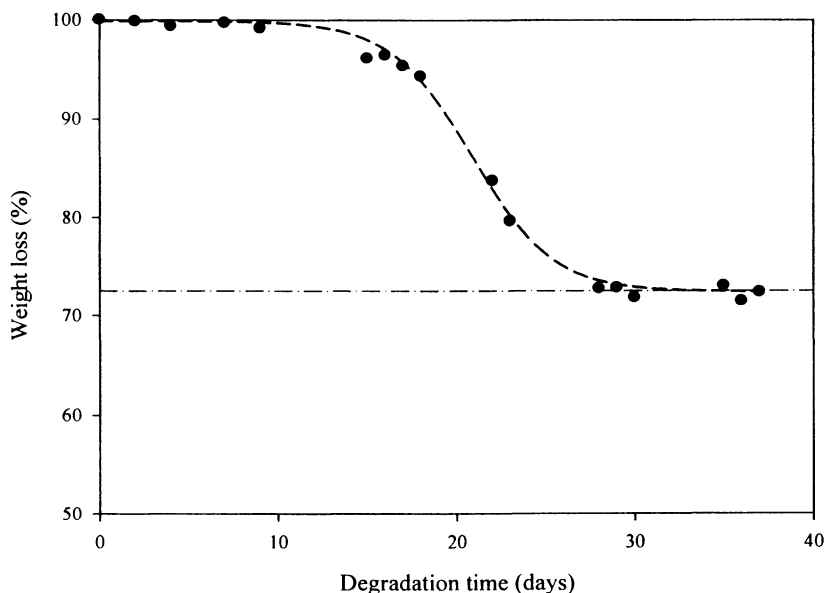


Figure 5. Weight loss (%) during PEtG degradation and (---) corresponding to the only loss of ethanol.

Table 1. GPC data during degradation.

Days	0	7	10	12	14	15
$\overline{Mn}$	73100	61800	27800	16300	5900	6100
PDI	2.6	3.8	7.6	9.5	16.0	21.9

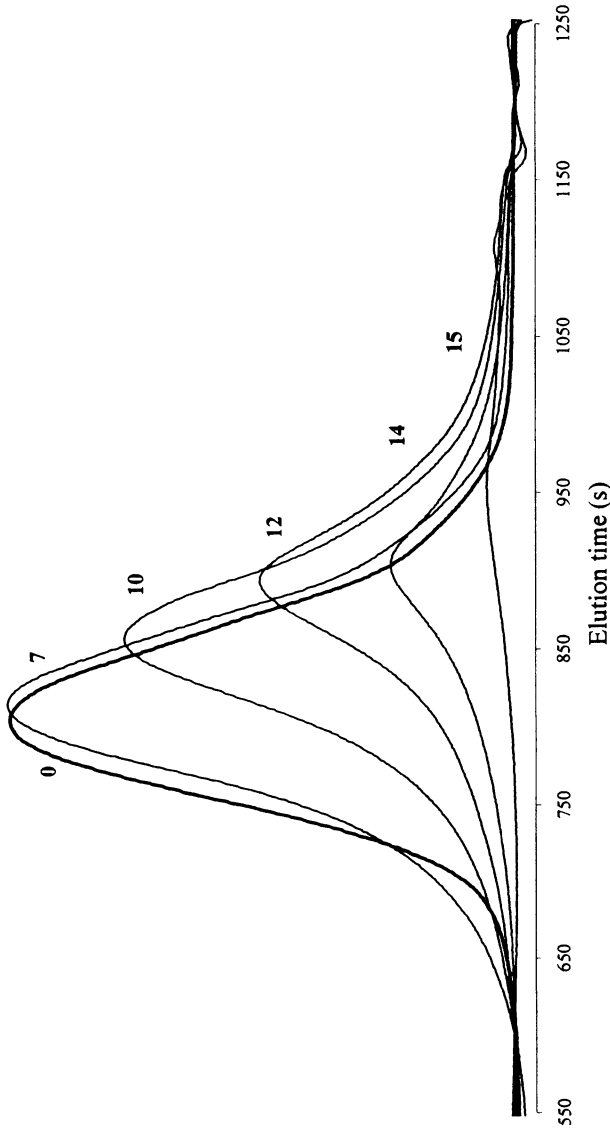


Figure 6. GPC chromatogram evolution of PEtG during degradation. (Reproduced with permission from reference 5. Copyright 2008 Elsevier.)

### NMR Studies

PEtG hydrolysis was followed in water and in buffered media, with sodium acetate as an internal standard. Because PEtG is insoluble in water, only the degradation products will be detected. Two main signals are observed. In  $D_2O$ , at first ethanol (EtOH) is detected owing to ester group hydrolysis. Then, glyoxylic acid hydrate (GAH) is observed, indicating chain scissions, (Figure 7).

After one month, a high degradation rate is observed and ethyl glyoxylate hydrate (EtGH), which is usually hydrolyzed into GAH, may be detected.

Similar results are observed at pH=4 and pH=7. At pH=9, which is still under investigation, only EtOH release is expected since polyacetals are generally stable in basic media.

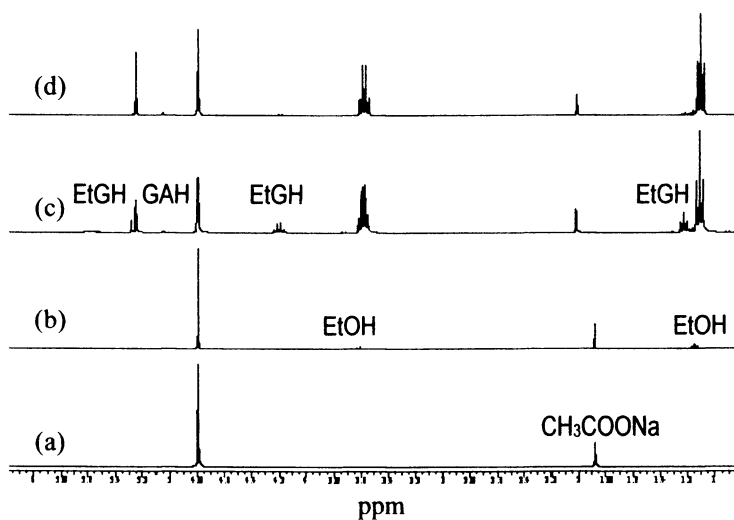


Figure 7.  $^1H$  NMR spectra of PEtG in  $D_2O$  versus degradation time :  $t = 0$  (a); 22 days (b); 39 days (c); 59 days (d). (Reproduced with permission from reference 5. Copyright 2008 Elsevier.)

According to these results, we proposed the following mechanism of degradation by hydrolysis which involves simultaneous chain scissions and further depolymerization together with ester group hydrolysis (Figure 8).

### Conclusion

Anionic polymerization of EtG leads to a new synthetic biodegradable polymer, namely poly(ethyl glyoxylate). Because of a low ceiling temperature and transfer reactions, PEtG has hydroxyl ends that can be end-capped with phenyl isocyanate.

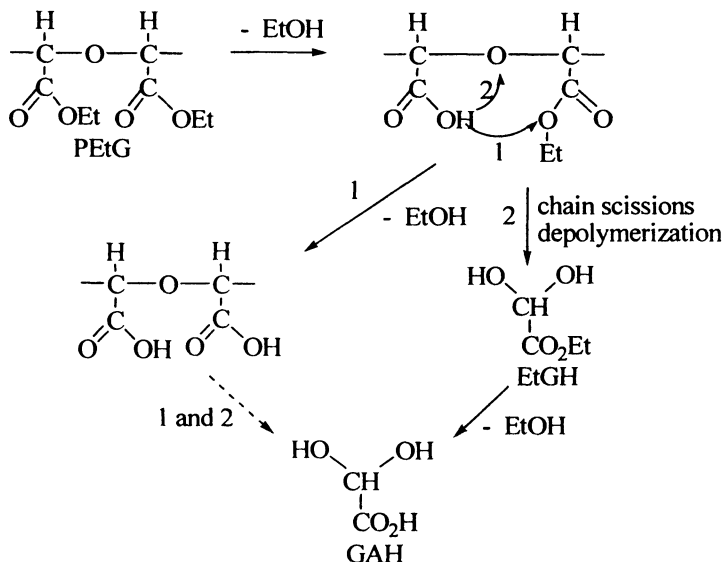


Figure 8. PEtG mechanism of degradation by *in vitro* hydrolysis.

The *in vitro* hydrolysis study, by means of potentiometry, weight loss, SEC and NMR, shows that the degradation mechanism involves simultaneous chain scissions and ester group hydrolysis. Indeed, ester hydrolysis was evidenced by the release of an acidic group as glyoxylic acid hydrate by NMR, or by the drop of pH and the loss of ethanol (weight loss and NMR). The decrease in molecular weight observed by SEC and the presence of small molecules by NMR prove that chain scissions occurred at the same time.

The ultimate degradation product is glyoxylic acid hydrate which is a Krebs cycle metabolite and allows us to think that PEtG is biodegradable.

## References

1. Brachais, C. -H.; Huguet, J.; Bunel, C. *Polymer* **1997**, *38*, 19, 4959-4964.
2. Burel, F.; Rossignol, L.; Pontvianne, P.; Hartman, J.; Couesnon, N.; Bunel, C. *e-Polymer* **2003**, *31*.
3. Brachais, C. -H.; Huguet, J.; Bunel, C.; Brachais, L. *Polymer* **1998**, *39*, 4, 883-890.
4. Vogl, O. *J. Polym. Sci. A: Polym. Chem.* **2000**, *38*, 13, 2293-2299.
5. Belloncle, B.; Burel, F.; Oulyadi, H.; Bunel, C.; *Polymer Degradation and Stability*; doi:10.1016/j.polyimdeggradstab.2008.03.004.

## Chapter 5

# Effect of Drug Loading on the Rate of Nicotine Release from Poly( $\epsilon$ -caprolactone) Matrices

Rachel T. Rosenberg<sup>1</sup>, Steven P. Siegel<sup>2</sup>, and Nily Dan<sup>1,\*</sup>

<sup>1</sup>Department of Chemical and Biological Engineering, Drexel University, Philadelphia, PA 19104

<sup>2</sup>Stanley Center for Experimental Therapeutics, Division of Neuropsychiatry, Department of Psychiatry, University of Pennsylvania, Philadelphia, PA 19104

Previous studies have shown that the rate of drug release from polymeric matrices depends on the polymer and drug properties. Here we examine the release of a highly hydrophilic drug, nicotine, from poly( $\epsilon$ -Caprolactone) (PCL). Quite surprisingly, we find that the rate of drug release increases with increasing drug loading, as does the water content of the matrix. We suggest that the hydrophilic drug partitions out of the hydrophobic polymer into water voids in the matrix, thereby enhancing the diffusion rate. A diffusion model developed for this scenario fits the data well with a single adjustable parameter.



## Introduction

The use of synthetic polymers to serve as structural components in drug delivery systems has widely increased over the last twenty years. Extensive studies have shown that the rate of drug release depends on both the polymer properties (1-3) and the drug characteristics (4,5). Two main mechanisms control the rate of drug release from polymeric systems (3,6): The first, a diffusion-controlling process, occurs when a concentration gradient is present. This process dominates release from non-degradable or slowly-degrading polymers. Drugs may be released also by erosion or degradation of the polymer, a process that dominates release in rapidly degradable matrices and/or when the diffusion rate of the drug is slow, e.g. because of high drug MW or matrix crystallinity.

Poly( $\epsilon$ -caprolactone) (PCL) is a biodegradable, non-toxic polymer of the polyester family suitable for implantable or injectable delivery devices (7). The degradation of PCL occurs at a very slow rate via the hydrolyzation of ester bonds, making it ideal for long term delivery systems (7). Previous studies (8-13) find that 35-55% of the initial hydrophilic drug load was released rapidly from PCL nano and micro particles, within a few hours. This 'burst' was followed by slow release over timescales of weeks to months (8-13).

## Materials and Methods

### Materials

The PCL matrix used in this study contains a 50:50 mixture of low (14,000 g/mol) and medium (65,000 g/mol) PCL, obtained from Sigma-Aldrich. The melting temperature of both polymers is 60°C (14). Nicotine hydrogen tartrate salt ( $C_{10}H_{14}N_2 \cdot 2C_4H_6O_6$ ) was purchased from Sigma-Aldrich. The solubility of this compound in our buffer solution was measured in our lab and found to be higher than 200 mg/ml at room temperature.

### Melt Mixing and Pellet Formation

A mixture of the 50:50 polycaprolactone (PCL) matrix and the appropriate weight nicotine drug load were placed in an oil bath at 150°C. A Teflon® stirrer slowly mixed the viscous material in a polypropylene cup for thirty minutes. After visually inspecting for homogeneity, the PCL/drug mixture was allowed to cool in the freezer until it hardened and could be removed from the cup with ease. It was then stored at room temperature until ready for pressing. To create

the pellets, the PCL/drug mixture was softened on a hot plate at 70°C and placed in a 6 mm diameter Teflon®-coated mold. The plate was first pressed at 80°C and 30,000 psi for thirty seconds and immediately placed in a second press which operates at room temperature and a pressure of 24,000 psi until cooled. This procedure was repeated until the pellets reached the density requirement of 1.1 mg/mm<sup>3</sup>. The pellets were weighed and measured by a digital caliper.

### Calibration Curve

In order to determine the concentrations of drug released into a phosphate buffered saline (PBS-B) solution, a calibration curve of known concentrations was generated. A 0.4 mg/mL solution of drug in PBS-B was used as the highest concentration on the curve. The solution was vortexed for two minutes and then diluted by half. This was repeated until a total of 10 solutions were made, where pure PBS-B was the lowest concentration.

### In Vitro Assay

For each study, at least three pellets of the same type were used so an average value could be achieved. Each pellet was placed in 100 mL of PBS-B solution and placed on a stirrer at 37°C to simulate a natural body state. Aliquots of 200 µL were taken from each jar to measure absorbance by the UV Spectrometer. These data are compared to the calibration curve, wherein, concentrations can ultimately be deciphered. For each set of conditions that was examined, corresponding positive and negative controls were present. The positive controls were the drug load of the pellet dissolved in PBS-B solution. The negative controls were pellets only containing the polymer and no drug. Further details of the experimental set up can be found in (5,15,16).

## Results and Discussion

To investigate the effect, if any, of drug load on the rate of release from PCL we compare three different nicotine concentrations: 10%, 40% and 50% (by weight). By measuring the concentration of nicotine in solution, as a function of time, we calculate the amount of drug released at any point in time. At the end of the release process, when UV indicated that all drug was released, we measured the weight of the polymer particles before and after drying to evaluate possible degradation of the matrix and the water content.

In all cases, we found that the weight of the dried matrix, after the UV-determined 100% drug release, corresponded (within 1%) to the initial mass of

the polymer. This confirms that the entire drug was released and that polymer degradation did not occur. This is as expected, since the degradation rate of PCL is known to be much longer than the time scales of our experiments (7-14).

Quite surprisingly, we find that the degree of matrix swelling, as defined by the water content in the matrix at 100% drug release, increases with drug loading. The water content, on average, was  $10.5 \pm 2\%$  (weight) in the 10% drug pellets,  $26.8 \pm 1\%$  in the 40%, and  $29.1 \pm 1\%$  in the 50%. This is unexpected, since at equilibrium the degree of polymer swelling should depend only on the polymer/solvent compatibility, as defined by the relevant Flory  $\chi$  parameter (17). One might argue that mixing the (hydrophobic) PCL with increasing amounts of (highly hydrophilic) nicotine would increase the average mixture hydrophilicity. However, while this argument may apply initially, it is invalid once the entire drug was released from the matrix.

One possible explanation for the increase in water content is the semi-crystalline nature of PCL at the temperature of our experiments ( $25^{\circ}\text{C}$ ): unlike a melt polymer, the semi-crystalline PCL is likely to hold its original pellet shape, even after the drug was released. As a result, the volume previously occupied by the drug becomes available to water. This hypothesis is supported by our visual observation of no change in the particle dimensions during the release process, even after  $\sim 50\%$  by weight of the original pellet, namely the drug, was released.

In Figure 1 we plot the mass of nicotine released from the PCL pellets, as a function of time. Contrary to previous studies (7-14), we do not find any signs of initial 'burst' in the first hours of the experiment. This may be due to the fact that our particles are macroscopic, rather than micro or nano.

As may be expected, the mass released, at any time point, increases with increasing initial loading. The time required for 100% release of the encapsulated drug decreases with increasing loading. Complete release is achieved after  $\sim 2$  days for the 50%,  $\sim 5$  days for the 40%, and  $\sim 11$  days for the 10%.

The classic diffusion model of drug release, when matrix degradation is neglected, can be written as (6, 18)

$$M(t) = M_0 \left( 1 - \sum_{n=1}^{\infty} e^{-\frac{Dn^2 \pi^2 t}{R^2}} \right) \quad (1)$$

where  $M$  is the mass of released drug at time  $t$ ,  $M_0$  is the initial mass of the drug in the system,  $D$  the drug diffusion coefficient in the matrix, and  $R$  the particle radius.

Equation (1) predicts that the time at which complete release is obtained (namely, when  $M=M_0$ ) should be independent of the initial loading, an uncton of the particle dimension and the diffusion coefficient of the drug in the matrix. However, as clearly demonstrated in our data, the time required to achieve complete release of nicotine from PCL decreases sharply with the drug loading.

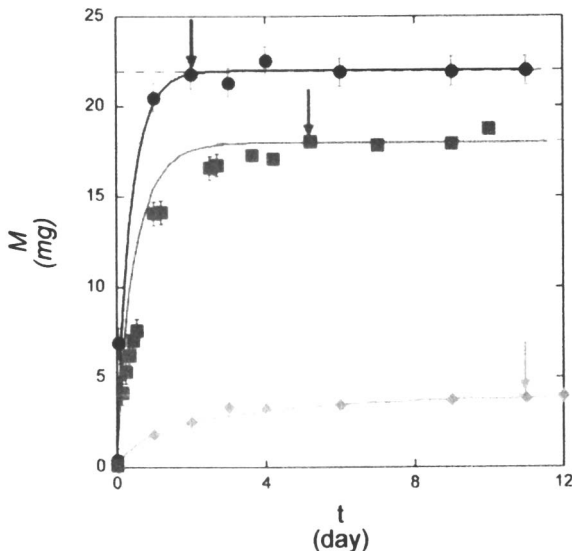


Figure 1. The mass of nicotine released from PCL,  $M$ , as a function of time. Diamonds denote 10% initial loading, Squares 40% initial loading, and circles 50% initial loading. The dashed lines show the maximal amount of drug in the system. Arrows mark the time at which 100% release was achieved. Solid lines are the result of a fit using equations (1-3). (See page 2 of color insert.)

Several studies suggest that matrix swelling may affect the rate of drug release (19,20). We hypothesize that the increase in the rate of nicotine release with initial loading may be associated with the concurrent increase in the water content in the pellet. Since nicotine is highly hydrophilic, it is likely to partition into any volume of available water, rather than remaining in the hydrophobic matrix. Since the rate of nicotine diffusion in water is much higher than in the polymer, the apparent diffusion coefficient of the nicotine out of the pellet increases with increasing water content. This scenario can be described by an effective, time dependant diffusion coefficient for the drug

$$D_{eff}(t) = D_{d,p} + xM_w D_{d,w} \quad (2)$$

where  $D_{d,p}$  is the diffusion coefficient of the drug in the polymer,  $D_{d,w}$  is the diffusion coefficient of the drug in water;  $M_w$  is the mass of water in the pellet- a function of time, and  $x$  a partition coefficient. The mass of water in the particle can be calculated by (18)

$$M_w(t) = M_w^\infty \left( 1 - \frac{6}{\pi^2} \sum_{n=1}^{\infty} \frac{1}{n^2} e^{-D_w n^2 \pi^2 t / R^2} \right) \quad (3)$$

where  $M_w^\infty$  is the maximal loading of water in the system, and  $D_w$  the diffusion coefficient of water in the matrix.  $M_w^\infty$  is known from our measurements of the maximal water content in the pellets.  $D_w$  has been found to be  $2 \times 10^{-7}$  cm<sup>2</sup>/s (21),  $D_{d,w}$  for nicotine is  $6 \times 10^{-6}$  cm<sup>2</sup>/s, (22) and  $D_{d,p}$  is on the order of  $10^{-8}$  cm<sup>2</sup>/s [note: The diffusion coefficient of a molecule in a liquid decreases with the molecular volume to the power of 0.5-0.6 (22). The molecular volume of caffeine and nicotine is about 10 times that of water (22). Using this correlation yields  $D$  in PCL of order  $1 \times 10^{-8}$  -  $5 \times 10^{-8}$  cm<sup>2</sup>/s]. Thus, we can calculate the value of  $f(t)$  from equation (1) by using the time-dependent diffusion coefficient (equation 2), a function of the water content (Equation 3). This set of equations has only one unknown parameter,  $x$ , which should be the same regardless of drug loading.

In Figure 1 we show the fit of this model to the release data, using the value  $x=0.06$  for all three loadings. We see that this value provides good agreement with all drug loadings.

## Conclusions

In this paper we examine the effect of drug loading on the release rate of a highly hydrophilic drug from PCL matrices. We find that the rate of drug release increases with increased loading, namely, the effective diffusion coefficient of the drug out of the matrix increases. Moreover, the water content in the matrix increases significantly with the initial drug loading.

We suggest that the semi-crystalline structure of PCL keeps the original pellet shape during the process of drug diffusion into solution, so that water diffuses into the voids. Since nicotine is highly hydrophilic, some of it partitions into the water contained in the matrix (see Figure 2). Thus, the effective diffusion coefficient of the drug is composed of an average of the diffusion coefficient in the polymer and in water. A single parameter fit yields good agreement for the three drug loadings examined.

It should be noted that the PCL/nicotine system is somewhat unique. First is the fact that PCL is semi-crystalline at the room temperature at which the experiments were conducted. Second is the high solubility of nicotine in water, which drives the drug to partition into the aqueous regions in the matrix. A similar study with PCL and caffeine, which has a solubility of ~20 mg/ml in water (i.e. 10% that of nicotine) does not show such a clear dependence of the rate of diffusion on drug loading (16).

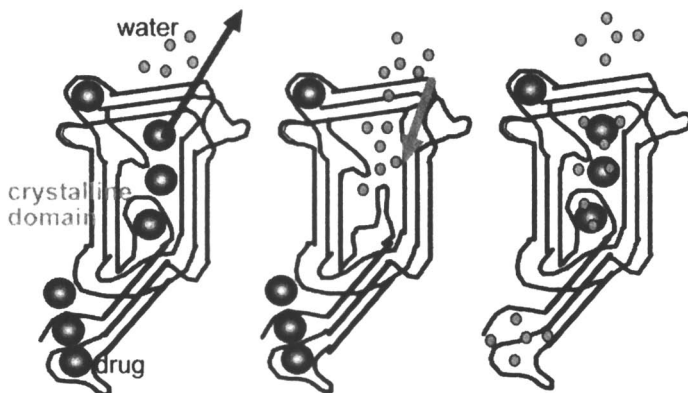


Figure 2. A sketch of our proposed mechanism for nicotine release. The crystalline PCL domains are rigid, and hold the matrix shape even when the drug begins to leach out (left). This leaves voids into which water can diffuse (center). The remaining, hydrophilic drug preferentially partitions into the aqueous regions (right).

## References

1. Amass, W.; Amass, A.; Tighe, B. *Polym. Int.* **1998**, *47* (2), 89-144.
2. Dittgen, M.; Durrani, M.; Lehmann, K. *STP Pharma. Sci.* **1997**, *7* (6), 403-437.
3. Siepmann, J.; Gopferich, A. *Adv. Drug Del. Rev.* **2001**, *48* (2-3), 229-247.
4. Frank, A.; Rath, S. K.; Venkatraman, S. S. *J. Cont. Rel.* **2005**, *102*, 333-344.
5. Siegel, S. J.; Kahn, J. B.; Metzger, K.; Winey, K. I.; Werner, K.; Dan, N. *Eur. J. Pharm. Biopharm.* **2006**, *64*, 287-293.
6. Higuchi, T. *J. Pharm. Sci.* **1961**, *50*, 874-875.
7. Sinha, V. R.; Bansal, K.; Kaushik, R.; Kumria, R.; Trehan, A. *Int. J. Pharm.* **2004**, *278*, 1-23.
8. Yang, Y. Y.; Chung, T. S.; Ng, N. P. *Biomaterials* **2001**, *22*, 231-241.
9. Perez, M. H.; Zinutti, C.; Lamprecht, A.; Ubrich, N.; Astier, A.; Hoffman, M.; Bodmeier, R.; Maincent, P. *J. Cont. Rel.* **2001**, *65*, 429-438.
10. Jackson, J. K.; Liang, L. S.; Hunter, W. L.; Reynolds, M.; Sandberg, J. A.; Springate, C.; Burt, H. M. *Int. J. Pharm.* **2002**, *243*, 43-55.
11. Dhanaraju, M. D.; Gopinath, D.; Ahmed, M. R.; Jayakumar, R.; Vamsadhara, C. *J. Biomat. Res. A* **2005**, *76*, 63-72.
12. Leong, K. F.; Wiria, F. E.; Chua, C. K.; Li, S. H. *Bio-Med. Mat. Eng.* **2007**, *17*, 147-157.
13. Chawla, J. S.; Amiji, M. M. *Int. J. Pharm.* **2002**, *249*, 127-138.

14. Sigma-Aldrich. URL [www.sigmaaldrich.com](http://www.sigmaaldrich.com).
15. Rosenberg, R. T.; Siegel, S. P.; Dan, N. *J. App. Polym. Sci.* **2007**, *Submitted*.
16. Rosenberg, R. T.; Devenney, W.; Siegel, S. P.; Dan, N. *Molecular Pharmaceutics*; DOI: 10.1021/mp70009, 2007.
17. Flory, P. *Principles of Polymer Chemistry*; Cornell University Press: Ithaca, NY, **1971**.
18. Crank, J. *The Mathematics of Diffusion*, 2<sup>nd</sup> ed.; Oxford University Press: London, **1975**.
19. Petropoulos, J. H.; Papadokostaki, K. G.; Amarantos, S. G. *J. Polym. Sci. B: Polym. Phys.* **1992**, *30* (7), 717-725.
20. Bernik, D. L.; Zubiri, D.; Monge, M. E.; et al. *Coll Surf A: Physiochem. Eng. Aspects* **2006**, *273*, 165-173.
21. Yoon, J. S.; Jung, H. W.; Kim, M. N.; Park, E. S. *J. Appl. Polym. Sci.* **2000**, *77* (8), 1716-1722.
22. *Perry's Chemical Engineers' Handbook*, 7<sup>th</sup> ed.; Perry, R. H., Green, D. W., Maloney, J. O., Eds.; McGraw-Hill: New York, **1997**; pp 2-330 -331.

## Chapter 6

# Fatty Acid-Based Biodegradable Polymers: Synthesis and Applications

**Marina Sokolsky-Papkov<sup>1</sup>, Ariella Shikanov<sup>1</sup>, Aviva Ezra<sup>1</sup>,  
Boris Vaisman<sup>1</sup>, and Abraham J. Domb<sup>1,2</sup>**

<sup>1</sup>Department of Medicinal Chemistry and Natural Products,  
School of Pharmacy – Faculty of Medicine, The Hebrew University  
of Jerusalem, 91120 Jerusalem, Israel

<sup>2</sup>Leonyl Jacobson Chair of Medicinal Chemistry, Affiliated with the David  
R. Bloom Center for Pharmacy and the Alex Grass Center for Synthesis  
and Drug Design at The Hebrew University of Jerusalem,  
91120 Jerusalem, Israel

Fatty acids have been used previously in the development of polymers for biomedical applications as they are considered to be inert, inexpensive and biocompatible, as well as possessing low toxicity. This review focuses on use of different fatty acids for synthesis of injectable polymers for intended use as drug carriers.

## Introduction

Fatty acids have been used previously in the development of polymers for biomedical applications as they are considered to be inert, inexpensive and biocompatible. The main fatty acids which are used as a base for synthesis of biomedical polymers (polyanhydrides) are stearic acid (1), erucic acid (C22 unsaturated fatty acid) dimer (2), bile acid dimer (3), ricinoleic acid (4) and other fatty acids (5), middle long carbon chain (C12 – 15) dibasic acids, such as dodecanedioic, brassylic acid, tetradecandioic acid and pentadecandioic acid (1).

Fatty acids are used in preparation of microspheres for controlled drug delivery. For example, poly(vinyl alcohol), substituted with lauric, myristic, palmitic, and stearic acids at different substitution degrees was employed for the preparation biodegradable microspheres containing progesterone or indo-



methacin (6). Microspheres were prepared by starting from an oil-in-water dispersion containing the polymer and drug in the inner phase, following by solvent extraction method. Microspheres were obtained with high loading efficiency, whose release properties were dependent on the nature of the acyl substituent and the substitution degree.

Fatty acids were incorporated into polymers to influence their physicochemical properties. For example, polyanhydrides based on short chain hydrophobic acids such as sebacic/adipic acids are brittle and hydrolyze under common storage conditions. Introduction of hydrophobic moieties as part of the polymer chain or as hydrophobic terminals resulted in better hydrolytic stability, pliability and affects biomedical applications such as release profile from the polymers (7). The same approach was used to influence the properties of widely used polyester – poly(lactic acid). Polyesters are useful materials for controlled drug delivery since they hydrolyze to hydroxyl acid monomers when placed in aqueous media. Polyesters for drug delivery systems are usually synthesized from lactic/glycolic acids. However enantiomerically pure PLA is a semi-crystalline polymer with Tg of 55°C and Tm of 180°C. The degree of crystallinity and melting point can be reduced by random incorporation of other monomers into the PLA chain leading to decrease in crystallization ability (8-10) Fatty acids are suitable candidates for incorporation into PLA, as they are natural components and they are hydrophobic and thus may retain an encapsulated drug for longer time period when used as drug carrier (4, 11). This article focuses on the use of fatty acids in the synthesis and properties of two types of the polymers, poly(ester anhydride)s and polyesters.

### **Poly(ester-anhydrides)**

Polyanhydrides as a class of degradable polymers have been used in a number of applications (12, 13) and in drug delivery. They have been extensively investigated for use in the controlled delivery of a number of drugs including chemotherapeutics (14, 15), antibiotics (15), anesthetics (16, 17), and polypeptides (18) in the past 20 years. Recently, polyanhydrides designed for use in the fields of orthopedics (19) and polymer drugs (20) have been reported. Consequently, curatorial researchers have attached increasingly importance to the polyanhydrides in medical applications.

Polyanhydrides prepared from fatty acids are good candidates for the delivery of hydrophilic drugs due to the desired hydrophobicity of the natural fatty acids in the main chain of the polyanhydrides (11). These polyanhydrides have two series of acid monomers: one has longer carbon chain, such as dimer erucic or oleic acid; another has shorter carbon chain, such as sebacic acid (2). Fatty acids can be incorporated into the polymer chain by one of two ways: by

conversion of monofunctional fatty acids into diacid monomers and including them as repeating units in the polymer (2) or by using monofunctional fatty acid as chain terminators.

The second approach was applied in the synthesis of fatty acid terminated polyanhydrides. Polyanhydrides based on sebacic acid, and terminated with oleic, stearic, linoleic or lithocholic acid, or combinations of several fatty acids were synthesized (21). The general structure of fatty acid terminated polyanhydrides is shown in Figure 1.

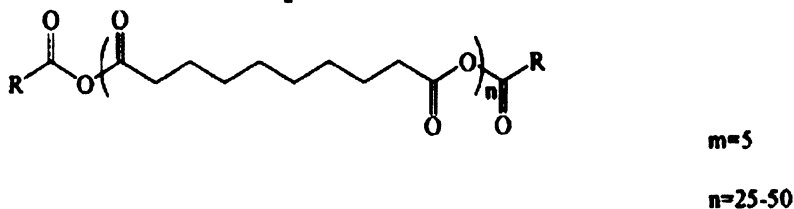


Figure 1. Fatty acid terminated polyanhydrides (reproduced from reference 7)  
R=Oleic, stearic, linoleic, lithocholic acids.

These polyanhydrides all possessed suitable properties including: low melting points (60-82°C), biodegradability and pliability. These polyanhydrides were able to retain both hydrophilic (5FU) and hydrophobic (triamcinolone) drugs. The release of 5FU continued for almost 2 weeks and of triamcinolone for 3 weeks.

The incorporation of fatty acids into a polyanhydride chain was investigated using two fatty acids: lithocholic acid and ricinoleic acid. Lithocholic acid containing polyanhydrides (Figure 2) were prepared by two step synthesis. Polyanhydrides reached molecular weights of 21000-115000 Da, depending on the polymer composition. Release of model drugs from these polymers showed sustained release of 5FU for almost 3 weeks and triamcinolone for 4 weeks (22).

The previously described polyanhydrides still have relatively high melting temperature and the only possible administration route is implantation or injection after heating. The polymer is melted and the drug of choice is mixed into it. The formulation needs to be preheated before administration, which makes the administration complicated and can cause burns at the injection site. Development of polyanhydrides which are pasty or liquid at room temperature is, therefore, desired.

Ricinoleic acid is a bifunctional fatty acid containing a hydroxy group along the fatty chain. The presence of both carboxylic and hydroxyl groups allows incorporation of ricinoleic acid into a polymer backbone by formation of an ester bond. The synthesis of poly(ester-anhydride) contains two steps: trans-

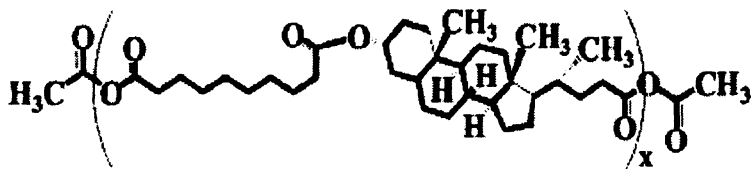


Figure 2. Lithocholic acid containing polyanhydrides (reproduced from reference 21)

esterification reaction between solid poly(sebacic anhydride) and hydroxyl group of ricinoleic acid. The ricinoleic acid hydroxyl group reacts with the anhydride group to form ester bonds and releases a polysebacic (PSA) anhydride chain with a carboxylic acid terminus. The next step is repolymerization of sebacic-ricinoleic acid (SA-RA) oligomers using conventional route for polyanhydride synthesis (23). The structure of poly(sebacic-co-ricinoleic acid) anhydride, p(SA-RA), is shown in Figure 3.

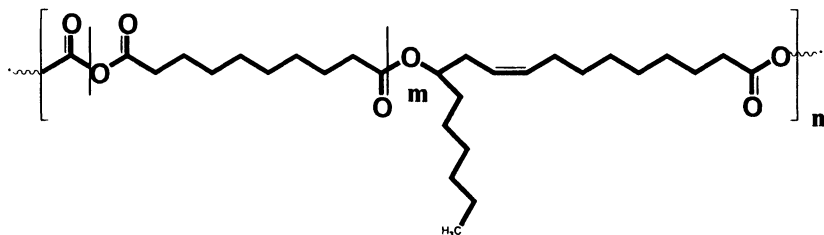


Figure 3. Structure of poly(sebacic-co-ricinoleic acid) anhydride. Reproduced from reference 23.

The physicochemical properties of these polymers are correlated with ricinoleic acid content in the polymer. The higher the ricinoleic content in the polymer, the lower is the melting temperature of the polymer. Polymers containing 30%w/w or less of ricinoleic acid are liquid at body temperature, with melting temperatures of 33°C and lower. These polymers are injectable at room temperature through a 23G needle, allowing simple administration of polymer formulations. The degradability of the polymers was also evaluated. When incubated in phosphate buffer pH 7.4 the liquid polymer lost 80% of its weight during 2 weeks of incubation. Liquid polymers solidified in phosphate buffer solution and decomposed completely after 8 weeks in the buffer. Drug release from both pasty and solid polymers was evaluated using cis-platin as model drug. Drug release from the pasty polymers was different from drug release from solid formulations. Solid formulations released up to 80% of the

drug for 3 weeks, while the pasty polymers released the entire drug load in 5 weeks. Solidification can be characterized as an increase in polymer viscosity. The rheological behavior of the polymer is important to characterize its injectability (24).

Poly(sebacic-co-ricinoleic acid) with 70% ricinoleic acid content or higher is liquid at body and room temperature. Poly(sebacic-co-ricinoleic acid) 3:7 (70% ricinoleic acid content) shows the properties of a non-Newtonian fluid at lower temperatures ( $<30^{\circ}\text{C}$ ), because of a non-constant shear rate/shear stress relationship, and the polymer can be classified as a pseudoplastic shear-thinning material displaying decreasing viscosity with increasing shear rate. This behavior is important for injectability of the polymer: as pressure is applied, the polymer paste becomes softer and pumps out through the needle. At higher temperatures ( $>30^{\circ}\text{C}$ ), poly(sebacic-co-ricinoleic acid) 7:3 acts as a Newtonian fluid and its viscosity is not affected by applied shear rate. After exposure to buffer, the viscosity of this polymer increased three fold, both at room and body temperature. After exposure to the aqueous medium the polymer shows a pseudoplastic behavior: this may be explained by reorganization of the polymer chains induced by the exposure to the buffer, which is destroyed at the moment of turning the spindle. The faster the rotation of the spindle (higher shear rate), the more the structure is destroyed, and the less the molecules slide together, the lower the viscosity will be.

The changes in polymer appearance after exposure to aqueous media were evaluated using light and SEM microscopy. Before exposure to buffer, the polymer is transparent. After exposure to buffer the polymer became opaque, and when it was cut, two different regions were found: the outer region which is gel and the core, which appears as a soft solid matrix. SEM analysis of the interface of the polymer exposed to buffer showed that a kind of a rigid network was formed across the polymer sample. This network causes the polymer drop to keep its shape in water.

To evaluate the *in-vivo* gelation mechanism of the polymer, mice were injected with three different volumes of polymer. The polymer remained at the injection site and maintained its shape for 24h post injection as happens when oil is injected in the subcutaneous space. Based on data presented in this work we can classify poly(sebacic-co-ricinoleic acid) as *in-situ* organogel forming.

The *in-situ* gelling mechanism of these pasty polyanhydrides suggests that after injection the polymer remains localized at the site of administration and releases the loaded drug at the site of administration. This characteristic of the polymer formulation allows many limitations of conventional therapy to be overcome, for example in anti-cancer therapy. When a drug is administered systemically by intravenous, intramuscular, or oral dosing, it is distributed in the body to various organs and tissues perfused with blood, and only a relatively small amount reaches its target tissue. Paclitaxel, a novel antitumor agent, has been shown to be highly cytotoxic and is clinically active against advanced

ovarian and breast cancer. It has a unique mechanism of action, inducing the assembly of stable microtubules and inhibiting the depolymerization process. The current clinical dosage form of paclitaxel consists of a 1:1 (v/v) mixture of ethanol and Cremophor EL. This pharmaceutical formulation, however, is associated with a number of concerns including stability, filtering requirements, and use of non-plasticized solution containers. Moreover, some of the side effects, such as severe hypersensitivity reactions, observed after paclitaxel administration are considered to be formulation related (25).

Incorporation of paclitaxel into a degradable polymer matrix allows local treatment of the tumor, providing therapeutic concentration of the drug at the tumor area, before or after surgical removal of the tumor. Implanting a biodegradable device loaded with antineoplastic agent in the cavity created by the tumor provides high local concentration of the drug killing the malignant cells that survived the surgery and also prevents the systemic side effects of the chemotherapy normally associated with the intravenous administration. Poly(sebacic-co-ricinoleic acid) is a suitable polymer for implantation into a tumor cavity after removal of the tumor (solid polymers) or injection into localized tumor (pasty polymers).

Drugs (paclitaxel or cis-platin) are incorporated into polymer by a trituration technique, resulting in uniform dispersion of the drug in polymer matrix. The incorporation of the drugs does not affect the polymer properties. The rate of paclitaxel release from the semisolid polymer differs as a function of the drug loaded in the polymer. As the percentage of paclitaxel is higher in the polymer, the rate of drug release is slower. The formulation containing 5% paclitaxel released 33% of the incorporated drug in 3 months. The release of paclitaxel from the solid formulation is faster than from the semisolid. During the first 50 days, formulations with 5 and 10% w/w paclitaxel released about 20% of the loaded paclitaxel, and the formulation containing 20% w/w paclitaxel released only 15% of the drug content during this time period (6). Cis-platin was incorporated into the poly(SA: RA) 3:7 and 2:8 (5% w/w). 30% of the incorporated drug was released in first two days and 85% in the following ten days from both polymers. No burst release was observed, only 5-7% of the drug was released in the first day, suggesting that no toxic effects are expected *in-vivo* (26). These promising results suggested that farther evaluation of paclitaxel polymer is desirable.

The polymer formulations containing anticancer agents (paclitaxel and cis-platin) were evaluated *in-vivo* in heterotrophic (mouse bladder tumor) and orthotrophic (rat prostate cancer) models. Single administration of polymer-paclitaxel formulation intratumorally in a mouse bladder tumor model increased the survival rate of the animals compared to untreated animals and to animals treated with paclitaxel dispersion (conventional administration method) (27). The optimal load of paclitaxel in the polymer was established as 10% w/w. Mice treated with this formulation showed median survival rate (MSR) of

35 days (animals were sacrificed at the end point of the experiment) compared to 16 days for the untreated group and 18 days for animals treated with paclitaxel suspension. 40% of the mice treated with 10% paclitaxel formulation survived for 77 days. The control groups survived up to 23 days. Treatment with polymer-paclitaxel formulation reduced the tumor size from 3.6g (untreated animals) and 2.5g (paclitaxel suspension) to 0.3 g (10% paclitaxel formulation) (27). In a second study tumor bearing mice were treated with cis-platin formulation (50  $\mu$ l, 1% cis-platin load). In this study the control animals were sacrificed 18 days post tumor cells inoculation when the tumor reached 3.5 cm<sup>3</sup>. In the group treated with polymer-cis-platin formulation (single injection, ten days post cell inoculation) in 8 out of 10 mice, the tumor absolutely disappeared during the first 10 days post treatment and did not appear until the end of study (42 days). In the two remaining mice a small nodule reappeared twenty days post treatment, however no increasing of its growth was seen until the end of the study. The treatment with the polymer formulation of paclitaxel and cis-platin had a positive outcome based on both qualitative observations and quantitative measurements of different parameters. The formulation increased the survival of mice bearing bladder tumors and decreased the growth rate of these tumors.

The polymer-paclitaxel formulation was also evaluated for treatment of orthotopic prostate cancer (28). Treatment with the polymer formulation of paclitaxel (single injection of 200  $\mu$ l polymer formulation with 10% w/w load) increased the survival rate of the rats. Rats treated with parental formulation of paclitaxel died 25 days post tumor cells inoculation. Only one rat in the polymer-paclitaxel group died three weeks post tumor cell inoculation, while all the remaining rats survived until the end point of the experiment (35 days). The control animals also developed lymph node metastases. No metastases were found in polymer-paclitaxel treated rats. The treatment with polymer-paclitaxel formulation reduced the prostate volume of the rats from 14.8 cm<sup>3</sup> (untreated animals) to 0.862 cm<sup>3</sup>, while the volume of healthy prostate gland injected with 200  $\mu$ l of polymer is about 0.4 cm<sup>3</sup>. The polymeric formulation released paclitaxel into local tumor tissues and induced necrosis and reduction of the tumor mass, while prolonging lifespan in an orthotopic prostate cancer rat model.

## Polyesters

Biodegradable polyesters are useful materials for controlled drug delivery (3). They degrade to hydroxy-acid monomers when placed in aqueous medium (7, 29, 30). Polyesters are less sensitive to hydrolysis and their degradation period is longer compared to polyanhydrides. The ester bond is less sensitive to hydrolysis, making preparation, handling and storage of this type of polymer easier. Polyesters can be synthesized by polycondensation of hydroxy acids or

by ring-opening polymerization of cyclic esters (lactones). A wide range of monomers has been used to produce biodegradable polyesters. The most useful monomers used for polycondensation are lactic, glycolic, hydroxybutyric, and hydroxycaproic acids. Polyesters of glycolic and lactic acids are the main group of interest due to their long history of safety (31-33).

Enantiomerically pure PLA is a semicrystalline polymer with Tg of about 55°C and Tm of about 180°C. The degree of crystallinity and melting temperature of PLA polymers can be reduced by random copolymerization with other comonomers, leading to the incorporation of units disturbing the crystallization ability of the PLA segments. Fatty acids are good candidates for incorporation into the poly(lactic acid) backbone. Ricinoleic acid, as previously described, possesses both carboxylic acid and hydroxyl functional groups, which allows its incorporation into polyester chains resulting in soft hydrophobic polymers. Ricinoleic acid hydrocarbon chain, cis-configuration and side chain may result in steric hindrance of the polymer to yield soft or even liquid polyesters. Several polymerization methods have been used for synthesis of these polymers: ring opening polymerization of lactide and ricinoleic acid lactones, polycondensation of lactic and ricinoleic acid and insertion of ricinoleic acid into poly(lactic acid) by transesterification followed by repolymerization. The polyester structure is shown in Figure 4.

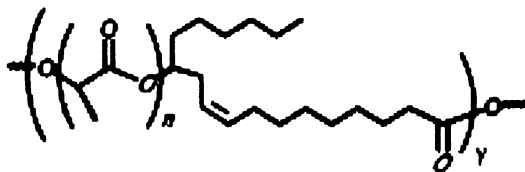
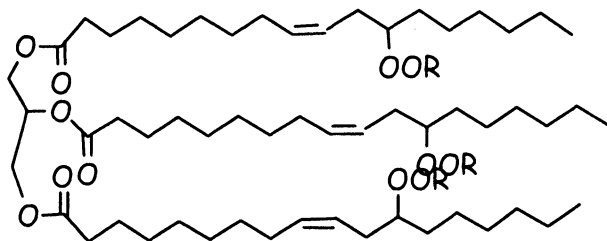


Figure 4. Structure of poly(lactic-co-ricinoleic acid) ester.

Liquid polyesters are formed when the feed ratio of ricinoleic acid is higher than 30% for polycondensation and 50% for transesterification. Polyesters synthesized by ring opening polymerization are solid at room temperature. These polyesters were evaluated as drug carriers for two drugs: 5FU and triamcinolone in vitro. Both drugs were released for over two weeks (34).

Additional polyesters were synthesized by the polycondensation of lactic acid and castor oil (Figure 5) and examined as injectable controlled delivery carriers for cytotoxic drugs (paclitaxel, methotrexate, 5FU and cis-platin).

Polyesters were synthesized using enantiomerically pure lactic acid (L or D) or racemic DL lactic acid. Polyesters containing 40% castor oil are viscous liquids at room temperature and released the incorporated drugs for over two months.



R=L/D/DL Poly(Lactic acid) (ester bond)

Figure 5. Poly(lactic acid-co-castor oil) polyesters.

## Conclusions

Fatty acid based biodegradable polymers have many biomedical applications. This short review focuses on controlled drug delivery using two classes of the polymers: polyanhydrides and polyesters based on fatty acids as drug carriers. Different polymer types and compositions are summarized showing the potential of these polymers as drug carriers.

## References

1. Guo, W. X.; Huang, K. X.; Tang, R.; Chi, Q. *Polymer* **2004**, *45*, 5743-5748.
2. Domb, A. J.; Maniar, M. J. *Polym. Sci. A*. **1993**, *31*, 1275-1285.
3. Domb, A. J.; Nudelman, R. J. *Polym. Sci. A* **1995**, *33*, 717-725.
4. Teomim, D.; Nyska, A.; Domb, A. J. *J. Biom. Mat. Res.* **1999**, *45*, 258-267.
5. Gousin, S.; Zhu, X.; Lehnert, S. *Macromolecules* **2000**, *30*, 5379-5383.
6. Orienti, I.; Zuccari, G.; Luppi, B.; Zecchi, V. *J. Microencapsul.* **2001**, *18*, 77-87.
7. Teomim, D.; Domb, A. J. *J. Polym. Sci. A*: **1999**, *37*, 3337-3344.
8. Grijpma, D. W.; Pennings, A. J. *Macromol. Chem. Phys.* **1994**, *195*, 1633-1647.
9. Grijpma, D. W.; Pennings, A. J. *Polym. Bul.* **1991**, *25*, 335-341.
10. Grijpma, D. W.; Nijenhuis, A. J.; Pennings, A. J. *Polymer* **1990**, *31*, 2201-2206.
11. Teomim, D.; Domb, A. J. *Biomacromolecules* **2001**, *2*, 37-44.
12. Uhrich, K. E.; Gupta, A.; Thomas, T. T.; Laurencin, C. T.; Langer, R. *Macromolecules* **1995**, *28*, 2184-2193.
13. Muggli, D. S.; Burkoth, A. K.; Keyser, S. A.; Lee, H. R.; Anseth, K. S. *Macromolecules* **1998**, *31*, 4120-4125.



14. Park, E. S.; Maniar, M.; Shah, J. C. *J. Control. Release* **1998**, *52*, 179-189.
15. Stephens, D.; Li, L.; Robinson, D.; Chen, S.; Chang, H. C.; Liu, R. M.; Tian, Y. Q.; Ginsburg, E. J.; Gao, X. Y.; Stultz, T. *J. Control. Release* **2000**, *63*, 305-317.
16. Masters, D. B.; Berde, C. B.; Dutta, S.; Turek, T.; Langer, R. *Pharm. Res.* **1993**, *10*, 1527-1532.
17. Shikanov, A.; Domb, A. J.; Weiniger, C. F. *J. Control. Release* **2007**, *117*, 97-103.
18. Carino, G. P.; Jacob, J. S.; Mathiowitz, E. *J. Control. Release* **2000**, *65*, 261-269.
19. Muggli, D. S.; Burkoth, A. K.; Anseth, K. S. *J. Biomed. Mater. Res.* **1999**, *46*, 271-278.
20. Erdmann, L.; Macedo, B.; Urich, K. E. *Biomaterials* **2000**, *21*, 2507-2512.
21. Krasko, M. Y., et al. *Polym. Adv. Tech.* **2002**, *13*, 960-968.
22. Krasko, M. Y.; Ezra, A.; Domb, A. J. *Polym. Adv. Tech.* **2003**, *14*, 832-838.
23. Krasko, M. Y.; Shikanov, A.; Ezra, A.; Domb, A. J. *J. Polym. Sci. A*: **2003**, *41*, 1059-1069.
24. Shikanov, A.; Domb, A. J. *Biomacromolecules* **2006**, *7*, 288-296.
25. Shikanov, A.; Vaisman, B.; Krasko, M. Y.; Nyska, A.; Domb, A. J. *J. Biom. Mat. Res. A*. **2004**, *69A*, 47-54.
26. Shikanov, A.; Domb, A. J. *Submitted*, **2007**.
27. Shikanov, A.; Domb, A. J. *Submitted*, **2007**.
28. Shikanov, A.; Domb, A. J. *Submitted*, **2007**.
29. Duda, A.; Penczek, S. *Polymer* **2003**, *48*, 16-27.
30. Ikada, Y.; Tsuji, H. *Macromol. Rap. Commun.* **2000**, *21*, 117-132.
31. Kumar, N.; Ravikumar, M. N. V.; Domb, A. J. *Adv. Drug Deliv. Rev.* **2001**, *53*, 23-44.
32. Penczek, S.; Szymanski, R.; Duda, A.; Baran, J. *Macromol. Symp.* **2003**, *201*, 261-269.
33. Seppala, J. V.; Helminen, A. O.; Korhonen, H. *Macromol. Biosci.* **2004**, *4*, 208-217.
34. Slivniak, R.; Ezra, A.; Domb, A. J. *Pharm. Res.* **2006**, *23*, 1306-1312.

## Chapter 7

# Synthesis of Soy Polymers Using a “Green” Processing Method

Zengshe Liu and Sevim Z. Erhan

Food and Industrial Oil Research, NCAUR, Agricultural Research Service,  
U.S. Department of Agriculture, 1815 North University Street,  
Peoria, IL 61604

Polymers with lower molecular weight ( $\leq 24,908$  g/mol), derived from soybean oil were prepared in supercritical carbon dioxide (scCO<sub>2</sub>) medium using boron trifluoride diethyl etherate, BF<sub>3</sub>·O(C<sub>2</sub>H<sub>5</sub>)<sub>2</sub> initiator. Influences of polymerization temperature, initiator amount, and carbon dioxide pressure on the molecular weight were investigated. Results showed that the higher polymerization temperature favors polymers with relatively higher molecular weights. Larger amounts of initiator also produced polymers with higher molecular weights. Higher pressure favored higher molecular weight polymers.

During the last few years, plant oils have attracted renewed attention as raw materials for the preparation of polymeric materials, to replace the traditional petro-chemical based polymers, because of their low production cost and biodegradability in some cases (1). Increasing social emphasis on issues concerning the environment, waste disposal, and the depletion of non-renewable resources are the reason driving application of bio-based products. Using plant oils as raw materials in polymer synthesis is a good use of green resources.

Soybean is the second largest crop plant in the U.S., accounting for about 28% of planted acreage, just behind corn, which accounts for about 30%, and ahead of wheat, which accounts for about 23% (2). About 3 billion bushels of soybeans are grown annually in the U.S. The current market demand is about 2.9 billion bushels. Thus, there is a need to develop new uses for surplus soybeans in order to prevent price depression due to oversupply.

Soybeans are comprised of (w/w), 40% protein, 30% carbohydrates, and 20% oil (3, 4). Currently, about 95% of soy protein is used in feed and 4% in food (for human consumption) applications. On the other hand, about 94% of soybean oil is used in food and only about 4% in industrial applications. Soybean oil is a triglyceride, which is a triester of glycerol and three fatty acids. The main fatty acid composition of soybean oil is (w/w): linoleic (54), oleic (23), and linolenic (8), (5). These fatty acids contain 1, 2, and 3 double bonds, respectively, in their hydrocarbon chains. These double bonds or unsaturations are reactive sites and allow for the development of soybean oil for various applications.

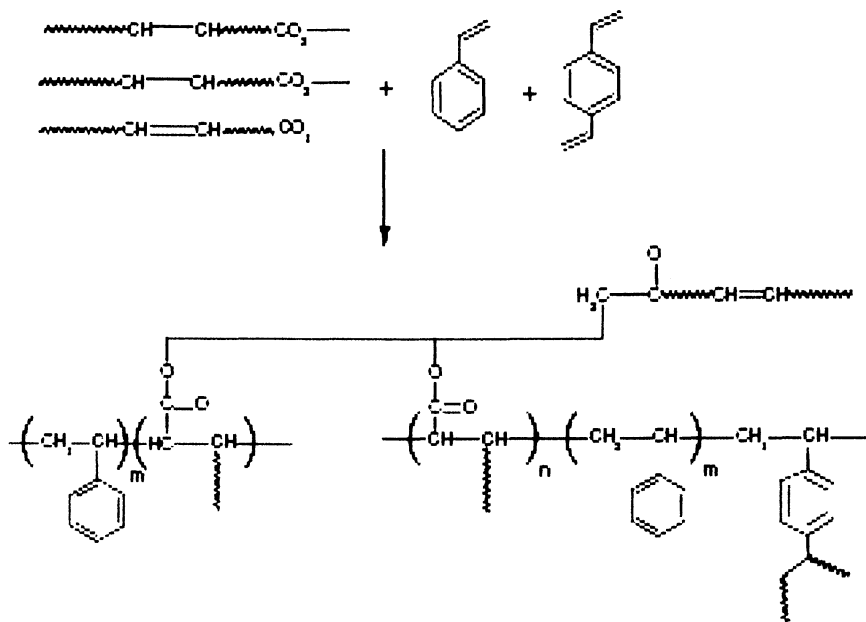
Plant oil-based polymers have been used for the production of coatings, inks, plasticizers, lubricants and agrochemicals (6-12). In general, drying oils (these can polymerize in air to form a tough elastic film) are the most widely used oils in coatings, although the semi-drying oils (these partially harden when exposed to air, such as soybean oil, corn oil etc.) also find use in some applications, for example in printing inks. Polymerization of semi-drying oils is difficult due to their lack of active functional groups.

Larock et al.(13-18) reported the direct conversion of soybean oil to useful solid polymers by cationic copolymerization of soybean oil with styrene and divinyl benzene comonomers initiated by boron trifluoride diethyl etherate ( $\text{BF}_3 \cdot \text{OEt}_2$ ). The resulting polymers formed range from soft rubbers to hard plastics, depending on the reagents, stoichiometry and initiator used (13). These copolymers have been characterized by various techniques, including dynamic mechanical analysis (DMA), thermogravimetric analysis (TGA), differential scanning calorimetry (DSC), scanning electron microscopy (SEM) and thermal mechanical analysis (TMA). Scheme 1 shows the proposed process of cross-linking of natural oils, such as soybean oil, fish oil, corn oil, linseed oil etc. with styrene and divinylbenzene in the presence of initiator (19).

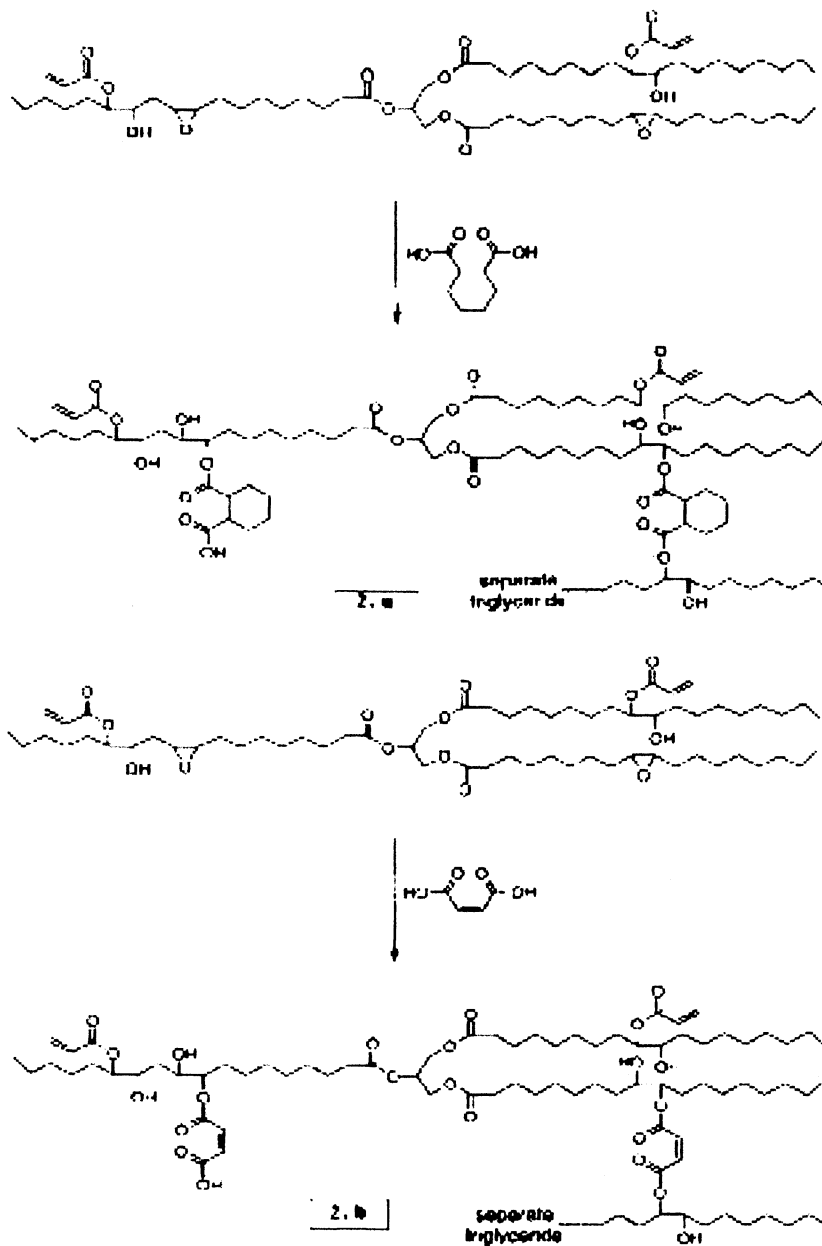
Wool and coworkers developed soybean oil resin based on acrylated epoxidized soybean oil (AESO) reacted with reagents to stiffen the polymer chain (20). Scheme 2 shows the oligomerization of an AESO with cyclohexane dicarboxylic acid (a) and with maleic acid (b), which introduces more doublebonds in the oligomers. They also reported using AESO to make composites with natural fiber mats, of flax, cellulose, pulp and hemp (21). The composites with natural fiber reinforcement of about 10-50 wt% increased the flexural modulus between 1.5 and 6 GPa, depending on the nature of the fiber mat. Guo et al. (22) reported the preparation of polyols and polyurethanes by hydroformylation of soybean oil. They studied the physical properties and mechanical properties of these polyurethanes. They also reported polyols synthesized by oxirane ring opening in epoxidized soybean oil with hydrochloric acid, hydrobromic acid, methanol, and hydrogen, as shown in Scheme 3 (23).

The brominated polyol had 4.1 hydroxy groups, whereas the other three polyols had slightly lower functionality. Applications of four polyols in

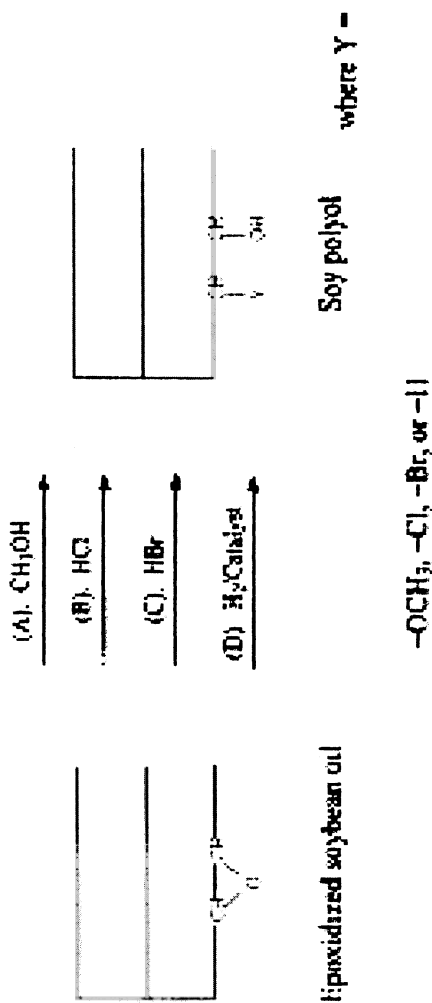
polyurethanes were investigated. In our previous articles (24-26), we reported preparation of epoxidized soybean oil/epoxy based composites, reinforced with carbon, glass, and mineral fibers or with combinations of fiber and clay, by the extrusion solid freeform fabrication method. More recently, Kundu et al. (27) reviewed polymers from natural oils and discussed the synthesis and characterization of new polymers from soybean, corn, tung, linseed and fish oils. The effects of different levels of unsaturation in the natural oils and various catalysts and comonomers on the properties of copolymers were considered. These polymers and polymeric composites demonstrate a variety of properties, ranging from elastomers to rigid plastics. Most of the aforementioned works converted soybean oils to useful solid polymers with other major components in polymer matrix. In other words, the research focuses on improving the physical properties of solid thermoplastics and thermoset materials because, the triglyceride-based materials demonstrated low molecular weights and, light cross-linking, incapable of displaying the necessary rigidity and strength required for structural applications.



*Scheme 1. The proposed process of cross-linking of natural oils with styrene and divinylbenzene in the presence of modified initiator (19).*



*Scheme 2. The modification of acrylated epoxidized soybean oil (AESO) shown using cyclohexane dicarboxylic anhydride or maleic anhydride. These AESOs were cured with styrene or other comonomers (20).*



**Hydroxylated soybean oil**

*Scheme 3. Schematic representation of the ring-opening reactions of ESBO with various reactants (23).*

Lubricants account for 1.2% of the total petroleum use. Those lubricants from petroleum stock are toxic to the environment and difficult to dispose of. There is also increasing concern for environmental pollution from excessive mineral oil use and disposal, especially in total loss lubrication, military applications, and in outdoor activities such as forestry, mining, railroads, dredging, fishing and agricultural hydraulic systems. Vegetable oils are potential substitutes for conventional mineral oil-based lubricating oils and synthetic esters. Vegetable oils are preferred over synthetic fluids because they are biodegradable and less expensive. On the other hand, vegetable oils have poor oxidation stability, primarily due to the presence of bis allylic protons. Also, low temperature studies have shown that most vegetable oils undergo cloudiness, precipitation, poor flow, and even solidification upon long-term exposure to cold temperature, which is in sharp contrast to mineral oil-based fluids. Before there will be widespread use of vegetable oils as the base fluid for environmentally friendly lubricants and hydraulic fluids, their oxidation and cold flow properties need to be improved. A useful approach is by the polymerization of vegetable oils. As mentioned above, polymerization of semi-drying vegetable oils like soybean oil is relatively difficult. Larock and coworkers (13) have reported the cationic homopolymerization of soybean oil using boron trifluoride diethyl etherate as the initiator and found the polymerization rate is low due to the relative high molecular weight and multiple chain structures of soybean oils. Furthermore, soybean oil has been found to be immiscible with the initiator employed. The copolymerization of soybean oil with styrene and norbornadiene or dicyclopentadiene, initiated by boron trifluoride diethyl etherate, resulted polymers with good mechanical properties and thermal stability.

Supercritical carbon dioxide ( $scCO_2$ ) has been shown to be a promising alternative solvent medium for organic transformations and polymerization reactions. This stems from a list of advantages ranging from solvent properties to practical, environmental, and economic considerations. Moreover, no residual solvent remains in the polymer product. Additionally carbon dioxide is inexpensive, readily available and nonflammable.

In our laboratory, we have reported the direct conversion of soybean oils in supercritical carbon dioxide to polymers with lower molecular weights (28). The resulting polymers could be used as lubricants and hydraulic fluids. The advantages of these polymers are their availability from a renewable resource, their biodegradability and their "green" processing method. Here, we discuss the synthesis and characterization of the resulting polymers from soybean oils.

## Experimental Section

### Materials

Soybean oil (SO-5) was purchased from Purdue Farms Inc., Refined Oil Division, (Salisbury, MD). Boron trifluoride diethyl etherate,  $BF_3 \cdot O(C_2H_5)_2$ , purified and redistilled, from Aldrich Chemical Inc. (Milwaukee, WI) was used

as received. Carbon dioxide (>99.8%) was obtained from Linde Gas LLC. (Independence, OH). Sodium bicarbonate, and magnesium sulfate were purchased from Aldrich Chemical Inc. (Milwaukee, WI). Tetrahydrofuran (THF, A.C.S. grade) was obtained from Aldrich Chemical Inc. (Milwaukee, WI).

## Analysis

### *Gel Permeation Chromatography (GPC)*

The original soybean oil (SBO), the processed soybean oil under similar conditions without catalyst (SBO control), and polymers of soybean oil (PSBO) were dissolved in THF. Molecular weights and molecular weight distribution were measured by GPC with a differential refractive index detector using THF as an eluent. The flow rate was 1.00 mL/min at 40 °C. The injection volume was 100  $\mu$ L. Linear polystyrene standards (Polymer Laboratories (PL), Mn = 580-100K, Mw/Mn = 1) were used for calibration of molecular weights of all polymers of PSBO. 2 PL gel 3  $\mu$ m mixed E columns (300 mm  $\times$  7.5 mm) in series were used to resolve the samples.

### *Nuclear Magnetic Resonance (NMR)*

$^1\text{H}$  and  $^{13}\text{C}$  NMR spectra for SBO and PSBO samples were recorded using a Bruker AV-500 spectrometer (Bruker, Rheinstetten, Germany) at an observing frequency of 500.13 and 125.77 MHz respectively on a 5 mm dual probe. For  $^1\text{H}$  and  $^{13}\text{C}$  experiments, sample solutions were prepared in deuterated chloroform ( $\text{CDCl}_3$ , 99.8% D, Aldrich, Milwaukee, WI) in 15 and 30% v/v concentrations respectively. Proton NMR spectra were obtained on 16 scans at a delay time of 1s. The integration values in  $^1\text{H}$  spectra were referenced to 4.00 between the ranges of 4.1-4.44 ppm.

### *Viscosity*

A Brookfield Engineering Rheometer, Model DV-III fitted with a Cone/Plate spindle CP-40 was used to measure the viscosity of the polymer samples. The CP-40 was chosen for its relatively small sample volume requirements (0.5 ml). The sample was measured and delivered with a syringe, allowed to equilibrate at temperature for 15 minutes and then rotational force was applied. Data was collected using Brookfield Engineering software



Rheocalc V2.4. The Bingham mathematic model was used to determine viscosity. The Bingham equation is:  $\tau = \tau_0 + \mu\gamma$ . Where  $\tau$  is the shear stress applied to the material,  $\gamma$  is the shear strain rate (also called the strain gradient),  $\tau_0$  is the yield stress and  $\mu$  is the plastic viscosity.

### Polymerization Procedure in scCO<sub>2</sub>

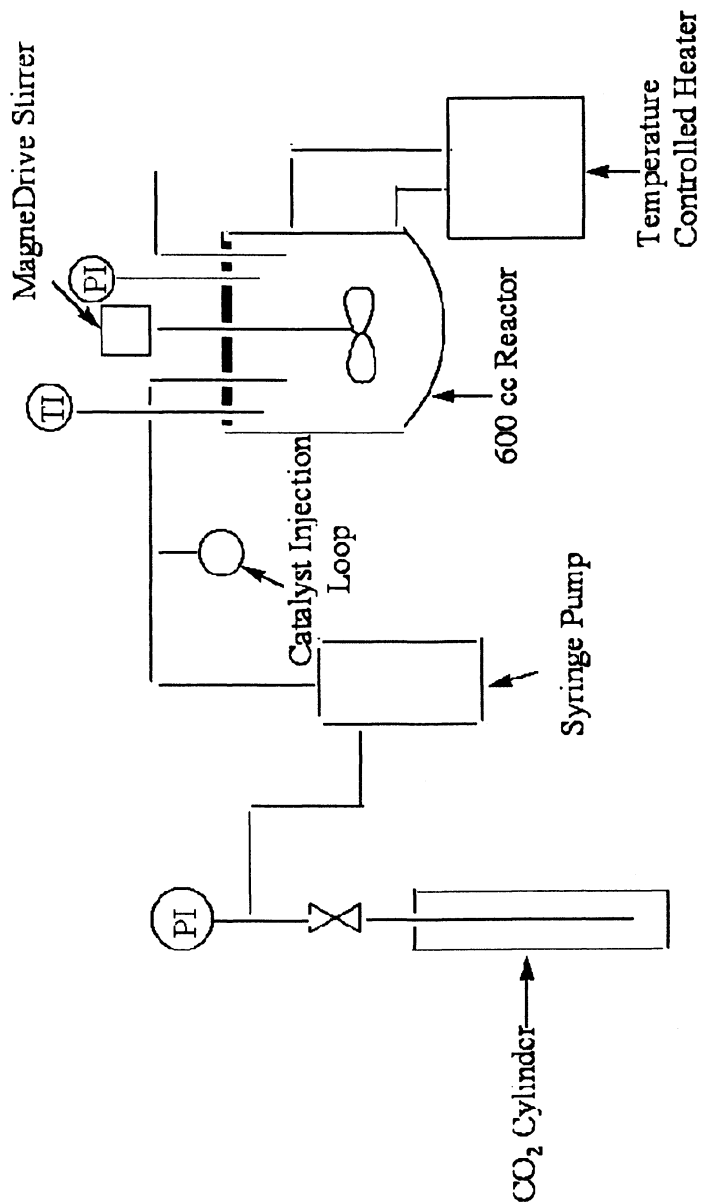
Polymerization reactions were carried out in a 600 mL high pressure reactor from Parr Instrument Co. (Moline, IL). The schematic diagram of the experimental set-up used for polymerization of soybean oil is depicted in Scheme 4. The reactor was attached to an Isco Model 260D high pressure syringe pump used to charge the reactor with CO<sub>2</sub>. In a typical experiment, 100 g of SBO was added to the reactor, which was then sealed. N<sub>2</sub> was purged into the reactor for 5 minutes. CO<sub>2</sub> was pumped in until the desired pressure was reached. A controller (Parr 4843) was used to control temperature. Once the reactor was brought to the appropriate temperature and pressure, BF<sub>3</sub>•O(C<sub>2</sub>H<sub>5</sub>)<sub>2</sub> was charged into the reactor by manual injection using a Rheodyne Injector. Then CO<sub>2</sub> was pumped in to clean initiator supplier line. After reaction of 2 hr, 2 mL of ethanol/H<sub>2</sub>O (1:1) was added into reactor to deactivate catalyst. Polymer product was dissolved in 100 mL hexane and washed sequentially with H<sub>2</sub>O and 5% aqueous sodium bicarbonate. Hexane solution was dried over sodium sulfate, filtered, and evaporated under reduced pressure. About 100 g of polymer was obtained.

## Results and Discussion

### Effect of Catalyst Amount

To investigate the effect of initiator amount on the molecular weight of the PSBO, amount of BF<sub>3</sub>•OEt<sub>2</sub> was varied from 0.0 g to 2.5 g, while keeping the monomer amount, SBO, at 100 g, and keeping other reaction conditions constant. Entry 1 in Table I is the soybean oil control without initiator catalyst, it shows that weight average molecular weight did not change after 2 hours under reaction conditions. Because soybean oil and SBO control have the same GPC profile. The results of catalyst concentration effect are presented in Table I.

Results show that as the BF<sub>3</sub>•OEt<sub>2</sub> amount increased, the weight average molecular weight also increased. The weight average molecular weight changed from 1,447 to 24,908 g/mol. From GPC profiles (Figure 1) it is of note that between the soybean oil (control) peak (1,097) and high molecular weight peak of PSBO (19,521), there are only two peaks at (1,638) and (2,649),



Scheme 4. The schematic diagram of the experimental reactor set-up.  
(Reproduced with permission from reference 28. Copyright 2007 American Chemical Society.)

**Table I. Effect of Catalyst Amount on the Molecular Weight of PSBO**

Entry	SBO (g)	P (bar)	T (°C)	Reaction	Cat.	Viscosity (mPa.s)	Mw (g/mol)
				Time (hr)	Amount (g)		
(control)							
1	100	110	120	2	0	46.7	1,103
2	100	110	120	2	1.0	108	1,447
3	100	110	120	2	1.5	222	5,648
4	100	110	120	2	2.0	722	10,480
5	100	110	120	2	2.5	1,909	24,908

corresponding to a dimer and a trimer of soybean oil molecule, respectively. Figure 1 shows the GPC profile of soybean oil control and PSBO.

It seems that formation of dimers and trimers from soybean oil is the slow step of polymerization, an evidence for step polymerization mechanism. Once formed, these dimers and trimers polymerize very quickly to a high molecular weight and exhibits chain reaction kinetics. This phenomenon is caused by the soybean oil molecule itself, a large molecule with low activity, due to mid chain double bond location. However, the formed dimers and trimers have more unsaturated carbon-carbon double bonds per molecule, and they are easily polymerized to high molecular weight polymers. We propose further investigation on the possible combination of two polymerization mechanisms for the polymerization of soybean oil in  $\text{scCO}_2$ . Kinetic study of soybean oil polymerization currently is carried out in our laboratory.

Figure 2 shows  $^1\text{H}$  NMR spectra of SBO and PSBO. The signals at 5.40 ppm are characteristic for olefinic hydrogens and signal at 5.1-5.3 ppm represents the methine proton of  $-\text{CH}_2-\text{CH}-\text{CH}_2-$  the glycerine backbone. The signals at 4.0-4.4 ppm are from the methylene protons of  $-\text{CH}_2-\text{CH}-\text{CH}_2-$  the glycerin backbone. The peak at 2.80 ppm corresponds to the protons in the  $\text{CH}_2$  groups between two carbon-carbon double bonds. The signals at 2.10 ppm are  $\alpha$  methylene proton  $\text{CH}_2$  adjacent to carbon-carbon double bonds. It can be seen from Figure 2 that the peaks at 5.1-5.4 ppm, 2.80 ppm, and 2.1 ppm of PSBO are greatly decreased compare to SBO. This observation indicated that the polymerization of SBO occurred, and the number carbon-carbon double bonds were reduced.

Figure 3 shows  $^{13}\text{C}$  NMR spectra for SBO and PSBO. The peaks at 127-132 ppm are due to olefinic carbons. It is also observed that peaks at 127-132 ppm are decreased after polymerization.

Figure 4 shows  $^1\text{H}$  NMR spectra of SBO and PSBO at different initiator concentrations ranging from 1.0 g to 2.5g. Figure 5 shows  $^{13}\text{C}$  NMR spectra of PSBO at initiator concentrations mentioned above. The intensities of olefins and associated peaks in  $^1\text{H}$  NMR spectra (5.1-5.3ppm, 2.80 ppm, and 2.1 ppm)

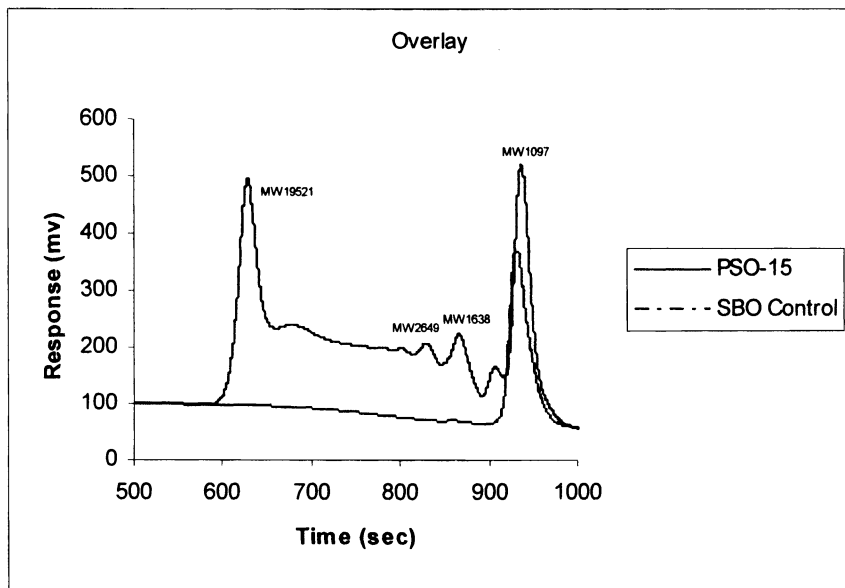
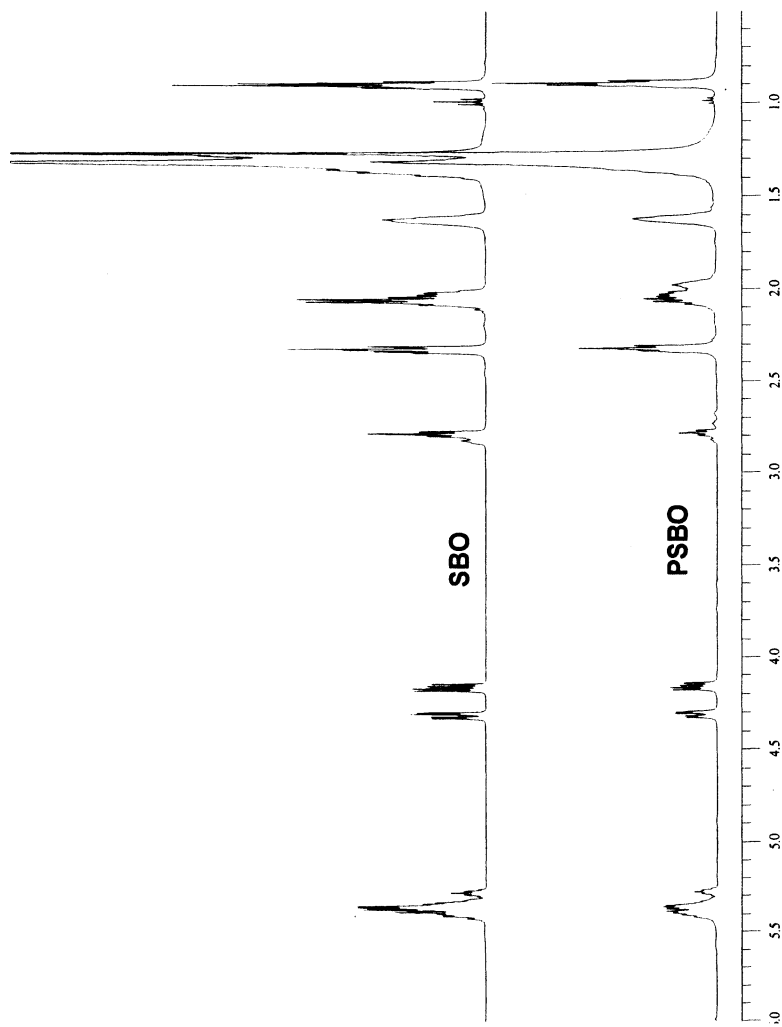


Figure 1. Overlays of SBO (control) and PSBO obtained from the RI detector of the GPC. (Reproduced with permission from reference 28. Copyright 2007 American Chemical Society.)

**Table II. Effect of Reaction Temperature on the Molecular Weight of PSBO**

Entry	SBO (g)	P (bar)	T (°C)	Reaction	Cat.	Viscosity (mPa.s)	Mw (g/mol)
				Time (hr)	Amount (g)		
1	100	110	110	2	2.0	297	1,384
2	100	110	120	2	2.0	722	10,480
3	100	110	130	2	2.0	6,790	17,451
4	100	110	140	2	2.0	80,233	22,814



*Figure 2. <sup>1</sup>H NMR spectra of SBO and PSBO. (Reproduced with permission from reference 28. Copyright 2007 American Chemical Society.)*

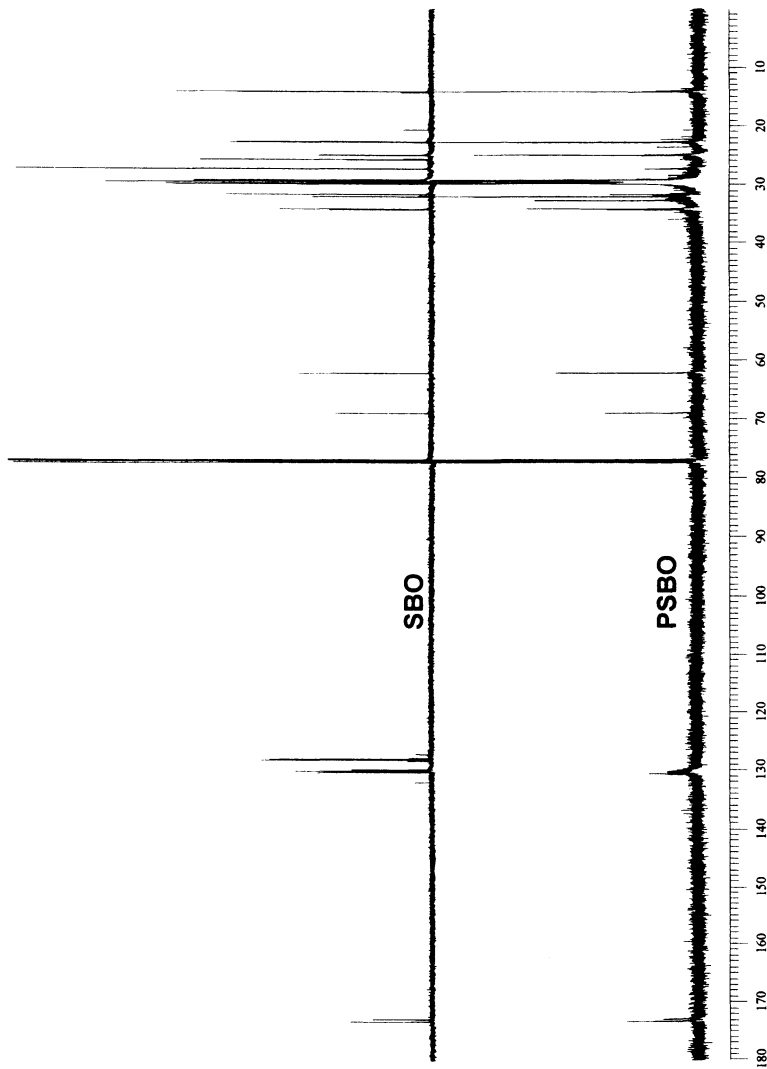


Figure 3.  $^{13}\text{C}$  NMR spectra of SBO and PSBO. (Reproduced with permission from reference 28. Copyright 2007 American Chemical Society.)

and  $^{13}\text{C}$  NMR (127-132 ppm) are apparently reduced further as catalyst concentration increased. The decrease in peak intensities of olefins and associated peaks show increased polymerization of SBO. The viscosity data also shows an increase with increasing catalyst amount.

### Polymerization Temperature Effect

The effect of polymerization temperature on the molecular weight was investigated in a series of polymerizations conducted at temperatures ranging from 100 to 140°C and at a constant pressure of 110 bars. In all of these experiments, the monomer, SBO, and other reaction conditions are kept constant. As shown in Table II the weight average molecular weight increased with increasing temperature. The molecular weight changed from 1,384 to 22,814 g/mol. A possible reason for the effect is that soybean oil itself has relatively large molecular weight, and the active site. The carbon-carbon double bonds are located in the middle of fatty acid chains. The activity of these double bonds is relatively low and higher activation energy is needed for reaction. Another reason is higher temperature increases the solubility of soybean oil in  $\text{scCO}_2$ , therefore increasing the polymerization rate.  $^1\text{H}$  NMR and  $^{13}\text{C}$  NMR spectra of PSBO confirmed the reaction increased with increased polymerization temperature.

### Pressure Effect

The pressure effect has been studied by changing the pressure of  $\text{CO}_2$ , while keeping temperature at 120°C and 100g of the monomer, SBO. The results listed in Table III were obtained as the pressure was increased from 55 bars to 121 bars. It is of note that the higher pressure resulted in higher molecular weight polymer. Additionally, it is important to note that as pressure was increased from 55 bars to 69 bars, a slightly increased molecular weight of PSBO was observed, changing from 1,536 g/mol to 2,863 g/mol.

When pressure increased to 121 bars, the molecular weight of PSBO increases to 11,349 g/mol. A possible explanation for this observed behavior at higher pressure is the increase in solubility of soybean oil in  $\text{scCO}_2$ . The better solubility of soybean oil in  $\text{scCO}_2$  will provide a higher polymerization rate.

## Conclusions

In this study, soybean oil was polymerized in the  $\text{scCO}_2$  medium initiated by  $\text{BF}_3 \cdot \text{O}(\text{C}_2\text{H}_5)_2$ . Analysis of the  $^1\text{H}$  NMR and  $^{13}\text{C}$  NMR spectra of the polymer

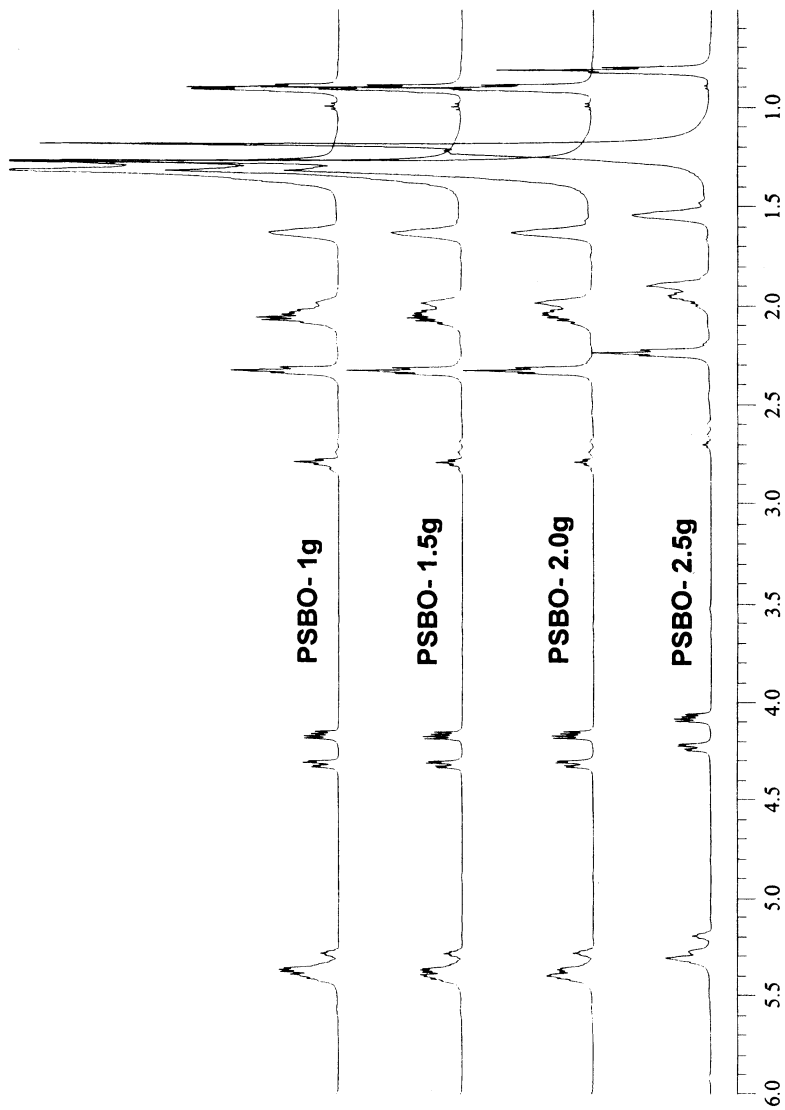


Figure 4. <sup>1</sup>H spectra of PSBO obtained from reactions using different catalyst amounts. (Reproduced with permission from reference 28. Copyright 2007 American Chemical Society.)



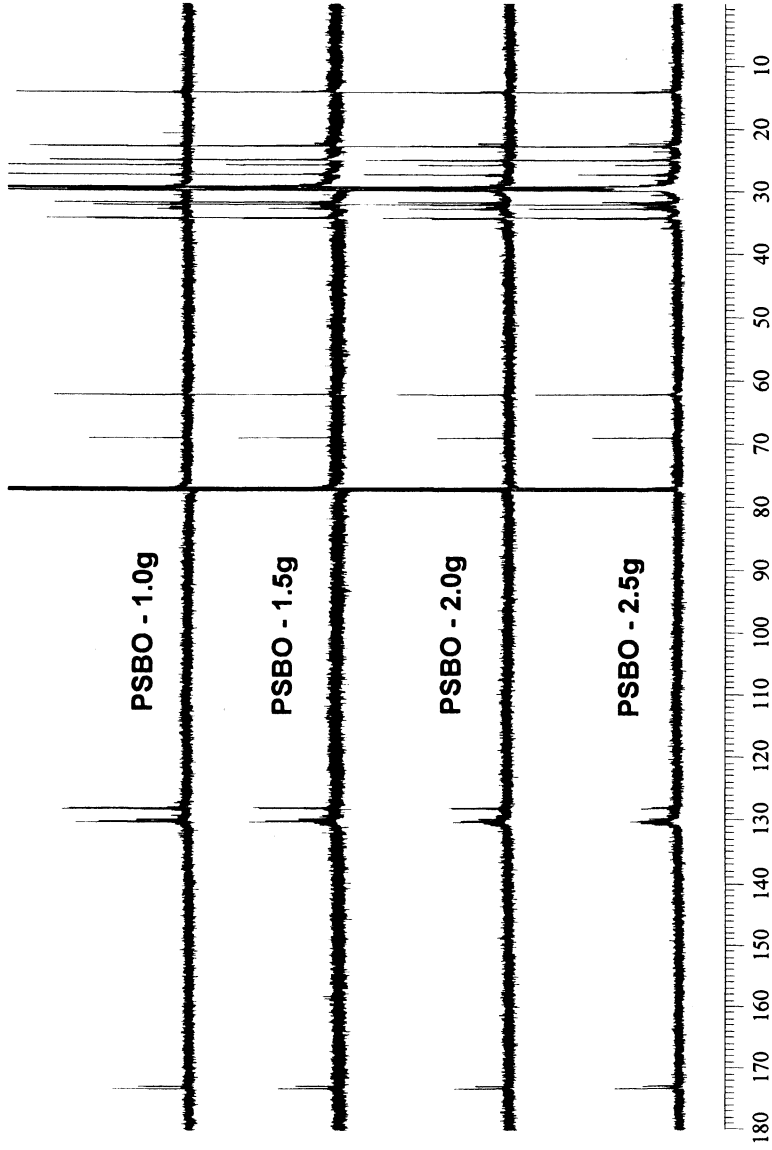


Figure 5.  $^{13}\text{C}$  NMR spectra of PSBO obtained from reactions using different catalyst amounts. (Reproduced with permission from reference 28. Copyright 2007 American Chemical Society.)

Table III. Pressure Effect on Molecular weight of PSBO

Entry	SBO (g)	P (bar)	T (°C)	Reaction	Cat.	Viscosity (mPa.s)	Mw (g/mol)
				Time (hr)	Amount (g)		
1	100	55	120	2	2.0	84	1,536
2	100	69	120	2	2.0	N/A	2,863
3	100	76	120	2	2.0	276	4,152
4	100	93	120	2	2.0	440	6,228
5	100	100	120	2	2.0	458	6,699
6	100	110	120	2	2.0	722	10,480
7	100	121	120	2	2.0	N/A	11,349

suggested soybean oil polymer formation. The resulting polymers with molecular weights ranging from 1,384 to 22,814 g/mol were observed. The effects of temperature, pressure and catalyst concentration were evaluated experimentally. Overall, this polymerization of soybean oil in the scCO<sub>2</sub> medium offers potential for several key advances, including (i) the ability to produce liquid soy polymers that could be used as lubricants and hydraulic fluids, and (ii) its potential as a “green” processing method.

## References

1. Kaplan, D. L. *Biopolymers from Renewable Resources*; New York: Springer, 1998.
2. Naeve, S. L.; Orf, J. H. *Quality of the United States Soybean Crop*; US Soybean Crop Quality Survey, US Soybean Board: 2006.
3. Liu, K. *Soybeans Chemistry, Technology, Utilization*; Aspen Publisher Inc.: Geithersberg, MD, 1999.
4. Bockish, M. *Fats and Oils Handbook*; AOCS: Champaign, IL 1998.
5. Lawate, S. S.; Lal, K.; Huang, C. *Vegetable oils - Structure and Performance, in Tribology Data Handbook*; Booser, E. R., Ed.; CRC Press: New York, 1997; pp 103-116.
6. Cunningham, A.; Yapp, A. U.S. Patent 3,827,993, 1974.
7. Bussell, G. W. U.S. Patent 3,855,163, 1974.
8. Hodakowski, L. E.; Osborn, C. L.; Harris, E. B. U.S. Patent 4,119,640, 1975.
9. Trecker, D. J.; Borden, G. W.; Smith, O. W. U.S. Patent 3,979,270, 1976.
10. Trecker, D. J.; Borden, G. W.; Smith, O. W. U.S. Patent 3,931,075, 1976.
11. Salunkhe, D. K.; Chavan, J. K.; Adsule, R. N.; Kadam, S. S. *World*

*Oilseeds: Chemistry, Technology and Utilization*; Van Nostrand Reinhold: New York, 1992.

12. Force, C. G.; Starr, F. S. U.S. Patent 4,740,367, 1988.
13. Li, F.; Hanson, M. V.; Larock, R. C. *Polymer* **2001**, *42*, 1567–79.
14. Li, F.; Larock, R. C. *J. Appl. Polym. Sci.* **2001**, *80*, 658–70.
15. Li, F.; Larock, R. C. *J. Polym. Sci. B Polym. Phys.* **2000**, *38*, 2721–38.
16. Li, F.; Larock, R. C. *J. Polym. Sci. B Polym. Phys.* **2001**, *39*, 60–77.
17. Li, F.; Larock, R. C. *Polym. Adv. Technol.* **2002**, *13*, 436–49.
18. Li, F.; Larock, R. C. *J. Appl. Polym. Sci.* **2002**, *84*, 1533–43.
19. Li, F.; Hasjim, J.; Larock, R. C. *J. Appl. Polym. Sci.* **2003**, *90*, 1830–1838.
20. Khot, S. N.; La Scala, J. J.; Can, E.; Morye, S. S.; Williams, G. I.; Palmese, G. R.; Kusefoglou, S.; Wool, R. P. *J. Appl. Polym. Sci.* **2001**, *82*, 703–723.
21. O'Donnell, A.; Dweib, M. A.; Wool, R. P. *Comp. Sci. Technol.* **2004**, *64*, 1135–1145.
22. Guo, A.; Demydov, D.; Zhang, W.; Petrovic, Z. S. *J. Polym. Environ.* **2002**, *10*, 49–52.
23. Guo, A.; Cho, Y.; Petrovic, Z. S. *J. Polym. Sci. A Polym. Chem.* **2000**, *38*, 3900–3910.
24. Liu, Z. S.; Erhan, S. Z.; Xu, J.; Calvert, P. D. *J. Appl. Polym. Sci.* **2002**, *859*, 2100–2107.
25. Liu, Z. S.; Erhan, S. Z.; Xu, J.; Calvert, P. D. *J. Appl. Polym. Sci.* **2004**, *93*, 356–363.
26. Liu, Z. S.; Erhan, S. Z.; Xu, J.; Calvert, P. D. *J. Amer. Oil Chem. Soc.* **2004**, *81*, 605–610.
27. Sharma, V.; Kundu, P. P. *Progr. Polym. Sci.* **2006**, *31*, 983–1008.
28. Liu, Z. S.; Sharma, B. K.; Erhan, S. Z. *Biomacromolecules* **2007**, *8*, 233–239.

## Chapter 8

# Degradation of Cross-Linked Unsaturated Polyesters by Using Subcritical Water

**Kanji Suyama<sup>1</sup>, Masafumi Kubota<sup>1</sup>, Masamitsu Shirai<sup>1</sup>,  
and Hiroyuki Yoshida<sup>2</sup>**

**Departments of <sup>1</sup>Applied Chemistry and <sup>2</sup>Chemical Engineering,  
Osaka Prefecture University, 1-1 Gakuen-Cho, Naka-Ku, Sakai,  
Osaka 599-8531, Japan**

The degradation of unsaturated polyesters crosslinked with styrene was performed in sub-critical water (SCW) at 300°C in the absence and presence of organic additives. The unsaturated polyesters were partially de-crosslinked by hydrolysis of ester chains to form polystyrene derivatives. The de-crosslinking rate was enhanced in the presence of hydroxy compounds with a long alkyl chain and alkylamines, while carboxylic acids and benzenesulfonate salts were ineffective despite having a long alkyl chain. The degree of de-crosslinking was reduced in the presence of diamines and amino acids because re-crosslinking occurred. In the case of aminoalcohol, the amino group reacted prior to the hydroxy group, and a polystyrene derivative with side-chains having terminal hydroxy groups was obtained without re-crosslinking. The hydroxy groups could be modified with maleic anhydride, and polymerized with styrene to yield a network polymer again.

## Introduction

Chemical recycling of polymers is an important target of modern society that consumes a great deal of petroleum-based polymeric materials. Although the chemical recycling of thermosetting polymers is also required, it is difficult because of their inherent insoluble and infusible properties.

Unsaturated polyesters (UPs) crosslinked with styrene are often used as a matrix of fiber reinforced plastics. Several reports treated the degradation of the crosslinked UPs with high temperature treatment in water (1,2), acetic acid (3), alcohols including glycols (4,5), and amines (6), often in the presence of catalysts. In these literatures, recovery of polymeric materials from the crosslinked UPs was not a main objective. However, in case we can hydrolyze polyester chains selectively, linear polystyrene derivatives can be obtained as recycled materials.

Recently, we have attempted the degradation of crosslinked polymers in sub-critical region of water. At high temperature and pressure, water shows drastic decrease in dielectric constant, which improves the solubility of organic compounds into water. Furthermore, the magnitude of ion product of water increases compared to room temperature. These properties are advantageous for dissolution and hydrolysis of organic materials (7). However, the ion product of water decreased at supercritical region. Furthermore, polystyrene units in crosslinked UPs were also decomposed in monomers or other small molecules. These properties suggest the advantages of sub-critical water (SCW) than supercritical water from the viewpoint of recovery of polystyrene derivatives. The drawback of the degradation of polymers in SCW is its slower reaction rate than supercritical water.

Recently, we have reported that the degradation of crosslinked UPs in SCW was enhanced by adding alcohols with a long alkyl chain (8) and amines (9). In this paper, we report the degradation behavior of a crosslinked UP using SCW treatment in the absence and presence of the additives and propose a new recycling system of polymers.

## Experimental

### Instrumentation

IR, UV, and  $^1\text{H}$  NMR spectra were obtained using Jasco FTIR-410, Shimadzu UV-2400PC, and Jeol JNM-GX270 (270 MHz) spectrometers, respectively. Size exclusion chromatography (SEC) was carried out on a Jasco GPC equipment consisting of a PU-980 pump, an RI-930, and a Shodex KF-806M column with polystyrene as a standard and tetrahydrofuran (THF) as an

eluent at 40°C. Thermogravimetric analysis (TGA) was carried out using a Shimadzu TGA50 thermogravimetric analyzer at a heating rate of 10 K / min under N<sub>2</sub>. The onset temperature from TGA curves was adopted as thermal decomposition temperature (T<sub>d</sub>). Gas chromatography (GC) was performed on a Shimadzu GC2010 with a thermal conductivity detector.

## Materials

Additives such as alcohols, phenols, and amines were used as received from Wako Chemical or Tokyo Chemical Industry, both in Japan. Maleic anhydride (MA) and phthalic anhydride (PA) were recrystallized from chloroform-hexane mixture and chloroform, respectively. 1,2-Propanediol (PG), styrene (St), and tetrahydrofuran (THF) were distilled before use.

## Preparation of Crosslinked Unsaturated Polyesters (UP)

A mixture of MA : PA : PG = 2 : 3 : 5.5 (mol/mol) was heated at 160°C for 4 h followed by heating at 210°C for 1 h under argon. After reprecipitation from chloroform / methanol system, UP1 was obtained in 36.1 % yield: T<sub>d</sub>: 314°C, M<sub>n</sub>: 2,600, M<sub>w</sub>: 5,300. MA : PA : PG = 16.1 : 32.7 : 51.1 (mol/mol) from <sup>1</sup>H NMR.

In a glass tube, 2.95 g of UP1 and 148 mg of AIBN were dissolved in 4.43 g of St monomer, argon-purged for 10 min, and heated at 60°C for 3 h. After cooling, the polymer was crushed, and the fraction of 0.25 ~ 2 mm diameter was separated using lida testing sieves. Resulting grains were extracted by THF with a Soxhlet for 3 h to remove the non-crosslinked fraction. After drying, 6.92 g (92.6 %) of crosslinked UP2 was obtained. MA : PA : PG : St = 4 : 9 : 14 : 73 (mol/mol) from IR. T<sub>d</sub>: 320°C.

## SCW Treatment

De-ionized water and additives (total 4.75 g), and 250 mg of UP2 were placed in a SUS316L stainless tube with 150 mm length and 8 mm inner diameter. After purging argon gas for 1 min, the tube was closed with Swagelok caps and plugs, and then heated in a salt bath of sodium nitrate and potassium nitrate mixture. After the SCW treatment, the tube was dipped in water at room temperature. SCW treating time is defined as the time between the moment of sintering the tube in the salt bath and that in water.

## Separation of Reaction Mixture

The weight of recovered solid (mg) is obtained by filtering of the reaction mixture followed by drying in vacuum for ca. 30 min. The solid was conducted to Soxhlet extraction using THF for ca. 3 h. Degree of de-crosslinking (%) is defined as  $(1 - I_{THF} / 250) \times 100$ , where  $I_{THF}$  is the weight (mg) of insoluble fraction in THF. The THF solution obtained from Soxhlet extraction was concentrated and poured in an excess hexane to afford non-crosslinked polymers whose weight (mg) was used to define the soluble fraction in THF ( $S_{THF}$ ).

## Re-crosslinking of a Polystyrene Derivative

Recovered polystyrene derivative on SCW treatment of UP2 at 300°C in the presence of 5-amino-1-pentanol was dissolved in chloroform, added triethylamine and MA, and heated at 50°C for 24 h. Resulting solid was purified by reprecipitation and dissolved in St. After the addition of AIBN, the St solution was degassed and heated at 60°C for 3 h.

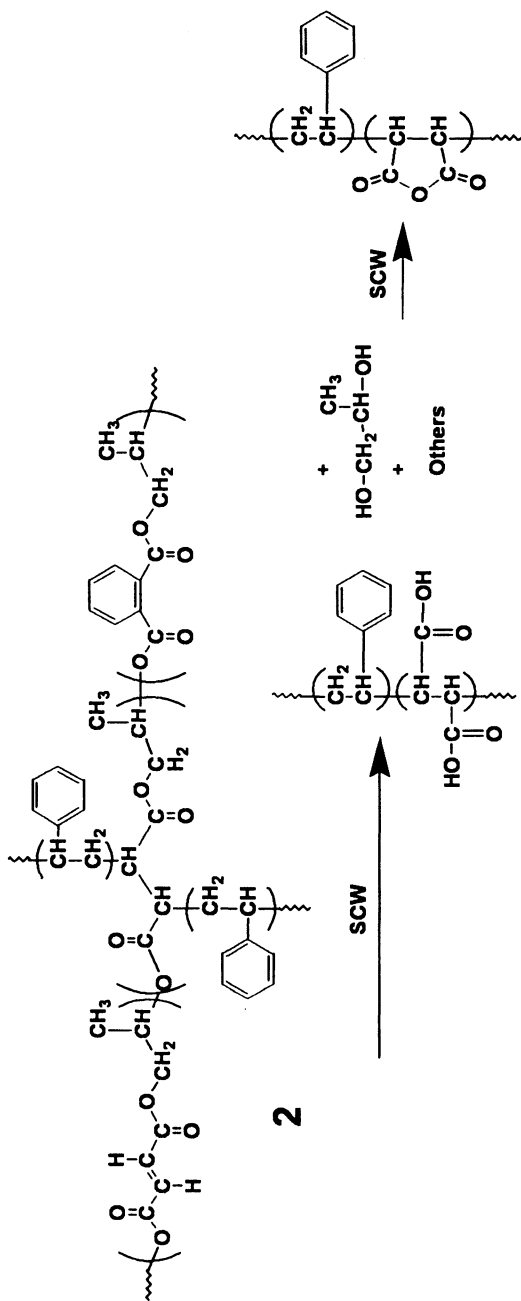
## Results and Discussion

### SCW Treatment of 2 in the Absence of Additive

In the absence of additives, 42.7 % of UP2 was de-crosslinked on SCW treatment at 300°C for 10 min (Table I entry 1). With an increase in SCW treating time, peaks at 1730 and 2500–3300  $\text{cm}^{-1}$  due to ester and carboxylic acid groups, respectively, decreased along with an increase of peaks at 1780 and 1860  $\text{cm}^{-1}$  due to carboxylic anhydride group. These changes clearly indicate that dehydration between neighboring carboxylic acid groups proceeded after hydrolysis of ester groups as shown in **Scheme 1**.

### SCW Treatment of UP2 in the Presence of Additives

The effect of alcohols and phenols on the degradation of UP2 is shown in Table I entries 2-11. The degree of de-crosslinking depended on the length of alkyl chain, and remarkable enhancement was observed for 1-undecanol, 1-dodecanol, 1-tetradecanol, 1-hexadecanol, and *m*-pentadecylphenol. The balance of hydrophobicity and bulkiness of the alcohols and phenol might play a major role in penetrating into the crosslinked resin. The number average molecular



*Scheme 1. Degradation and dehydration of UP2 in SCW.*



weight of the polystyrene derivatives obtained by SCW treatment at 300°C in the presence of 1-tetradecanol was 12,800.

When UP2 was SCW-treated in the presence of 0.24 g and 0.48 g of 1-tetradecanol, the degree of de-crosslinking was 51.6 and 94.4 %, respectively, while that was 75.4 % in the presence of 0.71 g of *m*-pentadecylphenol.

From the viewpoint of recovery of excessive additives from water, 1-tetradecanol is advantageous because this alcohol is solid and insoluble in water at room temperature. More than 80 % of 1-tetradecanol was recovered from hexane phase when UP2 was treated at 300°C for 10 min.

On the other hand, diols were ineffective for the enhancement of de-crosslinking even though they have a long alkyl chain (entries 12-14).

Sodium dodecylbenzenesulfonate, 1-tetradecanoic acid, and tetradecane did not enhance the de-crosslinking (Table I entries 15-17). These results indicate that the long alkyl chain was not effective to enhance the degradation, and functional groups that can react to ester groups would be crucial to promote the degradation.

On the other hand, amines were very effective for the enhancement of the de-crosslinking (Table I entries 18,19). 1-Pentylamine was also effective even it has a short alkyl chain. The length of alkyl chain did not affect the degree of de-crosslinking, and 1.3 equivalent of amino groups to ester units was enough to de-crosslink completely. These results show that amino groups were highly reactive to ester groups. In fact, the de-crosslinking in the presence of 1-tetradecylamine needed shorter SCW treating time and lower SCW treating temperature compared to 1-tetradecanol.

The effect of difunctional additives having an amino group at one end and other functional group at the other end was investigated (Table I entries 20-22). 5-Amino-1-pentanol was highly effective, while 1,8-octamethylenediamine and 6-aminohexanoic acid were not.

These results in Table I can be explained by reactions in Scheme 2. As shown in Figures 2b and 2c, peaks at 1270  $\text{cm}^{-1}$  due to C-O stretching band in conjugated ester disappeared, while peaks at 1730  $\text{cm}^{-1}$  due to ester C=O groups remained. These results indicate that the transesterification proceeded in the presence of alcohols and diols. In case of diol, the transesterification at both ends would afford re-crosslinking. A similar trend was observed for other difunctional additives such as diamine and amino acid. When amino compounds were added, recovered polymers had a peak at 1700  $\text{cm}^{-1}$  as shown in Figures 2d and 2e due to cyclic imide moieties.

When 5-amino-1-pentanol was used as an additive, amino groups reacted prior to hydroxy groups, leading to the formation of a polystyrene derivative with side-chains having terminal hydroxy groups. The hydroxy groups could be modified with MA, and polymerized with styrene to afford a network polymer again.

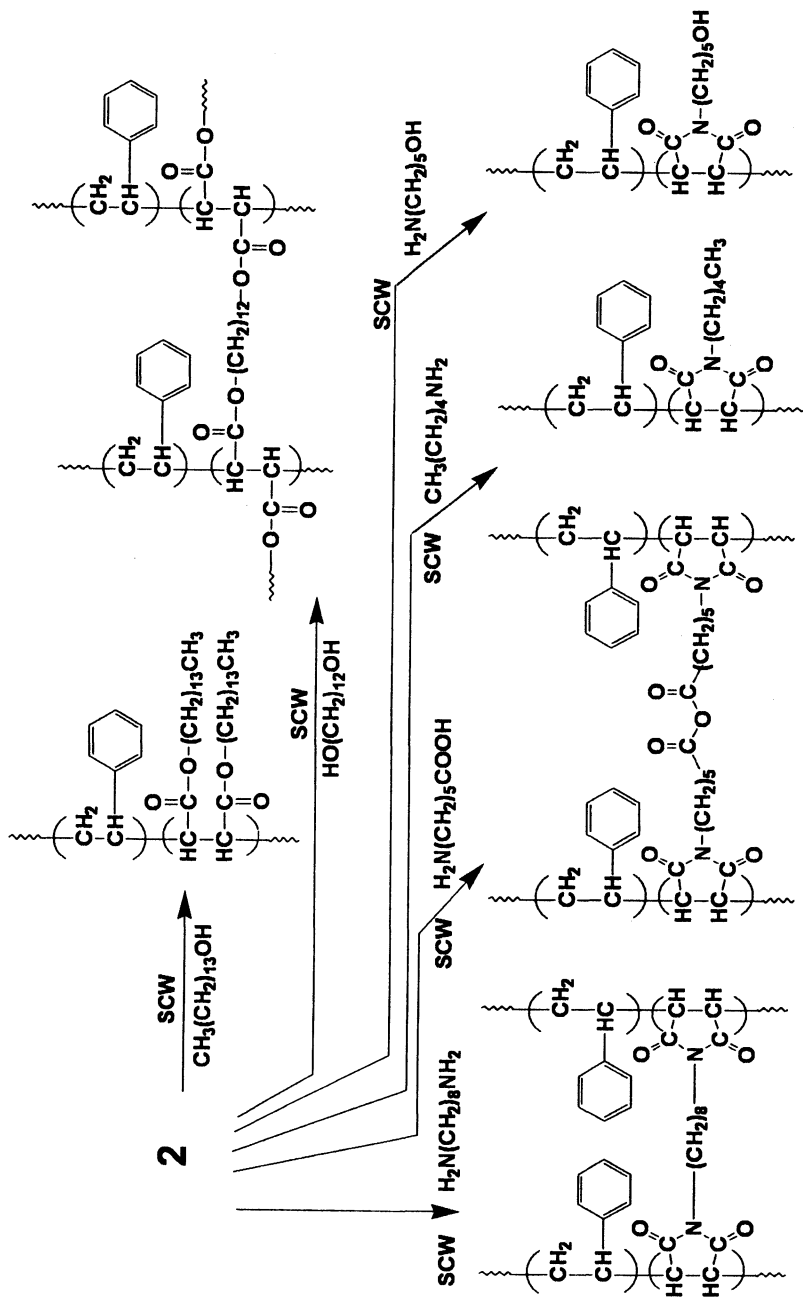
**Table I. Degradation of UP2 by SCW-Treatment at 300 °C for 10 min in the Presence of Additives.**

Entry	Additive <sup>a</sup>	Recovered solid (mg)	$I_{THF}$ (mg)	$S_{THF}$ (mg)	Degree of de-crosslinking (%)
1	none	172	143	28	42.7
2	CH <sub>3</sub> (CH <sub>2</sub> ) <sub>4</sub> OH	225	131	42	47.7
3	CH <sub>3</sub> (CH <sub>2</sub> ) <sub>7</sub> OH	211	127	58	49.3
4	CH <sub>3</sub> (CH <sub>2</sub> ) <sub>9</sub> OH	218	127	63	49.2
5	CH <sub>3</sub> (CH <sub>2</sub> ) <sub>10</sub> OH	215	85	84	65.8
6	CH <sub>3</sub> (CH <sub>2</sub> ) <sub>11</sub> OH	209	50	121	80.2
7	CH <sub>3</sub> (CH <sub>2</sub> ) <sub>13</sub> OH	203	6	172	97.8
8	CH <sub>3</sub> (CH <sub>2</sub> ) <sub>15</sub> OH	860	20	163	91.9
9	CH <sub>3</sub> (CH <sub>2</sub> ) <sub>17</sub> OH	– <sup>b</sup>	107	– <sup>b</sup>	56.3
10	C <sub>6</sub> H <sub>5</sub> OH	481	134	48	46.5
11	<i>m</i> -CH <sub>3</sub> (CH <sub>2</sub> ) <sub>14</sub> (C <sub>6</sub> H <sub>4</sub> )OH	– <sup>b</sup>	8	153	96.6
12	HO(CH <sub>2</sub> ) <sub>2</sub> OH	210	186	15	25.8
13	HO(CH <sub>2</sub> ) <sub>12</sub> OH	– <sup>b</sup>	152	607	39.5
14	HO(CH <sub>2</sub> CH <sub>2</sub> O) <sub>23</sub> H	215	171	36	31.6
15	CH <sub>3</sub> (CH <sub>2</sub> ) <sub>11</sub> C <sub>6</sub> H <sub>4</sub> SO <sub>3</sub> Na	186	178	23	28.8
16	CH <sub>3</sub> (CH <sub>2</sub> ) <sub>12</sub> COOH	351	162	36	35.5
17	CH <sub>3</sub> (CH <sub>2</sub> ) <sub>12</sub> CH <sub>3</sub>	259	158	27	36.9
18	CH <sub>3</sub> (CH <sub>2</sub> ) <sub>13</sub> NH <sub>2</sub>	– <sup>b</sup>	0	156	100
19	CH <sub>3</sub> (CH <sub>2</sub> ) <sub>4</sub> NH <sub>2</sub>	204	0	149	100
20	H <sub>2</sub> N(CH <sub>2</sub> ) <sub>8</sub> NH <sub>2</sub>	222	218	0	12.7
21	HO(CH <sub>2</sub> ) <sub>5</sub> NH <sub>2</sub>	– <sup>b</sup>	0	161	100
22	HOOC(CH <sub>2</sub> ) <sub>5</sub> NH <sub>2</sub>	– <sup>b</sup>	152	– <sup>b</sup>	39.2

a) Water: additive = 8 : 2 (wt/wt) except entry 1.

b) Not measured.

SOURCE: Reproduced with permission from reference 9. Copyright 2007 Elsevier.



Scheme 2. Plausible reactions of UP2 in SCW in the presence of additives.

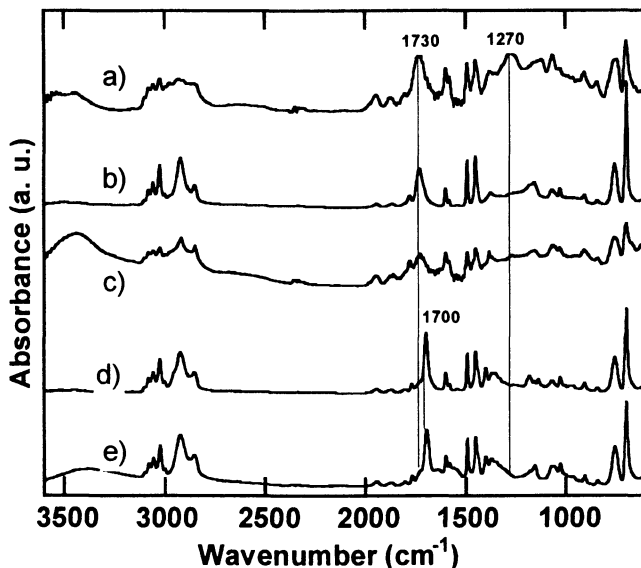


Figure 2. IR spectra (KBr) of UP2 before and after SCW treatment at 300°C for 10 min. a) Non-treatment. b) Soluble fraction in THF after SCW treatment in the presence of 1-tetradecanol. c) Insoluble fraction in THF after SCW treatment in the presence of 1,12-dodecanediol. d) Soluble fraction in THF after SCW treatment in the presence of 1-pentylamine. e) Soluble fraction in THF after SCW treatment in the presence of 5-amino-1-pentanol. Water: Additive = 8 : 2 (wt/wt). (Reproduced with permission from reference 9. Copyright 2007 Elsevier)

## Conclusions

Crosslinked UP2 was degraded by SCW treatment at 300°C. In the absence of additives, ester units in UP2 were hydrolyzed on SCW treatment and resulting carboxylic acid groups formed anhydrides at longer treatment times. Alcohols and phenols having a long alkyl chain effectively enhanced de-crosslinking. However, a carboxylic acid and a sulfonate salt were ineffective even though they have long alkyl chains. On the other hand, amines were very effective despite their alkyl chain lengths. Diols, diamines, and amino acids reacted at both terminal groups, showing no effects on the increase of degree of de-crosslinking. A polystyrene derivative obtained by SCW treatment in the presence of an aminoalcohol was modified with MA and crosslinked again by polymerization with St.

## Acknowledgement

This work was supported by a Grant-in Aid for 21st Century COE Program 24403 E-1 from the Ministry of Education, Culture, Sports, Science and Technology, Japan.

## References

1. Doss, N. L.; Habib, S.; Nossier, M. H. *J. Appl. Polym. Sci.* **1987**, *34*, 1117-1124.
2. Sugeta, T.; Nagaoka, S.; Otake, K.; Sako, T. *Kobunshi Ronbunshu* **2001**, *58*, 557-563 (in Japanese).
3. Economy, J.; Andreopoulos, A. G. *Polym. Adv. Technol.* **1996**; *7*, 561-570.
4. Hojo, H.; Ogasawara, K.; Chang, W. L.; Tsuda, K. *Adv. Composite Mater.* **1994**, *3*, 341-353.
5. Yoon, K. H.; DiBenedetto, A. T.; Huang, J. *Polymer* **1997**, *38*, 2281-2285.
6. Vallee, M.; Tersac, G.; Destais-Orvoen, N.; Durand, G. *Ind. Eng. Chem. Res.* **2004**, *43*, 6317-6324.
7. Patrick, H. R.; Griffith, K.; Liotta, C. L.; Eckert, C. A.; Gläser, R. *Ind. Eng. Chem. Res.* **2001**, *40*, 6063-6067.
8. Suyama, K.; Kubota, M.; Shirai, M.; Yoshida, H. *Polym. Degrad. Stab.* **2006**, *91*, 983-986.
9. Suyama, K.; Kubota, M.; Shirai, M.; Yoshida, H. *Polym. Degrad. Stab.* **2007**, *92*, 317-322.

## Chapter 9

# Degradation of Piezoelectric Fluoropolymers in Space Environments

Mathew Celina<sup>1</sup>, Tim R. Dargaville<sup>2</sup>, and Gary D. Jones<sup>1</sup>

<sup>1</sup>Sandia National Laboratories, Department 1821, P.O. Box 5800,  
Albuquerque, NM 87185-1411

<sup>2</sup>School of Physical and Chemical Sciences, Queensland University  
of Technology, Brisbane 4001, Australia

The performance criteria of piezoelectric polymers based on polyvinylidene fluoride (PVDF) in complex space environments have been evaluated. Thin films of these materials are being explored as in-situ responsive materials for large aperture space-based telescopes with the shape deformation and optical features dependent on long-term degradation effects, mainly due to thermal cycling, vacuum UV exposure and atomic oxygen. A summary of previous studies related to materials testing and performance prediction based on a laboratory environment is presented. The degradation pathways are a combination of molecular chemical changes primarily induced via radiative damage and physical degradation processes due to temperature and atomic oxygen exposure resulting in depoling, loss of orientation and surface erosion. Experimental validation for these materials to be used in space is being conducted as part of MISSE-6 (Materials International Space Station Experiment) with an overview of the experimental strategies discussed here.

## Introduction

The next generation of light-weight spacecraft will thoroughly challenge materials scientists owing to the demands for inflatable, rigidizable, shape memorizing and stimuli-responsive type craft, for example. High performance polymers are a key component for novel large-area spacecraft, such as solar sails, arrays and large telescope mirrors. Their intrinsic low density, functionality, easy processing and flexibility make them attractive considering the storage and weight limitations of launch vehicles. However, the difficult environment of space is extremely damaging to organic polymers, often severely restricting their performance and lifetimes (1-5).

Thin film piezoelectric polymers have the potential to be used in adaptive optics mirrors for low Earth orbit (LEO) based telescopes. Using piezoelectric polymers has the advantage of incorporating the actuation mechanism directly into the thin film such that any mirror shape changes can be adjusted using in-situ feedback. This allows for correction/compensation of misalignment errors, temperature fluctuations and even focus shifting (6). To achieve maximum weight savings, a mirror made from a piezoelectric polymer may fly unshielded, and could therefore be exposed to atomic oxygen (AO), vacuum ultraviolet (VUV) radiation, and the severe temperature variations in LEO. We are interested in examining how piezoelectric polymers based on the vinylidene fluoride backbone will perform in LEO conditions with the overall materials selection and performance requirements having been previously considered (7,8).

A brief summary of our extensive previous work using laboratory-based material characterization and performance assessment is presented here. We have examined the performance of piezoelectric PVDF and its copolymers over temperature ranges simulating the LEO environment, and examined the effects of radiation (gamma and vacuum ultraviolet) and atomic oxygen (7-13). Loss in the piezoelectric properties after exposure to high temperatures appears to be linked to film contraction and the Curie transition for PVDF and TrFE copolymer films, respectively (11). At sub-ambient temperatures, the piezoelectric performance is governed by the glass transition, which is more subtle in the copolymer and hence gives the copolymer greater flexibility and piezoelectric response at low temperature. The results from experiments measuring primary piezoelectric indicators such as  $d_{33}$  and remanent polarization, agreed well with the deflection of bimorphs made from each polymer.

When exposed to gamma radiation both polymers had almost identical gel formation, so it was surprising that when treated with VUV radiation the response of each polymer was dramatically different (10,12). The homopolymer showed signs of surface crosslinking with little change to the bulk, while the TrFE copolymer had a degree of crosslinking consistent with VUV radiation

initiated events throughout the film. VUV radiation damage is considerably more selective than gamma and is dependent on the absorption characteristics of the polymers. We proposed that the PVDF homopolymer absorbs the shorter wavelengths in the top few micrometers causing crosslinking, while the longer wavelengths are harmlessly dissipated by the polymer. In the copolymer the shorter wavelengths are also absorbed at the surface and the longer wavelengths, which penetrate into the bulk, interact with the comonomer units generating radicals, which combine to form crosslinking sites and lead to material degradation. This demonstrates that gamma radiation cannot be used as a reliable avenue to predict VUV radiation degradation in these polymers, which we had originally hoped could serve as a simple screening approach.

In LEO materials may also be exposed to atomic oxygen (AO). The high flux of AO, (approximately  $10^{15}$  atoms/cm<sup>2</sup>-s with an orbital speed of 8 km/s) formed by photo-dissociation of the small concentration of residual molecular oxygen in LEO, will cause surface pitting and erosion, while the VUV (115 – 200 nm) exposure may induce deleterious radiation events (2). The effects of simultaneous AO/VUV exposure of the two vinylidene fluoride based polymers were hence examined using laboratory-based experiments at NASA Glenn Research Center (9). In both cases significant weight loss and surface erosion resulted from AO attack. Erosion yields were  $2.8 \times 10^{-24}$  cm<sup>3</sup>/atom for PVDF and  $2.5 \times 10^{-24}$  cm<sup>3</sup>/atom for P(VDF-TrFE), consistent with previous literature data for similar materials. The film orientation of PVDF samples was reflected in the surface topology features after exposure, while the less orientated P(VDF-TrFE) samples had less regular surface patterning after exposure. Significantly, neither AO nor VUV irradiation dramatically altered the piezoelectric properties and we propose that these materials should perform satisfactorily under moderate LEO conditions.

Any use of novel responsive polymer components in space applications requires ground testing and ultimately space qualification to accommodate the complex LEO environment and better understand synergistic materials degradation. We have therefore participated in MISSE-6 (Materials International Space Station Experiment) with a combination of active and passive sample exposures that have been selected as a first flight experiment of piezoelectric polymers in LEO for space qualification. Two exposure conditions were available, the VUV backside and the VUV+AO ram direction of the MISSE assembly. Our experimental strategies for sample selection, exposure conditions and in-situ performance measurements are presented here.

## Experimental

In general, the polymers evaluated and discussed here are poled piezoelectric films of 30  $\mu$ m PVDF from MSI and 28  $\mu$ m P(VDF-TrFE) from



Ktech Corp. Our previous characterization and performance studies were conducted with similar polymers (9-11). Additional samples have been custom prepared in our laboratory by solution casting.

Sample details for MISSE-6, VUV exposure only are: two MSI PVDF bimorphs and two Ktech TrFE copolymer bimorphs with electrodes for actuation on either side. Passive sample are a combination of solution cast 80:20 P(VDF-TrFE), and 50:50 VF<sub>2</sub>-TrFE films, MSI homo PVDF, Ktech TrFE and pre-irradiated materials. Different coating thicknesses were applied.

Sample details for MISSE-6, combined VUV and AO exposure are: two MSI PVDF bimorphs and two Ktech TrFE copolymer bimorphs, again with electrodes on either side. Passive sample are also two PVDF and two Ktech TrFE films with different aluminum coatings. All coatings were made using vapor deposition.

## Materials International Space Station Experiment (MISSE-6)

Until as recently as the 1980s very little was known about the details of LEO environmental effects on polymeric materials. A significant step forward in the understanding of materials-space interactions was based on retrieval and evaluation of materials from the Long Duration Exposure Facility (LDEF) Experiment which spent 69 months orbiting the Earth between 1984 and 1990. LDEF was a 14-sided passive satellite equipped with almost every type of spacecraft surface or material that was in use in the 1980s, or envisaged for potential use in the foreseeable future (1,15,16). The LDEF mission demonstrated that all polymeric materials are greatly affected by the LEO environment with sometimes unexpected degradation occurring, that pre-LDEF knowledge of space environmental effects on materials had significant limits, and that synergistic effects of LEO environmental conditions must be considered to predict materials performance (1,15,16).

The LDEF mission spawned a number of subsequent smaller missions testing materials in the space environment aboard the Shuttle orbiter, Russian spacecrafts, and the International Space Station (ISS). Of these, only the Boeing/NASA experiments aboard the ISS (dubbed MISSE Experiments) had any continuity with MISSE-1 through MISSE-5 having been flown, and MISSE-6 having been deployed on March 22<sup>nd</sup> 2008. The MISSE program is designed to allow participation from government, academia and industry researchers, who require space testing of individual materials but may not have the multimillion-dollar budgets to host individual launches.

The MISSE experiments use a PEC (Passive Experiment Container) which is essentially a simple suitcase that houses the samples (Fig. 1). The PEC is launched as a closed container where the samples are located on the inside, and is then attached to the ISS during a spacewalk and opened fully inside-out to

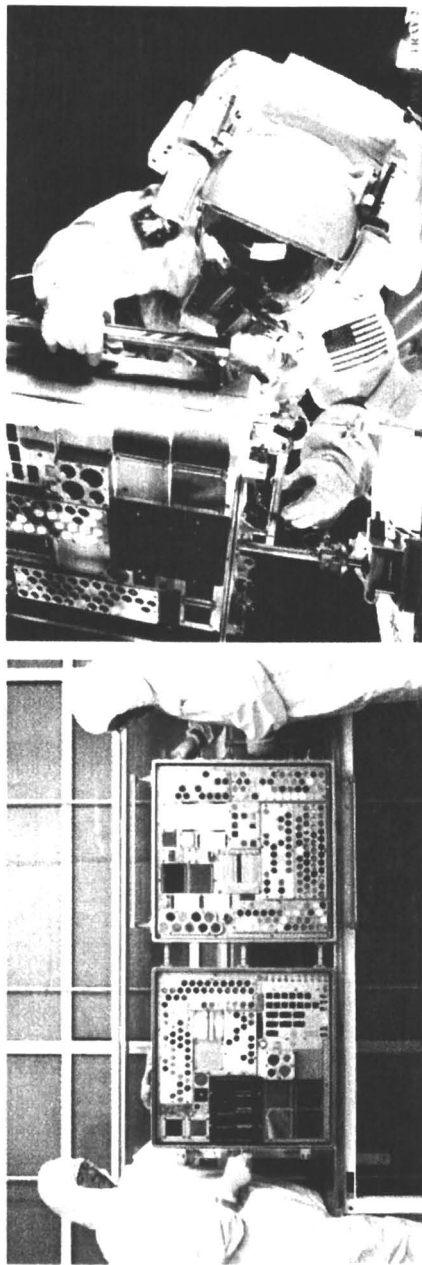


Figure 1. A MISSE PEC partially open (left); installation of a PEC outside the ISS (right) (pictures courtesy of NASA website).

expose the samples. Depending on which side of the PEC the samples are located, they will either receive mostly vacuum UV (VUV) radiation, or both VUV and atomic oxygen (AO) exposure (ram direction). We were allocated a 6 x 6" area on the VUV side and a 6 x 4" area on the AO/VUV side in which to locate our passive and active experiments.

### MISSE-6 experimental details

Since the piezoelectric materials are responsive it represented an opportunity to conduct *active* experiments, collect real-time data and evaluate the performance of these materials in space. MISSE-6 is the first time that active remote experiments have been part of the MISSE project. Both active and passive experiments are flown allowing for a range of experiments and materials to be tested over the course of the exposure (estimated at 6-8 months, depending on the Shuttle flight program for sample recovery).

Three experimental units each with different experimental focus were designed, fabricated and delivered to NASA Langley. The first unit contains four passive and four active films samples to be exposed to combined atomic oxygen and vacuum UV. The second unit contains 11 passive and four active samples to be exposed only to vacuum UV (see Fig. 2). The third unit has two passive samples with different thicknesses of protective aluminum layers to be exposed to atomic oxygen and vacuum UV. All passive samples will be characterized, both in terms of chemical and physical properties, after the mission and compared with pre-exposure characterization to determine the effects of the space environmental exposure. Thin foil-type thermocouples are attached and logged underneath the samples to measure actual temperatures experienced. By recording the temperature it will be possible to correlate the deflection properties with temperature conditions of the active samples.

The active experiments were designed with the aim of monitoring the changes in real-time piezoelectric operational performance with exposure time to be used for lifetime and performance predictions in LEO conditions. The active samples are designed in the form of thin film bimorphs mounted to move (flex) up and down with applied voltage at a frequency of once per 48 hrs (24 hours up and 24 hrs down). A design was required that would allow for actuation of the bimorphs with relatively low voltage to produce a deflection large enough for detection with very simple and robust sensors. The chosen design relies on the bimorphs mounted at one end in a counter-lever configuration to give maximum deflection for a low actuation voltage. Underneath the tip of each bimorph at the point of maximum deflection is a photodiode position sensor. These work by measuring the amount of reflected light off the bimorph from the reference LED beam supplied by the photodiode assembly which is calibrated to accurately determine the relative bimorph position. We initially considered small laser

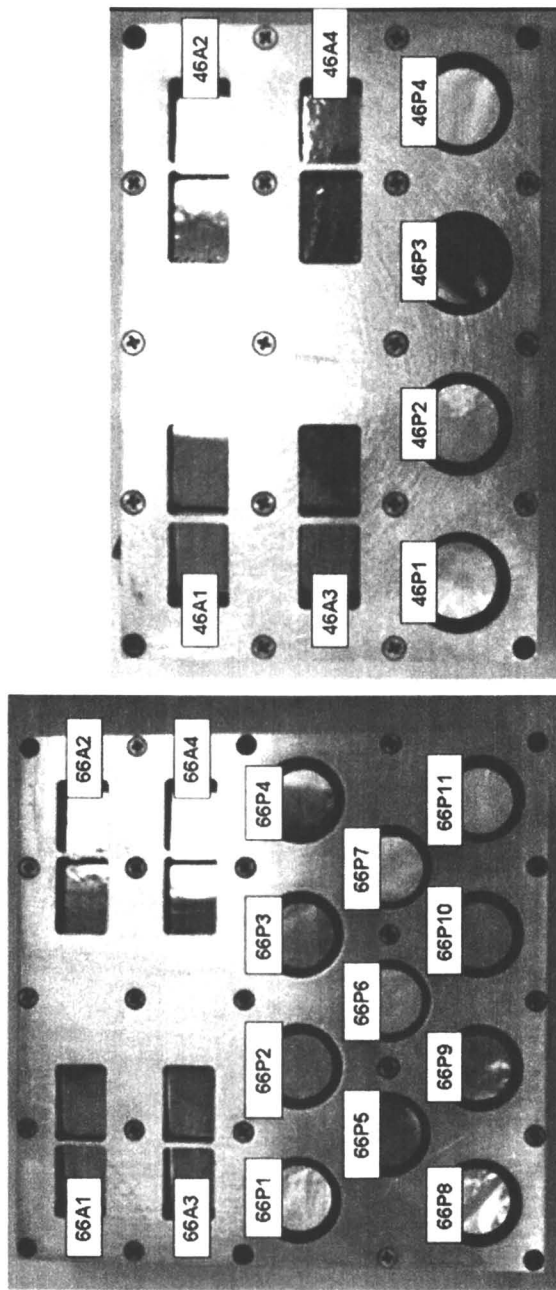


Figure 2. Sample arrangements for VUV side (left) and VUV+AO (right).

ranging devices, but due to space and weight limitations, working temperature range, power considerations, robustness issues, and sensitivity to displacement we decided on small LED/photo-sensors instead. They can work over a large temperature range, were found to be sufficiently radiation resistant and can accurately measure the bimorph tip deflection. Our sensor selection was optimized towards achieving the best resolution within a short distance. We selected a Honeywell HOA 1406-1 type sensor with integrated light source (an IR source) and photodiode that delivers an analog signal proportional to reflected light intensity. An example of relative signal output versus position of the reflective film surface is shown in Fig. 3. There is a good dynamic operating range where the sensor output sensitively equates to film position.

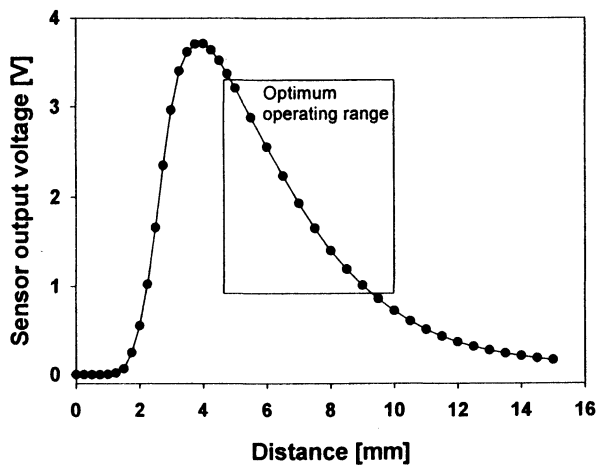


Figure 3. Photo-sensor signal intensity as a function of absolute film position.

The changes in the bimorph position, i.e. how much it will flex up or down with applied actuating voltage over time, are used to determine changes in the piezoelectric responsiveness as a function of LEO exposure. The excitation voltage is alternated every 24h between +100 V and -100V, so that up and downward film motion and positioning is achieved. Figure 4 shows the change in bimorph position (photodiode signal output rather than actual distance) with actuation voltage and time. While the position can clearly be controlled there are intrinsic noise and relaxation effects apparent in the film position with time. These films are not perfectly linear predictable materials; modulus, relaxation and their individual nature/behavior will mask and complicate recognition of long-term degradation trends. However, most importantly there is a clear difference between the up and down position and this delta value as a function of time will allow an assessment of performance changes with orbital exposure.

Measurements of the bimorph position and temperature (simultaneously logged) will be made every 30 mins using various data loggers to measure the output from the photodiodes and selective temperature locations (T-couples). In Fig. 5 a simulated lab experiment shows the change in the bimorph position monitored with the photo-sensor during a variation in temperature. The upper trace shows the change in bimorph position without excitation during a cooling and heating transition. The lower trace shows the up and down cyclic bimorph movement with excitation voltage applied for a similar temperature cycle. The magnitude of the displacement is dependent on film modulus, coefficient of thermal expansion, stiffness and temperature. It is obvious that time/temperature trends can be easily acquired.

The data loggers used are NASA-qualified Veriteq-brand loggers designed for temperature and analog voltage input. The capacity of the data-loggers is limited to 70KB 12-bit samples meaning they are not suitable for continuous position logging over the 6-9 months of the experiment. To obtain as much useful data as possible, measurements of the bimorph position and temperature (from the passive samples) will be made simultaneously three times every orbit plus 2 mins, with the actuation voltage reversed every 24 hours, so that over time data will be available over the entire temperature cycling range (orbit dependent solar position).

Other than a power feed from the ISS, the experiments need to be self-sufficient. The sensors are regulated by components that are part of the data acquisition and control printed circuit board that was designed specifically to fit the bimorph mounting case and integrate all electronic features into a single unit. It consists of resistors to provide bias voltages and fuses to protect the sensors and external power supply source. A programmable (non-volatile memory) IC processor PIC 12C671 and 2 driver transistors provide the 24 hour clock pulse that will reverse the 100 V bimorph excitation voltage via a miniature latching relay. All of these components are very low power consumption and are fuse protected as well. The PC board has a 15 pin D connector that provides the connections to the external 5 V and 100 V power supplies and four channels of analog voltage outputs (proportional to bimorph motion) to the external data loggers. The PC board is located inside the bimorph mounting unit where it will be shielded from direct solar irradiation, and to keep the wiring to the optical sensors and bimorph contacts as simple and compact as possible.

The electronics for driving and sensing the bimorphs are expected to receive a deeply penetrating radiation dose on the order of 50 krad (0.5 kGy) in LEO. This dose is far too low to cause any bulk material damage, however, it may cause lattice displacement and other ionization effects, which can temporarily or permanently damage the electronics. The Veriteq data-loggers recently retrieved from MISSE-1 and -2 were found to be fully functional with no evidence of any data corruption, which is encouraging considering that they were not radiation hardened. For qualification purposes an optical sensor was exposed to 1 KGy

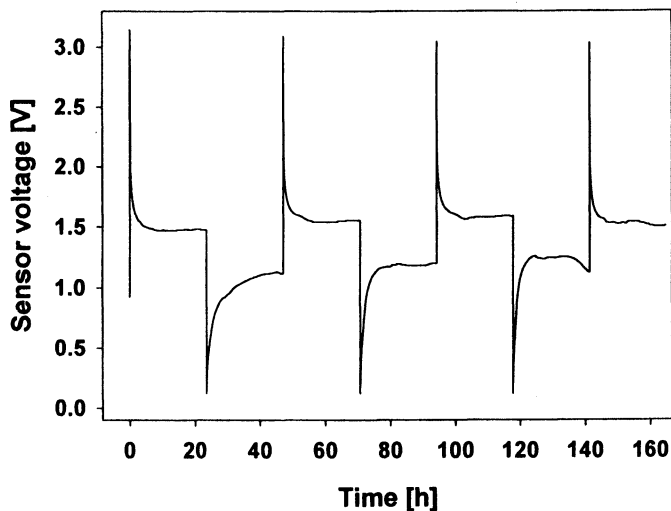


Figure 4. Bimorph 'position' as a function of 24h excitation cycling. Up and down position is induced by switching between +100 and -100V.

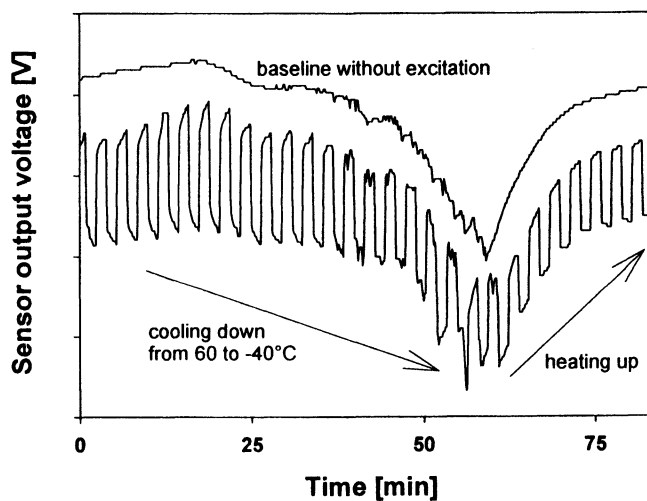


Figure 5. Bimorph 'position' as a function of excitation time and temperature.

(twice of what is expected in LEO) of  $\gamma$ -radiation and no negative effects on performance were observed, likewise we the PC board circuitry exposed to radiation during ground testing and it was found to remain operational.

The position sensors work by measuring reflected light from an infrared LED adjacent to the photodiode and as such, are sensitive to stray light. In laboratory tests we found that a 'rolling' baseline was created from the stray light from an infrared lamp switched on and off at regular intervals to simulate passing in and out of the Earth's shadow. By subtracting the baseline it was possible to isolate the output from the sensor relating to the bimorph position. For the MISSE-6 active experiments it is anticipated that some stray light will impinge on the sensor. It should be possible to correct for these variations providing they are not too intense that it causes the sensor to go off-scale. To minimize any stray sunlight effects the sensors are located in the shadow of the bimorph with a window (slightly smaller than the bimorph) covering the sides of the bimorph. This window will reduce the exposure of the bimorph sides to the space environment, but likely will not completely eliminate any issues. In addition to the window, the trough below the bimorphs are anodized resulting in a reduction of reflected light from the fixture onto the sensor.

## Conclusions

Our past laboratory-based materials performance experiments have established the major chemical and physical degradation pathways of PVDF-based polymers when operating in space. The current experiments will allow for actual space exposure of these piezoelectric polymers and verify the observed trends. MISSE-6, the Materials International Space Station Experiment is a joint effort between Boeing, NASA and various materials research groups. It represents an excellent and cost-effective opportunity to conduct performance evaluations under space LEO environments for a range of materials. This is the first time that PVDF-based adaptive polymer films will be remotely operated and exposed to combined atomic oxygen, solar UV and temperature variations in an actual space environment. The experiments are fully autonomous, involving cyclic application of excitation voltages, sensitive film position sensors and remote data logging. The experiment provides critical data for the long-term performance and qualification of selected polymers and multi-layer components utilizing these materials, and ultimately the feasibility of advanced low weight adaptive optical systems utilizing piezoelectric polymer films in space. We expect that as long as upper temperatures are limited to less than 110°C and film thicknesses can accommodate some expected losses due to AO erosion, sufficient useful piezoelectric properties should remain and allow for remote



actuation of bimorphs and hence physical displacement devices manufactured from these materials. We expect to recover data and samples in early 2009.

## Acknowledgements

Sandia is a multiprogram laboratory operated by Sandia Corporation, a Lockheed Martin Company, for the United States Department of Energy's National Nuclear Security Administration under Contract DE-AC04-94AL85000. The authors express their appreciation to Julie Elliott for technical support and the MISSE-6 team, in particular Gary Pippin from Boeing, for his guidance, dedication and useful discussions.

## References

1. Dursch, H. W.; Pippin, H. G. In *Materials Degradation in Low Earth Orbit (LEO)*; Srinivasan, V.; Banks, B., Eds.; The Minerals, Metals & Materials Society; 1990; pp 207-218.
2. Banks, B. A. In *Modern Fluoropolymers*; Scheirs, J., Ed.; Vol. 4, John Wiley & Sons: Chichester, 1997; pp 103-113.
3. Young, P. R.; Slemple, W. S.; Siochi, E. J. *Int. SAMPE Symp. Exh.* **1994**, *39*, 2243-2255.
4. Rasoul, F. A.; Hill, D. J. T.; George, G. A.; O'Donnell, J. H. *Polym. Adv. Technol.* **1998**, *9*, 24-30.
5. Dever, J. A.; De Groh, K. K.; Banks, B. A.; Townsend, J. A. *High Perform. Polym.* **1999**, *11*, 123-140.
6. Martin, J. W.; Redmond, J. M.; Barney, P. S.; Henson, T. D.; Wehlburg, J. C.; Main, J. A. *J. Intel. Mat. Syst. Str.* **2000**, *11*, 744-757.
7. Celina, M.; Dargaville, T. R.; Assink, R. A.; Martin, J. W. *High Perform. Polym.* **2005**, *17*, 575-592.
8. Celina, M. C.; Dargaville, T. R.; Chaplya, P. M.; Clough, R. L. *Mat. Res. Soc. Symp. Proc.* **2005**, *851*, 449-460.
9. Dargaville, T. R.; Celina, M.; Martin, J. W.; Banks, B. A. *J. Polym. Sci. B: Polym. Phys.* **2005**, *43*, 2503-2513.
10. Dargaville, T. R.; Elliott, J. M.; Celina, M. *J. Polym. Sci. B: Polym. Phys.* **2006**, *44*, 3253-3264.
11. Dargaville, T. R.; Celina, M.; Chaplya, P. M. *J. Polym. Sci. B: Polym. Phys.* **2005**, *43*, 1310-1320.
12. Dargaville, T. R.; Celina, M.; Clough, R. L. *Radiat. Phys. Chem.* **2006**, *75*, 432-442.

13. Dargaville, T. R.; Clough, R. L.; Celina, M. *ACS Symp. Ser. Polymer Durability and Radiation Effects* **2008**, *978*, 153-165.
14. Bharti, V.; Xu, H. S.; Shanthi, G.; Zhang, Q. M.; Liang, K. *J. Appl. Phys.* **2000**, *87*, 452-461.
15. George, P. E.; Dursch, H.W. *J. Adv. Mat.* **1994**, *25(3)*, 10-19.
16. Young, P.; Siochi, E. J.; Slemper, W. S. *ACS Symp. Ser. Irradiation of Polymers* **1996**, *620*, 264-292.

## Chapter 10

# Field and Laboratory Aging Effects on Poly(*p*-phenylene benzobisoxazole) Fibers Used in Body Armor

Joannie Chin<sup>1</sup>, Amanda Forster<sup>2</sup>, and Kirk Rice<sup>2</sup>

<sup>1</sup>Polymeric Materials Group and <sup>2</sup>Office of Law Enforcement Standards,  
National Institute of Standards and Technology, 100 Bureau Drive,  
Gaithersburg, MD 20899

In recent years, poly (*p*-phenylene benzobisoxazole) (PBO) fibers have become prominent in high strength applications such as body armor, ropes and cables. This study compared the mechanical and chemical properties of yarns extracted from PBO body armor exposed to elevated temperature and moisture in the laboratory with yarns from body armor that had failed in the field. During 26 weeks of laboratory aging, a 30 % decrease in yarn tensile strength was observed, which could be correlated to the disappearance of key PBO functional groups as measured via infrared spectroscopy. In field armor, a similar decrease in tensile strength was observed, but the changes in chemistry differed from those observed in the laboratory aging study. Differences in chemical degradation and mechanical damage mechanisms between the two sets of armor are discussed.

In recent years, poly(p-phenylene benzobisoxazole) (PBO) fibers have become prominent in high strength applications such as body armor, ropes and cables, and recreational equipment. However, degradation of PBO fiber mechanical properties following exposure to moisture has been documented by the manufacturer (1) and at least one failure of PBO-based body armor in the field has occurred (2). The objectives of this study were to compare changes in mechanical and chemical properties of yarns extracted from PBO-based body armor that was penetrated by a bullet in the field approximately 6 months after being deployed, with PBO-based body armor panels of the same model aged in the laboratory under elevated temperature and moisture conditions.

## Experimental (3)

### Materials

In the first phase of this research, a comparative analysis study was carried out on yarns from the back panel of the vest that had failed in the field (manufactured in November 2002, hereinafter referred to as the “officer’s” vest), a new, non-deployed vest of the same model and construction as the officer’s vest (manufactured in September 2003, hereinafter referred to as the “new” vest), and a vest from the National Law Enforcement and Corrections Technology Center (NLECTC) Compliance Test Program Archive, of the same model and construction as the officer’s vest (manufactured in March 2001 and submitted for compliance testing in May 2001, hereinafter referred to as the “archive” vest).

In the second phase of this research, a laboratory aging study was carried out on new, non-deployed vests of the same model and construction as described above. The ballistic panels from all vests analyzed in this research consisted of 20 layers of woven PBO fabric stacked together and diagonally stitched. The ballistic panels are inserted into a sealed protective fabric liner and then into a fabric carrier system.

All vest yarns were also compared to virgin PBO spool yarn, manufactured in August 2003 and provided to NIST by the fiber manufacturer for this study in May 2004. This material will be referred to as “virgin” yarn.

### Laboratory Aging

24 ballistic panels enclosed in liners and carriers were aged in a Cincinnati Sub-Zero Z32 environmental chamber at 50°C and 60 % RH for 84 d, and then

60°C and 37 % RH for an additional 73 d. The increase in temperature to 60°C and decrease in relative humidity to 37 % was intended to accelerate the kinetics of fiber degradation by increasing the temperature while maintaining the same absolute water content in the environment.

### **Tensile Testing**

To obtain yarn mechanical properties, tensile testing of yarns was carried out in accordance with ASTM D2256-02, "Standard Test Method for Tensile Properties of Yarn by the Single-Strand Method", using an Instron Model 4482 test frame equipped with a 91 kg (200 lb) load cell, and pneumatic yarn and cord grips (Instron model 2714-006). Jaw separation was 7.9 cm (3.1 in) and cross-head speed was 2.3 cm/min (0.9 in/min). In this study, yarns were nominally 38.1 cm (15 in) long, and given 60 twists on a custom-designed yarn twisting device. 10 replicates from each vest were tested to failure. The standard uncertainty of these measurements is typically  $\pm 5\%$ .

### **Fourier Transform Infrared Spectroscopy (FTIR)**

Infrared analysis was carried out using a Nicolet Nexus FTIR equipped with a mercury-cadmium-telluride (MCT) detector and a SensIR Durascope attenuated total reflectance (ATR) accessory. FTIR spectra were recorded between 4000  $\text{cm}^{-1}$  and 700  $\text{cm}^{-1}$  at three different locations on each yarn and were averaged over 128 scans. Spectral analysis, including spectral subtraction, was carried out using a custom software program developed in the Polymeric Materials Group at NIST to catalogue and analyze multiple spectra (4). All spectra were baseline corrected and normalized using the aromatic C-H deformation peak at 848  $\text{cm}^{-1}$ . Standard uncertainties associated with this measurement are  $\pm 2 \text{ cm}^{-1}$  in wavenumber and  $\pm 1\%$  in absorbance.

## **Results and Discussion**

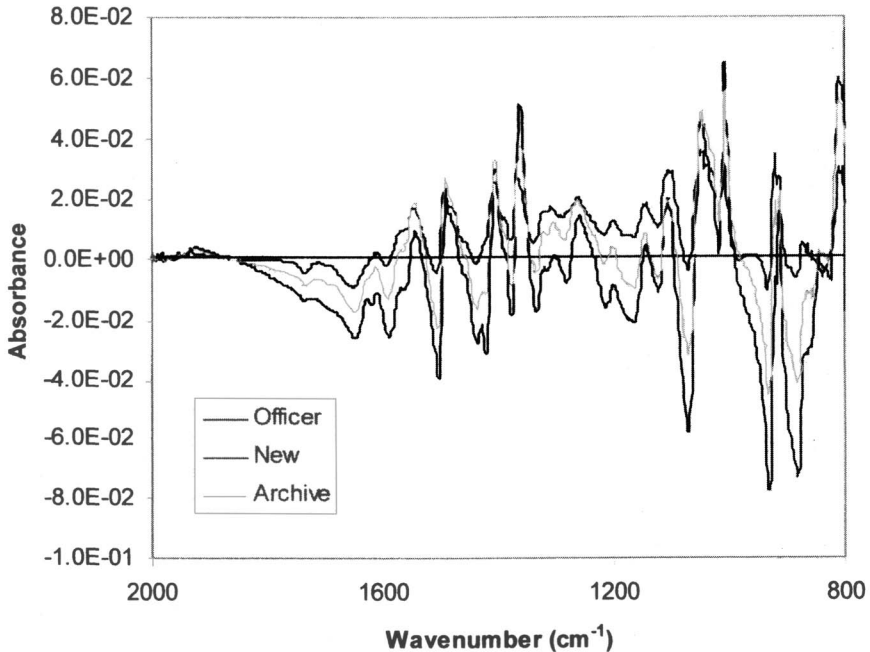
Tensile properties of yarns extracted from the back panel of the officer's vest, a new vest, an archive vest, and virgin yarn are tabulated in Table I. The yarns from the officer's vest are clearly lower in all tensile properties relative to yarns from the new and archive vests, as well as the virgin yarn. The tensile properties of the yarns from the archive vest are also lower than that of the new vest and virgin yarns.

Figure 1 shows the resulting difference spectra obtained by subtracting the infrared spectrum of the virgin yarn from the spectra of yarns from the officer's,

**Table I. Tensile Properties of Vest Yarns**

<i>Vest</i>	<i>Tensile Strength (GPa)</i>	<i>Strain at Break (%)</i>	<i>Tensile Modulus (GPa)</i>	<i>Break Energy (Nm)</i>
Officer	3.22 ± 0.24	2.50 ± 0.17	136.6 ± 2.6	0.31 ± 0.04
New	4.78 ± 0.19	3.29 ± 0.12	141.8 ± 3.6	0.61 ± 0.05
Archive	3.65 ± 0.10	2.65 ± 0.06	141.6 ± 5.0	0.37 ± 0.02
Virgin	5.34 ± 0.16	3.52 ± 0.12	147.1 ± 2.7	0.91 ± 0.05

new, and archive vests. Qualitatively similar difference spectra are obtained when the infrared spectrum of the yarns from the new vest is subtracted from the officer and archive vest yarn spectra. Downward-pointing (negative) peaks in the difference spectra are species that are lower in concentration relative to the reference material (virgin yarn, in this case) and upward-pointing (positive) peaks are species that are higher in concentration relative to the reference material, or are new species that are not originally present in the reference material.



*Figure 1. Difference spectra of the officer's, new and archive vest yarns, referenced to spectrum of virgin yarn. (See page 3 of color insert.)*

The primary negative peaks in the difference spectra of the vest yarns have low absorbance values and are seen at  $931\text{ cm}^{-1}$ ,  $1072\text{ cm}^{-1}$ ,  $1422\text{ cm}^{-1}$ ,  $1440\text{ cm}^{-1}$ ,  $1506\text{ cm}^{-1}$ ,  $1560\text{ cm}^{-1}$ ,  $1588\text{ cm}^{-1}$ ,  $1657\text{ cm}^{-1}$  and  $3400\text{ cm}^{-1}$ . The officer's vest yarn contains negative peaks with the highest intensity (absorbance), followed by the archive vest and the new vest, in decreasing order of intensity. This rank order in peak absorbance tracks the same rank order of tensile strength loss reported earlier.

It is generally assumed that negative peaks in infrared difference spectra are associated with peaks in the original spectrum; however, the negative peaks observed in these different spectra do not match peaks found in the original spectrum of PBO, and specifically are not peaks associated with benzoxazole ring vibrations. One possible explanation for these negative peaks is that they originate from residual intermediate products of the PBO synthesis. As shown in Figure 2, So et al. (5) proposed that intermediate products in the synthesis of PBO model compounds are aminophenylbenzoate, which undergoes rearrangement to hydroxyphenylbenzamide, which subsequently undergoes ring closure to generate the benzoxazole. Infrared analysis of 2-aminophenyl benzoate and 2-hydroxyphenylbenzamide model compounds revealed peaks that matched a number of the negative peaks in the difference spectrum, indicating the possible presence of these intermediate products in the PBO vest yarns. Both the aminophenylbenzoate and hydroxyphenylbenzamide intermediates are not as hydrolytically stable as benzoxazole and can undergo hydrolysis, presumably leading to decreased tensile properties.

Table II shows tensile strengths of yarns extracted from new vests subjected to environmental chamber aging, as a function of exposure time. Average yarn tensile strength dropped from 4.82 GPa to 3.08 GPa during the 157 d exposure period. Average strain to failure during the exposure period dropped from 3.31 % to 2.17 % while the tensile modulus remained steady in the range between 141 GPa and 149 GPa.

Figure 3 shows the resulting difference spectra as a function of exposure time, when the infrared spectrum of the unaged vest yarn is subtracted from each of the laboratory-aged vest yarn spectra. The changes observed in this set of spectra are much more clearly associated with benzoxazole ring hydrolysis. Negative peaks observed at  $914\text{ cm}^{-1}$ ,  $1056\text{ cm}^{-1}$ , and  $1362\text{ cm}^{-1}$  are assigned to the vibrations associated with the benzoxazole ring (6), and grow progressively larger and more negative with time. A positive peak at  $1650\text{ cm}^{-1}$  in the region associated with amide carbonyl or carboxylic acid also grew progressively larger with time. This observation suggests that benzoxazole ring-opening has occurred with the subsequent formation of hydroxybenzamide structures. Further breakdown of hydroxybenzamide groups could lead to the formation of aminophenol and benzoic acid groups; the width of the peak at  $1650\text{ cm}^{-1}$  allows for the possibility of a benzoic acid peak at  $1680\text{ cm}^{-1}$ . The growth of new, broad peaks centered at  $3300\text{ cm}^{-1}$  also suggests the presence of amide N-H stretch or carboxylic acid O-H stretch.

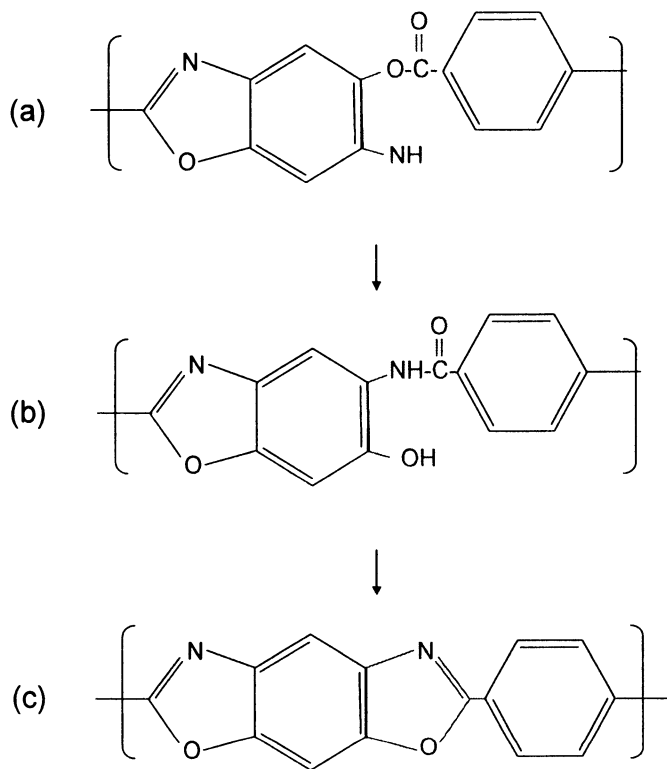


*Figure 2. Proposed intermediate products in the synthesis of PBO, showing (a) aminophenylbenzoate, (b) hydroxyphenylbenzamide, and (c) benzoxazole. (See page 4 of color insert.)*



**Table II. Tensile properties of vest yarns during environmental chamber exposure (50 °C/60% RH, 0 days to 84 days, followed by 60 °C/37% RH, 85 days to 157 days)**

<i>Time in Chamber (d)</i>	<i>Tensile Strength (GPa)</i>	<i>Strain at Break (%)</i>	<i>Tensile Modulus (GPa)</i>	<i>Break Energy (Nm)</i>
0	4.82	3.31	141.06	0.76
29	4.18	2.96	142.68	0.58
56	3.88	2.73	147.11	0.50
85	3.64	2.55	147.97	0.44
109	3.57	2.51	146.66	0.43
132	3.30	2.40	147.76	0.39
157	3.08	2.17	146.99	0.32

NOTE: Estimated relative standard uncertainties for tensile strength, strain at break, tensile modulus and break energy are 3.5 %, 3 %, 2.5 % and 6 %, respectively.

SOURCE: Reproduced with permission *Polym. Degrad. Stability* 2007, 92, 1234-1246. Copyright 2007.

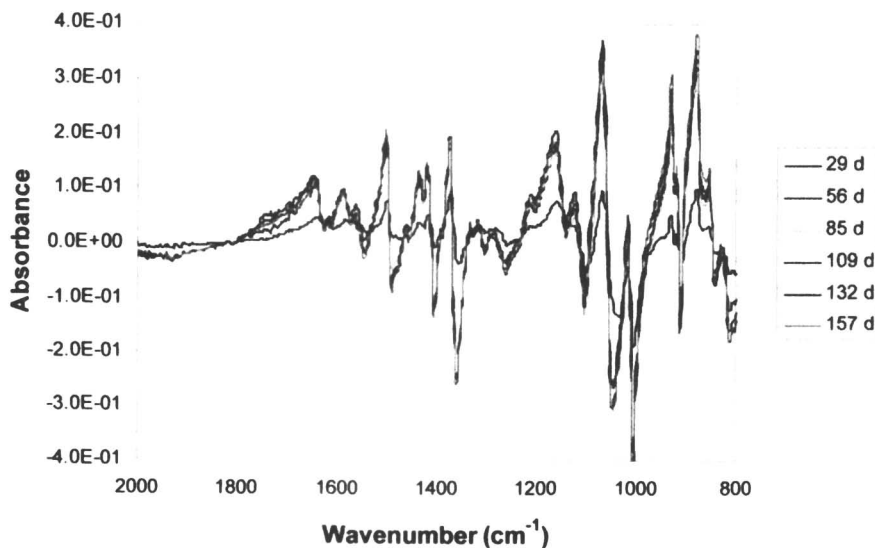


*Figure 3. Difference spectra for PBO yarns extracted from aged vests, referenced to spectrum of yarn taken at beginning of exposure. (See page 5 of color insert.)*

## Summary

Changes in mechanical and chemical properties of PBO fibers from armor worn in the field and armor artificially aged in the laboratory were compared. During 157 d of elevated temperature/elevated moisture laboratory aging, a 30 % decrease in yarn tensile strength was observed, which could be correlated to the disappearance of key PBO functional groups as measured via infrared spectroscopy. In the field armor, a similar 30 % decrease in tensile strength over the same period of time was observed, but the changes in chemistry differed from those observed in laboratory aging study. The chemical degradation observed in the laboratory aged armor is attributed to benzoxazole hydrolysis, whereas chemical changes in the failed field armor are tentatively identified as hydrolysis of low concentrations of residual intermediate products such as benzoate and benzamide.

Both benzoxazole hydrolysis and hydrolysis of intermediate products such as benzamide or benzoate potentially cause tensile strength degradation in PBO, by disrupting the conjugated rigid rod structure and by chain scission, respectively. The former mechanism appears to be the primary mode of degradation in the laboratory-aged armor; the latter mechanism appears to be predominant in the case of the failed field body armor.

## References

1. URL [http://www.toyobo.co.jp/e/seihin/kc/pbo/pdf/Attachment\\_1970KB.pdf](http://www.toyobo.co.jp/e/seihin/kc/pbo/pdf/Attachment_1970KB.pdf)
2. *Status Report to the Attorney General on Body Armor Safety Initiative Testing and Activities*; National Institute of Justice Special Report, December 27, 2004.
3. Certain trade names and company products are mentioned in the text or identified in an illustration in order to adequately specify the experimental procedure and equipment used. In no case does such an identification imply recommendation or endorsement by the National Institute of Standards and Technology, nor does it imply that the products are necessarily the best available for the purpose.
4. Dickens, B. In *Service Life Prediction Methodology and Metrologies*; Martin, J. W.; Bauer, D. R., Eds.; ACS: Washington, DC, 2001; pp 414.
5. So, Y. -H.; Heeschen, J. P. *J. Org. Chem.* **1997**, *62*, 3552-3561.
6. Tamargo-Martinez, K.; Villar-Rodil, S.; Paredes, J. I.; Martinez-Alonso, A.; Tascon, J. M. D. *Chem. Mater.* **2003**, *15*, 4052-4059.

## Chapter 11

# A Nonempirical Model for the Lifetime Prediction of Polymers Exposed in Oxidative Environments

X. Colin, B. Fayolle, L. Audouin, and J. Verdu

CIVIPOL, LIM (UMR 8006), ENSAM 151, Boulevard de l'Hôpital,  
75013 Paris, France

This paper presents a non-empirical kinetic model for the lifetime prediction of polymers exposed in their normal use conditions. After having described the different components (the core, the optional layers) of the model, its efficiency is demonstrated for polyethylene in large temperature and  $\gamma$  dose rate ranges. Future developments are briefly presented.

## Introduction

Since the end of the 90's, our group has been developing a non-empirical kinetic model, named KINOXAM, for the lifetime prediction of polymers and polymer matrix composites in their use conditions. The model is totally open. It is composed of a core, common to all types of polymers, derived from the now well-known "closed-loop" mechanistic scheme (1). Around this core, various optional layers can be added according to the complexity of oxidation mechanisms and the relationships between the structural changes taking place at the molecular scale and the resulting ones at larger scales (the macromolecular and macroscopic scales).

The efficiency of the kinetic model has been demonstrated for many substrates: polypropylene (2), polyethylene (3-4), poly(ethylene terephthalate) (5), polyisoprene (6), sulphur vulcanized polyisoprene (7), polybutadiene (8-9), amine crosslinked epoxy (10) and polybismaleimide (11) in large temperature,  $\gamma$  dose rate and oxygen pressure ranges.

In the following sections, particular attention is paid to polyethylene radio-thermal oxidation.

### Core of the Model

The core of the kinetic model describes the thermal oxidation at low temperature (typically at  $T < 200^\circ\text{C}$ ) at low conversion ( $[\text{PH}] = [\text{PH}]_0 = \text{constant}$ ) and in oxygen excess of unfilled and unstabilized saturated hydrocarbons. It is derived from the "closed-loop" mechanistic scheme (CLM) of which the main characteristic is that radicals are formed by the thermal decomposition of its main propagation product: the hydroperoxide group POOH (12). This closed-loop character explains the sharp auto-acceleration of oxidation at the end of an induction period (Figure 1).

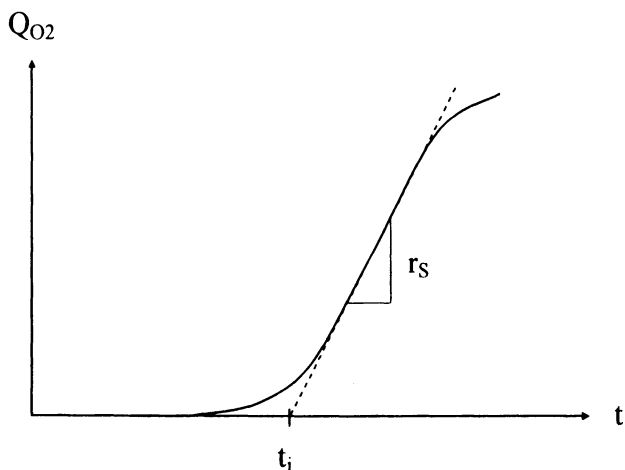
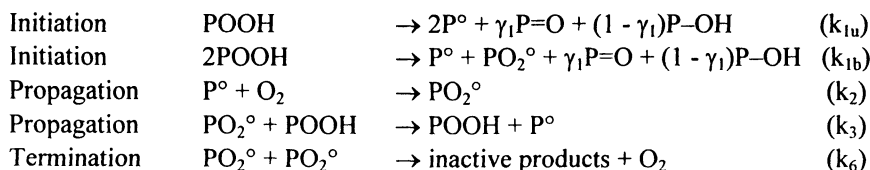


Figure 1. Typical shape of kinetic curves of  $\text{O}_2$  absorption. Determination of oxidation induction time ( $t_i$ ) and maximum oxidation rate ( $r_s$ ).

In its simplest form (in oxygen excess) the CLM involves five elementary reactions:



The only assumption, rarely justified and developed in the literature, is the uniqueness of the reactive site PH. PH corresponds to the most abstractable hydrogen atom in the monomer repeat unit: As an example, it corresponds to methyne C-H bonds in PP ( $[PH]_0 \approx 20 \text{ mol.l}^{-1}$ ) and methylene C-H bonds in PE ( $60 \text{ mol.l}^{-1}$ ).

The CLM leads to a system of three differential equations (SED), constituting the core of the kinetic model:

$$\frac{d[P^\circ]}{dt} = 2k_{1u}[POOH] + k_{1b}[POOH]^2 - k_2[O_2][P^\circ] + k_3[PH][PO_2^\circ] \quad (1)$$

$$\frac{d[PO_2^\circ]}{dt} = k_{1b}[POOH]^2 + k_2[O_2][P^\circ] - k_3[PH][PO_2^\circ] - 2k_6[PO_2^\circ]^2 \quad (2)$$

$$\frac{d[POOH]}{dt} = -k_{1u}[POOH] - k_{1b}[POOH]^2 + k_3[PH][PO_2^\circ] \quad (3)$$

It is assumed that  $O_2$  dissolution is instantaneous and obeys Henry's law:

$$[O_2] = [O_2]_0 = S \times P_{O_2} \quad (4)$$

where  $S$  is the coefficient of  $O_2$  solubility in the polymer and  $P_{O_2}$  the  $O_2$  partial pressure in the surrounding atmosphere. Initial conditions are: at  $t = 0$ ,  $[P^\circ] = [PO_2^\circ] = 0$  and  $[POOH] = [POOH]_0$ .

The numerical resolution of the SED gives access to the changes (with time) of concentrations of the reactive species:  $[O_2]$ ,  $[P^\circ]$ ,  $[PO_2^\circ]$  and  $[POOH] = f(t)$ . An interesting quantity, which can be directly determined from the SED without the use of additional assumptions (or additional adjustable parameters), is  $O_2$  absorption:

$$Q_{O_2} = \int (k_2[O_2][P^\circ] - k_6[PO_2^\circ]^2) dt \quad (5)$$

The changes (against time) of  $Q_{O_2}$  have been calculated for PE at different temperatures, with the parameter values reported in Table I, and compared to literature data (13). At temperatures higher than  $100^\circ\text{C}$ , good agreement has been obtained between theory and experiment (Figure 2). However, at temperatures lower than  $100^\circ\text{C}$ , deviations have been observed: the core of the model overestimates the oxidation induction time  $t_i$  and underestimates the maximum oxidation rate  $r_s$ , both deviations increasing when the temperature decreases.

An additional layer has been added around the core in order to reduce both deviations.

## Layer 1: Non-terminating Bimolecular Combination

A detailed kinetic analysis of a paper published more than 30 years ago by Decker et al. (14) led us to distinguish three distinct processes of bimolecular

**Table I. Parameters used for Kinetic Modeling.**

Rate constant ( $s^{-1}$ or $l.mol^{-1}.s^{-1}$ )	Pre-exponential factor ( $s^{-1}$ or $l.mol^{-1}.s^{-1}$ )	Activation energy ( $kJ.mol^{-1}$ )
$k_{1u}$	$2.0 \cdot 10^{12}$	145
$k_{1b}$	$1.9 \cdot 10^7$	86
$k_2$	$10^8$	0
$k_3$	$1.5 \cdot 10^{10}$	73
$k_6$	$5.6 \cdot 10^8$	0

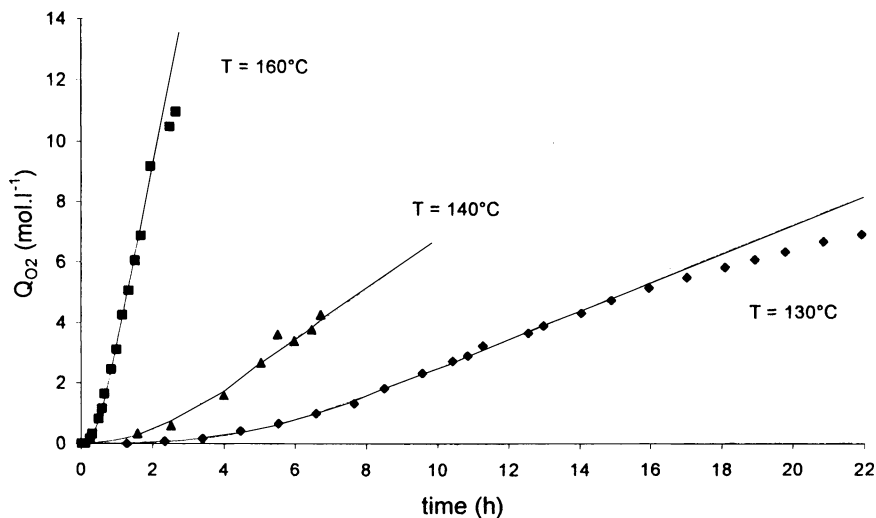
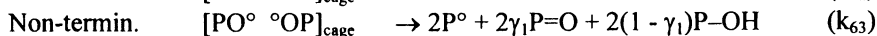
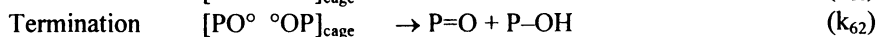
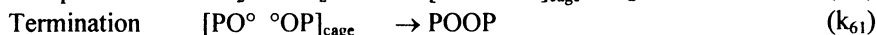


Figure 2. Examples of  $O_2$  absorption curves for PE at  $T \geq 100^\circ C$  in oxygen excess ( $P_{O_2} \geq 2 \cdot 10^4 Pa$ ). Points: Experimental data. Continuous lines: kinetic model based on equations 1–5.

combination of peroxy radicals:



Quantitative data obtained at 45°C by these authors indicate clearly that termination (by coupling or disproportionation) is not very efficient since a significant fraction of alkoxy radicals (typically 35–40%) escape from the cage to initiate new oxidation radical chains.

These four processes have been added to the CLM. The resulting mechanistic scheme leads to a new SED:

$$\frac{d[\text{P}^\circ]}{dt} = 2k_{1u}[\text{POOH}] + k_{1b}[\text{POOH}]^2 - k_2[\text{O}_2][\text{P}^\circ] + k_3[\text{PH}][\text{PO}_2^\circ] + 2k_{63}[\text{PO}^\circ \text{ }^\circ\text{OP}]_{\text{cage}} \quad (6)$$

$$\frac{d[\text{PO}_2^\circ]}{dt} = k_{1b}[\text{POOH}]^2 + k_2[\text{O}_2][\text{P}^\circ] - k_3[\text{PH}][\text{PO}_2^\circ] - 2k_{60}[\text{PO}_2^\circ]^2 \quad (7)$$

$$\frac{d[\text{POOH}]}{dt} = -k_{1u}[\text{POOH}] - k_{1b}[\text{POOH}]^2 + k_3[\text{PH}][\text{PO}_2^\circ] \quad (8)$$

$$\frac{d[\text{PO}^\circ \text{ }^\circ\text{OP}]_{\text{cage}}}{dt} = k_{60}[\text{PO}_2^\circ]^2 - (k_{61} + k_{62} + k_{63})[\text{PO}^\circ \text{ }^\circ\text{OP}]_{\text{cage}} \quad (9)$$

Initial conditions are: at  $t = 0$ ,  $[\text{P}^\circ] = [\text{PO}_2^\circ] = [\text{PO}^\circ \text{ }^\circ\text{OP}]_{\text{cage}} = 0$  and  $[\text{POOH}] = [\text{POOH}]_0$ .

The changes (with time) of  $Q_{\text{O}_2}$  have been calculated for PE at different temperatures from equation 5 with the parameter values reported in Table II. Values of  $t_i$  and  $r_s$  have been determined graphically as shown in Figure 1, over a large temperature range (typically between 40 and 200°C) and compared to literature data (4). Good agreement has been obtained between theory and experiment (Figures 3 and 4).

The model explains, without any additional assumptions, the discontinuity observed at about 110–120°C in the temperature dependence of both quantities. This discontinuity is due to the fact that the apparent termination rate constant  $k_6$  does not obey Arrhenius law (Figure 5).

## Layer 2: Polymer Radiolysis

In the case of radio-oxidation, a second important source of radicals is the polymer radiolysis, i.e. the breakdown of lateral bonds in the polymer chain. PE radiolysis leads to the formation of very reactive  $\text{H}^\circ$  radicals which recombine rapidly by hydrogen abstraction. Thus, the balance reaction can be written as follows:





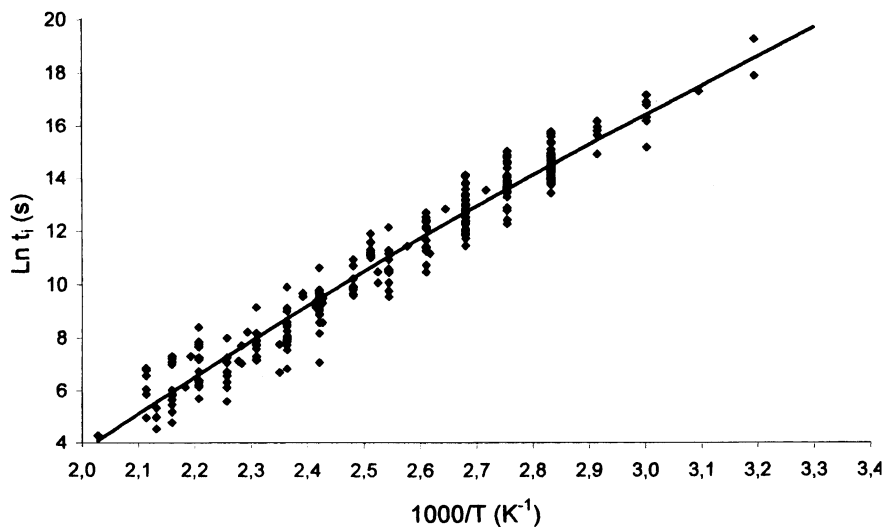


Figure 3. Arrhenius plot of the oxidation induction time for PE in oxygen excess ( $P_{O_2} \geq 2 \cdot 10^4$  Pa). Points: Experimental data. Continuous line: kinetic model based on equations 5–9.

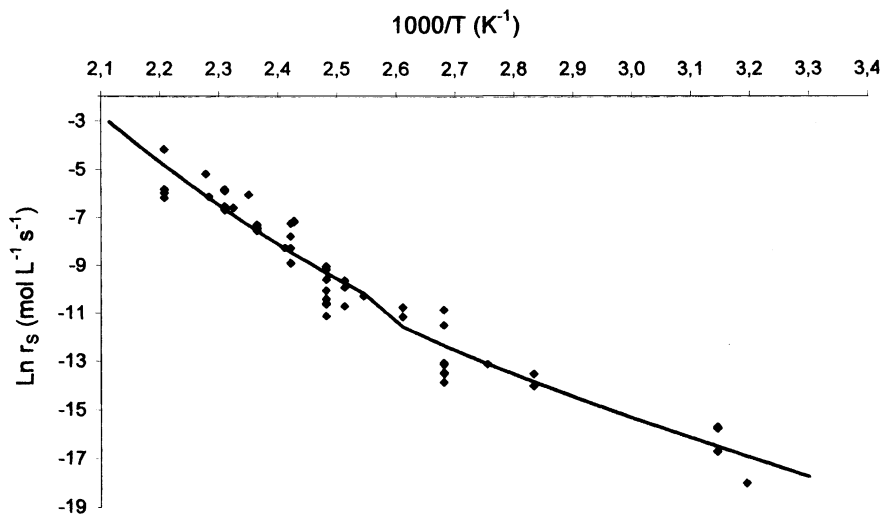


Figure 4. Arrhenius plot of the maximum oxidation rate for PE in oxygen excess ( $P_{O_2} \geq 2 \cdot 10^4$  Pa). Points: Experimental data. Continuous line: kinetic model based on equations 5–9.

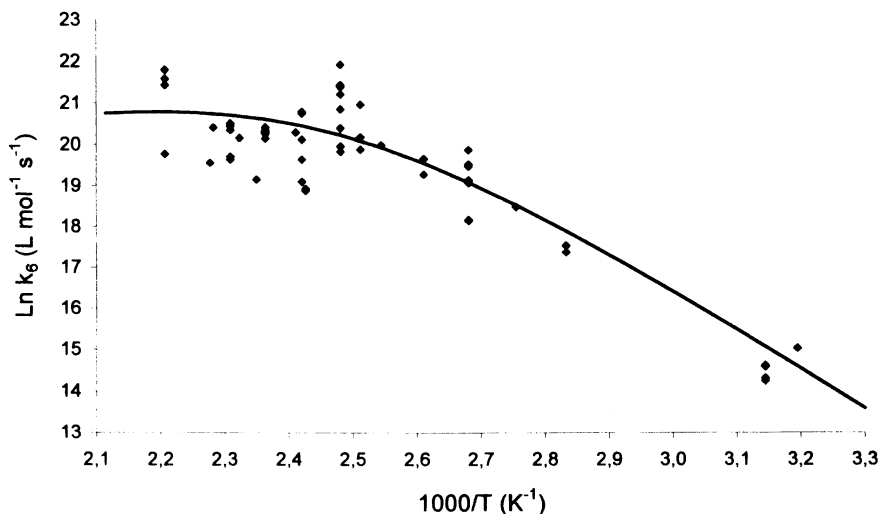
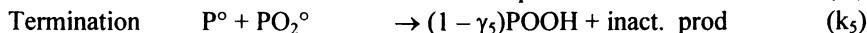
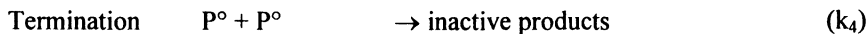


Figure 5. Arrhenius plot of the apparent termination rate constant  $k_6$  for PE. Points: Experimental data. Continuous line: kinetic model.

Table III. Radiochemical yields determined by Decker et al. at 45°C in oxygen excess ( $P_{O_2} \geq 2 \cdot 10^4$  Pa) (14). Comparison to theoretical ones predicted with equations 6–11.

	type	I (Gy.s <sup>-1</sup> )	G <sub>O2</sub>	G <sub>POOH</sub>	G <sub>POH</sub>	G <sub>POOP</sub>	G <sub>P=O</sub>
Experiment	ldPE	0.108	16	9.2		3	4.2
Modeling	ldPE		16.0	9.2	12.5	3.0	4.2
Experiment	hdPE	0.108	12	5.6		3	3.2
Modeling	hdPE		12.0	5.6	9.3	3.0	3.2
Experiment	ldPE	0.292	12	5.5		3.2	4.1
Modeling	ldPE		12.0	5.5	8.0	3.2	4.1
Experiment	hdPE	0.292	9.7	3.5		3	3.6
Modeling	hdPE		9.7	3.5	6.3	3.0	3.6



Both reactions have been added to the CLM. The resulting mechanistic scheme leads to a new SED:

$$\frac{d[P^\circ]}{dt} = r_i + 2k_{1u}[POOH] + k_{1b}[POOH]^2 - k_2[O_2][P^\circ] + k_3[PH][PO_2^\circ] - 2k_4[P^\circ]^2 - k_5[P^\circ][PO_2^\circ] + 2k_{63}[PO^\circ \text{ } ^\circ OP]_{\text{cage}} \quad (12)$$

$$\frac{d[PO_2^\circ]}{dt} = k_{1b}[POOH]^2 + k_2[O_2][P^\circ] - k_3[PH][PO_2^\circ] - k_5[P^\circ][PO_2^\circ] - 2k_{60}[PO_2^\circ]^2 \quad (13)$$

$$\frac{d[POOH]}{dt} = -k_{1u}[POOH] - k_{1b}[POOH]^2 + k_3[PH][PO_2^\circ] + (1 - \gamma_5)k_5[P^\circ][PO_2^\circ] \quad (14)$$

$$\frac{d[PO^\circ \text{ } ^\circ OP]_{\text{cage}}}{dt} = k_{60}[PO_2^\circ]^2 - (k_{61} + k_{62} + k_{63})[PO^\circ \text{ } ^\circ OP]_{\text{cage}} \quad (15)$$

Initial conditions are: at  $t = 0$ ,  $[P^\circ] = [PO_2^\circ] = [PO^\circ \text{ } ^\circ OP]_{\text{cage}} = 0$  and  $[POOH] = [POOH]_0$ .

In the case of thick samples (typically few mm thick), oxidation is restricted to superficial layers. As a result,  $O_2$  concentration in an elementary sublayer, located at a depth  $x$  beneath the sample surface, is all the more so small since this sublayer is deeper. The spatial distribution (in the sample thickness) of  $O_2$  concentration has been predicted from a balance equation expressing that  $[O_2]$  variation in an elementary sublayer is equal to the  $O_2$  supply by diffusion (predicted by the classical Fick's second law) minus its consumption by the chemical reaction:

$$\frac{d[O_2]}{dt} = D_{O_2} \frac{\partial^2 [O_2]}{\partial x^2} - k_2[O_2][P^\circ] + k_{60}[PO_2^\circ]^2 \quad (16)$$

where  $D_{O_2}$  is the coefficient of  $O_2$  diffusion into the polymer. In the superficial elementary layer (at  $x = 0$  and  $L$ ), the boundary conditions are given, at any time, by equation 4.

The numerical resolution of the new SED composed of equations 12–16 gives access to the spatial distribution (in the sample thickness) of concentrations of the reactive species and their changes (against time):  $[O_2]$ ,  $[P^\circ]$ ,  $[PO_2^\circ]$ ,  $[POOH]$  and  $[PO^\circ \text{ } ^\circ OP]_{\text{cage}} = f(x, t)$ .

The local  $O_2$  absorption has been calculated for PE at different temperatures and  $\gamma$  dose rates in atmospheric air from equation 16, with the parameter values

reported in Table III, and compared to literature data (13, 15). In some cases, from the spatial distribution of  $Q_{O_2}$  along  $x$ , a thickness of oxidized layer TOL has been determined according to an arbitrary criterion, as schematized in Figure 6. Good agreement has been obtained between theory and experiment in the case of both pure thermal oxidation, for instance at  $100^\circ\text{C}$  (Figure 7), and radio-thermal oxidation at ambient temperature in a large dose rate range (typically between  $10^{-10}$  and  $10 \text{ Gy}\cdot\text{s}^{-1}$ ) (Figure 8). In the case of radio-thermal oxidation, the model describes, without the use of additional assumptions, the negative curvature observed at intermediary dose rates and the horizontal asymptote reached when the dose rate tends towards natural radioactivity value ( $1.5 \cdot 10^{-10} \text{ Gy}\cdot\text{s}^{-1}$ ).

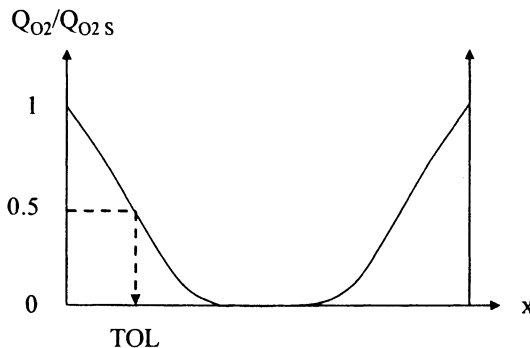


Figure 6. Typical shape of normalized oxidation profiles into thick PE samples (typically few mm thick). Determination of the thickness of oxidized layer using an arbitrary criterion.

The negative curvature is due to the fact that:

- Pure radio-oxidation predominates at high dose rates (typically higher than about  $0.5 \text{ Gy}\cdot\text{s}^{-1}$ ) and is characterized by a TOL quasi-proportional to the reciprocal dose rate.
- Pure thermal oxidation predominates at very low dose rates (typically lower than about  $10^{-7} \text{ Gy}\cdot\text{s}^{-1}$ ) and is characterized by a large TOL, typically 6 mm.
- At intermediate dose rates, no one initiation process can be neglected relative to the other one. The model covers all of these domains.

#### Layer 4: Lifetime Prediction

Finally, we have tried to use the model to predict the lifetime of relatively thin PE samples (typically lower than 1 mm thick) (15). As a first approach, the lifetime  $t_F$  has been determined starting from 2 assumptions:

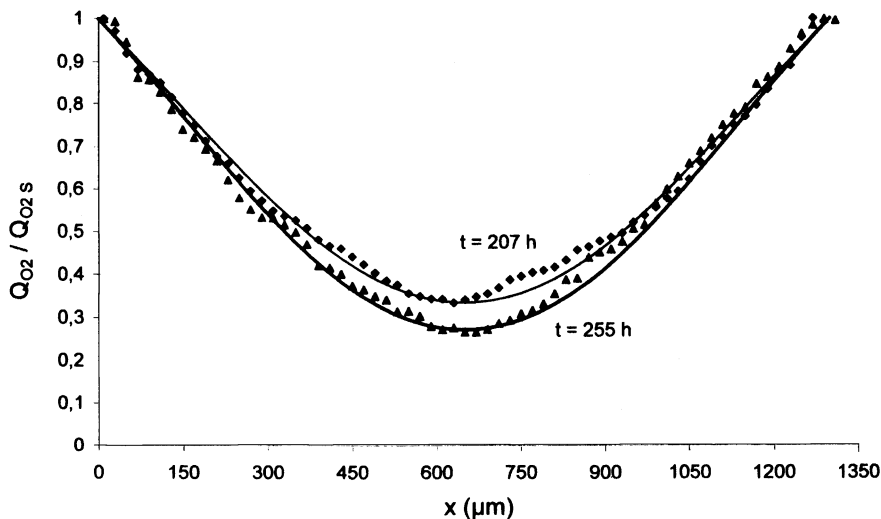


Figure 7. Spatial distribution of oxidation products for PE after 207 and 255 hours of exposure at 100°C in atmospheric air. Points: Experimental carbonyl profiles determined by microspectrophotometry. Continuous line: kinetic model based on equations 12–16.

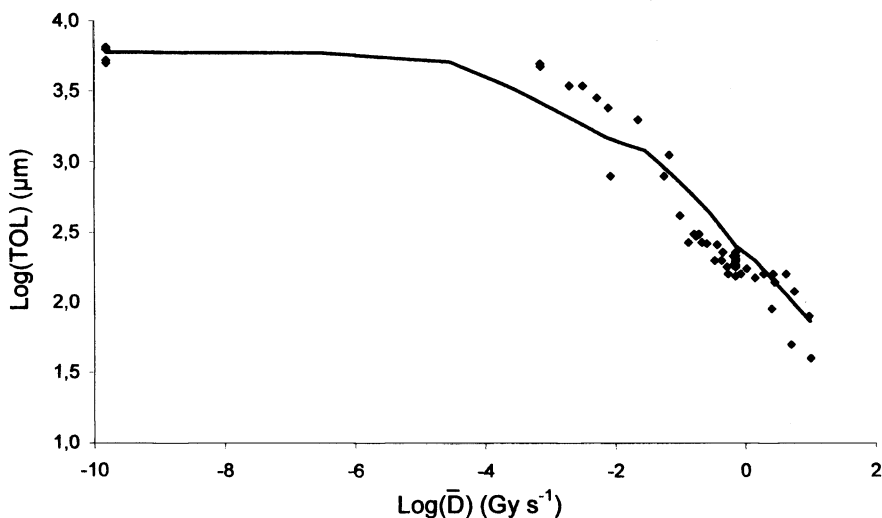


Figure 8. Plot in logarithmic co-ordinates of the thickness of oxidized layer for PE at room temperature in atmospheric air versus  $\gamma$  dose rate. Points: Literature experimental data. Continuous line: kinetic model based on equations 12–16.

1. First, it has been considered that embrittlement occurs when the endlife criterion is reached in the superficial elementary layer. For polymers predominantly undergoing chain scission during their oxidation, embrittlement corresponds to a critical number of chain scissions  $s_F$  (16). But, for polymers undergoing both chain scission and crosslinking, such as PE, the problem remains totally open.
2. Then, since, at the end of the induction period,  $[POOH]$  is sufficiently close to its steady state value  $[POOH]_\infty$  obtained in the case of pure thermal oxidation, oxidation accelerates sharply and the end life criterion is rapidly reached. As a result, it has been considered that embrittlement occurs for a critical hydroperoxyde concentration  $[POOH]_F$  such as:

$$[POOH]_F = \frac{[POOH]_\infty}{q} \quad (17)$$

corresponding to the onset of rapid autoacceleration,  $q$  being an arbitrary number, higher than unity but not by very much (typically  $q \approx 13$ ).

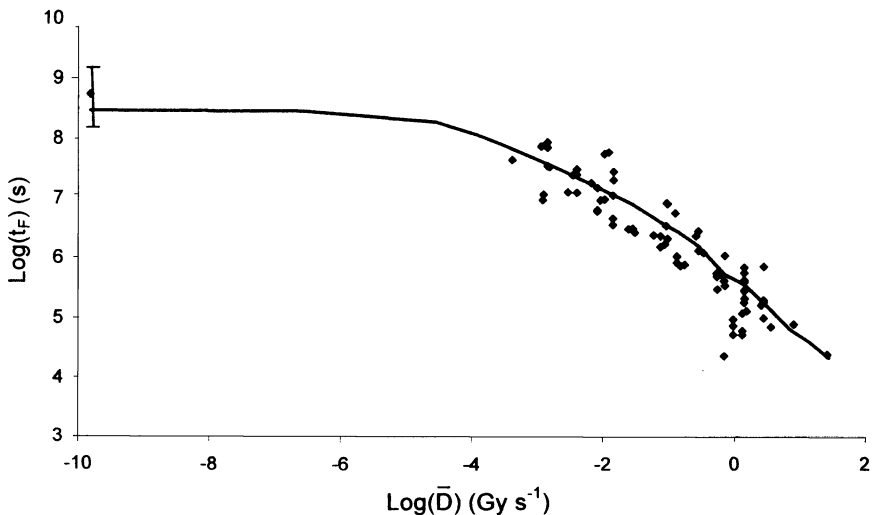


Figure 9. Plot in logarithmic co-ordinates of the lifetime for PE at room temperature in atmospheric air versus  $\gamma$  dose rate. Points: Literature experimental data. Continuous line: kinetic model based on equations 12–16 plus assumptions 1 and 2.

Here also, a good agreement has been obtained between theory and experiment (Figure 9). The model describes the negative curvature observed at intermediate dose rates and the horizontal asymptote reached when the dose rate tends towards natural radioactivity value. The corresponding ceiling lifetime is about 18.5 years.

## Conclusions

A non-empirical kinetic model was developed for the lifetime prediction of polymer parts in their normal use conditions. This model gives access to the spatial distribution (in the sample thickness) of the structural changes at the different scales and the resulting changes of normal use properties. Its efficiency was demonstrated for many substrates in large temperature and dose rate ranges. Here, we have paid special attention to PE radio-thermal oxidation.

Its main advantage is to be based on experimentally checkable physico-chemical parameters strictly obeying Arrhenius' law. These parameters can now be used for extrapolation. The next stage will introduce the stabilization reactions and the stabilizer transport phenomena into the kinetic model, and determining the corresponding rate constants and other physical parameters.

## References

1. Achimsky, L.; Audouin, L.; Verdu, J.; Rychly, J.; Matisova-Rychla, L. *Polym. Degrad. Stab.* **1997**, *58*(3), 283.
2. Richaud, E.; Farcas, F.; Fayolle, B.; Audouin, L.; Verdu, J. *Polym. Degrad. Stab.* **2006**, *91*(2), 398.
3. Khelidj, N.; Colin, X.; Audouin, L.; Verdu, J.; Monchy-Leroy, C.; Prunier, V. *Polym. Degrad. Stab.* **2006**, *91*(7), 1593.
4. Khelidj, N.; Colin, X.; Audouin, L.; Verdu, J.; Monchy-Leroy, C.; Prunier, V. *Polym. Degrad. Stab.* **2006**, *91*(7), 1598.
5. Assadi, R.; Colin, X.; Verdu, J. *Polymer* **2004**, *45*(13), 4403.
6. Colin, X.; Audouin, L.; Verdu, J. *Polym. Degrad. Stab.* **2007**, *92*(5), 886.
7. Colin, X.; Audouin, L.; Verdu, J. *Polym. Degrad. Stab.* **2007**, *92*(5), 898.
8. Coquillat, M.; Verdu, J.; Colin, X.; Audouin, L.; Nevière, R. *Polym. Degrad. Stab.* **2007**, *92*(7), 1334.
9. Coquillat, M.; Verdu, J.; Colin, X.; Audouin, L.; Nevière, R. *Polym. Degrad. Stab.* **2007**, *92*(7), 1343.
10. Colin, X.; Marais, C.; Verdu, J. *Polym. Degrad. Stab.* **2002**, *78*(3), 545.
11. Colin, X.; Verdu, J. *Comp. Sci. Technol.* **2005**, *65*, 411.

12. Audouin, L.; Achimsky, L.; Verdu, J. *Handbook of Polymer Degradation*, 2<sup>nd</sup> edition; Marcel Dekker Inc.: New-York, 2000; pp. 727.
13. Colin, X.; Audouin, L.; Verdu, J. *Polym. Degrad. Stab.* **2004**, *86*, 309.
14. Decker, C.; Mayo, F. R.; Richardson, H. *J. Polym. Sci.: Polym. Chem. Ed.* **1973**, *11*, 2879.
15. Colin, X.; Khelidj, N.; Monchy-Leroy, C.; Audouin, L.; Verdu, J. *Nucl. Instr. Meth. Phys. Res. B* **2007**, *265*, 251.
16. Fayolle, B.; Audouin, L.; Verdu, J. *Polym. Degrad. Stab.* **2000**, *70*, 333.



## Chapter 12

# Relating Kinetic Models to Embrittlement in Polymer Oxidative Aging

**B. Fayolle, X. Colin, L. Audouin, and J. Verdu**

**CIVIPOL, LIM (UMR 8006), Arts et Métiers Paris Tech 151,  
Boulevard de l'Hôpital, 75013 Paris, France**

A previously described kinetic model for polyethylene radical chain oxidation is tentatively extended to include the conditions relevant to embrittlement behavior in the case of thermal oxidation at 90°C. The important roles of chemi-crystallization and morphology as a follow-up to initial chemical changes are discussed. The philosophy of how chemical reactions will ultimately lead to physical polymer changes apparent in  $M_w$  and lamellar properties, and how these processes could be discussed in terms of advanced modeling strategies is briefly reviewed.

It is well known that thermal oxidation in polyethylene (PE) in the presence of oxygen leads to sudden and deep embrittlement, in which oxidative chain scission plays a key, but perhaps indirect, role. We have developed a kinetic model, derived from a branched radical chain mechanistic scheme, able to predict accurately molecular structural changes (*I*).

To extend this model to the prediction of embrittlement time, one needs first to identify the causal chain leading to embrittlement, second to express mathematical relationships corresponding to the elementary links of the chain, and third to define pertinent end life criteria. According to previous studies (2,3,4), two causal chains are possible in the case under study (Figure 1).

In both schemes, step 1 corresponds to the following question: "in the mechanistic scheme, which elementary reactions give chain scission? What is the relevant scission yield?" Step 2 relates to the following question: "if

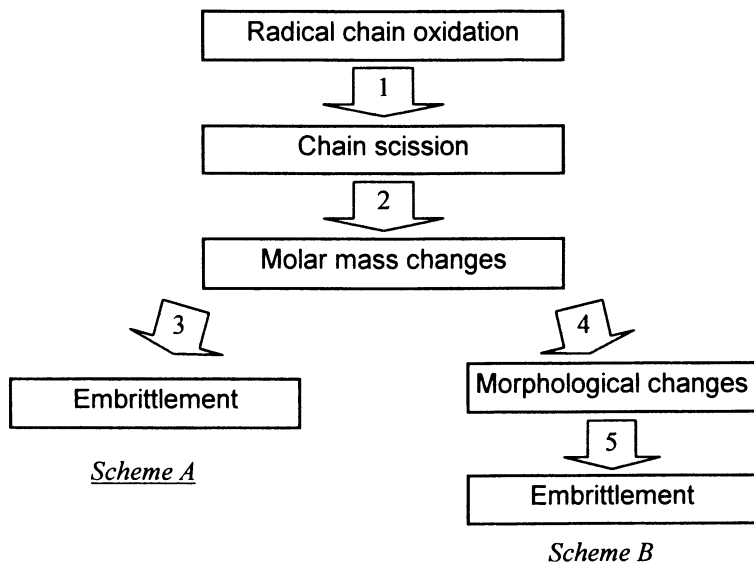


Figure 1. Possible causal chains for oxidation induced embrittlement of PE.

knowing the number of chain scissions, how can then molar mass changes be determined?"

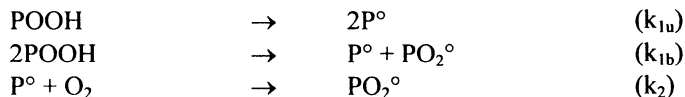
In scheme A, step 3 must combine in principle a fracture property molar mass relationship and a molar mass critical value  $M'_c$  corresponding to the ductile-brittle transition.

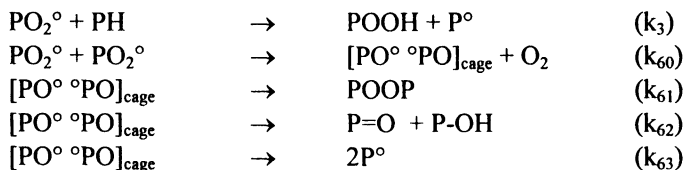
In scheme B, step 4 expresses the relationship between morphological changes induced by chain scission and molar mass, whereas step 5 expresses the influence of morphological changes on fracture properties.

The aim of the present paper is to propose some arguments for the most appropriate description and ways to explore the relationships linking the structural state and the fracture process.

## From Radical Chemistry to Molar Mass Validation

According to previous studies (see Colin et al. in the same Issue), the non-empirical kinetic model for PE thermal oxidation can be based on the following mechanistic scheme including non terminating bimolecular combination.





This mechanistic scheme leads to a system of differential equations expressing the build-up or consumption rate of the reactive species.  $\text{P}^\circ$ ,  $\text{PO}_2^\circ$ ,  $\text{POOH}$ ,  $\text{O}_2$  and  $\text{PH}$  concentrations can be derived from the above mechanistic scheme in which the only adjustable parameter is the initial hydroperoxide concentration. Oxygen diffusion and consumption can be coupled (see Colin et al. in the same Issue) but in the case under study here, the low sample thickness (70  $\mu\text{m}$ ) leads to a quasi uniform oxidation within that thickness.  $\text{POOH}$  build up (5) and oxygen consumption (1) can be measured, allowing us to partially verify this model. Carbonyl build-up can also be simulated by assuming that carbonyls result mainly from rearrangements of  $\text{PO}^\circ$  radicals and by using a new adjustable parameters  $\gamma_2$ , that accounts for the yield of carbonyl build-up in initiation and termination steps of the mechanistic scheme.

$$\frac{d[\text{CO}]}{dt} = \gamma_2 k_{1u} [\text{POOH}] + \gamma_2 k_{1b} [\text{POOH}]^2 + k_{62} [\text{PO}^\circ \text{ } ^\circ\text{OP}]_{\text{cage}} + 2\gamma_2 k_{63} [\text{PO}^\circ \text{ } ^\circ\text{OP}]_{\text{cage}}$$

Figure 2 shows a kinetic curve of carbonyl build-up at 90°C: the data points correspond to experimental measurements exhibiting an induction period close to 300 h. The solid curve corresponds to kinetic model data by using a  $\gamma_2$  value equal to 0.8. This  $\gamma_2$  value has been discussed elsewhere (6). One can observe a good agreement between experimental data and the fit obtained from the model.

One can consider that the kinetics carbonyl build-up is representative of the overall oxidation kinetics, at least when considered at the molecular scale (or monomer unit). It remains to establish a relationship between structural changes at this scale and molar mass changes. For the PE polymer understudy, random chain scission is predominant. It will be assumed that the main scission process is the rearrangement of alkoxy radical ( $\beta$  scission). Then, every elementary reaction generating alkoxy radicals will induce chain scission. In the chosen mechanistic scheme, both hydroperoxide decomposition processes and the non-terminating bimolecular peroxy combination are alkoxy sources. Thus, the number of moles of chain scissions per mass unit (s) is given by:

$$\frac{ds}{dt} = \gamma_1 k_{1u} [\text{POOH}] + \gamma_1 k_{1b} [\text{POOH}]^2 + 2\gamma_1 k_{63} [\text{PO}^\circ \text{ } ^\circ\text{OP}]_{\text{cage}}$$

where  $\gamma_1$  is the yield of chain scission per alkoxy radical ( $\gamma_1 = 0.2$ ).

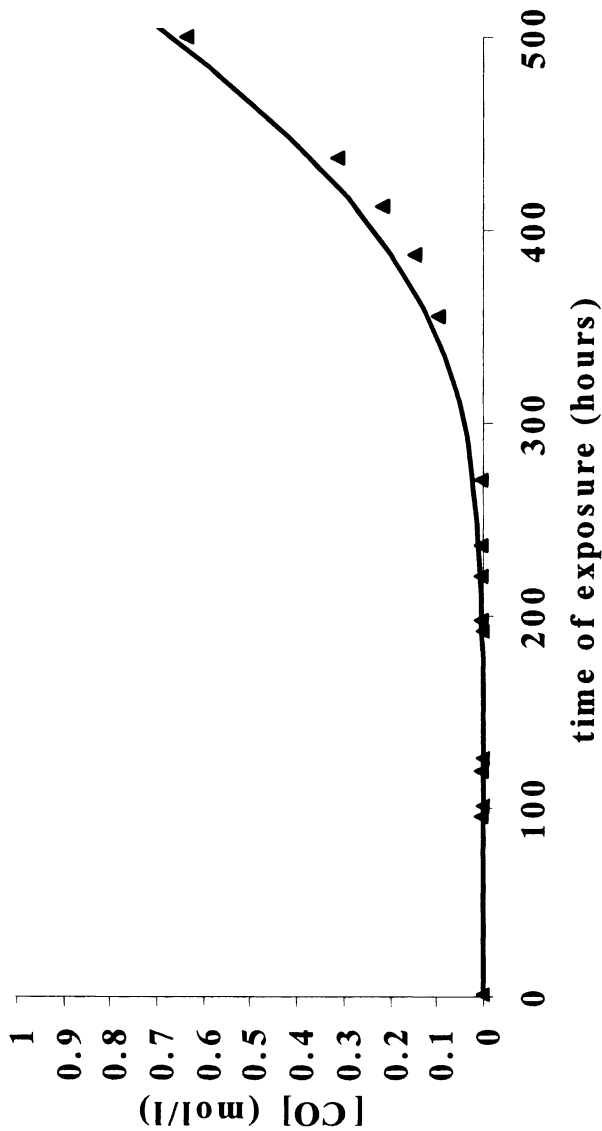


Figure 2. Carbonyl build up at 90°C in air: points correspond to experimental data and solid curve to kinetic model.

Figure 3 shows the number of chain scissions as a function of exposure time of exposure: one can observe a good correlation between experimental data (points) and kinetic data (solid curve).

For a purely random chain scission, it can be written:

$$s = \frac{1}{M_n} - \frac{1}{M_{n0}} \quad \text{and} \quad \frac{s}{2} = \frac{1}{M_w} - \frac{1}{M_{w0}}$$

which leads to: 
$$M_w = M_{w0} \left( 1 + s \frac{M_{w0}}{2} \right)^{-1}$$

By using the above equation,  $M_w$  changes during oxidation can be derived from kinetic data. These changes are illustrated in Fig. 4: A good agreement between data and model is also observed. After an induction period of 300 hours, molar mass decreases sharply although the number of chain scission is low. For instance,  $s \sim 0.1 \text{ mol.kg}^{-1}$  after 500 hours of exposure (Figure 3) leads to a  $M_w$  value close to  $20 \text{ kg.mol}^{-1}$ .

### Using Scheme A: Molar Mass Embrittlement Criterion

If fracture properties are governed by the molar mass (Scheme A in Figure 1), polyethylenes must display a ductile-brittle transition at a critical molar value ( $M'_c$ ) independently of the sample morphology. By assuming that scission events are homogeneously distributed in the amorphous phase, one can assume that a degraded PE sample is equivalent to a virgin PE sample of identical molar mass. Then, a way to establish a possible existence of a critical molar mass is to compile literature data showing simultaneously a pertinent fracture property and the sample average molar mass (5). This compilation led to Fig. 5 where strain at break has been plotted as a function of weight average molar mass. Only data relative to isotropic samples were reported.

The dependence of molar mass on the strain at break can be divided in three different regimes: a brittle regime if  $M_w < 40 \text{ kg.mol}^{-1}$ , a brittle-ductile regime transition for  $40 \text{ kg.mol}^{-1} < M_w < 100 \text{ kg.mol}^{-1}$  and a ductile regime for  $M_w > 100 \text{ kg.mol}^{-1}$ .

Thus, if scheme A is applicable, the embrittlement critical molar mass would be  $70 \pm 30 \text{ kg.mol}^{-1}$ , which would lead according to Fig. 4 to an embrittlement lifetime of about 350 hours versus 300 hours as the experimental value for the PE under study. This difference would be acceptable in practice, but two questions remain:

1. The entanglement molar mass  $M_e$  for PE is  $1.7 \text{ kg.mol}^{-1}$ . The ratio  $M'_c/M_e$  ranges thus between 23 and 59 versus  $\sim 5$  for low crystalline or amorphous polymers. This means that embrittlement occurs while the

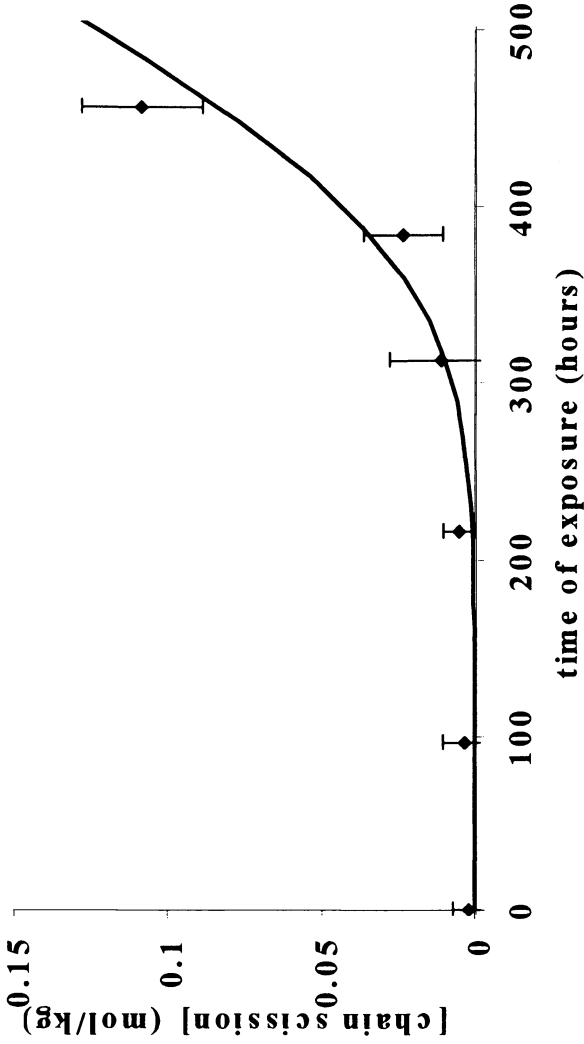


Figure 3. Number of chain scission versus time of exposure: points correspond to experimental data and the solid curve to kinetic model.

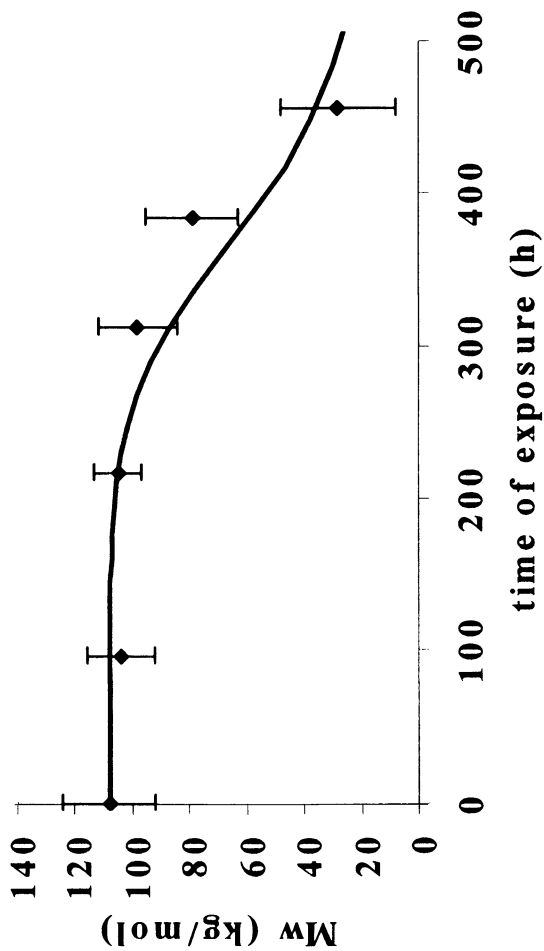


Figure 4. Weight average molar mass ( $M_w$ ) changes against time of exposure: points correspond to experimental data and solid curve to kinetic model.

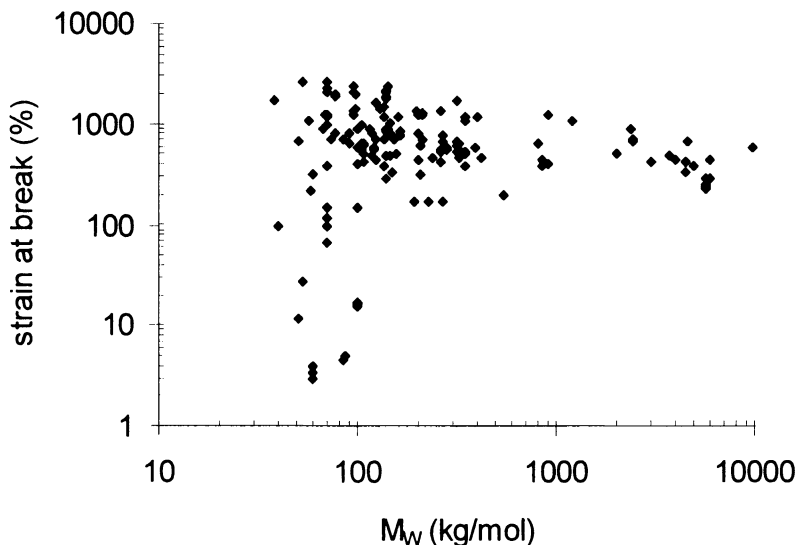


Figure 5. Strain at break as a function of weight average molar mass obtained by synthesis from different authors.

entanglement network has suffered only very little damage. How could this characteristic be explained?

- 2) The width of the ductile-brittle transition ( $40\text{-}100\text{ kg}\cdot\text{mol}^{-1}$ ) is implicitly attributed to data scatter. However, is there a better approach than the scheme A ?

These two issues lead us to examine the hypothesis of scheme B.

### Using Scheme B: A Morphological Embrittlement Criterion

The first condition to validate scheme B is that the degradation must induce really morphological changes. This is the case when degradation occurs at temperatures higher than the glass transition temperature of the amorphous phase. Then, chain scissions liberate chain segments initially trapped in the entanglement network, which allows them to migrate towards lamellae and to integrate within a crystalline phase. This process often called chemi-crystallization has been observed in practically all the semi-crystalline polymers including PE (7-10). Most of the experimental observations concern the increase of crystallinity, but one can reasonably accept that crystallinity increases through lamellae thickening.



The second condition to validate the scheme B is that embrittlement must correspond to a critical morphological state that is the only approach to explain its sudden character. The extensive and careful work of Kennedy et al. (11) on relationships between fracture behavior, molar mass and lamellar morphology, shows that this condition is fulfilled in the case of PE. Comparing various samples of different molar masses with different thermal histories, they found that the thickness of the amorphous layer ( $l_a$ ) separating two adjacent lamellae is the key parameter (Fig. 6). As a matter of fact, there is a critical value  $l_{aC}$  of the order of 6-7 nm. For  $l_a > l_{aC}$  the samples are always ductile whatever their molar mass, whereas for  $l_a < l_{aC}$  the samples are consistently brittle. As a result,  $l_{aC}$  appears to be independent of the molar mass. Indeed, there is a specific molar mass, probably close to  $70 \text{ kg}\cdot\text{mol}^{-1}$  for PE below which crystallization is so fast that it is impossible to have  $l_a$  values higher than  $l_{aC}$  whatever the processing conditions.

Within this framework, one can imagine a two dimensional ductile-brittle transition criterion which would be composed of two perpendicular boundaries in the graph  $l_a$ - $M_w$  (Fig. 7). The vertical boundary would correspond to a critical molar mass  $M'_C$ . In polymers of low crystallinity or fully amorphous,  $M'_C$  would be sharply linked to the entanglement molar mass  $M'_C \sim 5M_e$ . In polymers of medium to high crystallinity,  $M'_C$  would be the molar mass below which it is impossible to have  $l_a$  values higher than  $l_{aC}$ . The horizontal boundary would correspond to  $l_a = l_{aC}$ .

It has been tried to put the result of Kennedy et al (11) in a  $l_a$ - $M_w$  graph (Fig. 7). Two samples families are distinguished quenched samples and slowly crystallized samples. In both families, the ductile-brittle transition occurs at  $l_{aC} = 6 \text{ nm}$ . The corresponding "critical" molar mass defined in scheme A is higher for slowly crystallized samples ( $M'_C \sim 100 \text{ kg}\cdot\text{mol}^{-1}$ ) than for quenched ones ( $M'_C 60 \text{ kg}\cdot\text{mol}^{-1}$ ). This result can be considered as a proof that scheme B is more pertinent than scheme A.

However, in the case of thermal aging where annealing effects are relatively fast, one can expect that all the samples would rapidly tend towards a pseudo equilibrium morphological state. A point trajectory representative of thermal aging would have the shape shown in Fig. 8.

In these graphs (Figs. 7 and 8), the quasi vertical part of the curve would correspond to annealing, the rest would be due to chemicrystallization. In this case, all the trajectories would converge towards an "embrittlement point" not very far from the intersection of both boundaries  $l_{aC}$  and  $M'_C$  and the concept of a critical molar mass (scheme A) would apparently be valid.

## Conclusion

This work discusses non empirical lifetime prediction in the case where embrittlement is due to random chain scission as in the chosen example of PE

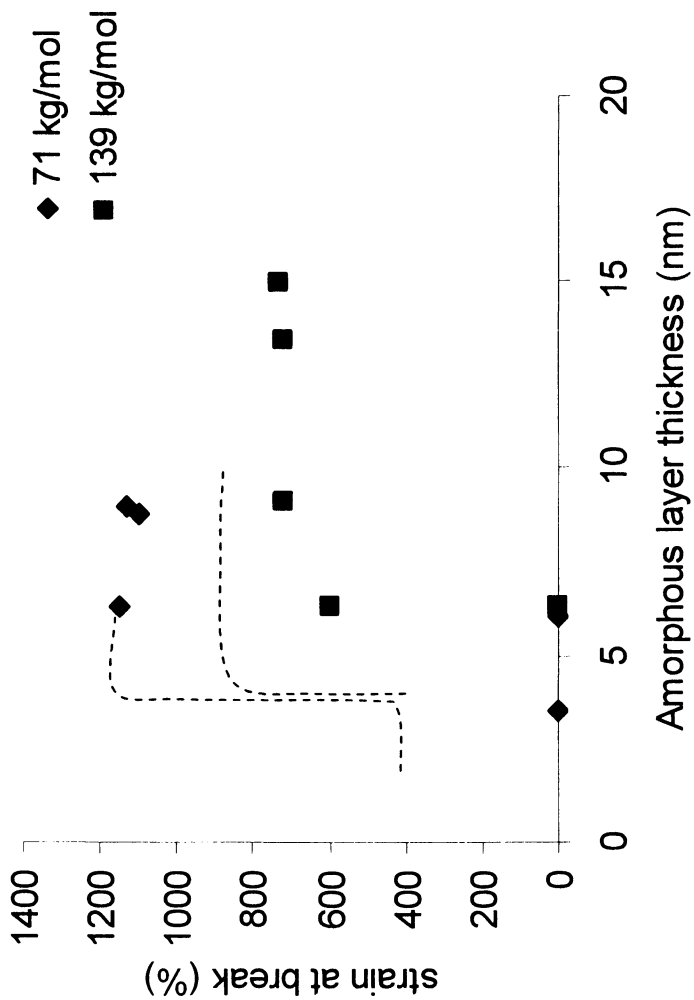


Figure 6. Strain at break as a function of amorphous layer thickness for two PE differing by molar mass ( $M_w$ ).

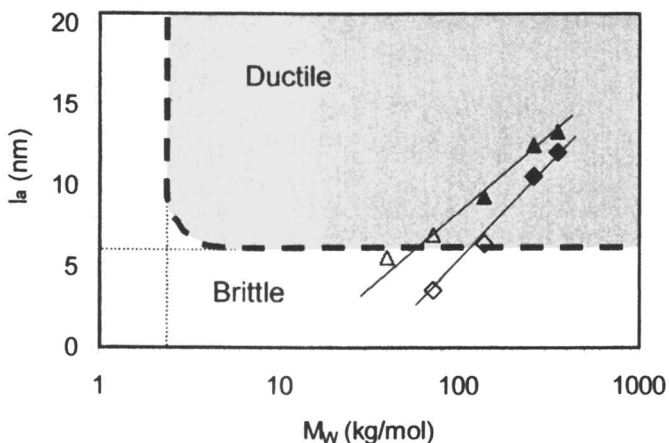


Figure 7. Ductile – brittle transition in a plot of  $l_a$  versus  $M_w$ : quenched ductile samples ( $\blacktriangle$ ) quenched brittle samples ( $\triangle$ ) and slowly crystallized ductile samples ( $\blacklozenge$ ) and slowly crystallized brittle samples ( $\diamond$ ). (Reproduced from reference 11. Copyright 1994 American Chemical Society.)

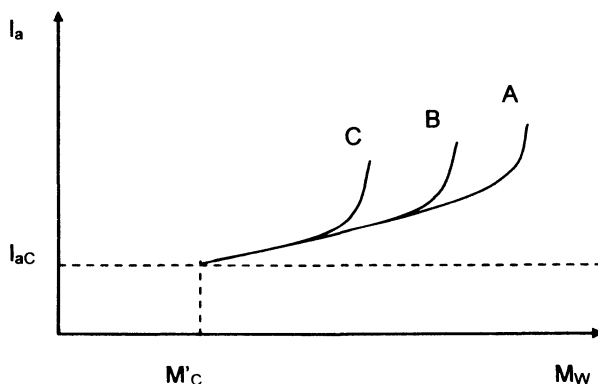


Figure 8. Presumed shape of thermal aging point trajectories in the  $(l_a - M_w)$  graph for three samples A, B and C of different initial molar mass and morphology.

thermal oxidation at 90°C. We propose that kinetic modeling should be based on the following causal chain: radical chain oxidation, chain scission, molar mass changes, morphological changes, and embrittlement (see Fig. 1).

The morphological changes are induced by a chemocrystallization process. They lead to embrittlement when the thickness of the amorphous layer between adjacent lamellae becomes lower than a critical value of the order of 6 nm in PE.

The method to extend the preexisting kinetic model to molar mass prediction was described and the corresponding parameters were determined. The critical  $l_a$  (lamellar thickness) value is already proposed in the literature for PE. A worthwhile remaining goal is development of a quantitative approach towards the coupling of molar mass changes during oxidation with chemocrystallization (see step 4 in Fig.1). This point is under investigation but, for the time being, it is possible to use the simplified scheme in which embrittlement is assumed to occur at a critical molar  $M^*C \sim 70 \text{ kg.mol}^{-1}$  for PE.

## References

1. Colin, X.; Fayolle, B.; Audouin, L.; Verdu J. *Polym. Degrad. Stab.* **2003**, *80*, 67.
2. Fayolle, B.; Audouin, L.; Verdu, J. *Polymer* **2003**, *44*, 2773.
3. Fayolle, B.; Audouin, L.; Verdu, J. *Polymer* **2004**, *45*, 4323.
4. Fayolle, B.; Colin, X.; Audouin, L.; Verdu, J. *Polym. Degrad. Stab.* **2007**, *92*, 231.
5. Richaud, E.; Farcas, F.; Fayolle, B.; Audouin, L.; Verdu, J. *Polym. Degrad. Stab.* **2007**, *92*, 118.
6. Kehldj, N.; Colin, X.; Audouin, L.; Verdu, J.; Monchy-Leroy, C.; Prunier, V. *Polym. Degrad. Stab.* **2006**, *91*, 1598.
7. Mathur, A. B.; Mathur, G. N. *Polymer* **1982**, *23*, 54.
8. Yue, C. Y.; Msuya, W. F. *J. Mater. Sci. Lett.* **1990**, *9*, 985.
9. Viebke, J.; Elble, E.; Ifwarson, M.; Gedde, U. W. *Polym. Eng. Sci.* **1994**, *34*, 1354.
10. Dudic, D.; Kostoski, D.; Djokovic, V.; Stojanovic, Z. *Polym. Degrad. Stab.* **2000**, *67*, 233.
11. Kennedy, M. A.; Peacock, A. J.; Mandelkern, L. *Macromolecules* **1994**, *27*, 5297.

## Chapter 13

# Fourier Transfer Infrared Measurement of CO<sub>2</sub> Photogeneration from Polyethylene, Polypropylene, and Polyesters

Paul A. Christensen, Terry A. Egerton<sup>\*</sup>, Sudesh S. Fernando,  
and Jim R. White

School of Chemical Engineering and Advanced Materials, Newcastle  
University, Newcastle upon Tyne NE1 7RU, United Kingdom

Fourier Transform Infra-Red (FTIR) measurements of the rate of carbon dioxide production during UV irradiation of pigmented and unpigmented polyethylene (PE) and polypropylene (PP) have been made. Experiments were conducted in wet oxygen and in dry oxygen. Evidence for an induction time was found with PP but not with PE. Inclusion of anatase caused a significant increase in CO<sub>2</sub> generation from both polymers. CO<sub>2</sub> generation from PE containing a lightly-coated rutile was intermediate between that for unpigmented PE and anatase-pigmented PE. A similar result was obtained with PP in dry oxygen but in wet oxygen the CO<sub>2</sub> generation rate for rutile-pigmented PP was similar to that for unpigmented PP. The same procedure was shown to be applicable to the study of poly(ethylene terephthalate) (PET) photo-oxidation.

Most procedures used to characterize the photodegradation of polymers involve long exposure times. A method that reduces the time required to assess the sensitivity of polymers to photo-oxidation has been introduced recently and applied in studies of polyethylene (PE) (1) and poly(vinyl chloride) (PVC) (2). The technique is based on the measurement of carbon dioxide generated *in-situ* in a closed cell during UV exposure. The photo-generated CO<sub>2</sub> is measured using continuous Fourier Transform Infra-Red (FTIR) monitoring of the gaseous phase in the cell (1,2). A typical run lasts about 5 hours, two orders of magnitude less than the time required for tests for the progress of oxidation in which the development of the carbonyl group is checked periodically.

The first experiments using this method were designed to determine the effect of TiO<sub>2</sub> pigments on photo-oxidation of PE and showed that the PE films containing the anatase form of TiO<sub>2</sub> gave the most rapid CO<sub>2</sub> generation (1). Anatase is a powerful photo-catalyst and this result was not unexpected. Rutile pigment can accelerate photo-oxidation or can provide some protection against it, according to the coating provided during manufacture, and the *in-situ* experiments on the series of PE films identified examples of both. The CO<sub>2</sub> results correlated well both with carbonyl-development measurements (1) and with practical experience of the pigment performance.

In experiments on PE films the UV was switched off after 3 hours exposure and CO<sub>2</sub> was monitored for a further hour afterwards. With PE, CO<sub>2</sub> emission ceased as soon as the UV was switched off (1). This was not so with all polymers; with PVC CO<sub>2</sub> emission continued for an extended period after irradiation ceased (2). Therefore, the *in-situ* method offers not just rapid assessment of the photo-oxidation sensitivity of polymer compounds but also the prospect of studying some of the finer details of the reaction mechanism. In the research described here one objective was to compare the photo-oxidation characteristics of polypropylene (PP) with those of PE. The work will be presented more fully in a forthcoming paper (3). A second objective was to conduct a preliminary study of the photo-oxidation of poly(ethylene terephthalate) (PET). In PET carbonyl groups are present as esters in the polymer chain and may be degraded by direct photochemical reaction (4). This makes it impractical to follow the progress of oxidation by monitoring the build up of carbonyl groups, and monitoring CO<sub>2</sub> emission seemed to offer an alternative method. PET samples with different processing history were used because an earlier study on PE samples showed that molecular orientation can influence photodegradation (5).

## Experimental

### Materials

PE and PP blown lay-flat tubes with wall thickness *ca.* 100 μm were provided by Huntsman Pigments (Calais, France) unpigmented and pigmented

with  $\text{TiO}_2$ . The results reported here concern one anatase grade and one rutile  $\text{TiO}_2$ . Both the anatase and rutile films had a pigment loading of 5 phr (parts per hundred resin). Unpigmented polyester films were provided by DuPont Teijin Films (Wilton, UK) in three forms: as-cast (PETc), uniaxially longitudinally drawn (PETu), and biaxially drawn (PETb). Drawing reduced film thickness from 540  $\mu\text{m}$  (PETc) to 150  $\mu\text{m}$  (PETu) to 80  $\mu\text{m}$  (PETb).

## CO<sub>2</sub> Monitoring

Samples in the form of ~11 mm diameter discs were held by a magnetisable ring against a magnetic plate sealed to the end of a ground glass cone. The cone fitted into a purpose built glass cell (Figure 1) opposite a  $\text{CaF}_2$  window onto which UV was channeled by a light guide. The UV source was a high pressure 150 W xenon lamp (Oriol ~300-800 nm) fitted with a 100 mm water filter and, in the experiments reported here, an AM0 filter to remove wavelengths < 290 nm.

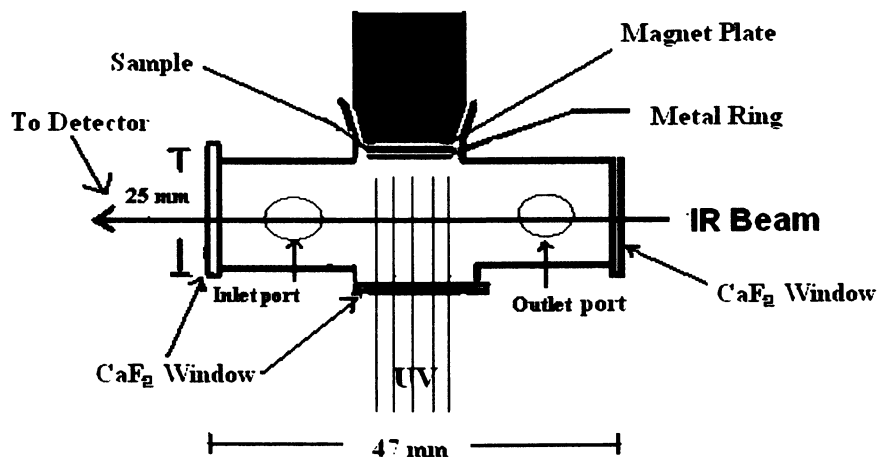


Figure 1. Purpose built cell. The polymer sample is held opposite a UV transmitting window, and the photogenerated  $\text{CO}_2$  is monitored by an IR beam.

After the sample was inserted, the cell was flushed for an hour with the selected gas. In the tests reported here, this was either dry oxygen (direct from the cylinder) or 'wet' oxygen (cylinder oxygen bubbled through water). The cell was then sealed and placed in the sample compartment of a nitrogen-purged Bio-Rad FTS-60 FTIR spectrometer fitted with a liquid nitrogen-cooled MCT detector. Any increase of carbon dioxide was monitored using the  $2360\text{ cm}^{-1}$  absorption (100 scans,  $4\text{ cm}^{-1}$  resolution) over a period of one hour in the absence

of UV. The UV was then switched on and the resulting growth of the  $2360\text{ cm}^{-1}$  band was monitored for 3 hours. Irradiation was then stopped but the gas phase was monitored for a further hour. In the absence of a polymer sample the  $\text{CO}_2$  signal after 3 hours exposure was  $\sim 8 \times 10^{-4}$  a.u. with wet  $\text{O}_2$  and negligible with dry  $\text{O}_2$ . Further practical details are given elsewhere (1,2,6).

### Carbonyl Group Development Monitoring

Disc shaped samples similar to those used in the  $\text{CO}_2$  equipment were exposed to irradiation by UVA-340 tubes in a QUV Accelerated Weathering unit (Q-Panel Company). A constant temperature of  $40^\circ\text{C}$  was used. The samples were removed from the exposure chamber periodically to record FTIR transmission spectra in the  $1700\text{-}1800\text{ cm}^{-1}$  region.

## Results

### Photogeneration of $\text{CO}_2$ from Polyethylene (PE) and Polypropylene (PP)

Figure 2 shows  $\text{CO}_2$  evolution for differently pigmented PE (a) and PP (b) during UV exposure in wet  $\text{O}_2$ . Duplicate runs showed excellent repeatability. After 3 hours irradiation, the absorbance of photo-generated  $\text{CO}_2$  from unpigmented PP was  $\sim 120 \times 10^{-4}$  a.u., double that for unpigmented PE. For both polymers the anatase pigmented film was the most photoactive. For PE, rutile pigmented film was more photo-active than the unpigmented sample, whereas for PP, the photoactivity of the rutile pigmented film was similar to that of unpigmented PP. A comparison of the results for both unpigmented PP and rutile-pigmented PP with corresponding results for PE suggests that photogeneration of  $\text{CO}_2$  in the first hour of UV exposure was much slower for PP, suggesting a possible induction phenomenon. This is confirmed by Figure 3, which also shows that no induction time was present for PE.

Comparison of the results in Figures 4 and 2b demonstrates that for PP, photogeneration of  $\text{CO}_2$  was much less in dry than in wet oxygen, as found earlier with PE (1,6). The relative photoactivities also depended on oxygen humidity. In dry oxygen, the photoactivity of rutile-pigmented PP was much higher than that of unpigmented PP, even though their photoactivities in wet oxygen were similar.

### Carbonyl Group Development in PE and PP

A typical sequence of spectra, for unpigmented poly(propylene), is shown in Figure 5. The initial spectrum had a maximum at  $1713\text{ cm}^{-1}$ . At increasing



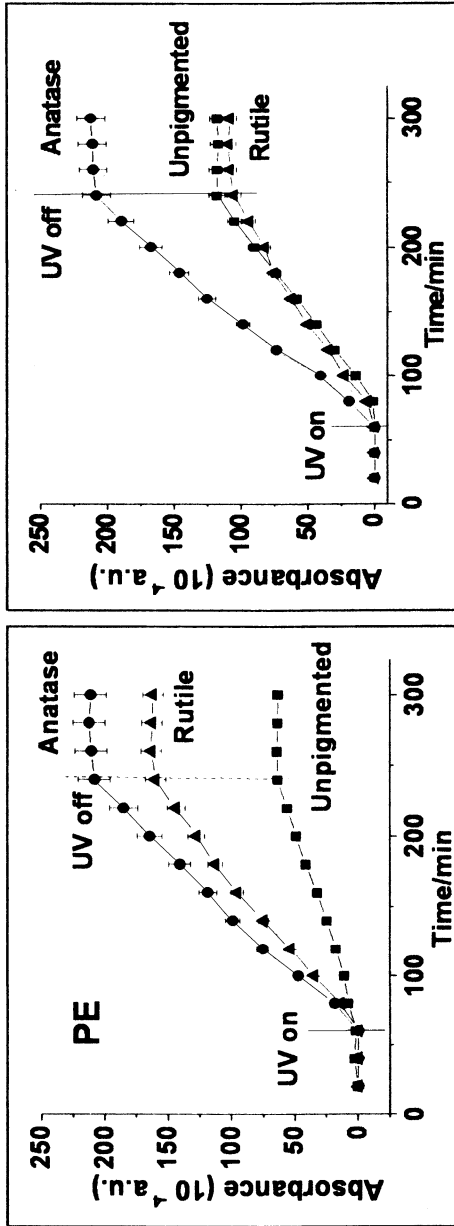


Figure 2. CO<sub>2</sub> emission from (a) PE and (b) PP during 180 min UV exposure in wet O<sub>2</sub>. Films contained anatase(●) or rutile(▲) or were unpigmented(■).

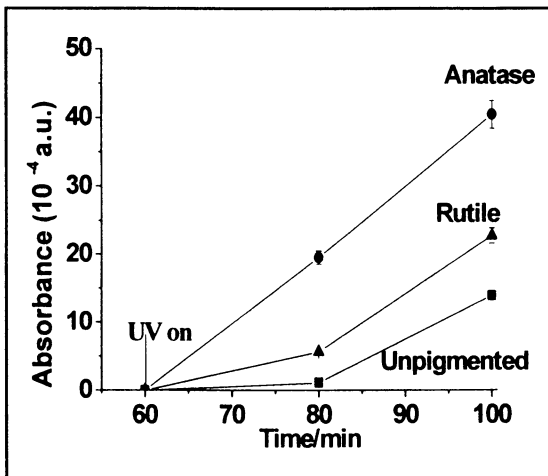


Figure 3. Extract from Figure 2(b), re-scaled.

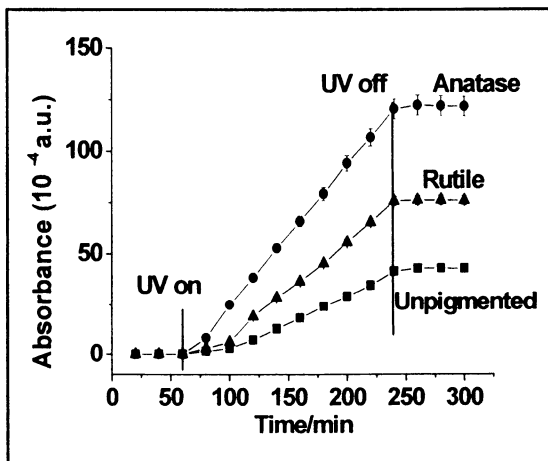


Figure 4. Photogeneration of CO<sub>2</sub> from PP in dry O<sub>2</sub>. Symbols as Figure 2.

exposure times, shoulders developed near 1730 and 1770  $\text{cm}^{-1}$  and for exposure times above 1000 hours the absorption appeared to broaden and decrease in peak intensity. Similar spectra were obtained for PE, though with less broadening by high frequency shoulders. Thus, the 1713  $\text{cm}^{-1}$  absorbance of anatase-pigmented PE began to fall after  $\sim 900$  hours exposure. (The film started to crack at about the same time. It has not been established whether or not this is a coincidence.) Delprat *et al* used  $\text{SF}_4$  and  $\text{NH}_3$  derivitization experiments to assign the 1713  $\text{cm}^{-1}$  absorption to ketones, aldehydes or  $\alpha$ -methylated carboxylic acid, the 1732  $\text{cm}^{-1}$  to esters, and the  $\sim 1770$   $\text{cm}^{-1}$  to peresters or lactones (7). Lacoste and Carlsson had made similar assignments (8). As the overlapping absorptions have not been resolved, and since the extinction coefficients may vary by a factor of three from band to band (8), no attempt to quantify these different contributions was made. Instead, as the spectra of both PP and PE up to  $\sim 700$  hours are dominated by the 1713  $\text{cm}^{-1}$  absorption, the photogenerated  $\text{CO}_2$  has been compared with the carbonyl absorption at 1713  $\text{cm}^{-1}$ , without allowing for any formation of new species which may be indicated by the development of the high energy shoulders. The 1713  $\text{cm}^{-1}$  absorbance at increasing irradiation time is plotted in Figure 6a for PE and Figure 6b for PP.

For exposures less than  $\sim 700$  hours, the photoactivity ranking of the three PE films was the same as that given by the  $\text{CO}_2$  method. The absorbance curves for unpigmented PE and the rutile-pigmented PE are concave upwards,

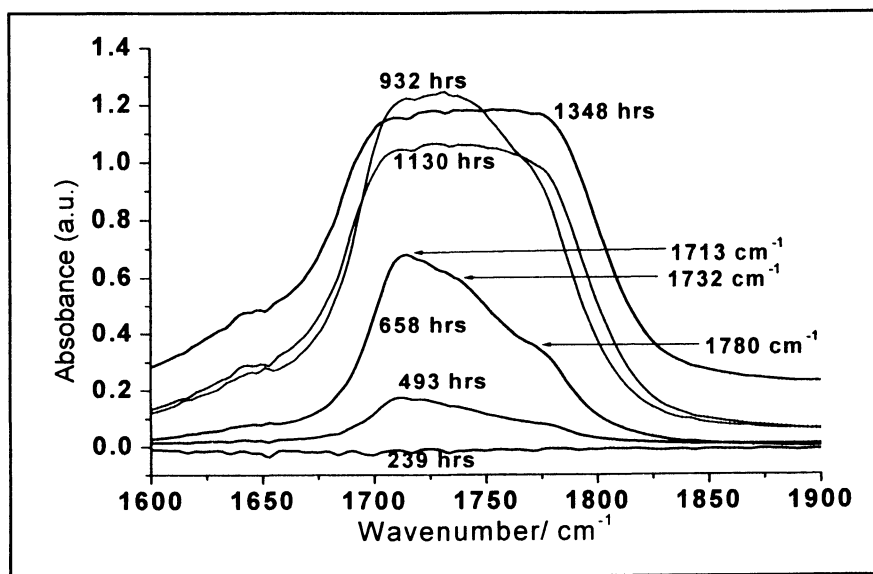


Figure 5. Infrared transmission spectra of unpigmented poly(propylene) exposed in QUV equipment for the number of hours indicated.

indicating auto-acceleration; the true effect is greater than it appears from Figure 5(a) because the underestimation of the total oxidation provided by the  $1713\text{ cm}^{-1}$  absorption becomes progressively worse as time advances. Results for PP are given in Figure 6(b), with the same reservation concerning the suitability of the absorbance at  $1713\text{ cm}^{-1}$  to represent oxidation as outlined above for PE. Unpigmented PP showed a long induction time (>200 hours) under UVA-340 illumination but then showed strong auto-acceleration. Cracking appeared after ~800 hours exposure and the slope of the absorbance curve for  $1713\text{ cm}^{-1}$  reversed soon afterwards, a similar observation to that for anatase-pigmented PE. The anatase-pigmented sample showed the highest rate of increase in absorbance in the early stages (< 500 hours exposure). The unpigmented PP absorbance at  $1713\text{ cm}^{-1}$  overtook that for the anatase pigmented sample after ~ 650 hours exposure.

### Photogeneration of CO<sub>2</sub> from Poly(ethylene terephthalate) (PET)

Figure 7 shows CO<sub>2</sub> evolution from the PET films with different thermo-mechanical histories and consequent differences in film thickness, crystallinity and molecular orientation (9). In all three cases strong CO<sub>2</sub> generation was observed and could be measured with good repeatability. Similar measurements have been made on poly( $\epsilon$ -caprolactone) (PCL) and on PCL/PVC blends (10). These measurements on different polyesters demonstrate the applicability of the CO<sub>2</sub> method to materials for which carbonyl absorption measurement is not very suitable.

## Discussion

### Correlation Between CO<sub>2</sub> Generation and Carbonyl Group Development

A primary concern of the studies presented here was the effect of the TiO<sub>2</sub> pigments on the photosensitivity of polyalkene films. In an earlier paper (1) a good correlation between the photogeneration of CO<sub>2</sub> and of carbonyl groups was demonstrated for a set of 10 PE films pigmented with a variety of rutile pigments with different surface coatings and photoactivities.

Casual inspection of Figures 2 and 6 indicates that both the CO<sub>2</sub> photogeneration and the conventional carbonyl development methods show that PP is more photoactive than PE. Also, CO<sub>2</sub> photogeneration and carbonyl development both show the high photoactivity of anatase pigmented films of both PE and PP.

To assist this comparison Figure 8 compares the CO<sub>2</sub> absorbance after 3 hours UV exposure with the  $1713\text{ cm}^{-1}$  absorbance after 658 hours UVA-340 illumination. 658 hours (~ 4 weeks) was chosen because at this time the  $1713\text{ cm}^{-1}$  absorption is still the major contribution to all the carbonyl absorptions.

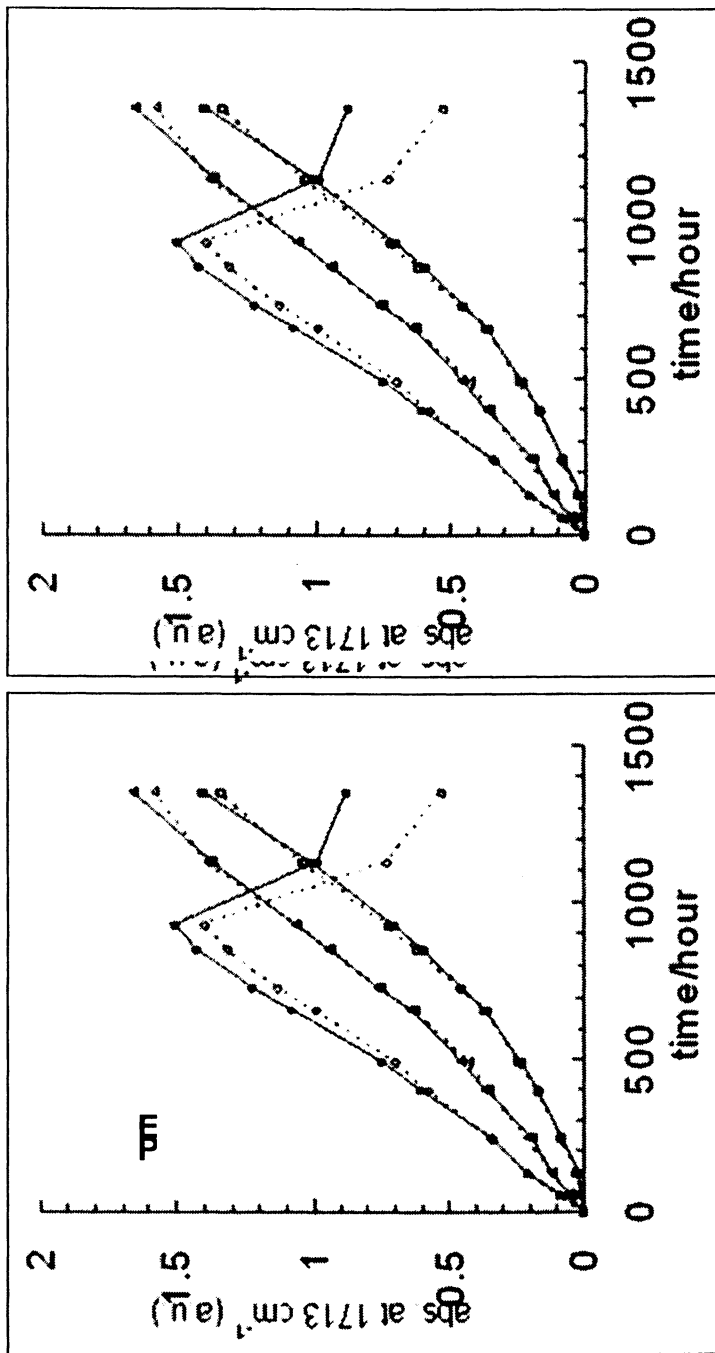


Figure 6. Absorbance at 1713 cm<sup>-1</sup> during UV illumination: (a) PE; (b) PP. Films contained anatase (○) or rutile(●) or were unpigmented(—).

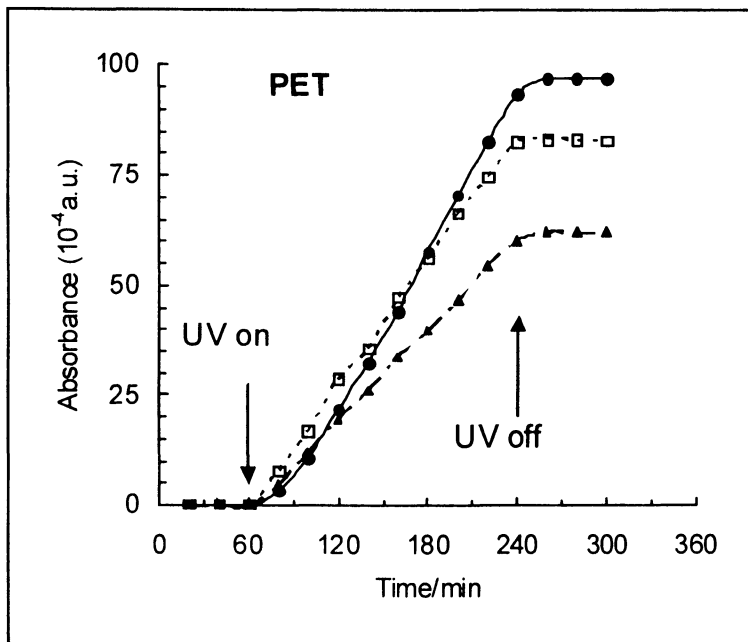


Figure 7.  $\text{CO}_2$  photogeneration from PET. ▲ as-cast; □ uniaxially drawn; ● biaxially drawn.

The overall correlation is seen to be fairly good. The results for PE lie quite close to the trend line (shown simply for guidance). The results for PP, though more displaced from the same trend line, are fairly evenly distributed about it.

### Mechanistic Implications of $\text{CO}_2$ Generation from Polyalkene Films

A second concern of this paper has been to show the sensitivity of the  $\text{CO}_2$  method and its convenience for controlling the conditions in degradation experiments and consequently demonstrate its potential for the study of degradation mechanism. The sensitivity has been demonstrated by the ability to compare the very early stages of PE and PP oxidation. Under both wet and dry UV exposure unpigmented PP films showed a clear induction period for  $\text{CO}_2$  generation, imitating the induction phenomenon observed under QUV exposure (c.f. Figures 2-4, 6). The  $\text{CO}_2$  method showed the presence of an induction phenomenon over a test period of the order of one hour, very much quicker than the observation period required with traditional QUV testing. (Note that it is necessary not only to record a negligible reaction rate at the start of the exposure but also to observe clearly a high subsequent rate of reaction to positively

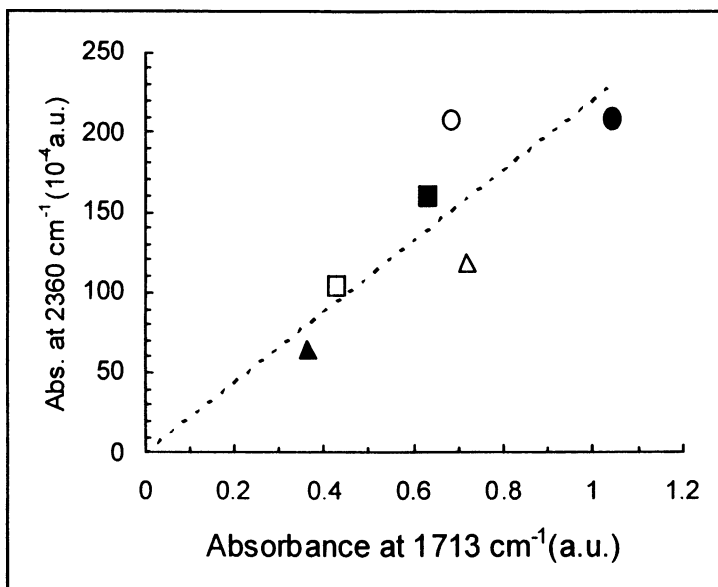


Figure 8.  $\text{CO}_2$  absorbance after 3 hours UV exposure versus  $1713 \text{ cm}^{-1}$  absorbance after 658 hours UVA-340 illumination for PE (solid symbols) and PP films (open symbols). ▲, △ unpigmented; ■, □ rutile pigmented; ●, ○ anatase pigmented.

identify induction). The delay in the start of significant carbonyl group development and carbon dioxide emission during oxidation of PP is attributed to the importance of hydroperoxide formation by intermolecular hydrogen atom abstraction in the initial stages of PP, but not PE, oxidation.

The  $\text{CO}_2$  method has also demonstrated the sensitivity of polyalkene photo-oxidation to the humidity of the oxygen environment. Previously, the effect of water has been attributed to factors such as dissolution and removal of reaction products by liquid water. This cannot be the case in the present experiments.

The authors are unaware of previous reports of this effect of increasing humidity, even though it changes the relative rankings of different polymers.

### Polyester Studies

The results of Figure 7 demonstrate that  $\text{CO}_2$  evolution from polyester films can also be measured and offers a convenient way of monitoring the photodegradation of polymers such as polylactones which are of increasing interest because of their biodegradability. However, unlike polyalkenes,

polyesters have significant intrinsic absorption of solar UV. Some polyesters (e.g. PET) are also relatively impermeable even to small molecules. such as CO<sub>2</sub>. Both factors must be considered when interpreting photogeneration of CO<sub>2</sub> from such systems.

## Conclusions

FTIR measurement of photogenerated CO<sub>2</sub> gives rapid analysis of the photosensitivity of PE, PP and PET. The induction phenomenon was observed clearly in PP in a short test period and contrasted with the behavior of PE. The influence of TiO<sub>2</sub> additives was shown, with anatase causing greatly increased photosensitivity in both PE and PP. The method provides a convenient way to test the influence of different atmospheres on photodegradation, and strong acceleration was shown to be produced by high humidity. Tests with PET confirmed that the method has great potential for studying photodegradation of polyesters.

## References

1. Jin, C.; Christensen, P. A.; Lawson, E. J.; Egerton, T. A.; White, J. R. *Polym. Degrad. Stab.* **2006**, *91*, 1086.
2. Jin, C.; Christensen, P. A.; Egerton, T. A.; White, J. R. *Mater. Sci. Technol.* **2006**, *22*, 908.
3. Fernando, S. S.; Christensen, P. A.; Egerton, T. A.; White, J. R. *Polym. Degrad. Stab.* **2007**, *92*, 2163.
4. Rivaton, A. *Polym. Degrad. Stab.* **1991**, *41*, 283.
5. Jin, C.; Christensen, P. A.; Egerton, T. A.; White, J. R. *Polymer* **2003**, *44*, 5969.
6. Jin, C. Q. PhD thesis, Newcastle University, Newcastle-upon-Tyne, 2004.
7. Delprat, P.; Duteurtre, X.; Gardette, J. -L. *Polym. Degrad. Stab.* **1995**, *50*, 1.
8. Lacoste, J.; Carlsson, D. J. *J. Polym. Sci.* **1992**, *30A*, 493.
9. Fernando, S. S.; Christensen, P. A.; Egerton, T. A.; Eveson, R.; Martins Franchetti, S. M.; Voisin, D.; White, J. R.; submitted *Mater. Sci. Technol.*
10. Christensen, P. A.; Egerton, T. A.; Martins-Franchetti, S. M.; Jin, C. Q.; White, J. R. *Polym. Degrad. Stab.* **2008**, *93*, 305.



## Chapter 14

# Lifetime Prediction: Different Strategies by Example

U. W. Gedde and M. Ekelund

Fibre and Polymer Technology, School of Chemical Science  
and Engineering, Royal Institute of Technology,  
SE-100 44 Stockholm, Sweden

Two different approaches for lifetime prediction are presented. The underlying lifetime limiting processes have been identified in two cases. Mathematical expressions of chemical/physical relevance were used for the lifetime predictions for PE hot-water pipes and cables insulated with plasticized PVC. Accelerated testing, extrapolation and validation of the extrapolation by assessment of the remaining lifetime of objects aged during service conditions for 25 years were successfully applied to cables insulated with chlorosulfonated polyethylene. Polyolefin pipes exposed to chlorinated water showed a very complex deterioration scenario and it was only possible to find a method suitable for predicting the time for the depletion of the stabilizer system.

## Introduction

Lifetime predictions of polymeric products can be performed in at least two principally different ways. The preferred method is to reveal the underlying chemical and physical changes of the material in the real-life situation. Expected lifetimes are typically 10-100 years, which imply the use of accelerated testing to reveal the kinetics of the deterioration processes. Furthermore, the kinetics has to be expressed in a convenient mathematical language of physical/chemical relevance to permit extrapolation to the real-life conditions. In some instances, even though the basic mechanisms are known, the data available are not sufficient to express the results in equations with reliably determined physical/chemical parameters. In such cases, a semi-empirical approach may be very useful. The other approach, which may be referred to as empirical, uses data obtained by accelerated testing typically at several elevated temperatures and establishes a temperatures trend of the shift factor. The extrapolation to service conditions is based on the actual parameters in the shift function (e.g. the Arrhenius equation) obtained from the accelerated test data. The validity of such extrapolation needs to be checked by independent measurements. One possible method is to test objects that have been in service for many years and to assess their remaining lifetime.

Before starting this analysis a clear formulation of a failure criterion for a given object is needed. In some cases, the criterion is self-evident, e.g. when failure occurs by fracture in a pipe whereas in other cases it requires significant experimental study and analysis.

This paper presents a selection of data including their interpretation with the purpose of predicting lifetimes of four different cases: polyethylene hot-water pipes, polyolefin pipes distributing chlorinated water, chlorosulfonated polyethylene and plasticized polyvinylchloride as insulating materials used in cables in nuclear power plants. The failure criteria for these applications were brittle fracture failure preceded by thermal oxidation or chemical degradation for the pipes and loss of mechanical integrity and a certain minimum resistance of the insulating layers during a simulated nuclear power plant accident in the two latter cases. Different extrapolation methods were used. In the case of the hot-water pipes, a detailed picture of the deterioration scenario was obtained permitting extrapolation using relevant physical/chemical equations. The extrapolation method used in the case of the chlorosulfonated polyethylene cables were based on an empirical approach including data from accelerated testing and data of the remaining lifetime for objects aged during service for 25 years. Plasticized PVC deteriorates by dehydrochlorination and plasticizer migration. The latter is dominant at lower temperatures. Lifetime predictions for service-like conditions (20–50°C) were based on extrapolating migration rate data obtained under conditions with prevailing evaporation control.

## Polyethylene Hot Water Pipes

Polyethylene pipes exposed to hot water with access to oxygen may undergo the following stages of change (1–3): Equilibration of a supersaturated solution of the antioxidant in the polymer which include loss of antioxidant by internal precipitation or phase separation (Regime A) (6), loss of antioxidant by migration to the surrounding media (Regime B) (2, 7) and finally, when the antioxidant system is depleted, oxidative polymer degradation (Regime C) (4, 5). Regime C constitutes only 5–10% of the total lifetime (4). Regime B is described by Fick's second law (Equ. 1) and the following boundary conditions (Eqs. (3, 4) (2):

$$\frac{\partial C(r,t)}{\partial t} = \left(\frac{1}{r}\right) \frac{\partial}{\partial r} \left( rD(r) \left( \frac{\partial C(r,t)}{\partial r} \right) \right) - R(C,r) \quad (1)$$

$$D(r) = D_0 \left( 1 + \frac{\lambda b}{d} \right) \quad (2)$$

$$D \left( \frac{\partial C}{\partial r} \right)_{r=b} = -\beta C \quad (3)$$

$$D \left( \frac{\partial C}{\partial r} \right)_{r=a} = \alpha C \quad (4)$$

where  $C$  is the concentration of antioxidant,  $r$  is the radial distance,  $t$  is time,  $D$  is the diffusivity of the antioxidant in the polymer,  $R$  is a term describing the reaction consumption of the antioxidant,  $D_0$  is the antioxidant diffusivity at the outer wall,  $\lambda$  is a constant expressing the radial dependence of the diffusivity (only relevant when the internal and external media are different),  $d$  is the pipe wall thickness,  $b$  is the outer wall radius,  $a$  is the inner wall radius,  $\beta$  is a parameter describing the evaporative loss of the antioxidant from the outer surface, and  $\alpha$  is a parameter describing the loss of antioxidant from the inner wall to the internal water medium. Given a suitable starting condition (antioxidant concentration profile), and a series of antioxidant concentration profiles from pipes pressure tested for different periods of time, Eqs. 1–4, can be solved by numerical methods to obtain values for the five adjustable parameters. It was shown in several studies (2, 7-9) that the reaction consumption term  $R$  was negligible with respect to the migrational loss rate. The good fit of these equations to a range of experimental data and the fact that realistic values were obtained for the diffusion coefficient and its temperature dependence make this method useful for extrapolation. The antioxidant concentration was determined by oxidation induction time measurements by DSC. This method of determining the antioxidant concentration is limited to phenolic antioxidants. Other stabilizers such as hindered amines have to be analyzed by other methods.

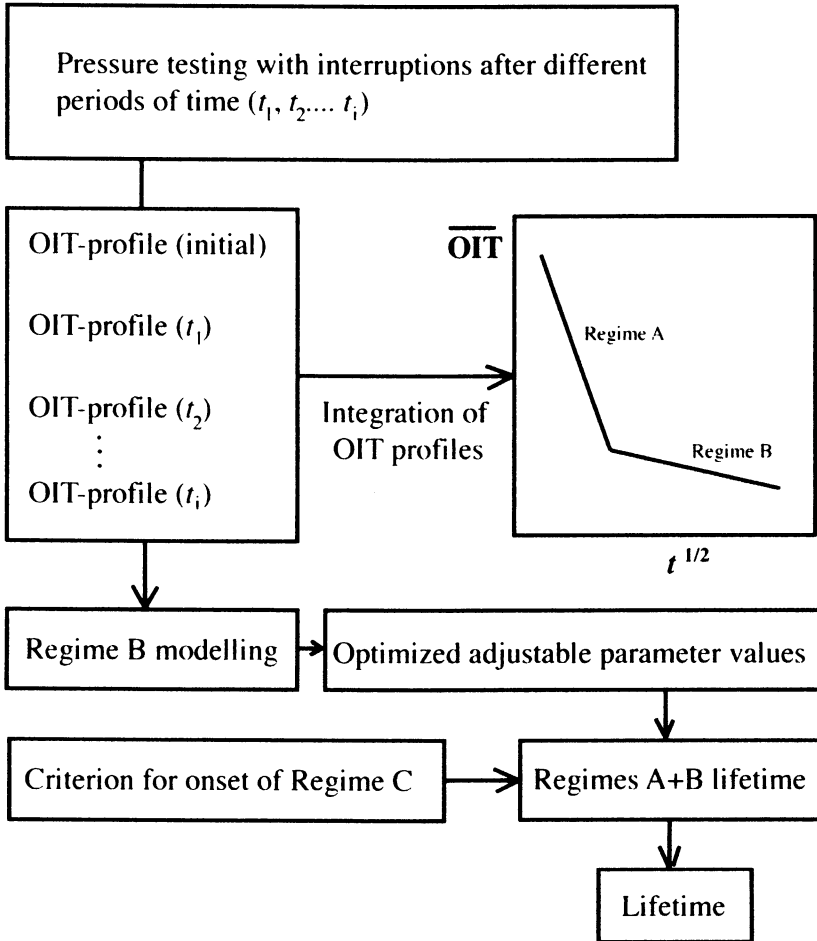


Figure 1. Schematic representation of the method to predict lifetime of pipes from oxidation induction time (OIT) data. Drawn after a chart presented in Viebke and Gedde, (10).

A method for the assessment of lifetime of polyethylene pipes undergoing thermal oxidation before failure was developed on the basis of oxidation induction time data (10). The method requires pressure testing for a limited period of time, sampling and determination of oxidation induction time profiles through the pipe wall (Fig. 1). The first task is to differentiate between Regimes A and B. The starting conditions (time and corresponding antioxidant concentration profile) for Regime B modeling (using Eqs. 1–4) are established. Based on the further antioxidant concentration profiles the adjustable parameters in Eqs. 1–4, are determined and used for extrapolation to obtain the time ( $t_{A+B}$ ) for the depletion of the antioxidant system. The predicted total lifetime is obtained by multiplication by a factor slightly larger than unity (1.1); Regime C constitutes only a minor fraction of the total lifetime, 5 to 10%. The average difference between actual and predicted lifetimes was 15% for the medium-density polyethylene pipes studied and the time saving was 30 to 80% with respect to that of conventional pressure testing (10). Pressure testing can be performed at relatively low temperatures (70–90°C) and hence, temperature extrapolation to service temperatures is short-range and can be performed with good accuracy using the Arrhenius equation.

Stabilizers showing limited solubility in water or a low vapor pressure in air constitute a major problem for the modeling (8, 9). The migration is then controlled by the boundary conditions and the numerical method used may not work properly. In these cases, data obtained from pressure testing with stagnant water may not represent the real-life situation with internal flowing water.

## Polyolefin Pipes Exposed to Chlorinated Water

The scenario for pipes distributing water with 0.5–3 ppm chlorine at pH=6.5 is more complex (11, 12). Standard stabilizers, combinations of hindered phenols and phosphates, are rapidly chemically consumed by the action of species from the chlorinated water reaching far into the pipe wall (11). The subsequent polymer degradation is strictly confined to the immediate surface layer and to the amorphous component of the polymer (11). The growth of cracks initiated at the degraded inner wall surface and temporarily blunting in the undegraded material layer is most probably assisted by further polymer degradation of the material at the crack tip. Lifetime prediction based on this complex scenario is still largely based on empirical methods and is only concerned with the assessment of the time for depletion of antioxidant system (12). Eqs. 1–4 are in principle useful for extrapolation but in this case the reaction term ( $R$ ) is important. A proper description of  $R$  would require at least two parameters. Hence, the total number of adjustable parameters in the modeling would be 6, which in our opinion, is too high for reliable use of this method.

Fig. 2 presents the analysis based on OIT data and the linear extrapolation of these data to longer times. The time to reach depletion of the antioxidant system can thus be predicted even after relatively short testing times (see insert figure in Fig. 2). Data by Hassinen et al. (11) for the antioxidant concentration profiles taken from high-density polyethylene pipes exposed to chlorinated water (3 ppm chlorine) at different temperatures between 25 and 105°C followed the Arrhenius equation with an activation energy of 85 kJ mol<sup>-1</sup> (0–0.1 mm beneath inner wall surface) and 80 kJ mol<sup>-1</sup> (0.35–0.45 mm beneath the inner wall surface). It is thus possible to make predictions about the time for antioxidant depletion at service temperatures (20–40°C) by extrapolation of high temperature data. However, there is currently not a sufficient set of data to reveal the kinetics of polymer degradation and crack growth that would allow reliable extrapolation to room temperature.

### Chlorosulfonated Polyethylene Cables

The chlorosulfonated polyethylene cables aged in nitrogen or in air at temperatures between 120 and 200°C showed a gradual hardening and loss of toughness finally reaching a critical brittleness (13). Indenter modulus – log ageing time data could be superimposed within this temperature range with a shift factor according to the Arrhenius equation with an activation energy of 110 kJ mol<sup>-1</sup> (Fig. 3) (13). The scatter of the master curve data was of the same order of magnitude as the scatter of the data taken at the individual temperatures.

Arrhenius extrapolation (activation energy = 106 kJ mol<sup>-1</sup>) to service temperatures (20–50°C) was validated by the assessment of the remaining lifetime of the cables exposed to 25 years of service (Fig. 4) (13). The latter was calculated according to Miner's law (14). The lifetimes based on the cables aged for 25 years in nitrogen were on an average 25% shorter than those obtained by extrapolation of the high temperature data (Fig. 4). In view of the long-range extrapolation, from 120°C to ca. 50°C, this difference is not very significant. It should be noted that the aging at the higher temperatures (120–200°C) was performed in nitrogen. The cables in the nuclear power plant (aged for 25 years) were kept in nitrogen for 11 months during each year of service. The temperature during the 1-month of air exposure was lower than during service.

Cables specimens aged in air at temperatures between 120 and 200°C showed also a temperature shift factor ( $a_T$ ) that followed the Arrhenius equation with activation energy of ca. 100 kJ mol<sup>-1</sup>. Calculation of the remaining lifetime of cables that had been exposed to air for 25 years yielded lifetimes at ca. 40°C that were approximately half of the lifetime obtained by extrapolation of the high temperature (120–200°C) data (13). This assessment was based on 6 service cables. Gillen and coworkers (15–20) have reported similar deviations for a

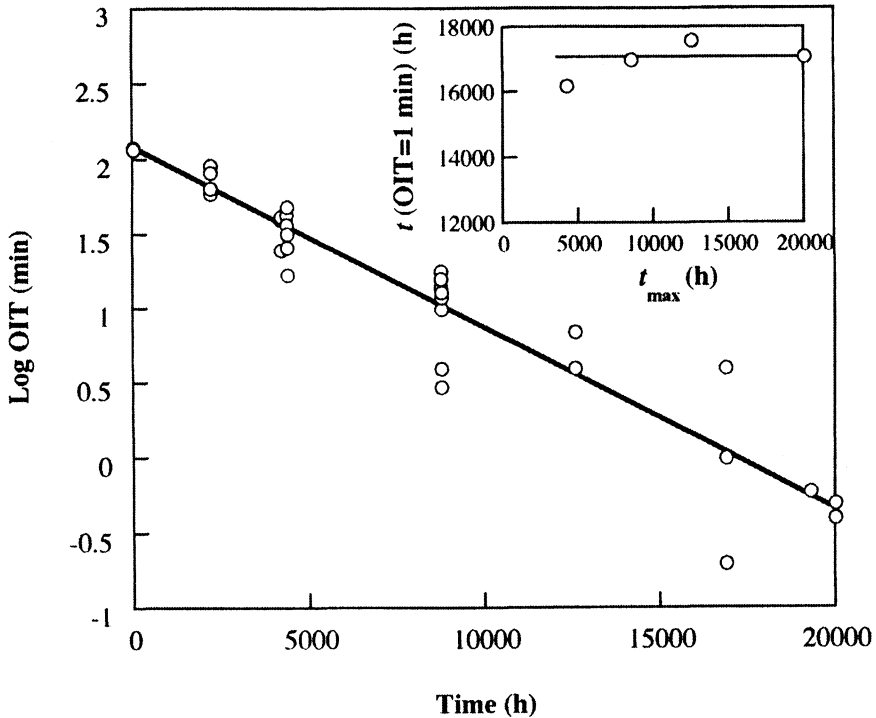


Figure 2. Oxidation induction time (OIT; not the log-scale) for samples taken at a certain depth (0.9–1.0 mm from the inner wall from PB pipes pressure-tested at 90°C with internal chlorinated water (0.5, 1.0 and 1.5 ppm Cl) as a function of the exposure time. The line is a linear fit of the data. The insert figure shows the results of extrapolation to OIT= 1 min based on OIT data from exposures shorter than  $t_{max}$ . From Lundbäck et al. (12) and with permission from Elsevier, UK.

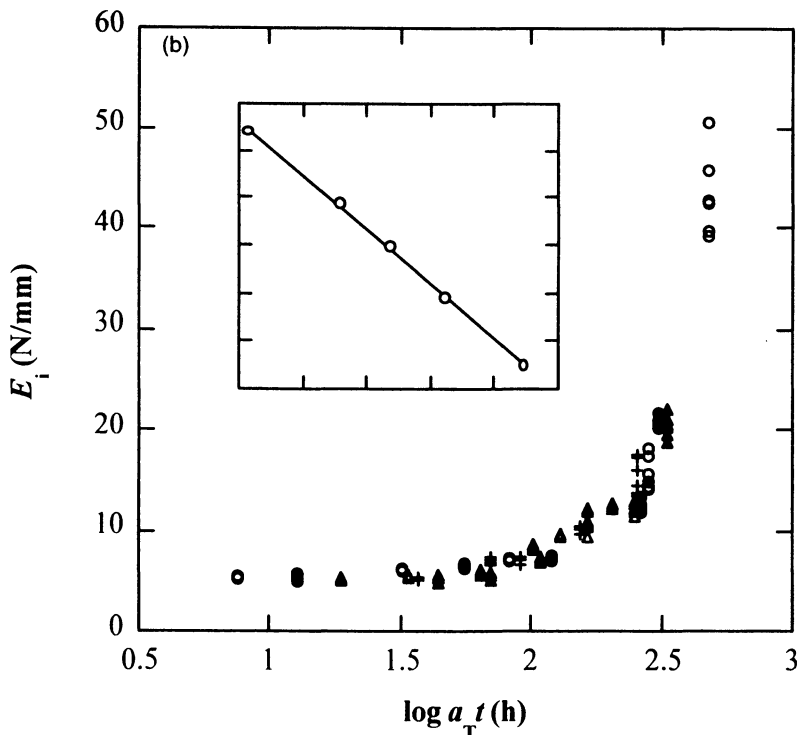


Figure 3. Master curve of indenter modulus of jacketing based on chlorosulfonated polyethylene at 155°C obtained by horizontal shifting of the data taken at the other temperatures (120–200°C) by  $\log a_T$  along the logarithmic time axis. The samples were aged in nitrogen. The temperature-dependence of the shift factor is shown in the insert figure. From Sandelin and Gedde (13) and with permission from Elsevier, UK.

range of rubbery materials in jacketings of cables aged in air. They aged the cables in air at elevated temperatures and recorded changes in their mechanical properties that followed the Arrhenius equation. They also measured the oxygen consumption rate even at very low temperatures and noticed a break in the  $\log a_T - 1/T$  line at 80–100°C. For chlorosulfonated polyethylene jackets the oxidation process changed activation energy from 107 kJ mol<sup>-1</sup> at high temperatures to a lower value at temperatures below 100°C (20). This change in activation energy meant that extrapolation of high temperature data overestimated the lifetime by a factor of two at 40°C (20). This difference is in accordance with the data presented by Sandelin and Gedde (Fig. 4) (13).



## PVC Cables

The mechanical data for PVC cable samples taken at room temperature after air ageing could be superimposed (shift factor according to the Arrhenius equation) with regard to ageing time and temperature (21). The jacketing material showed an immediate increase in stiffness and a decrease in the strain at break on ageing; these changes were dominated by loss of plasticizer by migration also confirmed by infrared spectroscopy, DSC and liquid chromatography of extracts (21, 22). The core insulation showed smaller and also delayed changes in these mechanical parameters; the loss of plasticizer by migration was according to data obtained by IR spectroscopy, DSC and HPLC prohibited by the closed environment and the changes in the mechanical parameters were due to dehydrochlorination of the polymer (21, 22). These data provide the basis for extrapolation to lower temperatures and the assessment of the relative importance of plasticizer migration and dehydrochlorination. Plasticizer migration was found to be the dominant process below 100°C (21). Data for plasticizer migration and evaporation (from a glass surface) was taken at temperatures (T) between 60 and 150°C (22). Two migration regimes were revealed (22): (i)  $T \geq 120^\circ\text{C}$ : diffusion-control with concentration-dependent diffusivity; (ii)  $T \leq 100^\circ\text{C}$ ; evaporation control with a constant evaporative loss rate. This loss rate was of the same order of magnitude as that from a free plasticizer film on a glass plate (22). Extrapolation of high temperature plasticizer evaporation data (60–100°C) yielded an accumulated plasticizer loss over 30 years of 0.3% for the jacketing, which is in accordance with data obtained for cables after 30 years of service (22).

## Conclusions

The lifetime-determining processes that prevail during service-like conditions were established for polyethylene hot water pipes and cables insulated with plasticized PVC. Lifetime predictions based on equations with physical/chemical relevance yielded reliable results. The lifetime of cables insulated with chlorosulfonated polyethylene aged in nitrogen were predicted with good precision by long-range extrapolation of accelerated testing data. An efficient method for predicting the time for depletion of the stabilizer system in polyolefin pipes exposed to chlorinated water was presented.

## Acknowledgements

This research is based on the financial support from several sources: the Swedish Research Council (grant #621–2001–2321), Studsvik Polymer AB

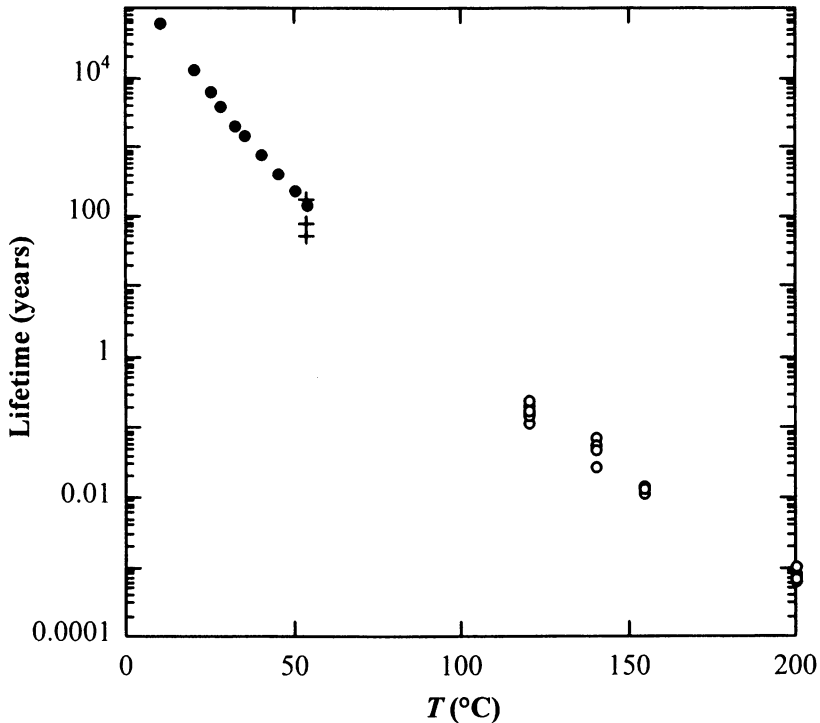


Figure 4. Lifetime (logarithmic scale; time to reach  $2\times$  the initial indenter modulus = failure criterion according to LOCA tests) as a function of temperature ( $T$ ) for the Hypalon core insulation aged in nitrogen. The high-temperature data (open circles) were obtained from experimental data. The low-temperature data (filled circles) were obtained by extrapolation of the high-temperature data according to the Arrhenius equation. The remaining lifetime of a Hypalon cable core insulation in service for 24.8 years at  $54^\circ\text{C}$  in nitrogen was obtained by subsequent ageing at  $155^\circ\text{C}$  and  $170^\circ\text{C}$  and the data were used to estimate the total lifetime at  $54^\circ\text{C}$  (indicated by crosses). From Sandelin and Gedde (13) and with permission from Elsevier, UK.

(now Bodycote Polymer AB), Ringhals AB and Forsmarks Kraftgrupp AB (both owned by Vattenfall AB). The following co-authors of the papers which this report is based on are gratefully acknowledged: the late Mr. Mats Ifwarson (Bodycote Polymer AB), Prof. Grant D. Smith (University of Utah), Dr. Jens Viebke (GE Healthcare), Mr. Jarno Hassinen (Bodycote Polymer AB), Prof. Mikael Hedenqvist (KTH), Dr. Marie Lundbäck, and Mr. Mikael Sandelin.

## References

1. Karlsson, K.; Smith, G. D.; Gedde U. W. *Polym. Eng. Sci.* **1992**, *32*, 649.
2. Smith, G. D.; Karlsson, K.; Gedde, U. W. *Polym. Eng. Sci.* **1992**, *32*, 658.
3. Gedde, U. W.; Viebke, J.; Leijström, H.; Ifwarson, M. *Polym. Eng. Sci.* **1994**, *34*, 1773.
4. Viebke, J.; Elble, E.; Ifwarson, M.; Gedde, U. W. *Polym. Eng. Sci.* **1994**, *34*, 1354.
5. Viebke, J.; Elble, E.; Gedde, U. W. *Polym. Eng. Sci.* **1996**, *36*, 458.
6. Viebke, J.; Hedenqvist, M.; Gedde, U. W. *Polym. Eng. Sci.* **1996**, *36*, 2896.
7. Viebke, J.; Gedde, U. W. *Polym. Eng. Sci.* **1997**, *37*, 896.
8. Lundbäck, M.; Strandberg, C.; Albertsson, A. -C.; Hedenqvist, M. S.; Gedde, U. W. *Polym. Degrad. Stab.* **2006**, *91*, 1071.
9. Lundbäck, M.; Hedenqvist, M. S.; Mattozzi, A.; Gedde, U. W. *Polym. Degrad. Stab.* **2006**, *91*, 1571.
10. Viebke, J.; Gedde, U. W. *Polym. Eng. Sci.* **1998**, *38*, 1244.
11. Hassinen, J.; Lundbäck, M.; Ifwarson, M.; Gedde, U. W. *Polym. Degrad. Stab.* **2004**, *84*, 261.
12. Lundbäck, M.; Hassinen, J.; Andersson, U.; Fujiwara, T.; Gedde, U. W. *Polym. Degrad. Stab.* **2006**, *91*, 842.
13. Sandelin, M.; Gedde, U. W. *Polym. Degrad. Stab.* **2004**, *86*, 331.
14. Miner, M. A. *J. Appl. Mech.* **1945**, A159.
15. Gillen, K. T.; Celina, M.; Clough, R. L.; Wise, J. *Trends Polym. Sci.* **1997**, *5*, 250.
16. Celina, M.; Wise, J.; Ottesen, D. K.; Gillen, K. T.; Clough, R. L. *Polym. Degrad. Stab.* **2000**, *68*, 171.
17. Celina, M.; Gillen, K. T.; Graham, A. C.; Assink, R. A.; Minier, L. M. *Rubber Chem. Technol.* **2000**, *73*, 678.
18. Gillen, K. T.; Celina, M.; Bernstein, R. *Polym. Degrad. Stab.* **2003**, *82*, 25.
19. Gillen, K. T.; Bernstein, R.; Derzon, D. K. *Polym. Degrad. Stab.* **2005**, *87*, 57.
20. Gillen, K. T.; Bernstein, R.; Celina, M. *Polym. Degrad. Stab.* **2005**, *87*, 335.
21. Ekelund, M.; Edin, H.; Gedde, U. W. *Polym. Degrad. Stab.* **2007**, *92*, 617.
22. Ekelund, M.; Azhdar, B.; Hedenqvist, M. S., Gedde, U. W. *Polym. Degrad. Stab.* submitted.

## Chapter 15

# Probing Degradation in Complex Engineering Silicones by $^1\text{H}$ Multiple Quantum NMR

**Robert S. Maxwell, Sarah C. Chinn, Jason R. Giuliani,  
and Julie L. Herberg**

**Lawrence Livermore National Laboratory, 7000 East Avenue,  
Livermore, CA 94550**

Static  $^1\text{H}$  Multiple Quantum Nuclear Magnetic Resonance (MQ NMR) has recently been shown to provide detailed insight into the network structure of pristine silicon based polymer systems. The MQ NMR method characterizes the residual dipolar couplings of the silicon chains that depend on the average molecular weight between physical or chemical constraints. Recently, we have employed MQ NMR methods to characterize the changes in network structure in a series of complex silicone materials subject to numerous degradation mechanisms, including thermal, radiative, and desiccative. For thermal degradation, MQ NMR shows that a combination of crosslinking due to post-curing reactions as well as random chain scissioning reactions occurs. For radiative degradation, the primary mechanisms are via crosslinking both in the network and at the interface between the polymer and the inorganic filler. For samples stored in highly desiccating environments, MQ NMR shows that the average segmental dynamics are slowed due to increased interactions between the filler and the network polymer chains.

Silica filled polydimethylsiloxane composite systems have a wide variety of important commercial and technological applications (1). This is in no small part due to their chemical and thermal stability and the tailorability of mechanical properties. This tailorability is a result of the wide range of structural architectures possible, including the degree and type of crosslinking, the molecular weight between crosslinks, the number of elastically ineffective chains (loops, dangling chain ends, sol-fraction) as well as filler content and surface properties (2-5). However, due to the complexity of the network structure and the poorly characterized interface between the polymer and the filler, quantitatively characterizing changes in these structures with time is difficult.

Nuclear magnetic resonance (NMR) has been used to characterize chemical speciation changes occurring in both soluble and insoluble fractions of silicone polymers for decades (6-9). One of the most common strategies for characterizing the effects of aging on these materials has been correlating changes in the  $T_2$  relaxation times measured by spin-echo methods to changes in crosslink density of the bulk polymer. In fact, these methods have been developed to an extent that they are used in production applications with low resolution, portable relaxometers (10-12). Unfortunately, spin-echo based methods are subject to a number of systematic errors which lead to over estimated changes in crosslink density, in chain order parameters, or in some cases completely incorrect trends (13).

Static  $^1\text{H}$  Multiple Quantum (MQ) NMR spectroscopy, on the other hand, has shown the ability to more reliably quantitatively characterize elastomer network structure and heterogeneities (14-19).  $^1\text{H}$  MQ NMR methods allow for the measurement of absolute residual dipolar couplings ( $\langle\Omega_d\rangle$ ) and segmental/cooperative dynamics without interference from magnetic susceptibility and field gradients which complicate relaxation measurements (13, 14, 20,21). It has previously been shown that the residual dipolar couplings are directly related to the dynamic order parameter,  $S_b$ , and the crosslink density (1/N) (9):

$$S_b = \frac{1}{P_2(\cos\alpha)} \frac{\langle\Omega_d\rangle}{\langle\Omega_d\rangle_{static}} = \frac{3r^2}{5N} \quad (1)$$

Thus, the MQ-NMR method allows for the direct measure of network topology and in many cases, filler-particle interactions. In the case of time dependent changes in structure due to aging, origins of degradation in material performance can be detected. A number of examples are shown here.

## Experimental

Experiments were performed on crosslinked, filled, silicone networks, described elsewhere (15-17, 29). The gum stocks for all formulations were

either co-block polymers of dimethylsiloxane, diphenylsiloxane, methylphenylsiloxane, and/or methylvinyl siloxane (29) or endlinked networks of PDMS chains of variable length (15, 17). The gum stocks were reinforced with silica filler and crosslinked with either peroxide or organometallic curing agents. These materials were tested in both new as well as laboratory aged conditions.

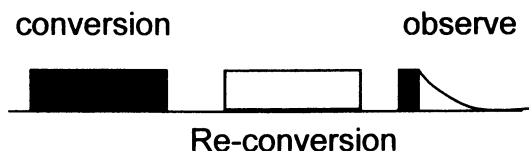


Figure 1. Multiple Quantum NMR pulse. Growth curves are obtained by incrementing either the interpulse delays or the number of multiple pulse excitation trains in the conversion and reversion sequences. (Reproduced from reference 13. Copyright 2005 American Chemical Society.)

All MQ-NMR experiments were performed on a Bruker Avance 400 MHz spectrometer equipped with a 5mm Bruker TBI probe. The pulse sequence used is illustrated in Figure 1. MQ growth curves, as illustrated in Figure 2A, were obtained generally by incrementing the loop counter,  $n$ . Alternately, the delay between pulses could be incremented instead. Further details are described elsewhere (13-18). Insight was obtained on the network structure from the distributions of the residual dipolar couplings extracted from the MQ growth curves using a fast Thikonov regularization (FTIKREG) algorithm (22) using the following analytical expression as the kernel:

$$I_{nDQ}(\langle \Omega_d \rangle; \tau_{DQ}) = 0.5 * (1 - e^{-\frac{2}{3} \langle \Omega_d \rangle^2 \tau_{DQ}^2}) \quad (2)$$

Illustrative fits to Equation 2 or a two site modification (16) are shown in Figure 2A. Results of FTIKREG regularization is shown in Figure 3.

## Results and Discussion

### Characterization of Thermally Degraded Materials

Silicone materials are known to be fairly resistant to thermal degradation under relatively harsh conditions (less than a few hundred degrees centigrade). However, they are known to be subject to post-curing reaction, oxidative chain scissioning and crosslinking reactions, hydrolysis and unzipping reactions (23-

25). These reactions are typically observed indirectly by measurement of offgassing signatures by mass spectrometry based methods, though interesting results have been obtained by  $^{17}\text{O}$  NMR (26, 27). The effects of these reactions on the remaining, insoluble network structure are unfortunately more difficult to characterize.

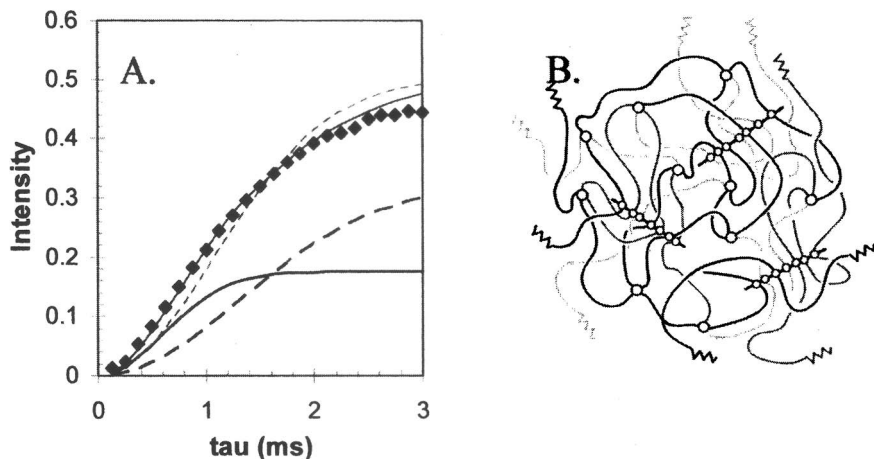


*Figure 2. (A) Growth curve for pristine sample showing results of one site fit (dotted line) and two site fit (solid line – components are shown underneath curve in red); (B) Schematic of network structure of typical engineering silicone with both short and long chain constituents and standard four site crosslinking species and highly functional crosslinking sites. (Figure 2B is reproduced from reference 17. Copyright 2005 American Chemical Society.) (See page 7 of color insert.)*

The MQ growth curve for a typical pristine material is shown in Figure 2A. The pristine material in this case was constructed from PDMS chains of three different MW using primarily two different types of crosslinking sites: a typical 4 site junction and a highly functional multi-site crosslinking species with 60 crosslinking sites (17), as illustrated in Figure 2B. The growth curve could not be fit to one single residual dipolar coupling with Equation 2 and required at least two sites to provide a reasonable fit. These two sites are assigned in this case to chains with high molecular weight between crosslinks and those chains with much shorter chain lengths. Estimates of the MW between crosslinks can be extracted from Equation 1 and yield averages of 7500 g/mol and 1600 g/mol, in agreement with the expected MW between entanglements in the first case and the MW from the starting material (17). Extraction of the distribution of the residual dipolar couplings from FTIKREG regularization is shown in Figure 3A

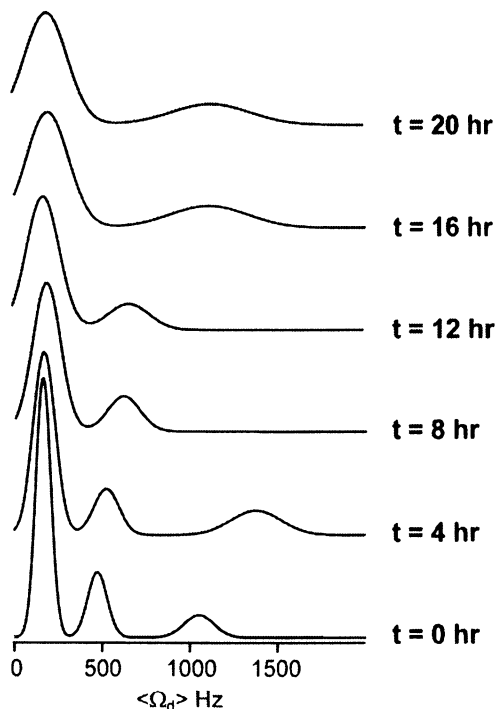


Figure 3. Distributions of residual dipolar couplings obtained from MQ-NMR analysis of thermally degraded (250°C for indicated times, in air) PDMS composites. (Reproduced from reference 18. Copyright 2007 American Chemical Society.)

and show surprisingly narrow distributions. Similar results have been obtained for the other pristine networks studied and can be found elsewhere (14-18).

We subjected the pristine material to thermal degradation at 250°C for times ranging from 0 to 20 hrs. TGA analysis indicated ~3% weight loss for 20 hrs of aging and standard Hanh-echo based experiments showed no change in the network  $T_2$  with aging time, but did show a steady, but small increase in the sol-fraction component (17). Despite these small changes, the material became markedly more brittle after 20 hours of aging. We applied MQ-NMR to these samples and the results obtained from FTIKREG regularization using Equation 2 as a Kernel are the results are shown in Figure 3. Changes in both the low ( $\langle \Omega_d \rangle \sim 200$  Hz) and high ( $\langle \Omega_d \rangle \sim 500$  Hz) frequency peak width were observed. A third distribution at  $\sim 1000$  Hz was also observed for zero and four hours of aging. This site has been assigned to a systematic fitting artifact due to the small sampling frequency at early MQ growth times. The small sampling frequency



was limited by the smallest tau resolvable by the specific pulse sequence used here (18). The low frequency site was observed to broaden with time, while the high frequency site was observed to broaden and move to higher average residual dipolar coupling.

The MQ NMR data is consistent with simultaneous crosslinking (increased residual dipolar couplings) and chain scissioning (reduction in residual dipolar couplings). Observation of scissioning reactions is consistent with degradation products observed by GC/MS and NMR analysis of volatile and soluble degradation products (23-25). Crosslinking during thermal aging at similar temperatures was previously observed for unfilled PDMS samples by Grassie et al. (30). Continued post-curing reactions of the residual silane species present from unreacted sites on the crosslinking moieties would lead to increased crosslink density for all chains.  $^1\text{H}$  MAS NMR of the pristine and aged samples showed no difference within experimental error. This, however, is not surprising, given the small amount of material present. The MQ NMR, however, provides detailed insight into the result of these degradation mechanisms on the network structure of the polymer composite.

### Characterization of Radiation Degraded Materials

Exposure of silicone polymers to ionizing radiation is generally understood to cause random crosslinking as the primary degradation mechanism (31). Previously, this insight has been obtained via observing relative changes in  $T_2$  relaxation times via spin-echo analysis (28, 33). The direct quantitative correlation of  $T_2$  relaxation times with network structural parameters such as crosslink density has proven difficult due to a number of limitations of the method, as described elsewhere (19-21). We have applied MQ NMR to the characterization of a highly filled, PDMS composite material (15, 16). Due to the high surface area of the filler used in these experiments and the network structure of the bulk polymer (roughly monomodal), the observed two site distribution obtained from deconvolution of the MQ growth curves were assigned to bulk polymer chains far from the surface ( $\langle\Omega_d\rangle \sim 1000$  rad/s) and polymer chains in close proximity to the polymer surface ( $\langle\Omega_d\rangle \sim 3000$  rad/s). As shown in Figure 4, upon exposure to  $\gamma$ -radiation at 1.2 MeV, 500kRad/hr, the residual dipolar couplings in both domains were observed to increase due to the effects of random crosslinking. In addition, we observed a steady increase in the amount of the chains associated with the filler surface, presumably due to formation of crosslinks to the filler surface or between chains already motionally constrained crosslinking to bulk polymer chains. These results have been described in more detail elsewhere (15, 16). Again, the MQ NMR investigation provided insights into the composite structure unobtainable previously.

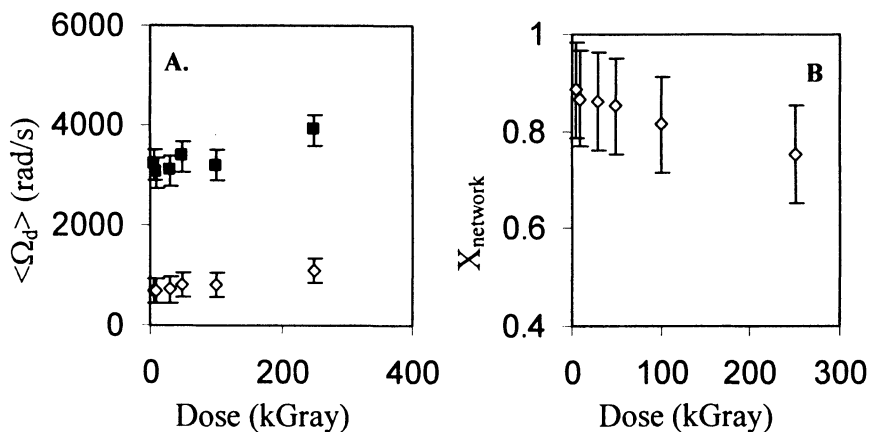


Figure 4. Results of MQ-NMR analysis of radiatively degraded silica highly filled PDMS networks. (A) Change in residual dipolar coupling ( $\langle \Omega_d \rangle$ ) with dose, (B) change in amount of polymer chains not interacting with the filler surface. (Reproduced from reference 16. Copyright 2007 American Chemical Society.)

### Characterization of Desiccatively Aged Materials

It has been postulated that hydrogen bonding between filler surface hydroxyls, water, and the oxygen atoms on the backbone of the polymer is a significant mechanism of reinforcement (1, 32). Aging of filled silicone materials in highly dry environments has the potential to alter the water speciation at the filler-polymer interface, as illustrated in Figure 5. In an effort to understand how altering water speciation affects the segmental dynamics, we applied MQ methods to highly filled samples aged in a sealed environment in the presence of a strong desiccating agent (including molecular sieve,  $P_2O_5$ , and LiH). Results of MQ NMR analysis of the pristine material and a sample aged for 4 years are shown in Figure 6 and clearly indicate that desiccation causes reduced the segmental dynamics both in the bulk polymer and in the polymer chains associated with the polymer interface. These data are consistent with recent MD simulations of modulus changes in filled composites where the interface interaction parameters are changed (34).

### Conclusions

Multiple Quantum NMR methods have been used to characterize the results of multiple degradation mechanisms on complex silicone polymer composites.

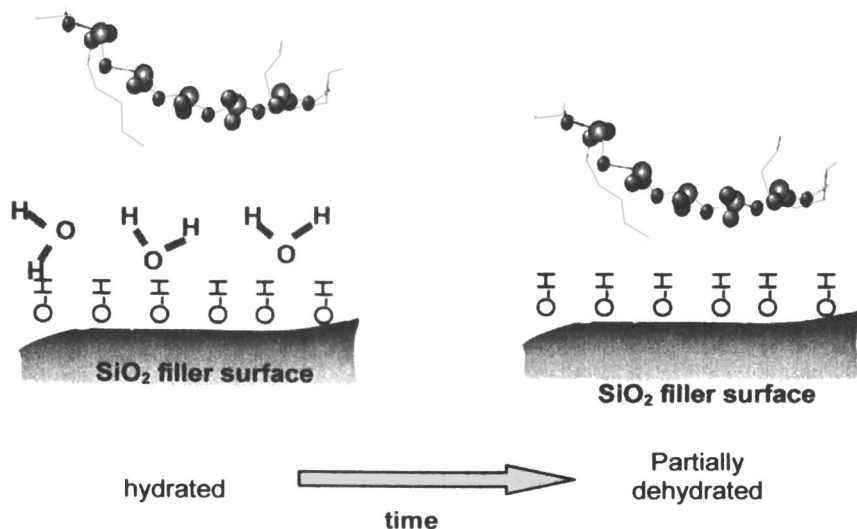


*Figure 5. Illustration of speciation changes at polymer-filler interface that would be expected to alter the interaction strength and effect reinforcement. (See page 7 of color insert.)*

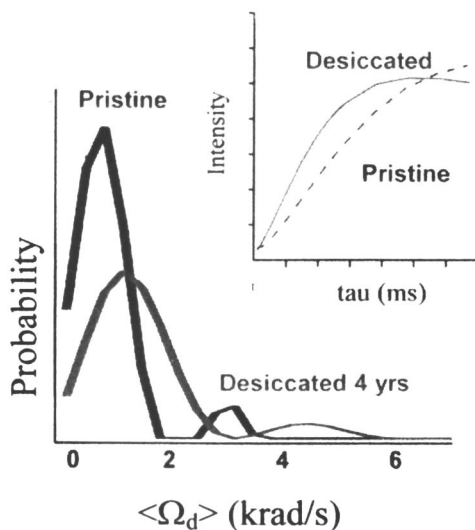


*Figure 6. Results of MQ-NMR analysis of highly filled PDMS sample exposed to highly desiccating environment for 4 years. Inset: MQ growth curves. (See page 7 of color insert.)*

The MQ NMR analysis provides direct, quantitative insight into the changes in the network structure and at the filler-polymer interface in these materials that has proven difficult to obtain via other characterization methods. For samples exposed to elevated temperatures, the MQ NMR indicated that degradation occurred via simultaneous chain scissioning and crosslinking reactions. For samples exposed to ionizing radiation, the MQ NMR indicated the dominance of random crosslinking. The MQ NMR analysis also indicated an increase in the amount of chains associated with the filler surface. For samples aged in a dry environment, MQ NMR measured a decrease in the segmental dynamics with aging time. This decrease occurred for chains in the bulk polymer network and associated with the filler surface. Many of these observations have not been observed prior to these analyses.

### Acknowledgements

This work performed under the auspices of the U.S. Department of Energy by Lawrence Livermore National Laboratory under Contract DE-AC52-07NA27344. Part of this work was supported by the LLNL Laboratory Directed Research and Development (LDRD) program (tracking number: 06-SI-005). Thanks to Eric Eastwood and Dan Bowen at Honeywell FM&T Kansas City Plant for supplying pristine materials and to April Sawvel and Erica Gjersing for preliminary studies.

### References

1. Brook, M. A. *Silicone in Organic, Organometallic, and Polymer Chemistry*; John Wiley & Sons: New York, NY, 2000.
2. Ferry, J. D. *Viscoelastic Properties of Polymers*; John Wiley & Sons: New York, 1980.
3. Flory, P. J. *Principles of Polymer Chemistry*; Cornell University Press: Ithaca, NY, 1953.
4. Bicerano, J. *Prediction of Polymer Properties; 3rd Edition*; Marcell-Dekker: New York, 2002.
5. Van Krevelen, D. W. *Properties of Polymers; 3rd Edition*; Elsevier: Amsterdam, 1997.
6. Bovey, F. A. *NMR of Polymers*; Academic Press: San Diego, CA, 1996.
7. Schmidt-Rohr, K.; Spiess, H. W. *Multidimensional Solid-State NMR and Polymers*; Academic Press: San Diego, CA, 1994.
8. Ando, I.; Asakura, T. *Solid State NMR of Polymers*; Elsevier: London, 1998.
9. Cohen-Addad, J. P. *Prog. NMR Spectr.* **1993**, *25*, 1.

10. Kuhn, H.; Klein, M.; Wiesmath, A.; Demco, D. E.; Blumich, B.; Kelm, J.; Gold, P. W. *Magn. Reson. Imaging* **2001**, *19*, 497.
11. Herberg, J. L.; Chinn, S. C.; Sawvel, A. M.; Gjersing, E.; Maxwell, R. S. *Polym. Degrad. Stab.* **2006**, *91*, 1701.
12. Chinn, S. C.; Cook-Tendulkar, A.; Maxwell, R. S.; Wheeler, H.; Wilson, M.; Xie, Z. H. *Polym. Test.* **2007**, *26*, 1015.
13. Saalwächter, K. *Macromolecules* **2005**, *38*, 1508.
14. Saalwächter, K. *J. Amer. Chem. Soc.* **2003**, *125*, 14684.
15. Chinn, S. C.; DeTeresa, S.; Sawvel, A.; Shields, A.; Balazs, B.; Maxwell, R. S. *Polym. Degrad. Stab.* **2006**, *91*, 555.
16. Maxwell, R. S.; Chinn, S. C.; Solyom, D.; Cohenour, R. *Macromolecules* **2005**, *38*, 7026.
17. Gjersing, E.; Chinn, S.; Maxwell, R. S.; Giuliani, J. R.; Herberg, J.; Eastwood, E.; Bowen, D.; Stephens, T. *Macromolecules* **2007**, *40*, 4953.
18. Giuliani, J. R.; Gjersing, E. L.; Chinn, S. C.; Jones, T. V.; Wilson, T. M.; Alviso, C. A.; Herberg, J. L.; Pearson, M. A.; Maxwell, R. S. *J. Phys. Chem. B* **2007**, *111*, 12977.
19. Saalwächter, K. *Prog. NMR Spectr.* **2007**, *51*, 1.
20. Kenny, J. C.; McBrierty, V. J.; Rigbi, Z.; Douglass, D. C. *Macromolecules* **1991**, *24*, 436.
21. Whittaker, A. K.; Bremner, T.; Zelaya, F. O. *Polymer* **1995**, *36*, 2159.
22. Weese, J. *Comput. Phys. Commun.* **1992**, *69*, 99.
23. Hall, A. D.; Patel, M. *Polym. Degrad. Stab.* **2006**, *91*, 2532.
24. Osthoff, R. C.; Bueche, A. M.; Grubb, W. T. *J. Amer. Chem. Soc.* **1954**, *76*, 4659.
25. Thomas, D. K. *Polymer* **1966**, *7*, 99.
26. Alam, T. M.; Celina, M.; Assink, R. A.; Clough, R. L.; Gillen, K. T.; Wheeler, D. R. *Macromolecules* **2000**, *33*, 1181.
27. Alam, T. M.; Celina, M.; Assink, R. A.; Clough, R. L.; Gillen, K. T. *Radiat. Phys. Chem.* **2001**, *60*, 121.
28. Charlesby, A.; Folland, R. *Radiat. Phys. Chem.* **1983**, *15*, 393.
29. Folland, R.; Charlesby, A. *Radiat. Phys. Chem.* **1977**, *10*, 61.
30. Maxwell, R. S.; Balazs, B. *J. Chem. Phys.* **2002**, *116*, 10492.
31. Grassie, N.; Macfarlane, I. G. *Eur. Polym. J.* **1978**, *14*, 875-884.
32. *Polymer Durability: Degradation, Stabilization, and Lifetime Prediction*; Clough, R. L.; Billingham, N. C.; Gillen, K. T., Eds.; Advances in Chemistry Series #249; ACS: Washington, D.C., 1996.
33. Kraus, G. *Rubber Chem. Tech.* **1965**, *38*, 1070.
34. Chien, A.; Maxwell, R. S.; Chambers, D.; Balazs, B.; LeMay, J. *Radiat. Phys. Chem.* **2000**, *59*, 493.
35. Gee, R. H.; Maxwell, R. S.; Balazs, B. *Polymer* **2004**, *45*, 3885.

## Chapter 16

### Accelerated Aging and Characterization of a Plasticized Poly(ester urethane) Binder

Debra A. Wroblewski<sup>1</sup>, David A. Langlois<sup>1</sup>, E. Bruce Orler<sup>1</sup>,  
Andrea Labouriau<sup>1</sup>, Mariana Uribe<sup>1</sup>, Robert Houlton<sup>2</sup>,  
Joel D. Kress<sup>3</sup>, and Brian Kendrick<sup>3</sup>

<sup>1</sup>Polymer and Coatings (MST-7), <sup>2</sup>Structure/Properties Relations (MST-8),  
and <sup>3</sup>Theoretical Chemistry and Molecular Physics (T-12), Los Alamos  
National Laboratory, Bikini Atoll Road, Los Alamos, NM 87545

This chapter describes accelerated aging studies of a plasticized commercial poly(ester urethane) (Estane<sup>®</sup> 5703). Oxidative and hydrolytic degradation mechanisms were investigated based on environmental conditions. Both studies evaluate degradation by <sup>1</sup>H NMR and GPC molecular weight analysis. The oxidative degradation study is focused on the kinetics of the oxidation of the hard segments and its impact on mechanical properties. The hydrolytic degradation study is focused on chain scission reactions of the polyester soft segments and agrees with a proposed hydrolysis model. <sup>1</sup>H NMR spin-spin relaxation times have been evaluated for hydrolytic degradation of Estane.

## Introduction

We have studied accelerated aging of the high explosive, PBX 9501, binder as a means of understanding degradation mechanisms under simulated aging conditions. Accelerated aging studies are important because it provides insights on aging mechanisms and helps modeling efforts for lifetime predictions. The composition of PBX 9501 is 95% HMX and 5% binder. The binder consists of 50% Estane<sup>®</sup> 5703 (Estane) and 50% nitroplasticizer (NP) and a small amount of hindered phenol stabilizer, Irganox 1010. Estane is a segmented poly(ester urethane) consisting of poly(butylene adipate) as the flexible soft segment and 4,4'-methylene-diphenyl-1,1'-diisocyanate (MDI) chain-extended with 1,4-butanediol (BDO) as the rigid hard segment shown in Figure 1. Incompatibility of the hard and soft segments causes phase separation into domains (1). The domain structure increases the mechanical strength of the material. The nitroplasticizer is a eutectic mixture of bis(2,2-dinitropropyl)formal (BDNPF) and bis(2,2-dinitropropyl)acetal (BDNPA). The nitroplasticizer is added to the binder to decrease the sensitivity and improve the performance of the high explosive. Since the binder provides mechanical integrity of the PBX 9501 composite, it is essential to understand how its mechanical properties change with aging and identify the chemical degradation mechanisms.

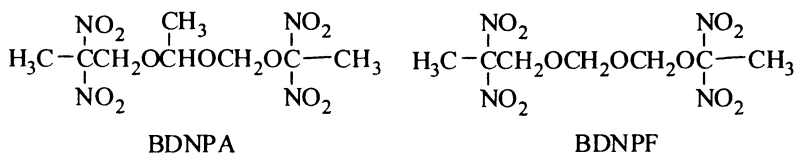
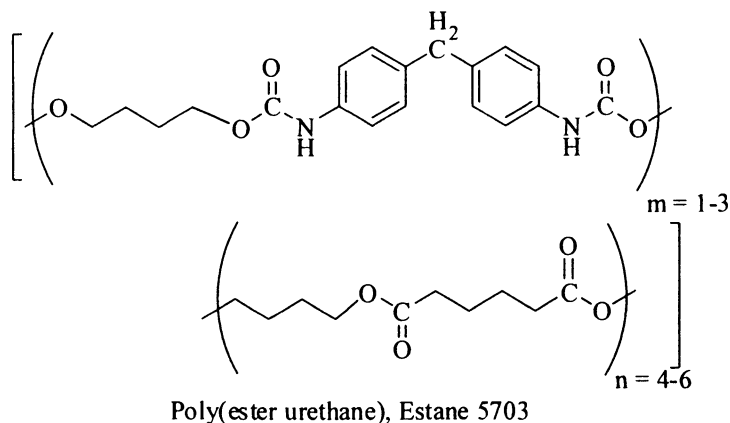


Figure 1. Chemical structures of Estane<sup>®</sup> 5703 and nitroplasticizer (BDNPA/F).

In previous studies, we have identified hydrolytic and oxidative degradation as aging mechanisms. Under accelerated aging conditions with water present, chain scission of the poly(ester urethane) dominates due to hydrolysis of the polyester soft segments (2,3). We identified the degradation product through isotopic labeling of the MDI unit in which the bridging methylene group of the hard segment MDI unit undergoes oxidation (4). This oxidation occurs in the absence of oxygen and is attributed to oxidation of Estane by decomposition products of NP (such as NO<sub>x</sub> gases). Under dry, inert atmosphere, we have observed by an increase in the Estane molecular weight. The mechanisms of branching or cross-linking reactions have not been determined although the presence of insoluble gel particles in highly aged Estane/NP samples have been observed in GPC solutions (5). Our present study directly correlates physical properties and kinetic models with these two degradation mechanisms.

## Experimental

### Materials

The Estane<sup>®</sup> 5703 was obtained as pellets from The BF Goodrich Co. Estane<sup>®</sup> 5703 contains approximately 23% wt. hard segments consisting of 4,4'-methylenediphenyl-1,1'-diisocyanate (MDI) and 1,4-butanediol (BDO) chain extender (6) and poly(butylene adipate) soft segment comprised of molecular weight in the range of 1000 AMU. Spectroscopic grade dimethylformamide (DMF) and methylethyl ketone (MEK) were obtained from Fisher Scientific. The nitroplasticizer, a (50/50) eutectic mixture of bis(2,2-dinitropropyl)formal and bis(2,2-dinitropropyl)acetal was obtained from the high explosives group at LANL. Irganox 1010 was obtained from Ciba Geigy.

### Binder Sample Preparation

Estane samples were compression molded at 110°C. The blends of Estane<sup>®</sup> 5703 and NP (50:50 wt ratio) or Estane/NP and Irganox 1010 (49:49:2 wt ratio) were prepared by dissolving the components in MEK to cast thin films followed by air-drying at room temperature. The films were dried *in vacuo* for 2 days, followed by drying at 65°C for 16 hours at ambient pressure. Samples were compression molded at 85°C into approx. 1 mm thick sheets and placed in aging chambers for the various studies.



## Oxidative Binder and Hydrolytic Binder Degradation Aging Studies

The oxidative binder samples of Estane/NP were placed in glass ampoules and flame sealed under argon. Tensile specimens were placed in metal aging chambers, evacuated and back filled with argon to provide a dry oxygen free environment. The samples were placed in aging ovens at 55, 65 and 75°C and removed periodically for analysis.

For hydrolytic aging, samples of Estane, Estane/NP or Estane/NP/Irganox were placed in metal cans in which an aqueous saturated salt solution supplied a constant relative humidity (RH). Saturated aqueous salt solutions were measured *in situ* to give humidity of 73 (NaCl), 53 (MgCl<sub>2</sub>), 35 (NaBr) and 15%RH (LiCl). The samples were placed in the chambers, flushed with argon and placed in a 70°C oven and were removed periodically for analysis.

### Instrumentation

Gel permeation chromatography (GPC) was used to determine molecular weights and molecular weight distributions,  $M_w/M_n$ , of polymer samples. The GPC consisted of an Alliance 2690 pump equipped with a Wyatt Rex Differential Refractive Index Detector and utilized three Polymer Labs PL Mixed B GPC Columns at 70°C (DMF) or 40°C (THF) at a flow rate of 1.0 mL/min. The molecular weights were calculated relative to the retention times of polystyrene and polyethylene oxide standards for DMF or polystyrene and polytetrahydrofuran standards for THF using Empower software.

<sup>1</sup>H NMR spectra were obtained on a Bruker AVANCE 300 NMR spectrometer at 300.13175 MHz using 11.0 μs 90° pulse with a 5.0 s recycle delay. Samples were dissolved in d<sup>7</sup>-dimethyl formamide for the oxidative binder degradation study and in CDCl<sub>3</sub> for the hydrolysis binder degradation study using methyl sulfone as an internal reference. T<sub>2</sub> measurements of hydrolyzed Estane were obtained using the minispec ProFiler by Bruker Optics using the CPMG pulse sequence on the NMR Mobile Universal Surface Explorer (NMR MOUSE).

For tensile properties, dog-bone samples were cut from the aged specimens using ASTM die. The mechanical properties were measured using two different instruments: a) an Instron (model # 4483) load frame with a 1KN load cell at a rate of 1.6 mm/sec (taken to break) and b) a load frame from the Ernest F. Fullam Company at a rate of 0.1 mm/sec using the Fullam Materials Testing System. The Fullam system uses the automated data acquisition package MTESTWindows™ from ADMET, Inc. Each data set is an average of 5 samples.

## Results and Discussion

Estane/NP binder was aged under inert atmosphere at 65, 75 and 85°C for the oxidative degradation study. These samples were analyzed by  $^1\text{H}$  NMR and GPC analysis. The first order kinetics was examined based on the relative amount of oxidation in Estane. Mechanical properties of this aged binder were examined and were correlated to the amount of Estane oxidation.

The hydrolytic degradation study examined the aging of Estane at various humidity using saturated salt solutions. The GPC and  $^1\text{H}$  NMR analysis quantified the amount of hydrolytic chain scission. These results were utilized to validate a hydrolytic degradation model for pristine Estane and Estane/NP/Irganox 1010. Estane/NP without Irganox showed signs of both hydrolytic degradation and oxidative degradation. These studies are discussed in detail in the next sections.

### Oxidative Binder Degradation Study

Under dry, inert atmosphere, Estane/ NP undergoes oxidative degradation in which the bridging methylene group of the hard segment MDI unit is oxidized. This oxidation occurs in the absence of oxygen and is attributed to oxidation decomposition products of NP. Identification of this oxidation degradation product and of associated  $^1\text{H}$  NMR resonances was accomplished by 1-D and 2-D NMR techniques using  $^{15}\text{N}$  HMCQ NMR techniques in our earlier study (4).  $^{15}\text{N}$  enriched Estane analogues and MDI model compounds were synthesized in which the nitrogen of the urethane methyl diisocyanate-unit (MDI-unit) was 100% enriched with  $^{15}\text{N}$  (4) and thermally aged.

In the present study, the GPC of aged Estane/NP in DMF or THF solvent showed an increase in the polydispersity index (PDI, Mw/Mn) from 1.8 to >3.0 upon aging. At long aging times, gel particles were observed while filtering GPC samples. Evidence of branching or cross-linking of Estane due to dimerization of the bridging methylene group and use of GPC PDI data to determine kinetics for this system is discussed in detail in another chapter in this volume (7). While the mechanisms of branching or cross-linking reactions have not been determined, the observed oxidation product is a possible precursor to these gels.

The aged Estane/NP samples were analyzed by proton NMR as seen in Figure 2. Deuterated DMF was used as the solvent because the NH resonances were well separated from aromatic protons due to solvent hydrogen bonding. Upon aging Estane/NP, a new NH resonance for oxidized Estane at 10.05 ppm grows in intensity relative to 9.5 ppm for unaged Estane. The phenyl protons collapse from a doublet of doublets at 7.1-7.6 ppm to a broad multiplet at

7.8 ppm. Integration of these two sets of resonances allowed us to quantitate the amount of oxidized MDI in the polymer summarized in Table I. Results are similar for either the NH or phenyl protons.

Proton NMR data for the relative amount of oxidized MDI can be plotted as a function of aging time to evaluate the kinetics of this process. The first order kinetics fit of the NMR data is shown in Figure 3. Rate (slope) of 0.0011/day (N-H) and 0.0012/day (Phenyl-H) agrees well with the rate derived on  $\text{NO}_x$  gas analysis data (8) and from the earlier NMR study. An Arrhenius treatment of the data at 65, 75, 85°C calculated the activation energy as  $E_a = 25.5$  kcal/mol.

The mechanical properties were evaluated by two sets of tensile measurements. Typical stress-strain curves are shown in Figure 4. The modulus and stress decrease with increasing aging time. Similar results are observed for all aging samples at all three temperatures. Both testing methods provided essentially the same tensile data at 400% extension. The scatter of the tensile data is due to the experimental error associated with the measurement.

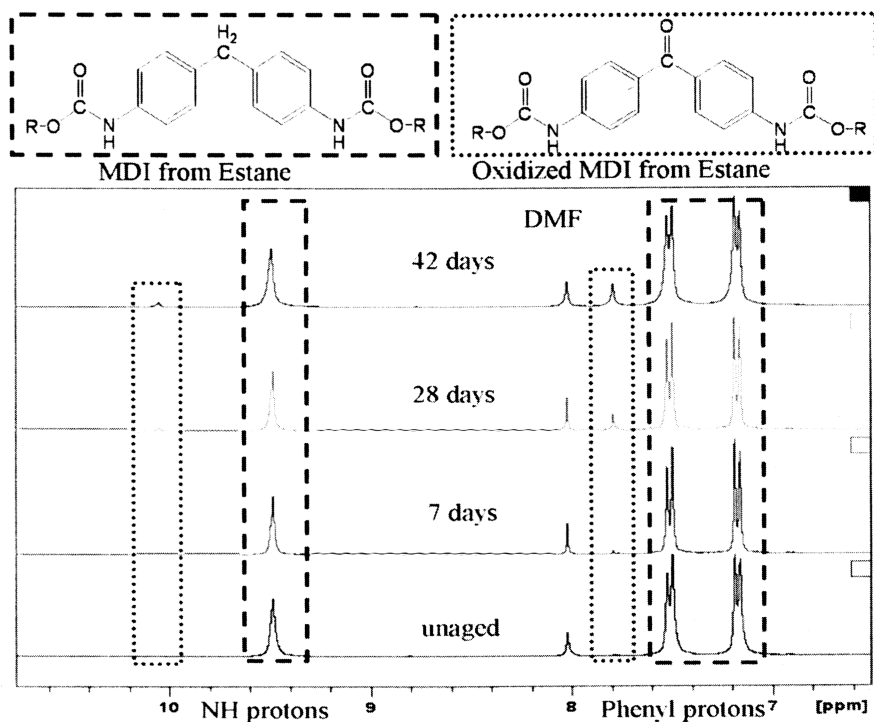
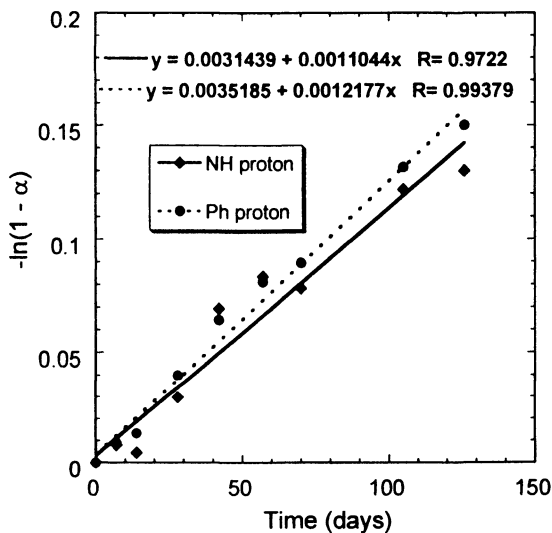


Figure 2.  $^1\text{H}$  NMR spectra of the Estane/NP binder aged at 85°C under argon.

**Table I. Percentage Oxidation of Estane Based on  $^1\text{H}$  NMR integration of Binder Aged at  $85^\circ\text{C}$**

Days aged	% Oxid. (N-H)	% Oxid. (Ph-H)	$-\ln(1-\alpha)$
0	0	0	0
7	0.79	0.90	0.00902
28	2.91	3.90	0.01322
42	6.69	6.23	0.03975
57	8.00	7.78	0.06437
70	7.52	8.56	0.08953
105	11.46	12.31	0.13147

$\alpha = \% \text{Oxid.}/100$



*Figure 3. First order kinetics based on NMR data of % oxidation of phenyl and N-H protons.*

This correlation implies that oxidative degradation is responsible for the observed decrease in the mechanical strength. Mechanical properties of multi-phase polymers such as Estane are determined by the domain structure. Accelerated aging at elevated temperatures is known to perturb the domain structure which reforms upon cooling. Change in MDI segments by oxidation or branching or cross-linking reactions, as discussed above, could alter the reformation of hard domains. Thus, the network structure would be irreversibly altered by aging, resulting in a weaker material (1) as seen by Wilkes for similar systems.

### Hydrolytic Binder Degradation Study

The soft segments of Estane have been shown to hydrolyze via an acid-catalyzed mechanism in which a water molecule attacks an ester link and forms an acid end group and an alcohol end group on the polymer chain. The breaking of the ester links leads to a decrease in molecular weight (MW) for Estane exposed to humid conditions and oxygen free environment. The hydrolytic degradation of Estane/NP has been studied with and without stabilizer. The stabilizer, Irganox 1010, is a free radical scavenger. The GPC chromatograms of hydrolyzed Estane or Estane/NP with Irganox show a smooth decrease in molecular weight with little change in peak width (PDI) indicating chain scission reactions dominate (Figure 6a). Pristine Estane hydrolyzes at a faster rate than Estane/NP/Irganox implying that stabilizer slows the hydrolysis process.

When Estane/NP is hydrolyzed without stabilizer, both a decrease in molecular weight and an increase in PDI were observed (Figure 6b). For samples aged for greater than 28 days, a high molecular weight tail is observed below 19 minutes retention time. This indicates both chain scission and branching reactions may be occurring with aged Estane /NP binder. NMR analysis of the aged Estane/NP binder without stabilizer showed signs of oxidation of the bridging methylene group similar to that seen in Figure 2. In contrast, samples of aged Estane and Estane/NP/Irganox show no signs of oxidation chemistry. This antioxidant may inhibit Estane oxidation due to decomposition of NP.

$^1\text{H}$  NMR analysis of hydrolyzed Estane in deuterated chloroform allows observation of hydrolysis products. Examination of the  $^1\text{H}$  NMR of aged binder revealed features associated with hydrolysis of the polyester soft segments of Estane (9) as seen in Figure 7. The ester hydrolysis yields an acid group and an alcohol end group for each chain scission reaction as shown below. Identification of the resonance at 3.65 ppm as the  $\text{CH}_2$  group adjacent to the hydroxyl group of the alcohol hydrolysis product provided a means to quantify

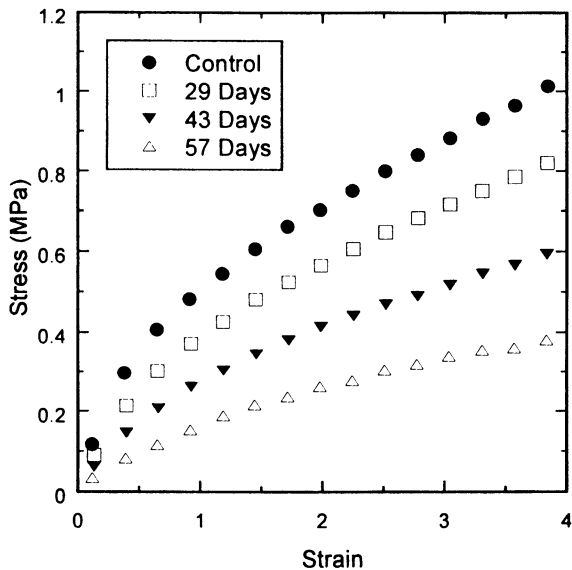


Figure 4. Stress – strain curves for tensile data of Estane/NP aged at 85°C.

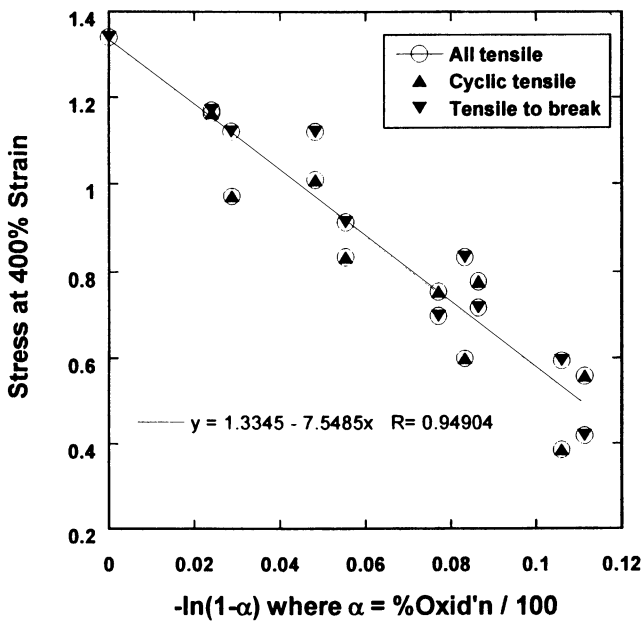


Figure 5. Correlation of tensile stress at 400% strain for samples with oxidation of the methylene carbon of Estane at 65, 75 and 85°C.

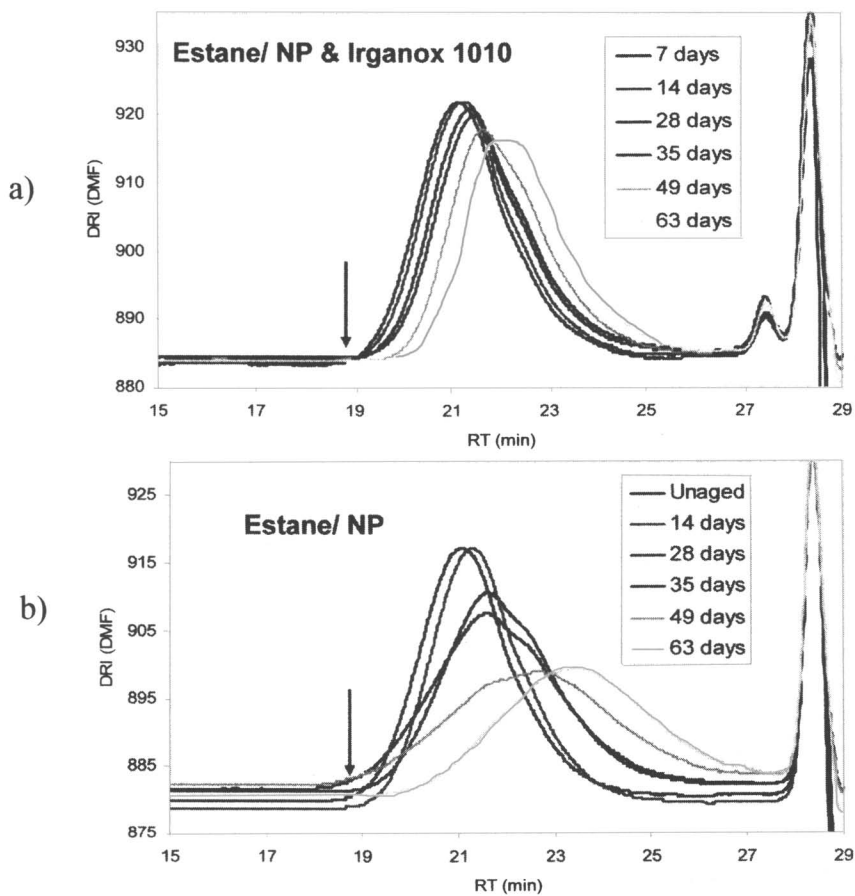


Figure 6. GPC of a) Estane/NP with Irganox 1010 and b) Estane/NP hydrolyzed at 70°C, 73%RH.

the amount of polymer hydrolysis occurring under different humidity conditions. Pristine Estane contains a small amount of alcohol end groups due to the manufacturing process. The relative amount of alcohol groups (L/L<sub>0</sub>) is determined by dividing the integration of the alcohol peak (L) at 3.65 ppm in the aged sample by amount of alcohol in the unaged Estane (L<sub>0</sub>).

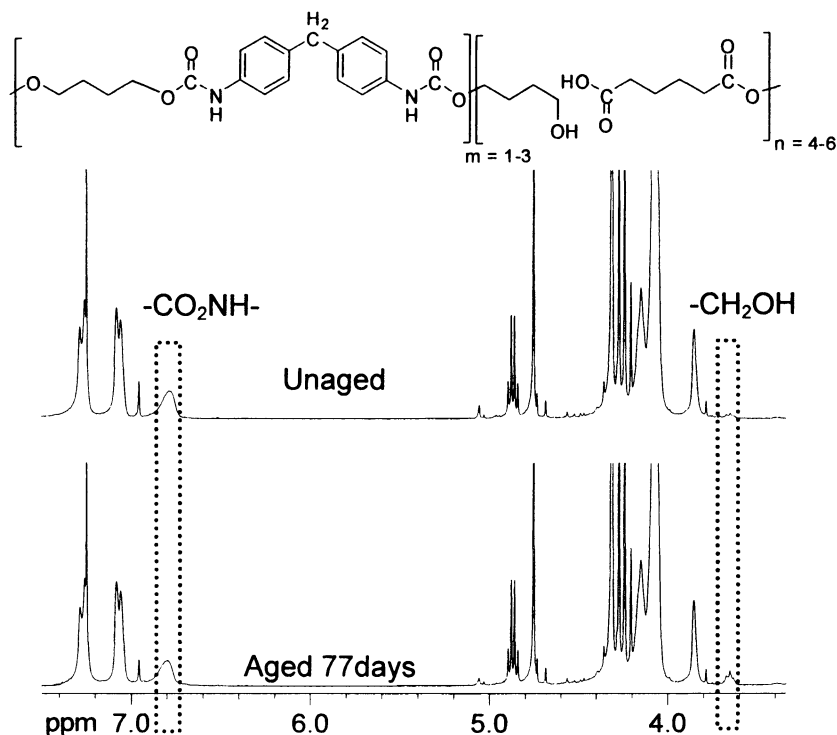


Figure 7.  $^1\text{H}$  NMR ( $\text{CDCl}_3$ ) of Estane/NP/Irganox 1010 aged at 73% RH 70°C.

The NMR and GPC results were utilized to validate predictive models based on Estane hydrolysis (2). The scission of the ester linkage leads to a decrease in molecular weight (MW) for Estane exposed to humid conditions. A single set of rate coefficients for this mechanism was obtained (2) by fitting to several different hydrolytic aging experiments for neat Estane and more recently (3) for the binder in PBX 9501 (which contains Estane, NP and Irganox 1010). The rate constants are employed in a kinetics model and the rate equations are integrated numerically to simulate the change in MW with time. In the present work, the rate coefficient for water adsorption was decreased slightly to best capture the change in MW of the binder over the wide range of relative humidity values. All of the other (hydrolysis) rate coefficients (3) were left unchanged.



This slight change in the water adsorption rate is probably due to the difference in water uptake between pure binder (used in this study) and the binder within PBX 9501 which is surrounded by HMX. As seen in Figure 8, good agreement is observed between the hydrolysis model and the experimental molecular weight hydrolysis data for several humidity's.

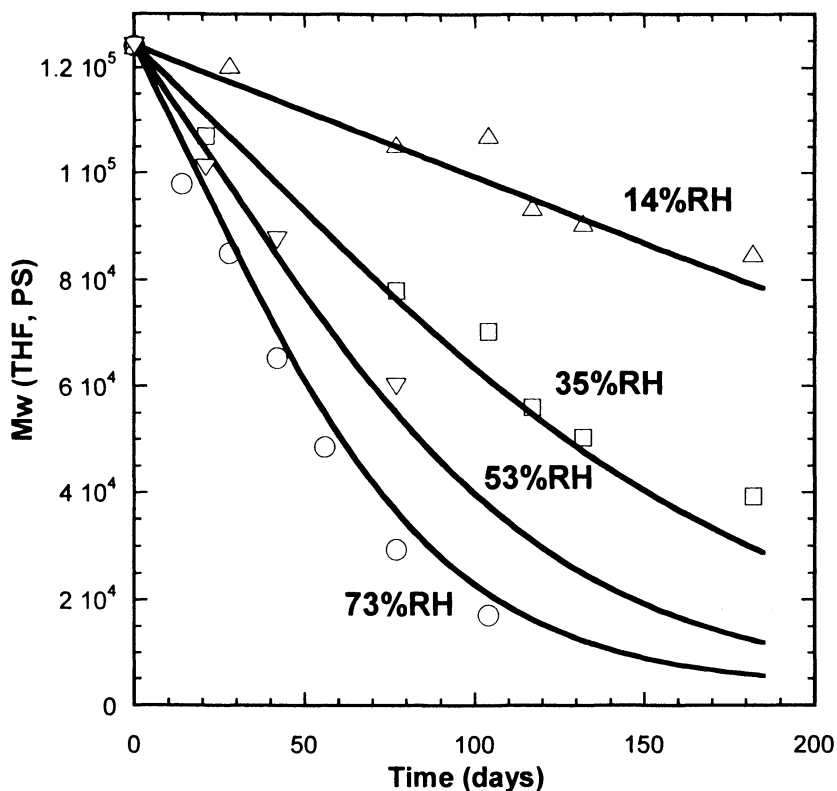


Figure 8. Comparison of the experimental data (open markers) with hydrolysis model (solid line) for Estane/NP/Irganox at 70°C at given humidity.

In addition to predicting molecular weight of Estane under various humidity conditions, the model can predict the relative amount of hydrolysis products with alcohol end-groups. An exponential relationship in Figure 9 is seen between L/Lo and the molecular weight for both Estane and Estane/NP/Irganox binder hydrolyzed under several different humidities at 70°C. Even though, the rates of hydrolysis for these samples were different, a relationship MW between L/Lo was observed.

The experimental data for molecular weight and L/Lo agree well with the hydrolytic degradation predictive model for Estane as shown in Figure 10. Ongoing experimental work validating the Estane hydrolysis model for Estane binder will contribute to providing a robust lifetime prediction for PBX 9501 explosives.

In addition, we have probed hydrolyzed Estane sample with the NMR Mobile Universal Surface Explorer (NMR MOUSE) (10). This technique is a quick non-invasive technique to determine the effect that polymer degradation has on its physical properties. Polymer chain mobility can be detected by proton spin-spin relaxation time measurements of hydrolyzed Estane using the NMR MOUSE. The spin-spin relaxation time decay curve shows increased chain mobility upon hydrolysis (Figure 11). The decay curve is fitted with a biexponential decay function to give two  $T_2$  values. The  $T_{22}$  associated with the more mobile polymer chains shows an inverse relationship to the molecular weight decrease as would be expected. This technique shows promise as an *in situ* probe of hydrolysis in high explosives in a non-destructive manner.

## Conclusions

Accelerated aging of PBX 9501 binder is a powerful technique for developing and validating models for lifetime predictions. Understanding of the aging mechanisms has provided valuable experimental data to the modeling effort. We probed two different degradation pathways for the HE binder: oxidative and hydrolytic degradation.

Oxidative degradation dominates when Estane/NP is thermally aged in the absence of water and oxygen. Through NMR analysis, the oxidation of the bridging methylene group was quantified. These data contributed to the development of kinetic models for prediction of oxidative degradation. We observed a correlation between oxidation and mechanical properties.

Hydrolytic degradation dominates for Estane and Estane/NP/Irganox 1010 in the absence of oxygen. This resulted in chain scission reactions in which Estane/NP/Irganox degraded less rapidly than Estane alone. Estane/NP without Irganox experiences both chain scissions and oxidation reactions. The Irganox 1010 additive is an antioxidant which may be protecting the NP from oxidative degradation reactions forming  $\text{NO}_x$  under the hydrolytic aging environment.

The potential value of the NMR MOUSE for detecting hydrolytic degradation in Estane was demonstrated. This technique is sensitive to increased chain mobility in the degraded Estane and showed a good correlation of the relaxation time with a decrease in molecular weight. Additional studies of aged Estane/NP/Irganox binder are underway to evaluate use of this instrument.

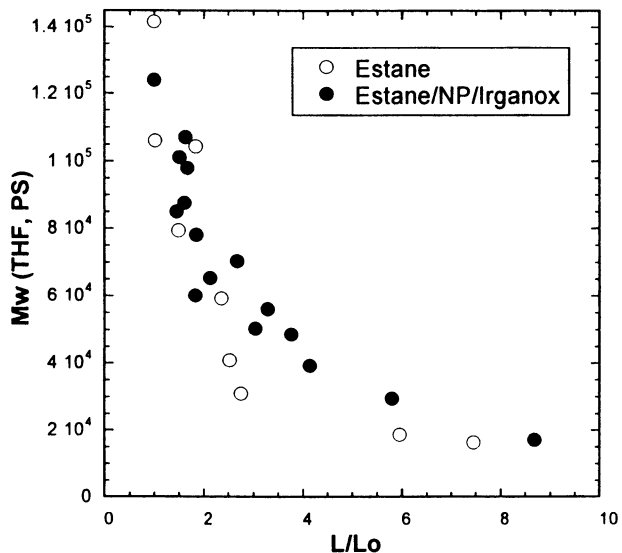


Figure 9. Plot of molecular weight vs. relative amount of alcohol end groups for hydrolyzed Estane and Estane/NP/Irganox at several humidities at 70°C.

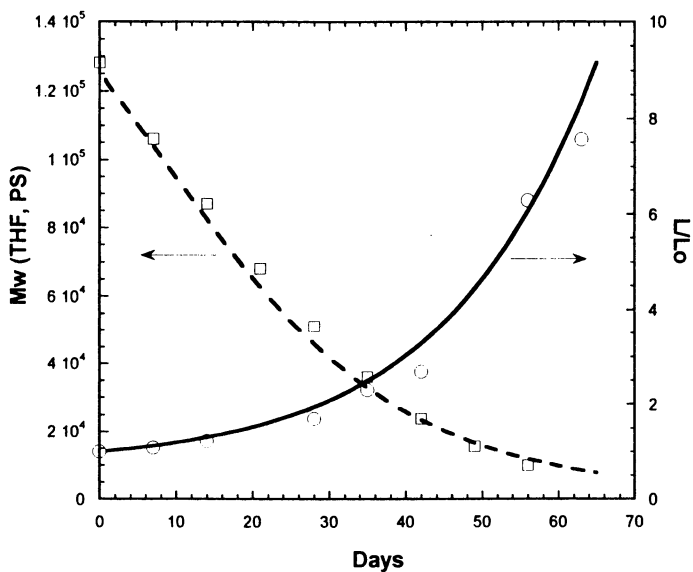


Figure 10. Comparison of experimental data (open markers) with model (line) for hydrolytic aging of Estane. Dashed line is the model for molecular weight and solid line is the model for relative alcohol content in the polymer.

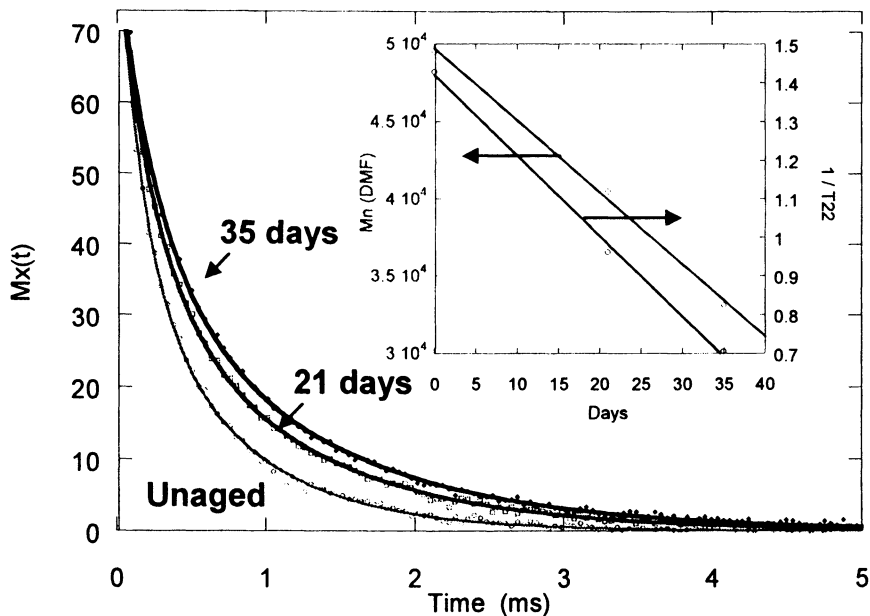


Figure 11. Proton spin-spin relaxation decay curve of Estane hydrolyzed at 53%RH and the correlation of aging time with molecular weight and inverse  $T_{22}$ .

### Acknowledgement

This work was supported by the U.S. Department of Energy at Los Alamos National Laboratory, operated by the University of California under contract number W-7405-ENG-36 and operated by Los Alamos National Security, LLC under contract number DE-AC52-06NA25396.

### References

- Ophir, Z. H.; Wilkes, G. L. In *Multiphase Polymers*; Editor, Cooper, S. L.; Estes, G. M, Eds.; Advances in Chemistry Series. No. 176; ACS: Washington DC, 1979; pp 53-67.
- Salazar, M. R.; Lightfoot, J. M.; Russell, B. G.; Rodin, W. A.; McCarty, M.; Wroblewski, D. A.; Orlor, E. B.; Spieker, D. A.; Assink, R. A.; Pack, R. T. J. *Polym. Sci. Part A: Polym. Chem.* **2003**, *41*(8), 1136-1151.

3. Kendrick, B. K.; Pack, R. T.; Salazar, M. R.; Kress, J. D. *Proceedings of the 27th Aging, Compatibility and Stockpile Stewardship Conference*, Los Alamos National Laboratory, 26-28 September 2006, LA-UR-06-6627.
4. Wroblewski, D. A.; Langlois, D. A.; Orlor, E. B.; Dattelbaum, D. M.; Small, J. H. *Polym. Prepr.* **2004**, *45(1)*, 789-790.
5. Orlor, E. B.; Wroblewski, D. A.; Cooke, D. W.; Bennett, B. L.; Smith, M. E.; Jahan, M. S.; King, M. C. *Polym. Prepr.* **2001**, *42(1)*, 428-429.
6. Hoffman, D. M.; Caley, L. E. *ACS Div. Org. Coat. Plast. Chem.* **1981**, *44*, 686-690.
7. Kress, J. D.; Wroblewski, D. A.; Langlois, D. A.; Orlor, E. B.; Lightfoot, J. M.; Rodin, W. A.; Huddleston, C.; Woods, L.; Russel, B. G.; Salazar, M. R.; Pauler, D. K., this volume.
8. Pauler, D. K.; Kress, J. D.; Lightfoot, J. M.; Woods, L.; Russell, B. G. *AIP Conf. Proc.* **2006**, *845*, pp 547-550.
9. LeMaster, D. M.; Hernandez, G. *Macromolecules* **2000**, *33*, 3569-3576.
10. Uribe, M.; Wroblewski, D.; Labouriau, D. A. *NMR-MOUSE: An Economical, User-Friendly Technique for Probing Polymeric Materials*; Los Alamos National Laboratory Report, LA-UR-06-8580 and references therein.

## Chapter 17

# New Cyanate Ester and Poly(*p*-phenylene) Resins with Low-Moisture Absorption and Improved Thermal Stability

Andrew J. Guenther<sup>1</sup>, Michael E. Wright<sup>1</sup>, Brian J. Petteys<sup>1</sup>,  
Jessica J. Cash<sup>1</sup>, and Gregory R. Yandek<sup>2</sup>

<sup>1</sup>Naval Air Warfare Center, Weapons Division, China Lake, CA 93555

<sup>2</sup>Air Force Research Laboratory, Propulsion Materials Applications  
Branch, Edwards Air Force Base, CA 93524

New cyanate ester and poly-*p*-phenylene (P3) resin materials that exhibit significantly reduced moisture absorption while maintaining thermal stability have been developed and their key properties investigated. The replacement of a single carbon atom by a silicon atom in the repeat unit chemical structure of the di(cyanate ester) of Bisphenol A (BADCy) resulted in a new silicon-containing resin (SiMCy) with a 50% reduction in water uptake and higher char yields in air after curing. Thermosetting Navy P3 resins were found to exhibit moisture uptake similar to poly-*p*-phenylene thermoplastics, a level which is about 85% lower than thermosetting polyimides. Like their thermoplastic counterparts, the Navy P3 resins exhibit outstanding resistance to high temperature degradation. Unlike their thermoplastic counterparts, these resins form low viscosity melts that are easily formed into carbon fiber reinforced composites.

## Introduction

In recent years, the need for lighter, more energy efficient structures, increased interest in new high speed aircraft and weapons systems, and a growing desire to incorporate structures with good electrical insulating characteristics and little or no interaction with electromagnetic radiation have all contributed to renewed research and development in the area of high-strength, high temperature polymer matrix composite materials. The successful development and utilization of these materials is often limited by undesirable properties of the polymer matrix resin materials that require significant cost and complexity to mitigate. These undesirable properties include 1) toxicity of many of the chemicals used to fabricate the resins, 2) poor performance (excessive flame and smoke, dripping, and generation of hazardous substances) during fires, 3) significant absorption of water in a humid environment (which has been linked to delamination during rapid heating (*I*), and 4) in the case of many of the materials with the highest use temperatures, difficulties in fabrication, especially when using inexpensive fabrication techniques. The second and third of the foregoing issues are of special concern to applications involving operation in a ship-board environment.

In order to address these concerns, new types of thermosetting polymeric resins that are potentially superior replacements for state-of-the-art materials have been developed. The following report describes these materials and their advantages compared to state-of-the-art commercial materials, covering two distinct classes of resin: cyanate esters and poly-p-phenylenes. In each case, the descriptions focus on the resistance to moisture uptake and thermal degradation, with a brief discussion of the processing characteristics. For both classes of resin, the newly created candidates are as easy, if not easier, than currently available materials to incorporate into composite structures using simple processing techniques. Moreover, they exhibit reduced uptake of water and improvements in thermo-oxidative resistance, illustrating that the next generation of polymer composite resin materials is likely to overcome many of the current obstacles to more widespread utilization.

## Experimental

### Materials and Sample Fabrication

The di(cyanate ester) of bisphenol A (BADCy) was supplied by Lonza and used as received (HPLC indicated the monomer was 99.4% pure). The chemical synthesis of a silicon-containing analog to BADCy, the di(cyanate ester) of dimethylbis(p-phenol)silane, (referred to as SiMCy), has been described

previously (2,3). An extensive set of additional physical data for SiMCy has been published elsewhere (3). The chemical structures of the BADCy and SiMCy monomers are shown in Figure 1. Castings for both BADCy and SiMCy were formed by melting the as-received powder at 80-100°C, then carefully pouring into 3 mm deep molds with lateral dimensions of 10 mm x 25.4 mm. The castings were cured via trimerization of the cyanate ester to form polycyanurates without added catalyst (note: phenolic impurities already present at a level of a few parts per thousand in the monomer can catalyze the trimerization) (4) using the following schedule: 100 °C for 30 min, followed by 150 °C for 30 min, 200 °C for 1 h, and lastly 250 °C for 3 h.

The synthesis of poly-p-phenylenes through the catalytic coupling of dichlorides (and monofunctional chlorides that serve as end caps) has been described in a number of reports (5-12). Phenyl ethynyl terminated poly-p-phenylene oligomers exhibiting the structure shown in Figure 2 (referred to as Navy P3-2300-PE, where 2300 represents the number average molecular weight) were synthesized at the Naval Air Warfare Center. Castings of Navy P3-2300-PE were made by sintering the powder in an open mold at 180°C. The castings were subsequently cured at temperatures ranging from 350-450°C by heating at 1°C/min. and holding at the cure temperature for up to 12 h. Curing of the phenyl ethynyl terminated oligomers has been shown to occur through a complex process primarily involving reaction of the acetylene bonds (13). In order to obtain good quality castings, the casting thickness was limited to 1 mm.

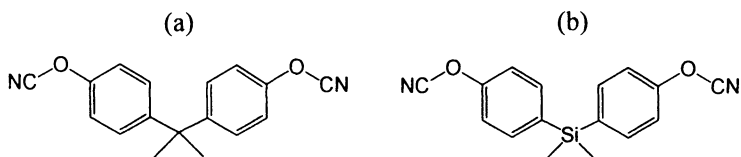


Figure 1. Structures of (a) BADCy and (b) SiMCy.

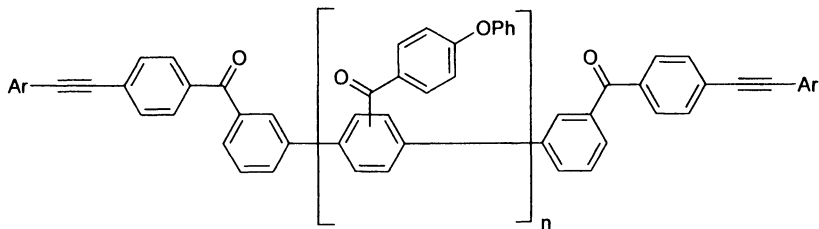


Figure 2. Structure of Navy P3-2300-PE, with  $n = \sim 6.5$  (number average).



## Methods of Analysis

Changes in the weight of 5 mg powdered samples of the cured resin materials were monitored using a TA Instruments 2950 Hi-Res Thermogravimetric Analyzer and/or a TA Instruments Q600 Simultaneous Differential Thermal Analyzer (for simultaneous weight change in heat flow measurements). The changes were observed by heating at 10 °C / min from room temperature to 600 °C. The experiments were conducted in both nitrogen (dew point approximately -70 °C) and laboratory air atmospheres. Viscometry was performed on an Anton Paar MCR500 rheometer in parallel plate configuration with a gap spacing of 1.5 mm under a nitrogen blanket. Exposure of casting samples to moisture was accomplished by immersion in deionized water either at room temperature or maintained at a slight boil. Each sample was weighed twice prior to exposure and twice after exposure. All castings were carefully patted dry with a clean laboratory cloth prior to weighing after exposure. Measurements of the glass transition temperature before and after immersion in water were performed on small sections of castings using either a TA Instruments Q100 Differential Scanning Calorimeter (DSC) at a heating rate of 10 °C/min, or using a TA Instruments Q400 Thermomechanical Analyzer (TMA) in expansion mode with a standard 2.5 mm diameter flat cylindrical probe and 0.02 N clamping force, at a slower heating rate of 2 °C/min (due to a more significant instrument thermal lag).

## Results and Discussion

### Cyanate Ester Resins

Figures 3a and 3b compare the TGA curves of BADCy and SiMCy under nitrogen (Figure 3a) and air (Figure 3b). Although BADCy performs slightly better under nitrogen, SiMCy performs better in air. On closer analysis, it is apparent that the secondary, higher-temperature weight loss in air observed in BADCy has been suppressed in SiMCy. Since many silicon-containing materials are known to generate SiO<sub>2</sub> during heating at high temperatures in air (14), a reasonable interpretation of the data is that the formation of SiO<sub>2</sub> in SiMCy has imparted additional thermal stability at temperatures in excess of 500 °C.

In Figure 4, the weight gain of castings of BADCy and SiMCy cured using an identical procedure is compared as a function of time of exposure to boiling water. The moisture uptake in SiMCy is about 50% lower than that of BADCy. It is worth noting that other modified versions of BADCy, such as those that utilize hydrophobic CF<sub>3</sub> groups in place of the CH<sub>3</sub> groups, or those that utilize additional CH<sub>3</sub> groups in the vicinity of the cyanate ester groups in the monomer,

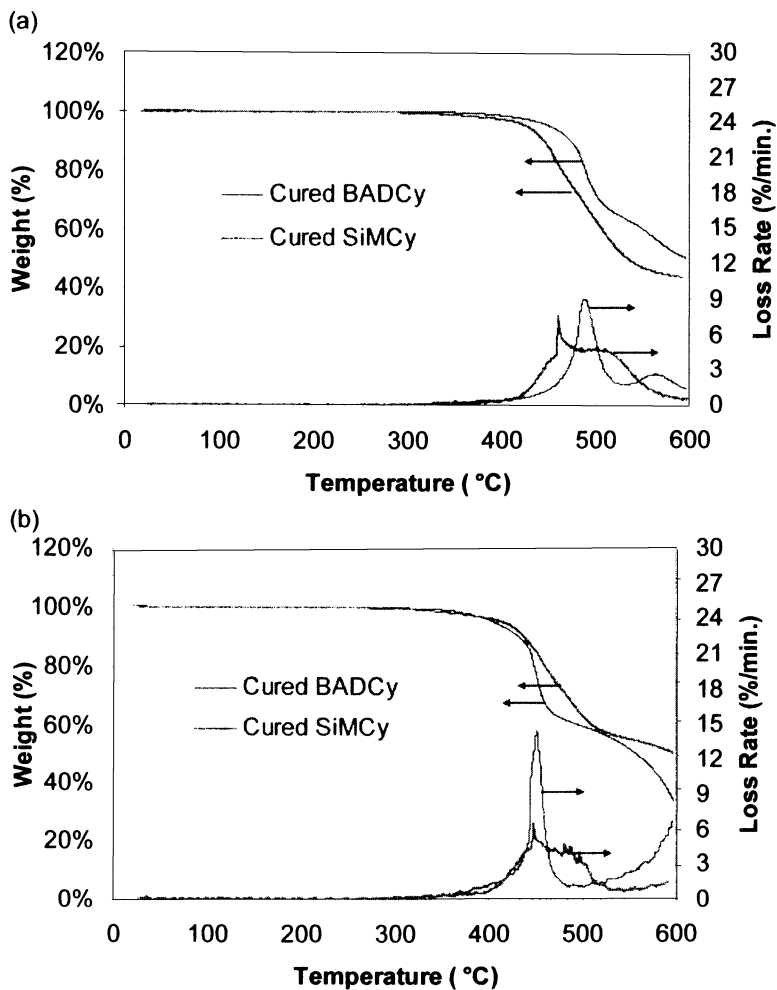


Figure 3. TGA curves of BADCy and SiMCy compared (a) under nitrogen, and (b) in air.

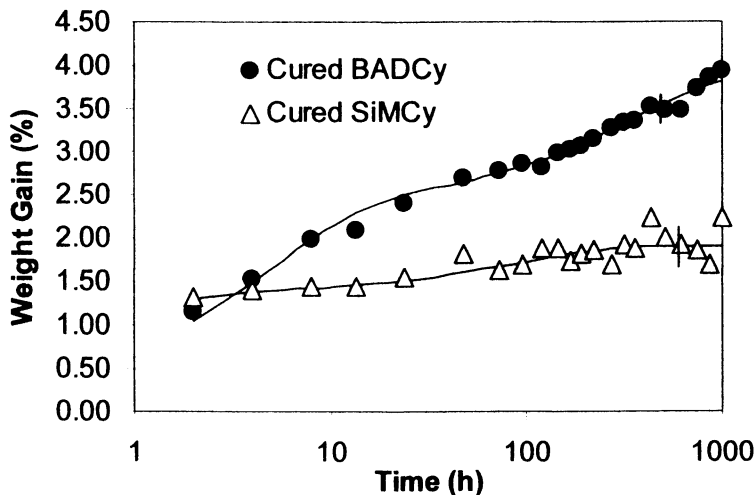


Figure 4. Weight gain of BADCy and SiMCy as a function of time of exposure to boiling water.

also exhibit reduced moisture uptake (15). In these cases, the reduced moisture uptake may be explained by the presence of more hydrophobic groups in the polymer, or by steric hinderance in the vicinity of the polar cyanate ester groups.

However, in the case of SiMCy, which differs from BADCy only by one atom that is remote from the cyanate ester groups, neither explanation seems feasible. Interestingly, observations of the crystal structures of SiMCy (3) and BADCy (16) by X-ray diffraction reveal unexpectedly large differences in how the monomers are packed into repeating asymmetric units. Moreover, measurements of the density of the cured amorphous BADCy and SiMCy castings show that the molar volumes of the repeating units differ substantially, with SiMCy being larger (3). It is therefore possible that differences in the preferred conformations and interchain spacing of cured BADCy and cured SiMCy are sufficient to reduce the number and/or quality of sites for absorbed water.

Based on the foregoing discussion, one might expect SiMCy to exhibit other significant differences compared to BADCy. However, SiMCy differs only slightly from BADCy in terms of cure kinetics when determined by non-isothermal DSC scans (3). In terms of processing, both BADCy and SiMCy were found to have low viscosities in melt form, with the melting point of SiMCy at about 60°C (compared to 80°C for BADCy). Thus, the improved thermo-oxidative stability and reduced moisture uptake provided by SiMCy are available with minimal impact on existing composite fabrication operations.

## Poly-p-phenylene Resins

Although poly-p-phenylene (P3) resins have historically been of interest because of their outstanding thermal stability, they also feature a non-polar chemical character that should make them a poor host for absorbed water. In the form of high molecular weight thermoplastics, these resins have recently been commercialized. The commercial resins form high viscosity melts and exhibit limited solubility (with very high solution viscosity) in organic solvents, therefore they are not well-suited to composite fabrication operations. In the oligomeric form with reactive end caps, though, these resins form much lower viscosity melts, as demonstrated by the rheometry data shown in Figure 5 for Navy P3-1500 (a non-reactive end-capped P3 oligomer with  $M_n \sim 1500$ ). The observed viscosities are sufficiently low to allow for the infiltration of carbon fiber mats using only minimal pressure at temperatures above 180 °C. For Navy P3 oligomers with reactive phenyl ethynyl end caps and a somewhat higher molecular weight, such as Navy P3-2300-PE, a slightly higher infiltration temperature of around 210 °C is needed. On further heating, the viscosity of Navy P3-2300-PE falls to 1.8 Pa s (1800 cP) at 300 °C. Using a heating rate of 1 °C/min, significant cross-linking of Navy P3-2300-PE requires up to 12 h at 350 °C, 4 h at 370 °C, 1 h at 390 °C, and no additional time at 450 °C.

In Figure 6, the TGA curve for Navy P3-2300-PE after curing at 390 °C for 1 h is displayed. With only limited weight loss observed in nitrogen at temperatures up to 900 °C, and very limited weight loss at temperatures below 400 °C, the thermal stability of the cured Navy P3 resin renders it suitable for a number of high temperature applications. Additional experiments have shown that carbon fiber mats infiltrated with molten Navy P3 oligomers and subsequently cured display self-extinguishing characteristics when exposed to flames. Thus, the Navy P3 resins appear to possess the same outstanding high temperature degradation and fire resistance characteristics seen in poly-p-phenylene thermoplastics.

In Table 1, the moisture uptake of cured and uncured Navy P3-2300-PE resin after 24 hours of immersion is compared to a number of other high-temperature polymer resins. The moisture uptake of the Navy P3 oligomer is nearly identical to that of the commercial P3 thermoplastic. Other commercial thermoplastics, such as poly(ether ether ketone), with very similar chemical compositions, exhibit similarly low levels of moisture uptake. On the other hand, the Navy P3 resins absorbs about 85% less water than the commercial polyimide Kapton® HN. Since thermosetting phenyl ethynyl end-capped polyimides have moisture uptake characteristics that are similar to Kapton® HN, with around 3% weight gain on exposure to 95% relative humidity (17), void-free composites based on Navy P3 resins should exhibit greatly reduced moisture uptake compared to those based on thermosetting polyimides.

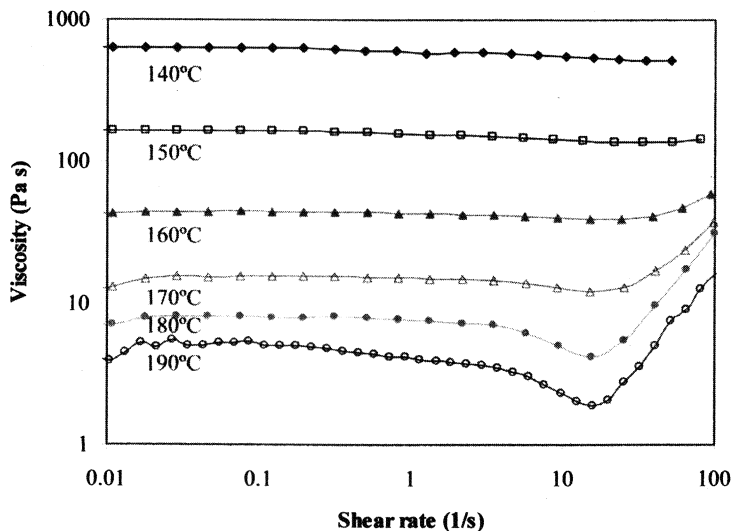


Figure 5. Shear viscosity of P3-1500 as a function of temperature.

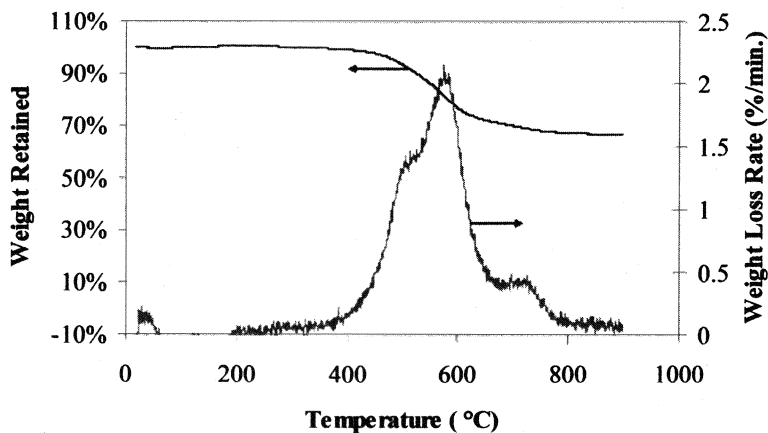


Figure 6. TGA of P3-2300-PE after curing at 390°C for 1 h, under nitrogen.

Table 2 compares the glass transition temperature of both cured and uncured Navy P3-2300-PE resin before and after exposure to boiling water, using DSC for the uncured samples and TMA for the cured samples. The absorption of water can produce both a reversible decrease in Tg due to plasticization, as well as irreversible changes in Tg due to chemical degradation. If the Tg can be

**Table 1. Moisture Content After 24 Hours of Immersion in Water**

Material	Condition	Weight Gain
P3-2300-PE	No cure (sintered at 180 °C)	0.4%
P3-2300-PE	Cured 1 h at 390 °C	0.5%
P3-2300-PE	Heated at 1 °C/min to 450 °C	0.5%
TECAMAX™ SRP	Commercial P3 thermoplastic	0.5%[18]
Victrex PEEK™ 450 PF	Commercial polyetheretherketone	0.5%[19]
Kapton HN®	Commercial polyimide film	2.8%[20]

**Table 2. Effect of Exposure to Boiling Water on Glass Transition Temperature of P3 Oligomers**

Sample	Cure	Boil Time(h)	Tg °C (Before)	Tg °C (After) <sup>a</sup>
P3-2300-PE	1 °C/min to 350 °C	120	129.2	129.0(d)123.1 (w) <sup>b</sup>
P3-2300-PE	1 °C/min to 350 °C	168	130.0	130.5 (d)
P3-2300-PE	1 °C/min to 350 °C	337	128.8	130.0 (d)
P3-2300-PE	350 °C for 12 h	24	216 ± 8 <sup>c</sup>	213 ± 8(d) <sup>c</sup>

<sup>a</sup> All Tg values determined by DSC, with an error of less than 1 °C, unless noted otherwise

<sup>b</sup> (d) indicates the sample was dry when the Tg was measured, (w) indicates the sample was still wet

<sup>c</sup> Determined by TMA based on change in thermal expansion coefficient.

measured while absorbed water is still present, both the reversible and irreversible changes in Tg will be observed, while only the irreversible change in Tg can be observed if the sample is dried prior to measurement, or dries out during measurement prior to reaching Tg. Conveniently, the endothermic loss of moisture may be observed in DSC traces, while the shrinkage that takes place upon loss of moisture is detectable in TMA traces, so for these experiments, it is possible to tell whether the sample is still wet when the Tg is measured. Fortunately, the Tg of uncured Navy P3-2300-PE is low enough that in some cases it can be measured while still wet, allowing both the reversible and irreversible changes in Tg to be determined. According to Table 2, then, the irreversible change in Tg for all Navy P3-2300-PE samples is negligible, while the reversible decrease in Tg for the uncured Navy P3-2300-PE is about 5 °C, which is significantly less than is typical for cyanate esters or polyimides.

## Conclusions

The new silicon-containing cyanate ester resin given the acronym SiMCy exhibits superior thermo-oxidative stability when compared to its carbon-containing analog (BADCy) above 500 °C, most likely due to the formation of SiO<sub>2</sub> during heating. Furthermore, the moisture uptake of SiMCy was 50% lower than BADCy. These improved properties are available with no decrease in ease of processing. Even more dramatic reductions in moisture uptake were observed in reactive end-capped oligomeric poly-p-phenylene (Navy P3) resins, up to 85% when compared to polyimide resins envisioned for similar high-temperature applications. These poly-p-phenylene oligomers show outstanding thermal stability up to 400°C and are easily formed into flame-resistant carbon fiber composites for use in high temperature applications.

## Acknowledgement

The authors wish to thank the Office of Naval Research (Code 332) for their support. In addition, the efforts of BJP and GRY were supported through the American Society of Engineering Education's Post-Doctoral Fellowship Program.

## References

1. Nadler, M. P. "Thermal Degradation Study of IM7/DMBZ-15 High Temperature Composite by TGA/FTIR" Technical Paper NAWCWD-TP-8568, Naval Air Warfare Center, Weapons Division, China Lake, CA 93555, Research Dept., September 2003.
2. Wright, M. E. *Polym. Prepr.* **2004**, *45* (2), 294.
3. Guenther, A. J.; Yandek, G. R.; Wright, M. E.; Petteys, B. J.; Quintana, R.; Connor, D.; Gilardi, R. D.; Marchant, D. *Macromolecules* **2006**, *39*, 6046.
4. Bauer, M.; Bauer, J. In *Chemistry and Technology of Cyanate Ester Resins*; Hamerton, I.; Ed.; Blackie Academic: Glasgow, 1994; pp. 61.
5. Stille, J. K.; Gilliams, Y. *Macromolecules* **1971**, *4*, 515.
6. VanKerckhoven, H. F.; Gilliams, Y. K.; Stille, J. K. *Macromolecules* **1972**, *5*, 541 and references therein.
7. Hamaguchi, M.; Sawada, H.; Kyokane, J.; Yoshino, K. *Chem. Lett.* **1996**, 527.
8. Gin, D. L.; Conticello, V. P. *Trends Polym. Sci.* **1996**, *4*, 217.
9. Percec, V.; Hill, D. H. *ACS Symp. Ser.* **1996**, *624*, 2.

10. Marrocco, M. L.; Gagne, R. R.; Trimmer, M. S. U.S. Patent 5,756,581, 1998.
11. Marrocco, M. L.; Gagne, R. R.; Trimmer, M. S. U.S. Patent 5,565,543, 1996.
12. Marrocco, M. L.; Gagne, R. R.; Trimmer, M. S. U.S. Patent 5,227,457, 1993.
13. Wright, M. E.; Schorzman, D. A.; Pence, L. E. *Macromolecules* **2000**, *33*, 8611, and references therein.
14. Zheng, L.; Farris, R. J.; Coughlin, E. B. *Macromolecules* **2001**, *34*, 8034.
15. Hamerton, I. In *Chemistry and Technology of Cyanate Ester Resins*; Hamerton, I., Ed.; Blackie Academic: Glasgow, 1994, pp. 217.
16. Fyfe, C. A.; Niu, J.; Rettig, S. J.; Burlinson, N. E.; Reidsema, C. M.; Wang, D. W.; Poliks, M. *Macromolecules* **1992**, *25*, 6289.
17. Bhargava, P.; Chuang, K. C.; Chen, K.; Zehnder, A. *J. Appl. Polym. Sci.* **2006**, *102*, 3471.
18. Data provided by supplier, published at URL [http://www.boedeker.com/tecamax\\_p.htm](http://www.boedeker.com/tecamax_p.htm), accessed 9/11/2007.
19. Data provided by supplier, published at URL <http://www.matweb.com/search/SpecificMaterial.asp?bassnum=PVICTA>, accessed 9/11/2007.
20. Data provided by supplier, published at URL [http://www2.dupont.com/Kapton/en\\_US/assets/downloads/pdf/summaryofpfp.pdf](http://www2.dupont.com/Kapton/en_US/assets/downloads/pdf/summaryofpfp.pdf), accessed 9/11/2007.



## Chapter 18

# Effects of Hydroxy Double Salts and Related Nanodimensional-Layered Metal Hydroxides on Polymer Thermal Stability

Everson Kandare and Jeanne M. Hossenlopp \*

Department of Chemistry, Marquette University, P.O. Box 1881,  
Milwaukee, WI 53201-1881

Poly(ethylene)/zinc copper hydroxy stearate (PE/ZCHS) nanocomposites were prepared via melt intercalation. Their structural morphology, thermal stability, and flammability were investigated using X-ray diffraction (XRD), thermogravimetric analysis (TGA), and cone calorimetry. Addition of zinc copper hydroxy stearate at mass percentages of 10 and below resulted in the shift of degradation temperatures to higher magnitudes. At the 10% mass loss point in TGA, the 5 and 10% loaded polymer nanocomposites are thermally more stable than pure PE by 59 and 48°C respectively. Peak heat release rates in cone calorimetry also decrease upon 5 and 10% loadings of ZCHS. Overall, the addition of 5% ZCHS generally led to better thermal and fire properties compared with PE alone or 10% additive loading.

## Introduction

Nanocomposites of polymers with layered metal hydroxide additives containing exchangeable anions, such as hydroxy double salts (HDSs) (1) and layered double hydroxides (LDHs) (1,2), are of interest due to the possibility of enhanced thermal stability and improved mechanical properties, similar to those observed with the widely studied polymer/smectite clay systems. HDSs, the primary focus of initial work in our laboratory, can be represented by the general formula  $[(M^{2+}_{1-x}, Me^{2+}_{1+x})(OH)_{3(1-y)}]^+ A^{n-}_{(1+3y)/n} \cdot zH_2O$  where the two divalent metals are represented as  $M^{2+}$  and  $Me^{2+}$  and interlayer anion is  $A^{n-}$ . Previous work in our laboratories has demonstrated that copper-containing HDSs or single-metal-containing copper layered hydroxy salts (LHSs) can influence thermal stability and flammability of poly(methyl methacrylate (PMMA) (3, 4) and poly(vinyl ester) (PVE) (5). In the case of PMMA, even with relatively poor dispersion of the additive (i.e. formation of micro composites rather than nanocomposites), improvement in thermal stability and formation of significant char was observed in thermo gravimetric analysis and a reduction in total heat release (THR) was observed in cone calorimetry, consistent with incomplete burning of the polymer. No significant reduction in peak heat release rates (PHRR) was observed. For copper hydroxy dodecyl sulfate with PVE, the orientation of anion n-alkyl chains was observed to play a role in nanocomposite formation. Similar trends in cone calorimetry measurements were observed in the PVE system as with PMMA.

Currently in our laboratories we are exploring the role of anion structure and packing as well as intrastructural metal ion composition of these potential components of fire retardant formulations, as well as investigating LDHs for this purpose. The focus of this report is on evaluation of the effects of a zinc/copper HDS on thermal stability and flammability of low density poly(ethylene).

## Experimental

Low-density poly(ethylene) (LDPE) with a melt index of 55 g/10 min (ASTM D 1238, 190°C/2.16 Kg), copper acetate monohydrate, (98.0%)  $[Cu(CH_3COO)_2 \cdot H_2O]$ , zinc oxide, (99.9%)  $[ZnO]$ , methanol, acetone, and HPLC grade chloroform ( $CHCl_3$ ) were obtained from Sigma Aldrich. Sodium stearate, (75.0%)  $[CH_3(CH_2)_{16}COONa]$  was supplied by Alfa Aesar. Zinc copper acetate (ZCA) HDS was prepared using a literature synthesis (6).  $ZnO$  (0.41 g; 5 mmol) was mixed with  $Cu(CH_3COO)_2 \cdot H_2O$  (0.91 g; 5 mmol) in 10 mL of water with vigorous stirring at room temperature. The resultant suspension was allowed to stand for 24 hours. The precipitate was recovered by filtration, washed repeatedly with water, and dried at room temperature.

Anion exchange was achieved by mixing 5 g of ZCA HDS with 500 mL of 0.1 M sodium stearate solution in chloroform for 24 h at room temperature with frequent shaking. The supernatant was decanted and replaced by a fresh solution for another 24 h with this process repeated for the third time. The exchanged HDS product, zinc copper hydroxy stearate (ZCHS) was recovered by filtration, washed with 500 mL of methanol, followed by 500 mL of acetone and plentiful amounts of water before drying at 100°C overnight to drive off residual solvents.

Poly(ethylene)/ZCHS nanocomposites were prepared via melt blending using established methods (7). Poly(ethylene) nanocomposites were prepared by mixing  $x$  g of the additive with  $(100 - x)$  g of pristine poly(ethylene) to achieve  $x$  % mass fractions. Melt blending was then performed on a Brabender mixer for 10 minutes at a temperature of about 130°C and speed of 60 rpm. The prepared nanocomposites are identified as PE/ZCHS-5 and PE/ZCHS-10 for 5% and 10% loadings respectively. A reference sample of pure poly(ethylene) was prepared by following the same procedure in the absence of additive.

Wide-angle x-ray scattering measurements were obtained with a Rigaku Ultima III WAXS at room temperature using Cu K $\alpha$  ( $\lambda = 1.54 \text{ \AA}$ ) radiation source. Data acquisition was performed using 0.02 ° steps, at scan rate of 0.05 ° per second. Peak positions were determined by fitting XRD data to a pseudo-Voigt function using XFIT (8), stripping off the Cu K $\alpha_2$  wavelength contributions. Basal spacings characterizing these layered compounds were obtained using Bragg equation,  $\lambda = 2 d \sin\theta$ , averaging over the observed orders in 00 $l$ .

Thermo gravimetric analysis (TGA) and differential thermal analysis (DTA) were performed on a SDT 2960 simultaneous DTA-TGA instrument from 50–600°C using  $20 \pm 1$  mg samples heated at 10°C/min with air as the purge gas (flow rate,  $85 \pm 5$  mL/min). Approximately 30g of poly(ethylene) composite samples were compression molded into 10cm x 10cm square plaques of uniform thickness (~3mm) before cone calorimetry was performed on an Atlas Cone 2 instrument, using an incident flux of 35kW/m<sup>2</sup> with a cone shaped heater; the spark was continuous until the sample ignited. All samples were run in triplicate and the average value, with standard deviation, is reported; results from cone calorimeter are generally considered to be reproducible to  $\pm 10\%$ .

## Results and Discussion

In order to improve compatibility between the hydrophobic PE chains and the layered inorganic/organic hybrid additive, ZCA was transformed into a stearate-intercalated HDS, ZCHS, via an anionic exchange process. Figure 1 shows powder X-ray diffraction patterns of ZCA (top trace), ZCHS (middle trace), and PE-ZCHS-10, a 10% ZCHS loaded PE composite (bottom trace).

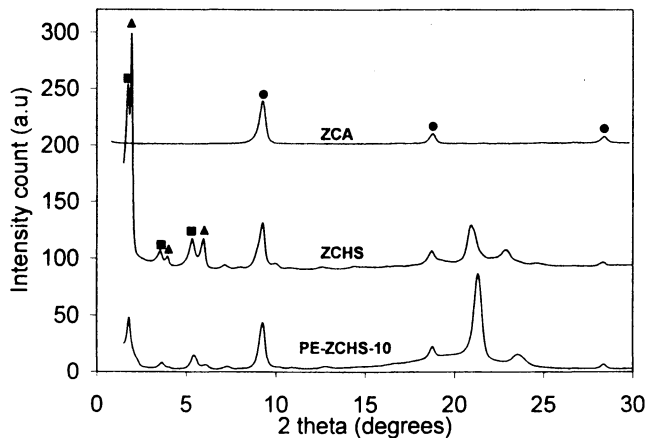


Figure 1. XRD data for ZCA (top trace) and the partially exchanged ZCHS (middle trace) revealing the presence of two new phases; (■) with basal spacing,  $d = 49.3 \text{ \AA}$  and (▲) with  $d = 44.5 \text{ \AA}$ . Reflections from the precursor, ZCA (●), are present in the exchange product. The PXRD pattern of the PE-ZCHS-10 is scaled by a factor of 0.4. Data for the ZCA and ZCHS are offset for clarity.

The basal spacing,  $d$ , for ZCA was calculated to be  $9.4 \pm 0.1 \text{ \AA}$  from the 00 $l$  reflections marked by the filled circles in the top trace of Figure 1. Partial displacement of acetate by stearate anions following anionic exchange is evident from the emergence of two distinct sets of 00 $l$  reflections marked in filled squares and triangles at lower  $2\theta$  values (Figure 1 middle trace). The residual acetate-containing phase provides a convenient marker for evaluating dispersion via PXRD since it remains intact after blending with the polymer. The average basal spacing for the phase marked in solid triangles was found to be  $44.5 \pm 0.9 \text{ \AA}$  while a larger  $d$  value of  $49.3 \pm 0.7 \text{ \AA}$  was calculated for the second phase marked in solid squares. A structural model that best describes the calculated basal spacings is one with a non-overlapping bilayer arrangement of stearate anions. Simultaneous formation of two new exchange phases is not uncommon in copper (II) containing layered inorganic/organic hybrids (5, 10).

In the PE composite, ZCA remains intact probably as an immiscible micro composite. The decrease of the ZCHS peaks relative to the ZCA phase after melt blending with PE could be due to nanocomposite formation (i.e. intercalation and/or exfoliation) or to thermal degradation of the layered structure during melt blending. However, thermo gravimetric analysis of ZCHS and other similar additives, suggests that these compounds are generally stable to temperatures above the  $130^\circ\text{C}$  used for melt blending. This suggests that there may be some extent of nanocomposite formation with this additive; however

other characterization methods, such as transmission electron microscopy, are necessary for a more complete evaluation of nanocomposite formation. In a similar case, copper hydroxy dodecyl sulfate, with a bilayer packing of anions was found to result in some nanocomposite formation when used in PVE (5).

### Thermo-gravimetric Analysis

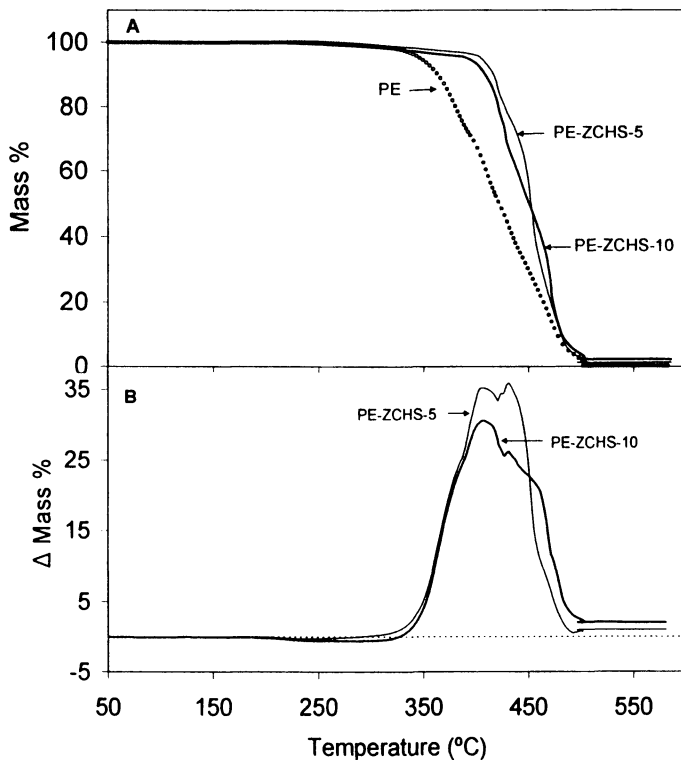
Thermo gravimetric analysis (TGA) of the decomposition behaviors of pure poly(ethylene) and its nanocomposites in an air atmosphere are shown in Figure 2A. Corresponding TGA data are presented in Table I. The onset of thermal degradation, measured as the temperature at which 10% mass loss occurs,  $T_{10}$ , is shifted to higher values by 59 and 48°C for PE-ZCHS-5 and PE-ZCHS-10 relative to pure PE respectively. Similarly, the temperature for 50% mass loss,  $\Delta T_{50}$  is also increased in the presence of the additives. No significant advantage in thermal stability is found at the higher (10%) loading.

Table I. TGA Data

Sample	$T_{10}$ (°C)	$T_{50}$ (°C)	$\Delta T_{50}$ (°C)	Char %
Pure PE	360±4	421±3	NA	0±0
PE-ZCHS-5	419±3	446±4	25±5	1±0
PE-ZCHS-10	408±0	449±1	28±4	2±0
ZCHS	318±1	469±0	NA	25±1

$T_{10}$ , temperature at which 10% mass loss occurs;  $T_{50}$ , temperature at which 50% mass loss occurs;  $\Delta T_{50} = T_{50}$  (nanocomposite) –  $T_{50}$  (pure PE).

Temperature shifts to higher magnitudes for the nanocomposites relative to the pure PE are seen throughout the degradation process. This is clearly illustrated in the mass difference curves of the nanocomposites relative to that of pure PE; (remaining mass % of PE nanocomposites minus remaining mass % of pure PE at the same temperature) shown in Figure 2B. The nanocomposites are remarkably stabilized in the temperature regions of 325 - 600°C with the maximum stabilization achieved at about 410°C for both nanocomposites.  $T_{50}$ , the temperature at which 50% mass loss occurs, is shifted to higher magnitudes by 25 and 28°C for PE-ZCHS-5 and PE-ZCHS-10 respectively. No meaningful destabilization is seen below 325°C, suggesting that the presence of ZCHS at these loading percentages has very little negative effect in the low temperature regime. This is in contrast to observations previously made in our lab where PVE was destabilized with respect to the temperature for 10% mass loss with the



*Figure 2. (A) TGA curves for pure PE (empty circles), PE-ZCHS-5 (solid line) and PE-ZCHS-10 (bold line). (B) Curves of mass loss differences for PE nanocomposites; pure PE (dashed line), PE-ZCHS-5 (solid line), and PE-ZCHS-10 (bold line) as a function of degradation temperature.*

addition copper hydroxy dodecyl sulfate (CHDS) at mass loadings of 10% or less (5).

Differential thermal analysis (DTA) curves of pure PE, PE-ZCHS-5, and PE-ZCHS-10 nanocomposites are shown in Figure 3. The DTA pattern for pure PE is similar to that for its respective nanocomposites in the temperature range of 50 – 300°C. An endothermic feature common in all traces at 140°C may be attributed to the melting of PE, a process that requires energy. At temperatures higher than 300°C the DTA behavior for pure PE significantly differs from those of the nanocomposites. Two overlapping exothermic events are observed for pure PE in the temperature of 300 – 450°C, while the same event is significantly delayed in both PE-ZCHS-5 and PE-ZCHS-10. Apart from the notable differences in the 390 – 475°C regions the rest of the DTA patterns beyond

480°C are similar for pure PE and its nanocomposites. A strong exothermic feature around 500°C is common in all three samples and this may be attributed to thermo-oxidative degradation of oligomeric PE chains.

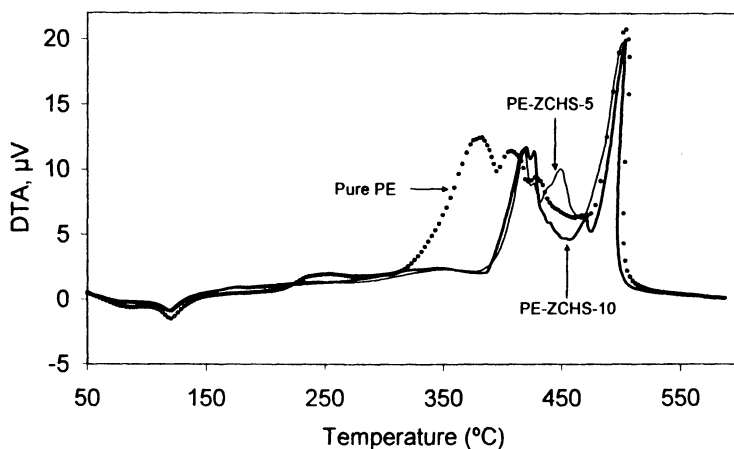


Figure 3. DTA curves for pure PE (empty circles), PE-ZCHS-5 (solid line), and PE-ZCHS-10 (bold line).

### Cone Calorimetry

Cone calorimetry was used to measure the effectiveness of the additives on reducing the flammability of PE; the parameters available include the heat release rate and especially its peak value, the peak heat release rate (PHRR) and time to peak heat release rate (tPHRR); total heat release (THR); time to ignition (tig); average mass loss rate (AMLR); and average specific extinction area (ASEA), a measure of smoke formation. A decrease in the PHRR, THR, AMLR, and ASEA are desired along with an increase in tig and tPHRR. The heat release rate (HRR) curves as a function of time for pure PE and its nanocomposites are shown in Figure 4A and cone data are summarized in Table II.

The heat release rate curves shown in Fig. 4A are consistent with the characteristic burning patterns of intermediate thick, non-charring samples (11). The PHRR values for PE-ZCHS-5 and PE-ZCHS-10 nanocomposites are reduced by 27 and 25% relative to the pure PE respectively. For smectite clay/polymer nanocomposites, reduction in PHRR has been shown to be correlated with nanodispersion of the additive in the polymer matrix (12). With HDS and related layered metal hydroxide additives, we have also only found PHRR reduction in the case of PVE with CHDS, a system with some

nanocomposite formation (5). Figure 4B shows the mass loss rate curves as a function of time for pure PE and its nanocomposites. The shapes of the MLR curves are very similar to the HRR curves for the polymeric materials, consistent with having materials with constant effective heat of combustion (10).

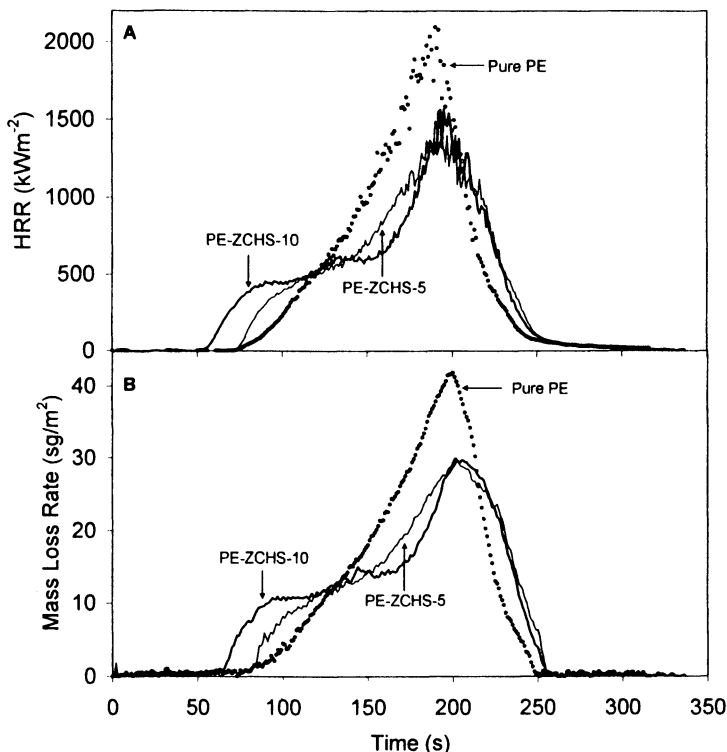


Figure 4. (A) Heat release rate curves for pure PE (empty circles), PE-ZCHS-5 (solid line), and PE-ZCHS-10 (bold line) from cone calorimetry measurements at  $35 \text{ kW/m}^2$ . (B) Mass loss rate curves for pure PE (empty circles), PE-ZCHS-5 (solid line), and PE-ZCHS-10 (bold line).

The time to ignition remains unchanged for the PE-ZCHS-5 but is reduced for PE-ZCHS-10. The THR is observed to be reduced by approximately 13%, a smaller change than observed when copper-containing additives catalyze cross-linking and thus enhance char formation (3). The amount of smoke measured from cone calorimetry as ASEA increases with the additive fraction. Combining the TGA and cone data, the 5% loading provides the best combination of thermal stability and fire properties.



**Table II. Cone Calorimetry Results**

Sample	t <sub>ig</sub> (s)	PHRR (kW/m <sup>2</sup> )	tPHRR (s)	THR (MJ/m <sup>2</sup> )	AMLR (g/stm <sup>2</sup> )	ASEA (m <sup>2</sup> /kg)
Pure PE	87±4	1915±165	190±11	137±4	26±1	392±12
PE-ZCHS-5	88±3	1400±137	189±8	120±3	19±1	479±25
PE-ZCHS-10	68±15	1511±165	169±22	118±7	19±1	493±29

The fire properties of PE-ZCHS nanocomposites can also be evaluated using fire indices derived from cone data. One fire index is PHRR divided by t<sub>ig</sub> while the fire growth index (FIGRA) is defined as the PHRR divided by tPHRR (10). The values are shown in Table III. Only the 5% loading exhibits improvement on these scales. It is important to note that nanocomposite additives are not effective fire retardants by themselves and should be considered as candidates for formulations that include other additives (13) in order to optimize all fire-related properties.

**Table III. Fire Indices**

Sample	PHRR/t <sub>ig</sub> (kW/m <sup>2</sup> -s)	FIGRA PHRR/tPHRR (kW/m <sup>2</sup> -s)
Pure PE	22.1±0.1	10±1.0
PE-ZCHS-5	15.8±0.1	7.4±0.8
PE-ZCHS-10	22.1±0.3	9.0±1.4

## Conclusions

An HDS additive, zinc/copper hydroxy stearate, was melt-blended with low density poly(ethylene). X-ray diffraction analysis of the composite materials was similar to that found with copper hydroxy dodecyl sulfate combined with poly(vinyl ester), where nanocomposite formation was observed, but additional work is necessary for full characterization of the dispersion. The (nano) composites were found to have better thermal stability via TGA and improvement in PHRR in cone calorimetry. However, smoke production was observed to increase. The 5% loading had better overall performance than 10% in terms of thermal stability and most fire properties.

## Acknowledgements

Support of the National Institute of Standards and Technology Fire Research Division (Grant 60NANB6D6018) is gratefully acknowledged.

## References

1. Rajamathi, M.; Thomas, G. S.; Kamath, P. V. *Proc. Indian Acad. Sci., Chem. Sci.* **2001**, *113*, 671-680.
2. (a) Bellotto, M.; Rebours, B.; Clause, O.; Lynch, J.; Bazin, D.; Elkaim, E. *J. Phys. Chem.* **1996**, *100*, 8527-8534. (b) Mavis, B.; Akinc, M. *Chem. Mater.* **2006**, *18*, 5317-5325.
3. Kandare, E.; Hall, D.; Jiang, D. D.; Hossenlopp, J. M. In *Fire and Polymers IV: Materials and Concepts for Hazard Prevention*; Wilkie, C. A.; Nelson, G. L., Eds.; ACS Symp. Ser. 922; Washington, DC, 2006; pp. 131-143.
4. Kandare, E.; Deng, H.; Wang, D.; Hossenlopp, J. M. *Polym. Adv. Technol.* **2006**, *17*, 312-319.
5. Kandare, E.; Chigwada, G.; Wang, D.; Wilkie, C. A.; Hossenlopp, J. M. *Polym. Degrad. Stab.* **2006**, *91*, 1781-1790.
6. Morioka, H.; Tagaya, H.; Karasu, M.; Kadokawa, J.; Chiba, K. *Inorg. Chem.* **1999**, *38*, 4211-4216.
7. Wang, D.; Zhu, J.; Yao, Q.; Wilkie, C. A. *Chem. Mater.* **2002**, *14*, 3837-3843.
8. Cheary R. W.; Coelho A. A. *Programs XFIT and FOURYA, deposited in CCP14. Powder Diffraction Library*, Engineering and Physical Sciences Research Council, Daresbury Laboratory, Warrington, England, URL <http://www.ccp14.ac.uk/tutorial/xfit-95/xfit.htm> ), 1996.
9. Gilman J. W.; Kashiwagi, T.; Nyden, M.; Brown, J. E. T.; Jackson, C. L.; Lomakin, S.; Giannelis, E. P.; Manias, E. In *Chemistry and Technology of Polymer Additives*; Al-Maliaka, S.; Golovoy, A.; Wilkie, C. A., Eds.; London Blackwell Scientific: 1999; pp. 249-265.
10. Fujita, W.; Awaga, K. *Inorg. Chem.* **1996**, *35*, 1915-1917.
11. Schartel, B.; Hull, T. R. *Fire and Materials* **2007**, *31*, 327-354.
12. Su, S.; Jiang, D. D.; Wilkie, C. A. *Polym. Degrad. Stab.* **2004**, *83*, 321-331.
13. Kandare, E.; Chigwada, G.; Wang, D.; Wilkie, C. A.; Hossenlopp, J. M. *Polym. Degrad. Stab.* **2006**, *91*, 1209.

## Chapter 19

# Degradative Transformation of Poly(vinyl chloride) under Mild Oxidative Conditions

Györgyi Szarka and Béla Iván<sup>\*</sup>

Department of Polymer Chemistry and Material Science, Institute  
of Materials and Environmental Chemistry, Chemical Research Center,  
Hungarian Academy of Sciences, Pusztaszeri u. 59-67, P.O. Box 17,  
H-1525 Budapest, Hungary

Nowadays there are more and more demands to reuse waste materials, especially in the case of polymers. Our research seeks to reveal the oxidative degradation processes of poly(vinyl chloride) (PVC), which may provide new methods for treating and recycling of PVC waste materials.

## Introduction

Poly(vinyl chloride) (PVC) is produced and used in the third largest amounts among polymers in the world nowadays. This material is one of the most versatile polymers. It can be processed with a variety of conventional and economic techniques to products with an enormously broad spectrum of properties, that is from soft rubbery to very hard materials. However, it is well-known that PVC severely degrades at elevated temperatures, i.e. at the usual processing temperatures (see e.g. Refs. 1-3 and references therein). Therefore, the use of stabilizers is inevitable for obtaining PVC products. The large amounts of PVC production and use result in large quantities of waste materials as well. In relation to oil, energy and environmental concerns recycling and reuse of plastic wastes have become an important issue nowadays. This is even more significant in the case of non-biodegradable materials, such as the major commercial polymers including polyethylene, polypropylene, polystyrene, PVC etc.

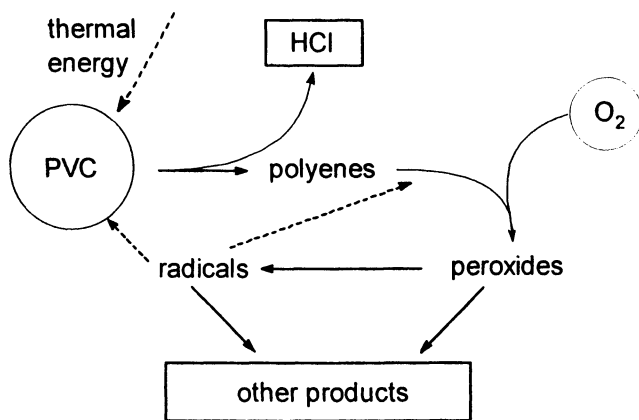
Considering the importance of PVC recycling, we have carried out investigations aiming at utilizing the inherent low stability of PVC in order to find new ways for broadening the reuse of this polymer. Recently, we have published (4-6) that epoxidation of degraded PVC and chemical modification of vinyl chloride copolymers with functional comonomers may be utilized to obtain new properties which PVC itself does not possess. Epoxidation of PVC has already been performed successfully under usual processing conditions (7). In this study, we report on our recent findings on an environmentally advantageous mild thermooxidative degradative process for oxidative transformation and/or decomposition of PVC containing conventional stabilizers.

### **Effect of Lead Stearate on the Thermo-oxidative Degradation of PVC**

Production and use of PVC occur in the presence of air, i. e. in the presence of oxygen. Therefore, it is surprising that the mechanistic details of thermo-oxidative degradation of PVC are still not fully revealed. The major reactions of this process are shown in Scheme 1. As indicated in this Scheme, thermal dehydrochlorination yields HCl and simultaneously sequences of conjugated double bonds (polyenes) in the chain. The reactive polyenes lead to peroxides in a reaction with oxygen followed by the formation of radicals. Subsequent chain reactions result in additional initiation of HCl loss and further oxidative processes (1, 8).

It has been shown that conventional PVC stabilizers act according to the *reversible blocking mechanism* (9, 10) even under oxidative conditions. However, there is no information on the fate of the polymer chains in this process in the presence of additives. It has been reported earlier that thermo-oxidative degradation of solid PVC leads to simultaneous cross-linking and chain scission (1, 11). In order to avoid the problems arising in the course of investigating degradation of solid PVCs, such as mixing, mechanical effects, inhomogeneous distribution of additives etc., we have carried out thermo-oxidative treatment of PVC in solution, using dioctyl phthalate (DOP) as solvent, that is the most widely applied plasticizer of PVC.

Figures 1 and 2 show the molecular weight distributions (MWDs) of PVCs treated with oxygen in the absence and presence of lead stearate (PbSt<sub>2</sub>) stabilizer for different times. As shown in these Figures, the MWDs in both cases are significantly shifted towards lower molecular weights with increasing degradation times. This clearly indicates that chain scission occurs, the extent of which increases with increasing degradation times. The MWDs are monomodal in all cases, that is, there are neither low or high molecular weight tailings in these MWD curves. This means that the chain scission of PVC chains is a random process, on the one hand. The absence of high molecular weight



*Scheme 1. The major reactions of thermo-oxidative degradation of PVC.*

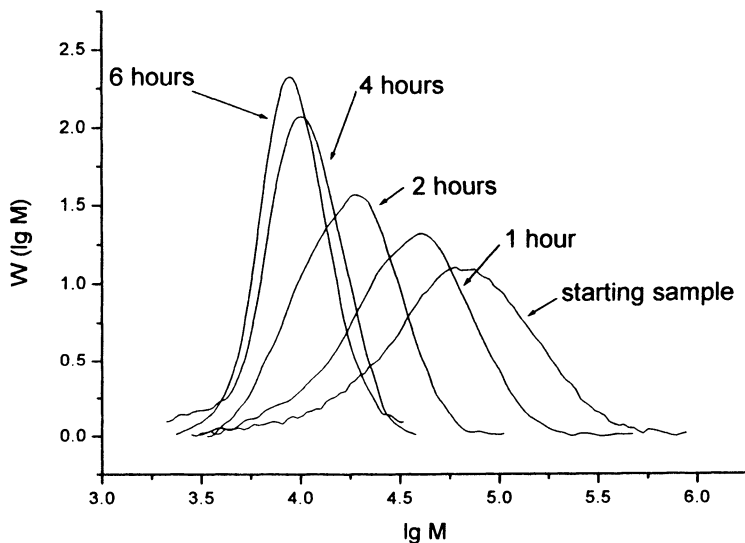


*Figure 1. Molecular weight distributions of PVCs in the absence of stabilizer (DOP, O<sub>2</sub>, 200 °C) at different degradation times.*

bimodality proves that cross-linking of PVC does not take place under the investigated conditions, on the other hand. The absence of cross-linking in DOP solutions is quite surprising on the basis of results obtained with solid samples; in which simultaneous chain scission and cross-linking occur during thermo-oxidative degradation of PVC (1, 11).

It is important to note that the oxidative chain scission of PVC is a relatively rapid process indicated by the considerable shift in the MWD curves even after one hour degradation time. At longer times, the molecular weight of most of the polymer chains fall in the range of 1000 – 10000, that is in the oligomeric region. The MWDs of the low molecular weight polymers appear narrower than that of the rest of the polymers which might be due to loss of the even lower molecular weight polymers, i. e. below few thousand, formed by the scission process.

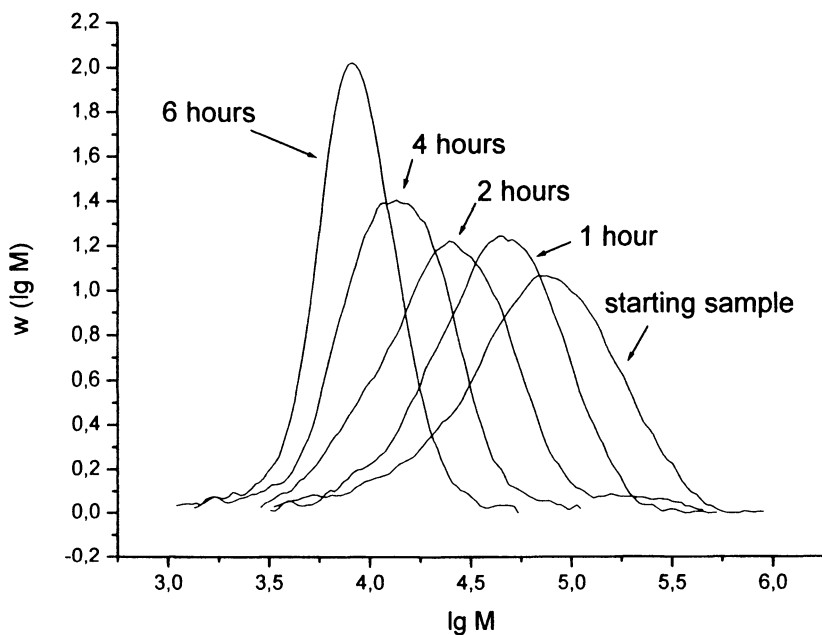


Figure 2. Molecular weight distributions of PVCs in the presence of lead stearate stabilizer (DOP, O<sub>2</sub>, 200 °C) at different degradation times.

The oxidative chain scission of PVC is better illustrated in Figure 3 depicting the decrease of the number average molecular weight ( $M_n$ ) of PVC samples as a function of reaction time. As shown in this Figure, significant decrease of  $M_n$  takes place in a short period of time followed by slower  $M_n$

decrease. Surprisingly, there is no difference between the stabilized and unstabilized cases indicating that  $\text{PbSt}_2$  does not act as stabilizer for oxidative chain scission of PVC.

This is also confirmed by the data in Figure 4 exhibiting the number of chain scission per monomer units ( $S$ ) as a function of time. This was calculated according to the following equation:  $S = MVC (1/M_n - 1/M_{n,0})$  where  $MVC$ ,  $M_n$  and  $M_{n,0}$  are the molecular weights of the vinyl chloride monomer unit, the number average molecular weights of the oxidized and starting PVC samples, respectively. It is interesting to note that chain scission proceeds with constant rate independent of the extent of degradation for a relatively long period of time.

The structural change during oxidation of PVC was followed by FTIR spectroscopy. Figure 5 shows a representative FTIR spectrum. As shown in this Figure, strong carbonyl signals ( $\sim 1600\text{-}1800\text{ cm}^{-1}$ ) and a broad hydroxyl signal ( $\sim 3100\text{-}3600\text{ cm}^{-1}$ ) appear indicating the formation of carbonyl and hydroxyl containing new functional groups in the PVC chain formed during the oxidative process. This structural transformation may offer new application possibilities for the oxidized PVCs, such as subsequent functionalizations, blending with other polar polymers which cannot be mixed with untreated PVC etc.

### **Effect of 2,6-di-tert-butyl-4-methylphenol Antioxidant on the Thermo-oxidative Degradation of PVC**

In another set of experiments, we have investigated the effect of 2,6-di-tert-butyl-4-methylphenol (BHT) antioxidant on the thermo-oxidative degradation of PVC. As data in Table 1 indicate, the presence of this antioxidant leads surprisingly to more chain scission than that observed in the absence of this compound. The molecular weight data in Table 1 show the large differences. After 3 hours of treatment, the molecular weight decreases under 1000 which means extremely large numbers of chain scissions. Comparing the  $M_n$  values of PVC samples with and without BHT antioxidant interestingly indicates that the BHT antioxidant (the additive given to avoid degradation) makes the chain breaking faster. After 4 hours degradation, oily products were obtained. Thus, it can be concluded that even the presence of BHT does not prevent the oxidative chain scission of PVC and this additive even accelerates the chain breaking decomposition process.

### **Conclusions**

Systematic experiments were conducted with poly(vinyl chloride) (PVC) in order to introduce functional groups in the polymer chain by mild thermo-oxidative conditions in dioctyl phthalate (DOP), a widely used plasticizer in this

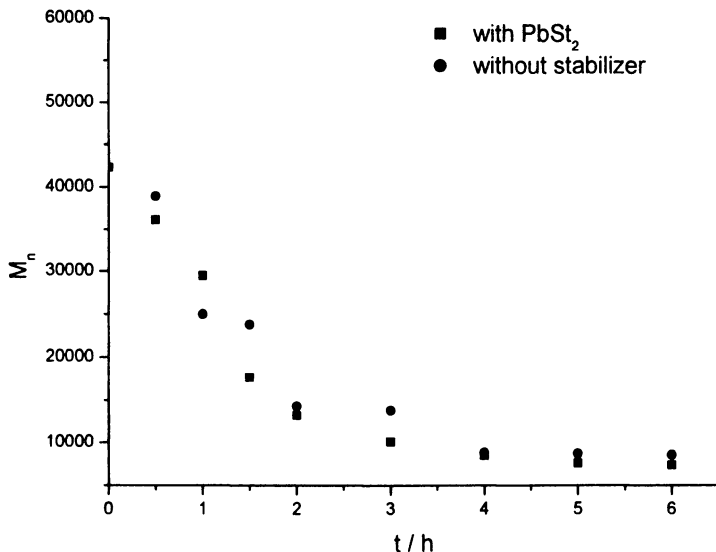


Figure 3. Number average molecular weight ( $M_n$ ) of PVC as a function of degradation time during thermo-oxidative degradation of PVC in the absence and presence of lead stearate stabilizer (DOP, O<sub>2</sub>, 200 °C).

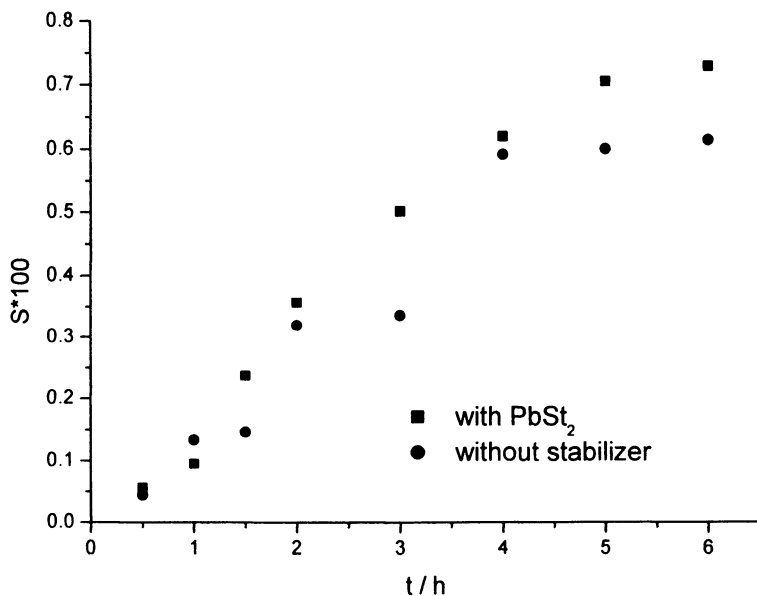


Figure 4. Number of chain scission ( $S$ ) as a function of degradation time during thermo-oxidative degradation of PVC in the absence and presence of stabilizer (DOP, O<sub>2</sub>, 200 °C).



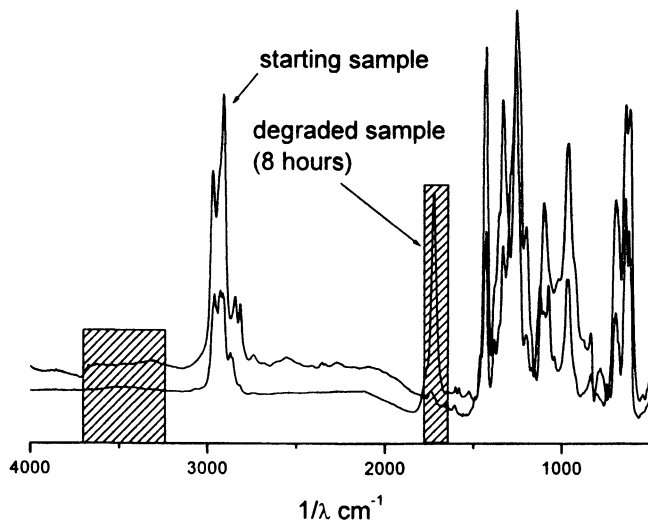


Figure 5. FTIR spectra of the starting and oxidized PVC.

**Table 1. Number average molecular weights ( $M_n$ ) of PVC as a function of reaction time in the absence and presence of BHT antioxidant during thermo-oxidative degradation (DOP,  $O_2$ , 200 °C).**

<i>BHT</i> (mmol / VC)	$M_n$ (g/mol)		
	0 h	3 h	6 h
0	42300	13800	8550
2	42300	750	-
10	42300	930	-

polymer. The effects of lead stearate ( $PbSt_2$ ) stabilizers and 2,6-di-tert-butyl-4-methylphenol were also investigated. Analysis of the resulting products by gel permeation chromatography showed that chain scission of PVC occurs under the investigated conditions in both the presence and absence of  $PbSt_2$  and BHT antioxidant. Thus it can be concluded that neither the  $PbSt_2$  stabilizer nor the BHT antioxidant are able to prevent chain scission in thermo-oxidation of PVC in dilute solutions. Surprisingly, the BHT antioxidant even accelerated the chain scission in dioctyl phthalate. The formation of polar oxo groups in the polymer

was confirmed by IR spectroscopy. The appearance of oxygen containing groups in PVC is expected to result in easier blending of such degradation products with a large number of other polymers, organic and inorganic materials. Thus, the mild thermooxidative degradation and simultaneous functionalization of PVC may lead to new environmentally advantageous, profitable recycling processes of PVC waste materials.

### Acknowledgements

GPC measurements by Dr. M. Szesztay and Mrs. E. Tyroler are gratefully acknowledged.

### References

1. Iván, B.; Kelen, T.; Tüdös, F. In *Degradation and Stabilization of Polymers*; Jellinek, H. H. G.; Kachi, K., Eds.; Elsevier Sci. Publ. Co.: 1989; Vol. 2, pp. 483-714.
2. Iván, B. In *Polymer Durability: Degradation, Stabilization and Lifetime Prediction*; Clough, R.; Billingham, N. C.; Gillen, K. T., Eds.; Adv. Chem. Ser.; Am. Chem. Soc.: Washington, D. C., 1996; Vol. 249, 19-32.
3. Starnes, W. H., Jr. *Prog. Polym. Sci.* **2002**, *27*, 2133-2170.
4. Szakács, T.; Iván, B. *Polym. Prepr.* **2000**, *41*(2), 1540-1541.
5. Szakács, T.; Iván, B.; Kupai, J. *Polym. Degrad. Stab.* **2004**, *85*, 1029-1033.
6. Szakács, T.; Iván, B. *Polym. Degrad. Stab.* **2004**, *85*, 1035-1039.
7. Bicak, N.; Serkal, B. F.; Gari, M. *Polym. Bull.* **2003**, *51*, 231-236.
8. Nagy, T. T.; Turcsányi, B.; Kelen, T.; Tüdös, F. *React. Kin. Catal. Lett.* **1978**, *8*, 7-11.
9. Iván, B.; Turcsányi, B.; Kelen, T.; Tüdös, F. *J. Vinyl Technol.* **1990**, *12*, 126-135.
10. Iván, B.; Turcsányi, B.; Kelen, T.; Tüdös, F. *Angew. Macromol. Chem.* **1991**, *189*, 35-49.
11. Iván, B.; Nagy, T. T.; Turcsányi, B.; Kelen, T.; Tüdös, F. *Polym. Bull.* **1980**, *2*, 461-467.

## Chapter 20

# Aging of the Binder in Plastic-Bonded Explosive PBX 9501 and Free Radical Oxidation

J. D. Kress<sup>1</sup>, D. A. Wroblewski<sup>1</sup>, D. A. Langlois<sup>1</sup>, E. B. Orler<sup>1</sup>,  
J. M. Lightfoot<sup>2</sup>, W. A. Rodin<sup>2</sup>, C. Huddleston<sup>2</sup>, L. Woods<sup>2</sup>,  
B. G. Russell<sup>2</sup>, M. R. Salazar<sup>3</sup>, and D. K. Pauler<sup>4</sup>

<sup>1</sup>Los Alamos National Laboratory, Los Alamos, NM 87545

<sup>2</sup>BWXT Pantex, LLC, Amarillo, TX 79120

<sup>3</sup>Department of Chemistry, Union University, Jackson, TN 38305

<sup>4</sup>Colorado School of Mines, Division of Engineering, Golden, CO 80401

Estane® 5703 is a segmented poly(ester urethane) that binds HMX explosive crystals together and provides mechanical integrity to the composite plastic-bonded explosive PBX 9501. A mixture of bis-2,2-dinitropropyl acetal and formal is used to plasticize the Estane. Upon heating, this nitroplasticizer (NP) loses NO<sub>2</sub> groups and produces oxidizing species that can react with the urethane links of Estane. We report on aging studies of the oxidative degradation of Estane/NP/HMX mixtures for multiple temperatures between 40° and 85°C. Product gases (such as N<sub>2</sub>O, NO, N<sub>2</sub> and CO<sub>2</sub>) were identified and quantified as a function of aging time. Changes in molecular weight of the Estane as a function of aging time were measured by gel permeation chromatography (GPC). Oxidation products of both non-enriched and isotopically enriched Estane and Estane analogues were identified by <sup>1</sup>H NMR and LC/MS techniques and quantified as a function aging time. The gas product evolution rates, Estane crosslinking rates from GPC, and oxidation rates of Estane from NMR are compared.

## Introduction

The plastic-bonded explosive PBX 9501 is 94.9% by weight HMX explosive, 2.5% nitroplasticizer (NP), 2.5% Estane<sup>®</sup> 5703, and 0.1% stabilizer (anti-oxidant), either Irganox 1010 or diphenylamine. Estane<sup>®</sup> 5703, a segmented poly(ester urethane), together with the NP forms a binder that binds the HMX crystals together and provides mechanical integrity to the composite. The urethane units segregate (phase separate) into “hard” domains that act as physical crosslinks between the “soft” polyester domains, (see Figure 1). The NP softens the Estane and decreases the mechanical sensitivity of the PBX. Currently, we are studying the chemical mechanisms of degradation in PBX 9501 and developing kinetics models. Since the binder has a significant affect on the mechanical properties of the PBX 9501 composite, the overarching goal is to understand how the mechanical properties of the binder change with aging and to identify the chemical degradation mechanisms that cause the mechanical properties to change. We are interested in understanding all possible degradation mechanisms (thermolysis, photolysis, hydrolysis, and oxidation). The hydrolytic aging of the ester links in Estane<sup>®</sup> 5703 and a chemical kinetic model have been reported previously (1) and recent results are discussed elsewhere in this volume (2). In the present contribution, we describe recent progress in the study of the free-radical oxidation of the urethane segments. Free-radical oxidation may be as important as hydrolysis, especially as the PBX dries out, i.e., the PBX loses water to surrounding environment that is low in both moisture and oxygen content.

The nitroplasticizer (NP) is composed of a eutectic of bis-2,2-dinitropropyl acetal (BDNPA) and formal (BDNPF). The chemical structures are shown in Figure 1. Various research efforts at Los Alamos and Pantex are showing that upon heating NP loses nitro (NO<sub>2</sub>) groups and produces oxidizing species that can degrade Estane in the absence of O<sub>2</sub>, (for example, the oxidation of the methylene bridge between the two phenyl groups in Figure 1). The established (3) free radical model for hydrocarbon polymer oxidation is based on O<sub>2</sub> propagating a chain reaction. Since the Estane is oxidized in the absence of O<sub>2</sub>, one challenge in this work is to develop an alternative mechanism. Throughout, we will refer to this oxidation process due to NP decomposition in the absence of O<sub>2</sub> as “NP-driven.” Recently, electronic structure calculations have been performed (4, 5) to examine the decomposition of NP. In Figure 2, a proposed mechanism is shown for a model compound, 2,2-dinitro-1-methoxypropane, whose structure resembles “one-half” of a NP molecule. A likely mechanism for NP decomposition is that nitro (NO<sub>2</sub>) groups dissociate from the NP molecules (step 1, Figure 2), produce oxidizing species (via HONO elimination). HONO readdition forms a nitroso-alcohol compound (step 2, Figure 2) that very readily decomposes (step 3, Figure 2) to form CO, CO<sub>2</sub>, NO and N<sub>2</sub>O. Presumably HONO, NO<sub>2</sub>, or other oxidizers formed in the NP decomposition also attack and

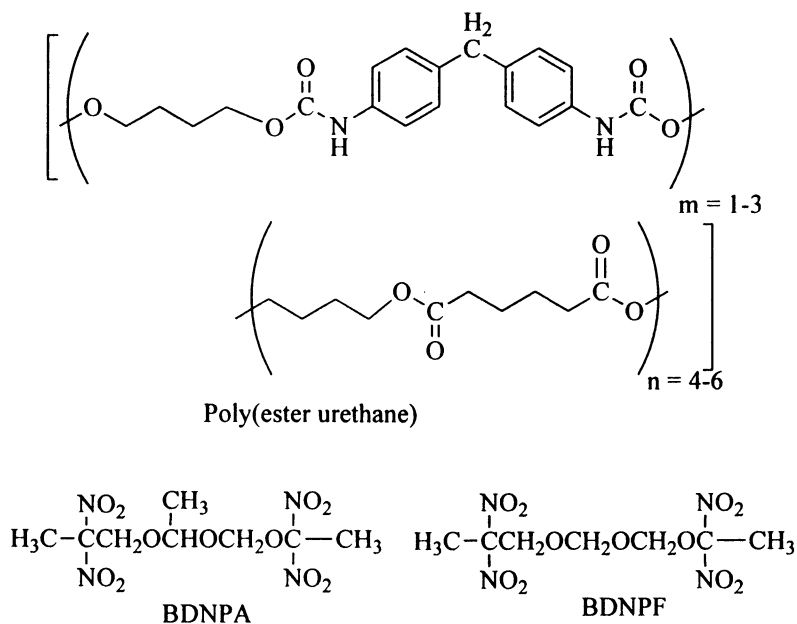


Figure 1. Chemical structure of Estane and nitroplasticizer (BDNPA/F).

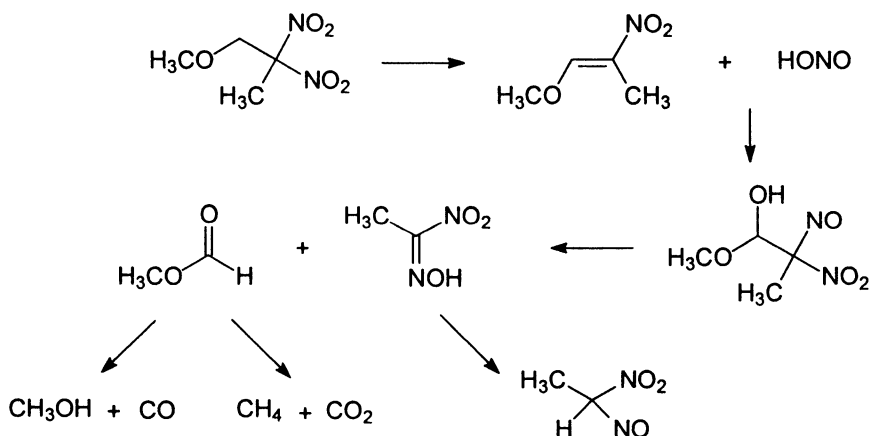


Figure 2. Proposed mechanism for the decomposition of a model compound whose structure resembles one half of a NP molecule. [Adapted from Ref. (5)].

oxidize the hard segments in Estane. The oxidation of the Estane polymer can cause chain scission (decreased MW) and crosslinking (increased MW and gel formation), while small molecule remnants of the reactions can be detected in gas analyses.

Changes in MW can lead to changes in the mechanical properties of the binder. The effect of thermal aging at 50°C on the tensile properties of binder containing 15 wt% NP (vs. 50% NP in the present work) has been reported (6). After a year of aging, the modulus decreases by about a factor of three. GPC data showed branching reactions occurred first and eventually a cross-linked gel (increased MW) was observed. A recent aging study (2) for the binder found a correlation between increased oxidative degradation and decreased tensile strength, where the extent of NP-driven oxidative degradation was measured using NMR.

**Table I. Combinations of the constituents of PBX 9501 considered in the present work**

CAS Sample ID #	Combination	Mass ratio	Temperatures (°C)	Total mass (g)
9	E,NP	1:1	40, 48, 56, 64	10
17	E,H,NP	1:1:1	40, 48, 56, 64	15
18	E,D,NP	1:0.04:1	40, 48, 56, 64	15
19	E,I,NP	1:0.04:1	40, 48, 56, 64	15
22	E,H,D,NP	1:1:0.04:1	40, 48, 56, 64	20
23	E,H,I,NP	1:1:0.04:1	40, 48, 56, 64	20
24	PBX 9501 (E,H,D,NP)	0.025:0.95:0.001:0.025	40, 48, 56, 64	56
25	PBX 9501 (E,H,I,NP)	0.025:0.95:0.001:0.025	40, 48, 56, 64	56

Key: E=Estane, H=HMX, D=Diphenylamine, I=Irganox, NP=Nitroplasticizer.  
Mass ratio = ratio of masses of constituents in order as listed in column 2.

## Results and Discussion

### Gas Product Analysis

Results on the oxidative degradation of Estane have been obtained from the Constituent Aging Study (4, 7) (CAS). The goals of the CAS were to artificially age the PBX 9501 constituents (HMX, Estane, NP, and stabilizer) in 25 different

combinations at accelerated rates, detect chemical reactions that take place, identify reaction products and possible degradation mechanisms, and provide data for lifetime prediction modeling. The samples were aged at different temperatures (ranging from 40° to 64°C) in a dry, oxygen-free environment. Over 1000 samples were aged for a period of three years, with typical samples analyzed at 1/2 year intervals. The CAS samples considered in the present work are listed in Table I. One of the most striking findings is that combinations containing NP (NP + Estane and NP + Estane + stabilizer) show a strong correlation between the total amount of gas products generated and significant changes in the molecular weight of the Estane.

The product gases (such as N<sub>2</sub>O, NO, N<sub>2</sub>, CO<sub>2</sub>, and CO) were identified and quantified as a function of aging time (7). The gas data show diverse chemistry between the CAS samples and initial first order kinetics for gas formation. To capture the temperature (T) dependence of the gas formation rates, an Arrhenius equation was employed, where the rate =  $A \exp(-E_a/RT)$  and R = gas constant. Analysis of the initial gas production rates for multiple temperatures yielded linear behavior in the Arrhenius plots [plotting  $\ln(\text{rate})$  vs.  $1/T$ ]. The activation energies ( $E_a$ ) and Arrhenius prefactors (A, frequency factors) extracted from the Arrhenius analysis, for the formation of the individual gas products from each CAS sample analyzed (samples #9, 17, 19, 23, and 25), are shown in Figure 3. The data lie on a single linear kinetic compensation (KC) plot,  $\ln(A)$  vs.  $E_a$ . A single linear kinetic compensation plot very strongly suggests a common degradation mechanism between all the individual CAS samples (the unstabilized CAS 9 and 17, the stabilized CAS 19 and 23, and the stabilized PBX 9501) since all samples were run independently of one another. The slope of this single KC plot gives a  $1/RT$  value of 1.53 mol/kcal (or T value of 55.8°C) and intercept of -27.90. The decomposition of neat HMX conducted under a variety of thermal conditions (temperatures from 150 – 383°C) reported by Brill et al. (8) also falls on a single KC plot and is reproduced as the solid line in Figure 3. This line has a slope of 0.96 mol/kcal (or T value of 251.1°C) and intercept of -5.4. As can be seen from the figure, the slopes of the CAS experiments and that of neat HMX decomposition are different and suggest differing degradation processes. Thus, the presence of NP in the CAS samples significantly alters the degradation kinetics of HMX and ultimately of PBX 9501.

### Molecular Weight Analysis

Changes in number-average molecular weight ( $M_n$ ), weight-average molecular weight ( $M_w$ ) and polydispersity ( $MWD = M_w/M_n$ ) of the Estane were measured by gel permeation chromatography (GPC). Two different methods were used: (1) average molecular weight measurements relative to polystyrene

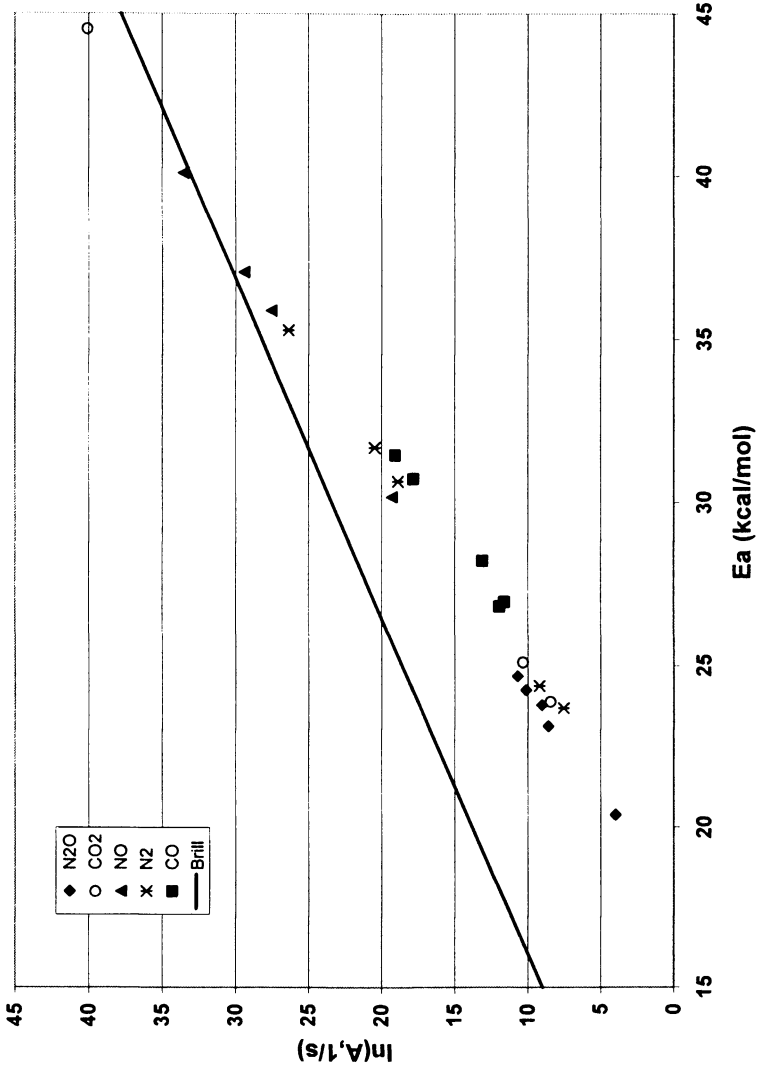


Figure 3. Kinetic compensation plot for the rate of evolution of product gases from the degradation of CAS samples (symbols) and for neat HMX [solid line, Ref. (8)].



standards with a tetrahydrofuran (THF) solvent and differential refractive index (RI) detection, and; (2) absolute molecular weight measurements using a multi-angle light scattering (MALS) technique. Waters Corp. GPC instruments (150C and GPC 2000) with differential RI detectors were used, where THF was used as the mobile phase. Twelve narrow MWD polystyrene standards from 580 to 2 million Daltons were used to generate a third-order calibration curve. The Wyatt DAWN EOS MALS detector was placed in series with the GPC 2000. To interpret the GPC measurements, Flory-Stockmayer (FS) theory of random crosslinking is used. (The statistical FS theory has subsequently been shown (9) to be equivalent to crosslinking kinetics second order in the polymer chain concentrations.) FS theory predicts that, as a function of time  $t$ :

$$\frac{M_w(t)}{M_w(0)} = \frac{1}{(1 - 2f_n k_{FS} t)} \quad (1)$$

and

$$\frac{MWD(t)}{MWD(0)} = \frac{(1 - 0.5 f_n k_{FS} t)}{(1 - 2 f_n k_{FS} t)} \approx (1 + 1.5 f_n k_{FS} t), \quad (2)$$

where  $k_{FS}$  is the rate of extent of reaction and  $f_n$  is the number-average degree of polymerization. The second expression in Equation (2) is the 1<sup>st</sup> order expansion for small  $t$ . For unaged Estane,  $M_w(0) = 8 \times 10^4$  Dalton (as measured with GPC-MALS) and  $MWD(0) = 2$  (as measured with GPC-RI) thus yielding  $M_n(0) = M_w(0)/MWD(0) = 4 \times 10^4$  Dalton. Since the molecular weight of a repeat unit is 1093 Dalton [as derived from the NMR studies (10) and discussed in Ref. (1)],  $f_n = 4 \times 10^4 / 1093 = 36.6$ .

In Figure 4 we show the change in Estane molecular weight for CAS sample #19 (see Table I) as a function of aging time at a temperature of 64°C. The change in  $M_w$  is plotted as  $M_w(0)/M_w(t)$  so to facilitate comparison with Flory-Stockmayer theory, Equation (1). The slope of a straight line fit to the data between  $t=0$  and 40 weeks (GPC-RI data) and between  $t=0$  and 48 weeks (GPC-MALS data) is determined. The latter time is chosen as where the data begins to deviate noticeably from linear. At later times the deviation from linear is due to an inaccurate determination of the distribution due to insolubility and gel formation of the higher molecular weight fractions in the GPC. The variation in  $M_w$  above 50 weeks is different between the RI and MALS detection schemes because the change in physical property (RI vs. LS) responds differently once gelation of the polymer occurs. From the slope and the value of  $f_n$  derived above, we determined from Flory-Stockmayer theory the following values for the rate of extent of reaction ( $k_{FS}$ ) for sample #19 at 64°C:  $1.2 \times 10^{-4}$ /week ( $M_w$  GPC-MALS),  $5.3 \times 10^{-5}$ /week ( $M_w$  GPC-RI), and  $1.2 \times 10^{-4}$ /week (MWD GPC-RI). Gel formation can also be predicted from the FS theory, for example, by setting  $M_w(t)/M_w(0) = \infty$  [setting  $(1 - 2 f_n k_{FS} t) = 0$ ] and solving for  $t$ . Using  $k_{FS}$

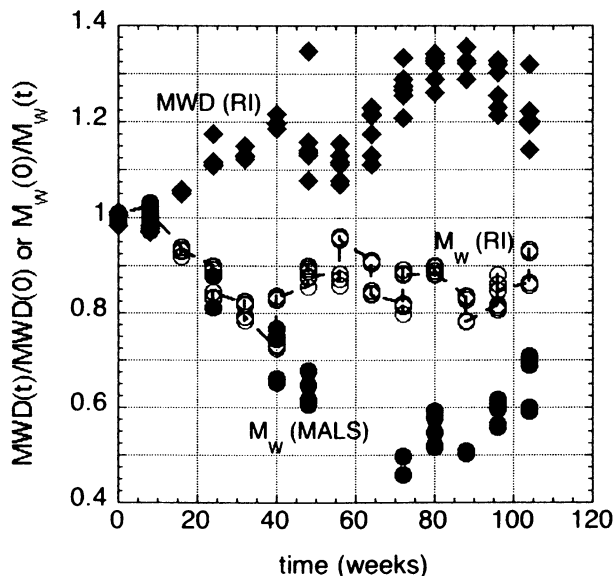


Figure 4. Change in Estane molecular weight distribution at  $T = 64\text{ }^{\circ}\text{C}$  for CAS Sample #19 (Estane/Irganox/NP) as a function of aging time ( $t$ ) as measured with GPC. Solid diamonds =  $MWD(t)/MWD$  determined with RI detection. Open circles =  $M_w(0)/M_w(t)$  determined with RI detection. Solid circles =  $M_w(0)/M_w(t)$  determined with MALS.

derived from the GPC-MALS result yields a gel formation time = 114 weeks. This gel time is consistent with: (1) the GPC-MALS results in Figure 3, where the data deviates significantly from linear after 48 weeks; and, (2) the fact that 20% or more of each sample for  $t > 80$  weeks was found insoluble in polymer recovery measurements.

### NMR Studies

Proton NMR studies were utilized to determine the kinetics of the degradation process by quantifying the relative amount of oxidation of the MDI-units in Estane at different aging times and temperatures. Identification of the oxidation degradation product and of the associated  $^1\text{H}$  NMR resonances is based on earlier work using isotopic enrichment (11). In this previous study,  $^{15}\text{N}$  enriched Estane analogues and MDI model compounds were synthesized in which the nitrogens of the urethane methylene diisocyanate-unit (MDI-unit) were

enriched with  $^{15}\text{N}$  (2, 11). Identification of oxidation degradation product and of the associated  $^1\text{H}$  NMR resonances was determined (11) by 1-D and 2-D NMR using  $^{15}\text{N}$  HMCQ NMR techniques. In the absence of atmospheric oxygen, the primary oxidation product was one in which the bridging methylene carbon of the MDI unit is oxidized to a carbonyl. We monitored the degradation of two sets of samples containing  $^{15}\text{N}$  Estane and NP (50:50 by wt.) or non-enriched Estane/NP, aged at 50°, 70° and 85°C and at 65°, 75° and 85°C respectively, under inert atmosphere.

By comparing the relative amounts of the oxidized product(s) to the starting material at different aging times and temperatures using  $^1\text{H}$  NMR, the kinetics of the degradation process was determined. Kinetic results are summarized in Table II. The rate of change of the NMR signal was well described by first order kinetics. Arrhenius parameters (prefactor A and energy of activation  $E_a$ ) for the rate  $k_{\text{NMR}}$  were determined. For example, for the disk samples,  $A = 7.03 \times 10^{12}/\text{day}$  and  $E_a = 25.5 \text{ kcal/mol}$  based on integration of the phenyl proton NMR signal for the Estane/NP system. The energy of activation agrees well with the value previously derived (4, 7) from the CAS for the evolution of  $\text{NO}_x$  ( $\text{N}_2\text{O}$  and  $\text{NO}$ ) gases due to NP decomposition.

In a similar aging study, a sample of an n-butanol capped MDI model compound (MC) plus NP was prepared and aged under inert atmosphere. The MC was labeled with  $^{13}\text{C}$  in the bridging methylene position and simulates the hard segment of Estane. The samples were aged at 50°, 70° and 85°C. The rate of change of the degradation products was monitored both by  $^1\text{H}$  NMR and by LC/MS. For the LC/MS, a UV-VIS detector was employed and the area under the mass peak for the unreacted MC was determined for each sample as a function of aging time. At 50°C no sign of reaction was seen in the NMR study. However, at 70° and 85°C, the rate of change of both the  $^1\text{H}$  NMR signal and the LC/MS peak area was well described by first order kinetics. At 70°C the rate of degradation as determined using LC/MS is 2.0 times faster than observed by NMR. At 85°C the rate determined by LC/MS was 1.2x faster than by NMR. There is good agreement between the rates determined by LC/MS and NMR techniques confirming that the degradation of the hard segment MDI unit is due to oxidation of the bridging methylene carbon. In a second model compound study aimed at elucidation of the cross-linking site,  $^{13}\text{C}$  enriched MC was aged at 100°C for up to 45 days with NP (50:50 by weight). A dimeric species of the MC was identified among several decomposition products using LC/MS/MS. The MDI dimer was presumed to form through bond formation between bridging methylene groups on the MDI segments. The same results were observed using model compounds containing naturally occurring carbon. These results provide evidence for explaining the presence of insoluble gels, observed in GPC solutions of aged Estane/NP, through branching or cross-linking reactions.

**Table II. Observed rates at T = 64°C normalized by the initial amount of NP,  $[\text{NP}]_0$**

	Normalized Rate ( $10^{-4}$ /week)	Experiment
$R_{\text{N}_2\text{O}}/[\text{NP}]_0$	0.4 to 5	CAS $\text{N}_2\text{O}$ gas evolution
$R_{\text{C=O}}/[\text{NP}]_0$	3 to 4	NMR MDI Oxidation
$R_{\text{X-link}}/[\text{NP}]_0$	0.20 to 0.34	CAS $M_w$ (GPC-MALS)
$R_{\text{X-link}}/[\text{NP}]_0$	0.16 to 0.36	CAS $M_w$ (GPC-RI)
$R_{\text{X-link}}/[\text{NP}]_0$	0.17 to 0.45	CAS MWD (GPC-RI)

### Summary

In Table II, we summarize our analyses of the kinetics of oxidation of Estane in the absence of  $\text{O}_2$  due to NP decomposition and compare rates at  $T = 64^\circ\text{C}$ . Since differing amounts (masses) and ratios of Estane and NP were used in the various CAS samples (Table I), we attempt to place all of the CAS results on an equal footing by dividing (normalizing) the observed rates by the initial amount of NP (denoted  $[\text{NP}]_0$ ). For the rate of evolution,  $R_{\text{N}_2\text{O}}$ , of  $\text{N}_2\text{O}$  gas (7) from eight different CAS samples (#9, #17, #18, #19, #22, #23, #24, and #25) the normalized rates  $R_{\text{N}_2\text{O}}/[\text{NP}]_0$  ranged between  $0.4 \times 10^{-4}$ /week and  $5 \times 10^{-4}$ /week. As derived from the NMR experiments described above, the rate of carbonyl formation ( $R_{\text{C=O}} = k_{\text{NMR}} \times [\text{MDI}]_0$ ) of the methylene bridge on the urethane unit gives a normalized rate of  $R_{\text{C=O}}/[\text{NP}]_0 =$  from 3 to  $4 \times 10^{-4}$ /week. The initial MDI-unit concentration  $[\text{MDI}]_0 = f_n \times [\text{Estane}]_0$ , where  $[\text{Estane}]_0 =$  initial concentration of Estane. Finally, the crosslinking rate ( $R_{\text{X-link}} = k_{\text{FS}} \times [\text{MDI}]_0$ ), with  $k_{\text{FS}}$  determined in the same fashion described above for CAS sample #19, was calculated from GPC-MALS, using three different CAS samples (#19, #23, and #25), and from GPC-RI, using five different CAS samples (#9, #17, #19, #23, and #25). These results are displayed in Figure 5. This yielded normalized rates  $R_{\text{X-link}}/[\text{NP}]_0$  between  $0.2 \times 10^{-4}$ /week and  $0.5 \times 10^{-4}$ /week. Note that both the GPC-MALS and GPC-RI analyses give consistent values for  $R_{\text{X-link}}/[\text{NP}]_0$ . The normalized  $\text{N}_2\text{O}$  evolution rate is about 0.1 to 2 times the normalized observed carbonyl formation rate. Also, the normalized observed crosslinking rate is about equal to 30 times slower than the normalized observed carbonyl formation rate. Similar values (i.e., within an order of magnitude) of all of the observed rates normalized by the initial amount of NP may suggest that NP decomposition is the rate limiting step in both the carbonyl formation and Estane crosslinking in Estane/NP mixtures. This can be demonstrated using a simple mechanism (NP decomposition, activation of Estane by decomposition products, and a branching competition between carbonyl formation and crosslinking) and steady state kinetic analysis.

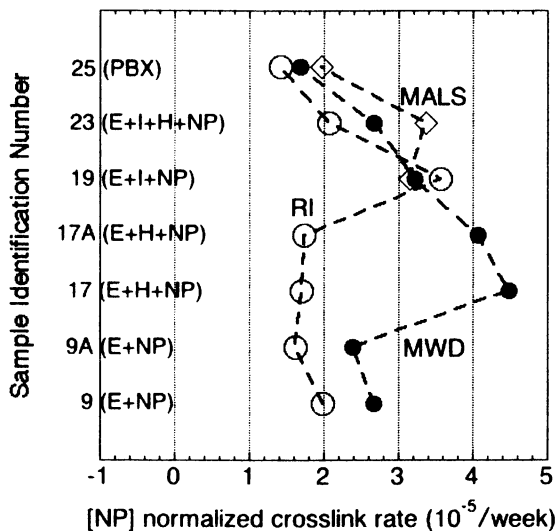


Figure 5. NP normalized crosslinking rate ( $R_{X-link}/[NP]_0$ ) at  $T = 64\text{ }^{\circ}\text{C}$  for CAS Samples #9, #9A, #17, #17A, #19, #23, and #25. E=Estane, NP=nitroplasticizer, H=HMX, I=Irganox, PBX=PBX 9501 (See Table I for composition of each sample.) Open circles=rate determined from weight-averaged MW with RI detection. Closed circles=rate determined from MWD with RI detection. Open diamonds=rate determined from weight-averaged MW with MALS detection.

Future work will include combining the chain scission kinetics of ester hydrolysis ( $I$ ) with crosslinking kinetics of urethane oxidation to provide an overall kinetic model of Estane molecular weight change. This combined hydrolysis/oxidation kinetic model will allow us to make lifetime predictions for the PBX 9501 binder.

### Acknowledgements

The authors would like to acknowledge Russ Pack, Sheldon Larson, and Robert Houlton for useful discussions and Gail Watson for obtaining analytical results. This work was supported under the Enhanced Surveillance Campaign by the U.S. Department of Energy at Los Alamos National Laboratory, operated by Los Alamos National Security, LLC under contract number DE-AC52-06NA25396.

## References

1. Salazar, M. R.; Lightfoot, J. M.; Russell, B. G.; Rodin, W. A.; McCarty, M.; Wroblewski, D. A.; Orlor, E. B.; Spieker, D. A.; Assink, R. A.; Pack, R. T. *J. Polym. Sci. A* **2003**, *41*, 1136-1151.
2. Wroblewski, D. A.; Langlois, D. A.; Orlor, E. B.; Labouriau, A.; Uribe, M.; Houlton, R.; Kress, J. D.; Kendrick, B., this volume.
3. Bolland, J. L.; Gee, G. *Trans. Faraday. Soc.* **1946**, *42*, 236-243.
4. Pauler, D. K.; Kress, J. D.; Lightfoot, M. L.; Woods, L.; Russell, B. G. *AIP Conf. Proceedings* **2006**, *845*, 547-550.
5. Pauler, D. K.; Henson, N. J.; Kress, J. D. *Phys. Chem. Chem. Phys.* **2007**, *37*, 5121-5126.
6. Orlor, E. B.; Wroblewski, D. A.; Cooke, D. W.; Bennett, B. L.; Smith, M. E.; Jahan, M. S.; King, M. C. *Polym. Prepr.* **2001**, *42*, 428-429.
7. Salazar, M. R.; Kress, J. D.; Pack, R. T.; Pauler, D. L.; Lightfoot, J. M.; Russell, B. G.; Rodin, W. A.; Woods, L. *Propel. Explos. Pyrotech.*, in press.
8. Brill, T. B.; Gongwer, P. E.; Williams, G. K. *J. Phys. Chem.* **1994**, *98*, 12242-12247.
9. Cozewith, C.; Graessley, W. W.; Verstrate, G. *Chem. Eng. Sci.* **1979**, *34*, 245-248.
10. LeMaster, D. M.; Hernandez, G. *Macromolecules* **2000**, *33*, 3569-3576.
11. Wroblewski, D. A.; Langlois, D. A.; Orlor, E. B.; Dattelbaum, D. M.; Small, J. H. *Polym. Prepr.* **2004**, *45*, 789-790.

## Chapter 21

# Degradative Thermal Analysis and Dielectric Spectroscopy Studies of Aging in Polysiloxane Nanocomposites

J. P. Lewicki<sup>1</sup>, J. J. Liggat<sup>1</sup>, D. Hayward<sup>1</sup>, R. A. Pethrick<sup>1</sup>,  
and M. Patel<sup>2</sup>

<sup>1</sup>Department of Pure and Applied Chemistry, Westchem, University of Strathclyde, 295 Cathedral Street, Glasgow G1 1XL, United Kingdom

<sup>2</sup>Atomic Weapons Establishment, Aldermaston, Reading RG7 4PR, United Kingdom

The characterization of the physical and chemical changes that occur in montmorillonite/PDMS nanocomposite elastomers as they are thermally aged is reported. Broadband Dielectric Spectroscopy (BDS) was used to track changes in the physical interaction between the polymer and clay associated with increases in non-oxidative thermal stability (as determined by TGA). The evolution of volatile siloxane species from the elastomers was characterized with Thermal Volatilization Analysis (TVA). Results suggest that the improved thermal stability and the increases in polymer/clay association are a result of significant re-structuring of the polymer network.

## Introduction

Filled polysiloxane elastomers, as with the majority of polymeric materials, are known to 'age' under normal environmental conditions during their lifetime (1,2). Aging in a simple amorphous polymeric material can be categorized as physical or chemical. In amorphous polymers below  $T_g$ , physical aging is the gradual movement of the segmental structure of the polymer towards thermodynamic equilibrium (3). This re-ordering of the polymer chains' spatial arrangement affects several physical properties of the polymer such as its free volume, density and  $T_g$ . Due to the restricted segmental mobility below  $T_g$  the process is often slow – occurring over a period of years. Physical aging is also considered to be reversible.

Chemical aging or chemical degradation is distinct from physical aging in that it involves often irreversible changes to the chemical structure of the polymer. Examples include oxidative crosslinking, de-polymerization, and UV-induced chain scission. These chemical changes can alter many of the physical and chemical properties of a polymeric material and again, often occur over extended timescales.

### Polysiloxane Nanocomposites

Historically, polysiloxane elastomers have been reinforced with micron scale particles such as amorphous inorganic silica to form polysiloxane microcomposites. However, with the continued growth of new fields such as soft nanolithography, flexible polymer electronics and biomedical implant technology, there is an ever increasing demand for polysiloxane materials with better defined, improved and novel physical, chemical and mechanical properties. In line with these trends, researchers have turned towards the development of polysiloxane nanocomposites; systems which incorporate a heterogeneous second phase on the nanometer scale. Over the last decade, there has been much interest in polymeric nanocomposite materials and the reader is directed towards the reviews by Alexandre and Dubois (4) or Joshi and Bhupendra (5) on the subject.

Examples of the synthesis of polysiloxane nanocomposites reported in the literature include: Work by Ma *et al.* (6) who modified montmorillonite with short segments of PDMS and blended this into a polymer melt/solution to yield examples of fully exfoliated or intercalated PDMS/clay nanocomposites. Pan, Mark *et al.* (7) synthesized well defined nano-fillers by reacting groups of four vinyl terminated POSS cages with a central siloxane core. These materials were subsequently chemically bonded into a PDMS network yielding a significant improvement in the mechanical properties of the polymer.



## Aging of Polysiloxane Elastomers

Polysiloxane microcomposites are known to age through a combination of irreversible chemical changes occurring in the bulk polymer network and reversible physical changes that occur at the polymer-filler interface: Maxwell *et al.* (8,9) have made use of solid state NMR techniques to study the changes in the motional dynamics of crosslinked PDMS in relation to silica filler particles under the influence of ionizing radiation or desiccating environments. Patel *et al.* (1,10) have carried out accelerated thermal aging studies on commercial room temperature vulcanized, diatomaceous earth filled PDMS elastomer systems; establishing that significant alterations in the mechanical properties of these materials are brought about by chemical degradation of the PDMS network. Recently, Labouriau *et al.* (11) have published a study on the effects of both natural and accelerated aging on commercial elastomeric siloxane foams highlighting the significance of tin catalyst residues present in such commercial systems.  $^{119}\text{Sn}$  Mössbauer spectroscopy analysis has shown that as these systems are aged, the tin changes from a (IV) to a (II) oxidation state and these catalyst residues play a role in promoting chemical aging of PDMS networks.

The aging behavior of conventional filled polysiloxane materials has been relatively well studied. However, there is little currently known about the long term stability and aging behavior of polysiloxane nanocomposites. This is a key issue that must be addressed if polysiloxane nanocomposites are to become part of the next generation of polymeric materials.

## Experimental

### Broadband Dielectric Spectroscopy

BDS can be used as a powerful non-invasive technique to study heterogeneous polymer systems: Daly *et al.* (12) studied the morphology of polycarbonate/styrene-acrylonitrile copolymer composites with BDS by analyzing the low frequency loss processes resulting from the accumulation of virtual charges in the interfacial regions of the copolymer system. Such interfacial polarization processes are often termed Maxwell-Wagner-Sillars (MWS) processes. The dielectric losses attributed to MWS processes can yield valuable information on the nature and morphology of a heterogeneous system.

MWS processes occur due to the accumulation of charge at the interface between two materials with differing permittivities. The resulting polarization at the interface effectively adds an additional loss component to any observed dielectric response. In polymeric systems these additional loss components

usually occur at significantly lower frequencies than the primary dipolar relaxations of the system.

The majority of interfacial polarization loss processes can be closely approximated by some modification of the Debye description of orientational dipole polarization in homogeneous media (13). The subject of interfacial polarization effects and the dielectric properties of many classes of heterogeneous systems have been reviewed by Van Beek (14).

In this study, both the normal mode relaxation of the siloxane network and the MWS processes arising from the interaction of the dispersed nanoclay platelets within the polymer network have been observed. Although it is routine practice to observe the primary alpha relaxation of a polymeric system at temperatures below  $T_g$ , in this work it is the MWS processes associated with the clay particles within the polymer matrix that are of interest. Therefore, all BDS analyses were conducted at 40°C over a frequency range of  $10^{-2}$  to  $6.5 \times 10^5$  Hz. At these temperatures, interfacial polarization effects dominate the dielectric response of the filled systems and although it is possible to resolve a normal mode relaxation of the polymer in the unfilled system (see Figure 2), MWS processes arising from the presence of the nanoclay mask this comparatively weak process.

The instrument used for all BDS analyses was a Strathrow Dielectric Spectrometer. This instrument was based upon a Solartron SI 1250 Broadband Frequency Response Analyzer. The instrument had a working frequency range of  $10^{-3}$  to  $6.5 \times 10^5$  Hz. All BDS analysis reported in this paper were carried out using a computer controlled frequency domain method, as described by D. Hayward *et al.* (15). All samples were analyzed in a parallel plate capacitance cell having two nickel plated copper electrodes. The lower and upper (*low* and *high*) electrodes were 25 and 20 mm in diameter respectively – providing an effective sample diameter of 20 mm. All samples were ~3 mm in thickness.

### Thermal Volatilization Analysis

TVA is a unique evolved gas analysis technique that was developed in the late 1960s by McNeill and co-workers (16,17) to study polymer degradation. TVA is based upon the principle of accurate measurement of the pressure of volatile species evolved from an analyte undergoing a heating regime. TVA monitors the evolution of volatile degradation products from a sample as it is subjected to a linear heating ramp under vacuum. The use of Sub-Ambient TVA allows the simultaneous capture of condensable volatile species and the monitoring of all evolved species that are non-condensable under vacuum at -196°C. Subsequent differential distillation of all captured volatiles is achievable which greatly facilitates the identification of degradation products. Although TVA was primarily developed as a technique to study polymer

degradation, the inherent versatility of the technique lends itself to other applications. All TVA analysis in this study was carried out using a TVA line (see Figure 1) which was built in-house, based upon the apparatus and techniques described by McNeill *et al.* (16).

The apparatus consisted of a sample chamber (heated by a programmable tube furnace) connected in series to a primary liquid nitrogen cooled sub-ambient trap and a set of four secondary liquid nitrogen cooled cold traps. The system was continuously pumped to a vacuum of  $1 \times 10^{-4}$  Torr. High boiling point volatiles were condensed immediately above the furnace at a water cooled 'cold ring' ( $T \sim 12^\circ\text{C}$ ). All other condensable products were captured in primary sub-ambient trap ( $T \sim -196^\circ\text{C}$ ). Two linear response Pirani gauges positioned at the entrance and exit of the primary sub-ambient trap monitored the evolution of condensable and non-condensable volatiles as a function of pressure vs. temperature/time. Captured volatile species were distilled into separate fractions by slowly heating the sub-ambient trap to ambient temperatures. Separated fractions were subsequently removed into gas-phase cells for FTIR and GC-MS analysis.

### Preparation of Siloxane-Montmorillonite Nanocomposites

A series of five nanocomposite elastomer systems were prepared for this study incorporating 0, 1, 2, 4 and 8% (on total resin mass) of the organically modified montmorillonite clay; Cloisite 6A. The appropriate level of Cloisite was dispersed in a starting resin blend of OH terminated PDMS ( $M_n \sim 77,000$  and  $M_n \sim 550 \text{ g mol}^{-1}$  in a 3:1 ratio) by a combination of mechanical mixing and ultrasonic processing to give a nano-dispersion of clay platelets. The blend was subsequently crosslinked with a stoichiometric level of tetrapropoxysilane (TPOS) in the presence of 5% diphenylmethylsilanol (DPMS) chain terminator and 5% tin(II) 2-ethylhexanoate catalyst, cured in an open mould at  $65^\circ\text{C}$  for twenty minutes, then removed from the mould and post cured for a further fifteen hours at  $65^\circ\text{C}$  to give an elastomeric mat.

### Accelerated Aging Methodology

All samples were aged simultaneously, sealed in separate environmental chambers under two contrasting sets of conditions; moisture saturated air and dry nitrogen. All aging was carried out at  $150^\circ\text{C}$  in order to accelerate the aging processes. Total aging time was 504 hours with sampling intervals at 0, 24, 72, 168, 336 and 504 hours. Two duplicate sets of samples were prepared (one for each environment. Each set comprised all five variant subsets of 0, 1, 2, 4 and 8% Cloisite.

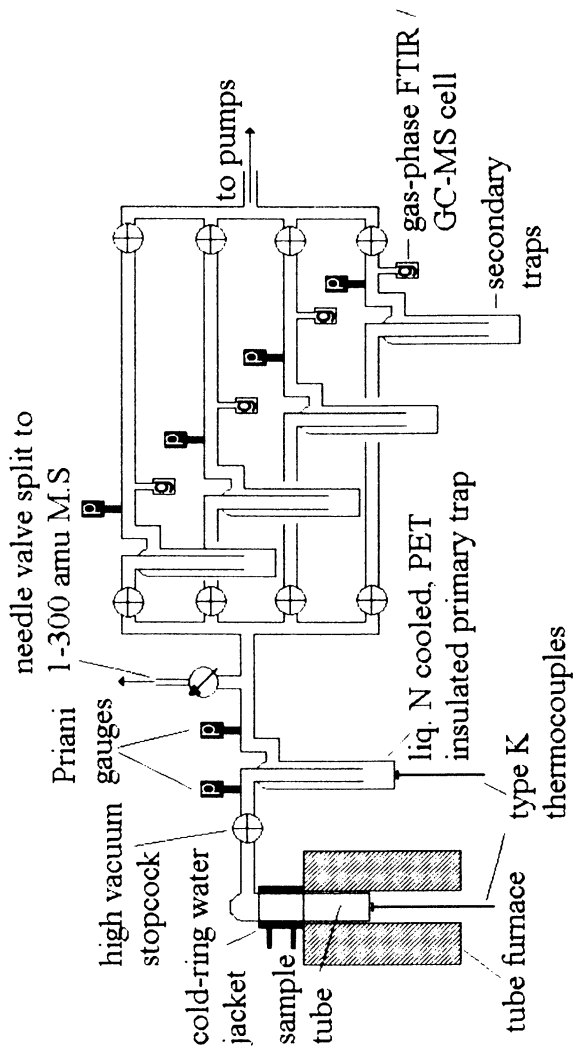


Figure 1. Schematic diagram of the TVA system showing the degradation section connected in series to the S-A trap and four secondary fraction traps.

## Results and Discussion

### Broadband Dielectric Spectroscopy (BDS) Analysis

The unfilled elastomer system was initially studied by BDS and it can be seen in Figure 2 that the dielectric response is a combination of a dipolar relaxation process (assigned as the normal mode relaxation of the PDMS chains) and a dc conductivity contribution. The complex response in Figure 2 has been mathematically resolved into its individual components for clarity by separating the complex experimental data into components of  $\epsilon'$ ,  $\epsilon''$  and  $\sigma$  using an empirical minimization function running from MathCAD. The program used a Levenberg-Marquardt routine to arrive at parameters which fit one or more Havriliak-Negami (18) H-N dispersion curves to the experimental data. (It has been found that minimizing on the modulus of the complex permittivity gives the most stable solutions).

It can be observed from Figure 3 that the inclusion of Cloisite particles into the system introduces two distinct new processes, a low frequency MWS response and a broad relaxation in the kHz region. Both processes increase in intensity

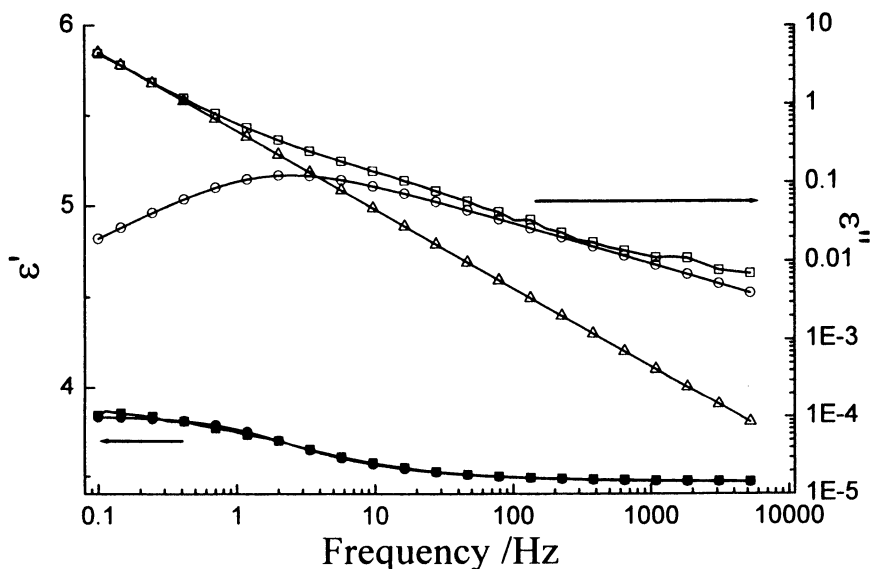


Figure 2. BDS spectrum of the unfilled elastomer at 40°C. Solid squares and circles represent the experimental and resolved real permittivity components respectively. Hollow squares, circles and up-triangles represent the experimental complex imaginary permittivity, the resolved component of the imaginary permittivity and the resolved dc conductivity contribution.

with increasing filler loading. The low frequency response is directly linked to an interfacial polarization of the clay platelets within the polymer matrix and the kHz region response is also thought to be MWS in origin with an associated contribution due to the relaxation of water associated with the clay particles.

Figures 4 and 5 illustrate the changing dielectric response of the 2% Cloisite filled system measured at 40°C, as a function of sample age under dry nitrogen and moist air conditions.

It can be observed from Figures 4 and 5 that as the 2% Cloisite system is aged under both environments there is a gradual decrease in the permittivity of the system. This is attributed to a loss of mobile ionic species including water and the catalyst breakdown product, 2-ethylhexanoic acid. In the nitrogen aged system there is an associated decrease in the intensity of kHz region MWS process, not observed in the moist air aged system. This is indicative of the loss of the water contribution to the kHz relaxation which is consistent with thermal aging under anhydrous conditions. The low frequency MWS relaxation does not change significantly after the initial 24 hours of aging in the nitrogen aged system. However in Figure 5, a clear shift in the low frequency MWS process towards lower frequencies is observed. This is a clear indication that thermal aging under moist air has induced a change in polymer/clay structure. It is thought that an increase in the level of polymer/clay association is decreasing the local ionic mobility around the clay platelets, leading to a shift in the low frequency MWS relaxation.

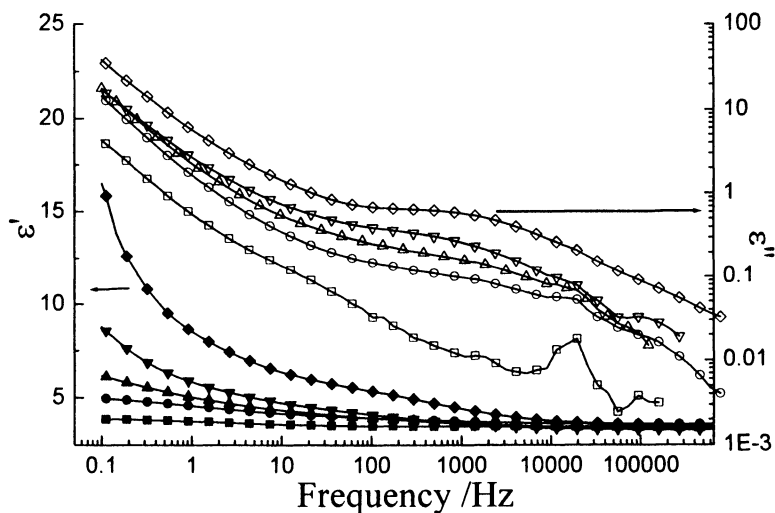


Figure 3. BDS spectra of nanocomposite systems at 40°C. Solid symbols represent real permittivity and hollow symbols represent imaginary permittivity. Squares, circles, up-triangles, down-triangles and diamonds represent levels of 0, 2, 4 and 8% Cloisite respectively.

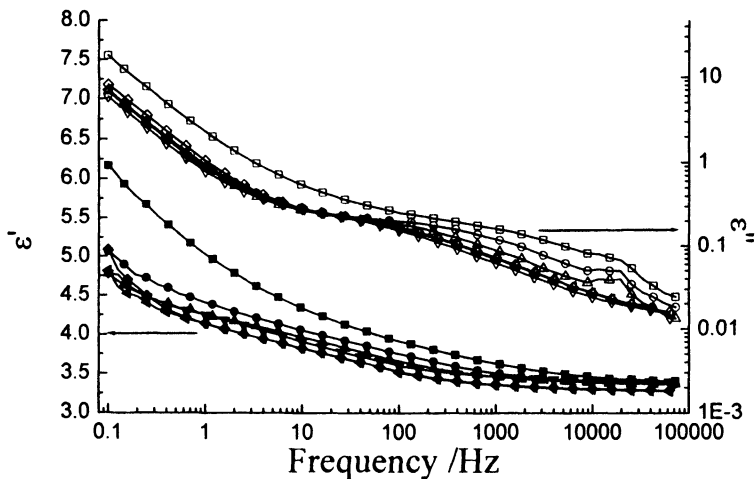


Figure 4. BDS spectra of 2% Cloisite system aged under dry  $N_2$ . Solid symbols represent real permittivity and hollow symbols represent imaginary permittivity data. All measurements were performed at  $40^\circ\text{C}$ . Squares, circles, up-triangles, down triangles, diamonds and crosses correspond to 0, 24, 72, 168, 336 and 504 hours aging time.

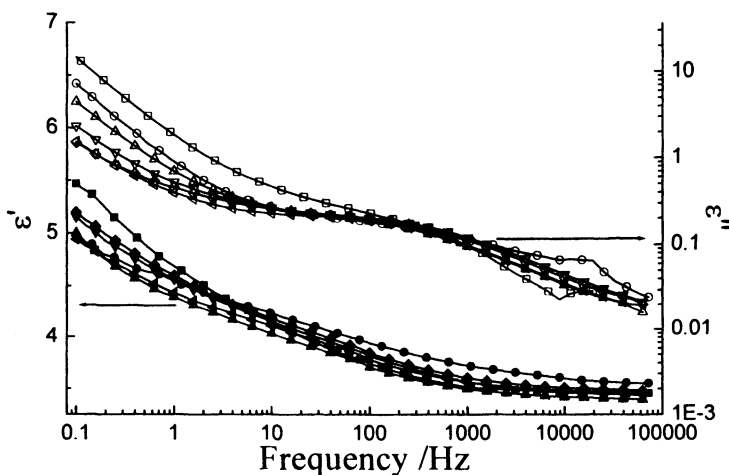


Figure 5. BDS spectra of 2% Cloisite system aged under moist air. Solid symbols represent real permittivity and hollow symbols represent imaginary permittivity. All measurements were performed at  $40^\circ\text{C}$ . Squares, circles, up-triangles, down triangles, diamonds and crosses correspond to 0, 24, 72, 168, 336 and 504 hours aging time.

### Thermogravimetric Analysis

TGA was utilized to monitor the non-oxidative degradation behavior of the nanocomposite systems as a function of age time. Onset temperatures for non-oxidative degradation were determined from the first derivative of the sample mass. Figures 6 and 7 illustrate the trends in non-oxidative degradation temperature with age time for all systems under both environments.

It can be observed that the non-oxidative stability of all systems increases as a function of age time under both environments. Each system exhibits an initial rapid increase in thermal stability over the first 24 hours of aging followed by a more gradual increase over the remainder of the study. It is reasonable to assume that these initial increases are in part due to the loss of pro-degradants such as 2-ethylhexanoic acid and other reaction by-products such as propanol from the elastomer system (2-ethylhexanoic acid is a hydrolysis product of the active organotin catalyst, tin(II) 2-ethylhexanoate and propanol is formed during the TPOS/silanol condensation reaction).

It can also be seen, however that the magnitude of the increase in thermal stability is dependant on the aging environment. In Figure 7 it is observed that moist air aging has induced greater increases thermal stability when compared to dry nitrogen aging.

For example, the 1% Cloisite filled system experiences a 40°C increase in onset degradation temperature after 504 hours aging under moist air compared with the same system under dry N<sub>2</sub> conditions, which exhibits an 11°C increase after the same period. Such changes cannot wholly be accounted for by passive degradant loss and these data suggest that a chemical aging process is responsible.

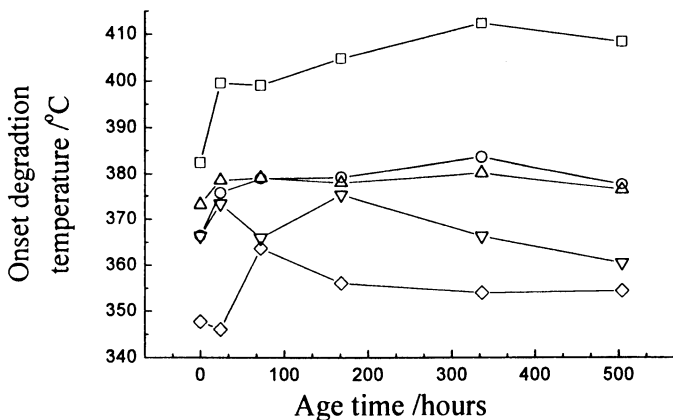


Figure 6. Onset degradation temperature as a function of age time for systems aged under dry N<sub>2</sub>. Squares, circles, up-triangles, down triangles and diamonds correspond to 0, 1, 2, 4 and 8% Cloisite filled systems respectively.



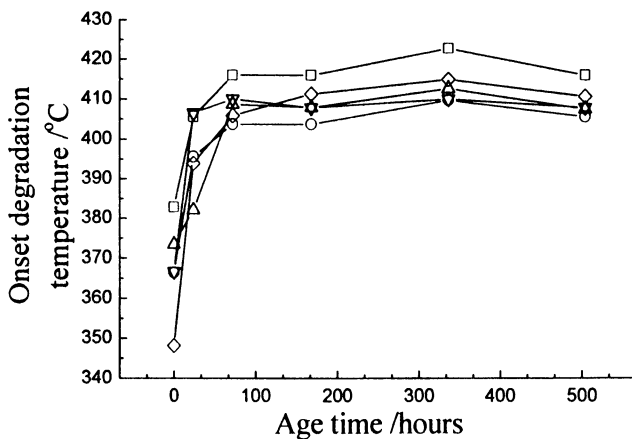


Figure 7. Onset degradation temperature as a function of age time for systems aged under moist air. Squares, circles, up-triangles, down triangles and diamonds correspond to 0, 1, 2, 4 and 8% Cloisite filled systems respectively.

### Sample Mass Analysis

Prepared samples of each nanocomposite system were accurately weighed at each aging interval. This provided a useful indication as to whether a significant change in sample mass was being induced by the aging conditions. It can be seen from Figure 8 that as the systems are aged, they lose material. The mass loss is most pronounced in the moist air environment with the nanocomposites losing 3-5% of their total mass. In both systems the rate of mass loss decreases with increasing Cloisite level.

It is reasonable to link the mass loss with the observed changes in thermal stability and dielectric response, indeed some of this material that is evolved from the systems on aging is likely to be water and the reaction residues implicated as pro-degradants. However, the level of material lost the ongoing nature of the process and the clear link once again with a moist air environment points to an explanation other than simple passive loss of volatile residues from the nanocomposites. Clearly, an identification of this volatile material is desirable if the nature of the aging processes occurring within these polysiloxane nanocomposites is to be elucidated.

### Thermal Volatilization Analysis

TVA was employed in order to characterize the volatile species that were evolved from the nanocomposite systems on aging. The goal of the study was

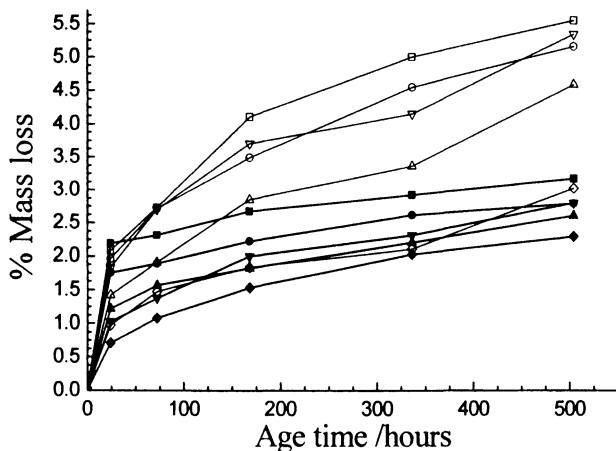


Figure 8. Percentage mass loss as a function of sample age. Solid symbols represent  $N_2$  aged systems and hollow symbols represent air aged systems. Squares, circles, up-triangles, down triangles and diamonds correspond to 0, 1, 2, 4, and 8% Cloisite filled systems respectively.

to provide a 'snapshot' of the material evolved from different systems of differing ages. Each sample variant was held isothermally at  $150^\circ\text{C}$  for a period of  $\sim 3$  hours. Evolved material was captured at the cold ring and in the sub-ambient trap. Differential distillation of captured volatiles was carried out, FTIR and GC-MS were used to identify the separated species.

GC-MS analysis of collected cold-ring fractions identified them as consisting primarily of a series of cyclic oligomeric siloxanes with ring sizes ranging from  $D_5$  to  $D_{23}$  (see Figure 9). FT-IR analysis of the cold-ring fractions also identified an aromatic contribution corresponding to the di-phenyl end-cap, indicating that it had detached from the network.

Sub-ambient differential distillation identified significant alterations in the profile of evolved volatiles with aging. The captured volatiles from the 2% Cloisite system were divided into three main fractions (labeled 1 to 3 on Figure 10). Fraction 1 was identified as a low molecular weight alkyl siloxane. The  $D_3$  cyclic siloxane oligomer was identified in fraction 2 with complex siloxane residues and water. (Water is responsible for the twin peak in the virgin system). Fraction 3 was identified as containing cyclic oligomeric siloxanes from  $D_4$  to  $D_{10}$  and a significant quantity of 2-ethylhexanoic acid in the virgin system. Smaller quantities of alkyl silanoate esters were detected by GC-MS in fraction 3 of the aged systems.

From Figure 10 it can clearly be observed that aging under both conditions results in the loss of the low boiling peak 1, the near complete loss of peak 3 and

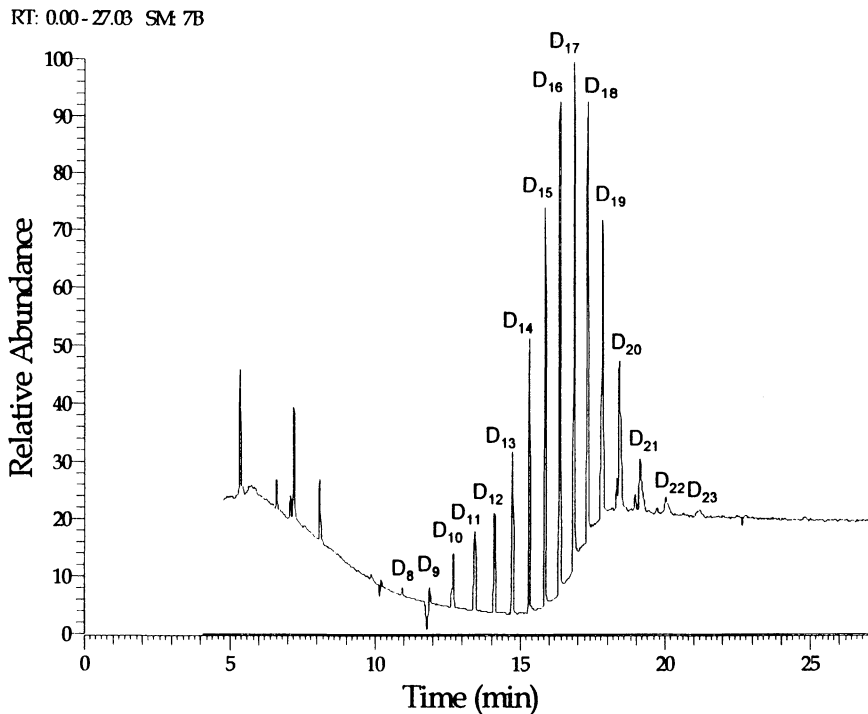


Figure 9. GC-MS chromatogram of the collected cold-ring fraction from the virgin unfilled elastomer showing a series of cyclic siloxanes from  $D_8$  to  $D_{21}$ .

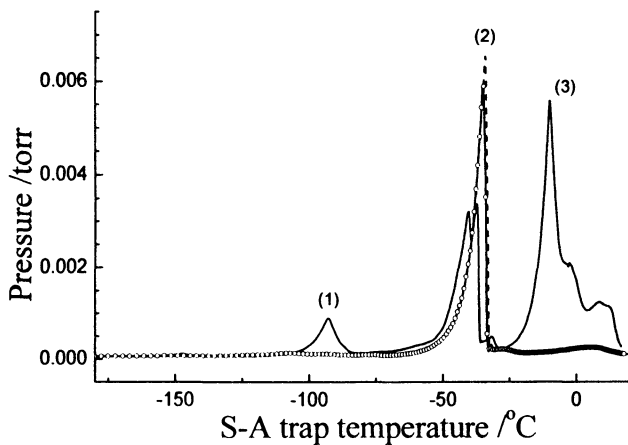


Figure 10. Composite differential distillation profiles for the 2% Cloisite filled system a virgin state and after 504 hours of aging. Solid, dashed and lines with circle symbols correspond to virgin,  $N_2$  aged and air aged samples respectively.

an increase in the intensity of peak 2 with the loss of the water shoulder. These data confirm that the nanocomposites do indeed lose water, 2-ethylhexanoic acid and other small species upon aging. However, after 504 hours of thermal aging, they still evolve significant quantities of cyclic oligomeric siloxanes and small, yet significant quantities of more complex alkyl silanoate ester species and di-phenyl based residues.

This strongly suggests that these cyclic oligomeric siloxanes are being actively produced within the nanocomposite systems as a result of the thermal aging and are not simply passive residues from the initial synthesis.

### A Model of Network Reformation

It is reasonable to assume that the production of cyclic oligomers is linked to the observed physical and chemical changes occurring in the nanocomposite systems and is indicative of a chemical process occurring within the siloxane network. It thought that the main engine driving the formation of the cyclic siloxanes within the elastomer systems are a series of backbiting reactions similar to those proposed by Grassie *et al.* (19) as a mechanism of the thermal de-polymerization of PDMS (see Figure 11).

PDMS backbiting reactions typically occur at temperatures of 350-400°C. However, Grassie and co-workers (18) also reported that the presence of a Lewis acid or base could catalyze the de-polymerization allowing significant backbiting to occur at temperatures as low as 110 °C. In the systems reported here, the catalyst residues; tin hydroxide and 2-ethylhexanoic acid are thought to serve as the catalysts for these low temperature backbiting reactions.

Water strongly influences the aging of the nanocomposite systems. The Si-O bond is labile to acid/base catalyzed hydrolysis and hydrolysis is recognized in the literature as one of the primary low temperature degradation reactions which occur in polysiloxanes (20). It is thought that significant levels of chain hydrolysis occur within the moist air aged systems. Hydrolysis of the network will provide large numbers of free OH-terminated chain ends which can participate in backbiting reactions. Water is also thought to be responsible for the loss of the di-phenyl end-cap through acid/base catalyzed hydrolytic attack.

Free OH-terminated chain ends generated by hydrolysis can also undergo condensation to give a new Si-O bond. Hydrolysis and recombination reactions such as this can lead to significant re-arrangement of a siloxane network.

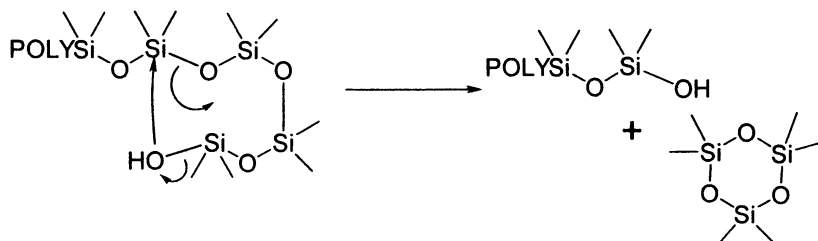
It is proposed that the overall combination of chain scission, backbiting and recombination within the network results in significant re-arrangement and optimization of the network. The driving force behind this form of reformation process is primarily thermodynamic and it in effect mirrors the equilibration reactions that are used in order to build high molar mass PDMS polymers from small oligomeric starting materials (21).

## Conclusions

The results of the BDS and TGA analysis of the Cloisite/PDMS nanocomposite systems which underwent thermal aging strongly suggest that there is an active process occurring in these nanocomposite elastomers that is inducing significant alterations in the nature of the polymer/clay association and increasing the thermal stability of the systems. It is also clear that these physical and chemical changes are linked to a significant mass loss from the siloxane elastomers and that moist, oxidative aging conditions promote the most significant changes. TVA analysis identified that the material lost from the siloxane elastomers consists of cyclic oligomeric siloxanes (ring sizes D<sub>3</sub>-D<sub>26</sub>), 2-ethylhexanoic acid and a complex mixture of alkyl silanoate esters, di-phenyl silanol and related residues. Importantly, TVA analysis also demonstrated that significant quantities of cyclic oligomeric siloxanes are still present in aged samples which strongly suggest that these cyclic siloxanes are being actively produced within the siloxane networks upon aging.

It is proposed that thermal aging of the Cloisite/PDMS elastomers promotes the reformation of the siloxane network into a more thermodynamically stable form though a series of catalytically driven chain backbiting, hydrolysis and recombination reactions. This produces a siloxane network with increased thermal stability which is more intimately associated with the nano-filler.

Backbiting at a free chain end:



Continuous chain backbiting:

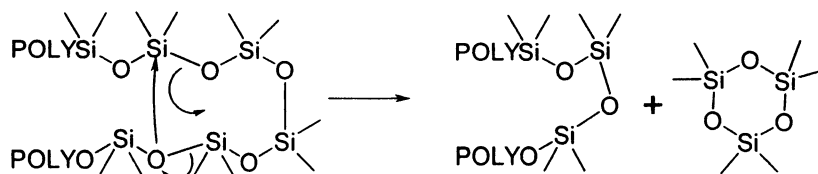


Figure 11. Intramolecular chain backbiting mechanisms.

## References

1. Patel, M.; Skinner, A. R. *Polym. Degrad. Stab.* **2001**, *73*, 399.
2. Oldfield, D.; Symes, T. *Polym. Test.* **1996**, *15*, 115.
3. Struik, L. C. E. *Physical Aging in Amorphous Polymers and Other Materials*; Elsevier Scientific Publishing: Amsterdam, 1978; pp 2-25.
4. Alexandre, M.; Dubois, P. *Materials Science and Engineering R-Reports* **2000**, *28*, 1.
5. Joshi, M.; Bhupendra, S. B. *J. Macromol. Sci. Part C: Polym. Rev.* **2004**, *44*, 389.
6. Ma, J.; Xu, J.; Ren, J.; Yu, Z.; Mai, Y. *Polymer* **2003**, *44*, 4619.
7. Pan, G. R.; Mark, J. E.; Schaefer, D. W. *J. Polym. Sci. B Polym. Phys.* **2003**, *24*, 3314.
8. Maxwell, R. S.; Chinn, S. C.; Gjersing, E.; Herberg, J. L.; Giuliani, J. *Polym. Prepr.* **2007**, 47.
9. Balazs, B.; Deteresa, S.; Maxwell, R. S.; Kokko, E.; Smith, T. *Polym. Degrad. Stab.* **2003**, *82*, 187.
10. Patel, M.; Soames, M.; Skinner, A. R.; Thomas, S. *Polym. Degrad. Stab.* **2004**, *83*, 111.
11. Labouriau, A.; Cox, J. D.; Schoonover, J. D.; Patterson, B. M.; Havrilla, G. J.; Stephens, T.; Taylor, D. *Polym. Degrad. Stab.* **2007**, *92*, 414.
12. Daly, J. H.; Guest, M. J.; Hayward, D.; Pethrick, R. A. *J. Mater. Sci. Letters.* **1992**, *11*, 1271.
13. Hedvig, P. *Dielectric Spectroscopy of Polymers*; Adam Hilger Ltd: Bristol, UK, 1977; pp 283-291.
14. Van Beek, L. K. H. *Progress in Dielectrics* **1967**, *7*, 69.
15. Hayward, D.; Gawayne, M.; Mahboubian-Jones, B.; Pethrick, R. A. *J. Phys. E: Sci. Instr.* **1984**, *17*, 683.
16. McNeill, I. C. *Eur. Polym. J.* **1967**, *5*, 409.
17. McNeill, I. C.; Ackerman, L.; Gupta, S. N.; Zulfiquar, M.; Zulfiquar, S. J. *Polym. Sci. A: Polym. Chem.* **1977**, *15*, 2381.
18. Havriliak, S.; Negami, S. *Polymer* **1967**, *8*, 161-210.
19. Grassie, N.; MacFarlane, I. G. *Eur. Polym. J.* **1978**, *14*, 875.
20. Lewis, F. M. *Rubber Chem. Tech.* **1962**, *35*, 1222.
21. Osthoff, R. C.; Bueche, A. M.; Grubb, W. T. *J. Amer. Chem. Soc.* **1954**, *76*, 4659.

## Chapter 22

# Aging of Foamed Polysiloxanes Incorporating Nanoparticles

**Julian J. Murphy, Jon Meegan, Mogon Patel, Paul R. Morrell,  
Anthony C. Swain, and Jenny L. Cunningham**

**Atomic Weapons Establishment, Aldermaston,  
Reading RG7 4PR, United Kingdom**

Here we outline an approach that has been taken to develop Poly(dimethylsiloxane) (PDMS) systems, which have property changes that are easier to predict. The problems associated with the inclusion of a filler phase that is required for PDMS systems to have many useful physical properties have been addressed by producing nano filled equivalents. It is shown that such systems offer easier control over the materials produced whilst also resulting in a simplification of physical properties. The production of foamed systems, which introduces an additional variable, is also discussed. The influence of foam structure upon the measured properties of a material is outlined and implications for sample production and the development of predictive ageing models are explored.

NOTE: © Crown Copyright (2004)

“This Document is of United Kingdom origin and contains proprietary information which is the property of the Secretary of State for Defence. It is furnished in confidence and may not be copied, used or disclosed in whole or part without prior written consent of the Intellectual Property Rights Group, IPR-PL1, Ministry of Defence, Abbey Wood Bristol BS34 8JH, England”.

## Introduction

The development of predictive ageing models for individual polymer systems is a very complex process. Many materials are formulations of a number of different components, any of which can affect observed ageing trends. In filled systems there are additional effects since the properties of the material are dependent upon interactions at the polymer/filler interface. These interactions can be highly complex and are often influenced by subtle chemical and morphological changes in the polymer phase. Understanding how the performance of a complex component changes over time adds significantly to the level of difficulty. In structured components such as foams the precise nature of the cell structure has a significant influence on physical properties.

The implications of small differences in cell structure for accurate measurement of physical properties are significant. Very small differences in manufacturing methodology or environmental conditions during production can tip a structure from fully open to partially closed cell. This causes a large change in the resulting compression properties since gas contained within closed cells has to be compressed during deformation. The properties are also time dependent since gas diffusion through the cell walls will take place over extended timescales. Small changes in the size of cells and/or the thickness of cell walls will also affect the properties of a foamed component. Collapse of the cell structure during deformation gives regions of different stress strain response resulting in physical property measurements that are highly strain dependent.

The following paper details the approach that has been taken to develop Poly(dimethylsiloxane) (PDMS) systems, which have property changes that are easier to predict. One of the biggest problems with PDMS systems is associated with the inclusion of a filler phase that is required for a system with useful physical properties (1) PDMS elastomers are typically reinforced with a filler phase to improve the physical properties of the resulting composite material since load transfer between the soft polymer and hard filler components results in enhanced properties (2). The most commonly used fillers in PDMS systems are particulate silica fillers due to their affordability, high surface area and compatibility with the polymer matrix (3). However, the incorporation of these irregular shaped, hydroscopic, high surface area fillers lead to complicated degradation trends (4,5) as well as the exhibition of complex mechanical behaviors such as the Mullins effect (6). Some of the interfacial effects in filled systems can be inhibited through careful choice of filler phase and there is a great deal of work that concentrates on modifying the filler component (7, 8, 9). The introduction of uniform nanotubular fillers (silica and carbon) or molecular equivalents (PolyoctahedralOligomericSilSesquioxane (POSS) and Carboranes) into PDMS elastomers can be used to both modify and simplify the mechanical and ageing behaviors of these composite materials, and work on such materials will be discussed in detail.



As PDMS elastomers are often used to produce foamed systems, understanding the influence that the foam structure has upon the measured properties of a material is crucial to the development of a confident ageing model. Moreover, understanding the variations in foam structures that are introduced by production processes is critical for the prediction of long term performance for components. Work detailing the precise characterization of foam structures using a number of techniques is discussed. Variation introduced by production processes and the implications for performance prediction will also be outlined. Strategies for producing idealized foam structures that overcoming such problems and the implication for performance prediction are detailed.

## Experimental Details

Poly(*m*-carboranyl-siloxane) elastomers containing a mixture of di-methyl- and methyl(phenyl)-silyl units were synthesised using the Ferric Chloride catalyzed condensation reaction between di-chloro-di-organosilane and 1,7-bis(di-methyl(methoxy)silyl)-*m*-carborane. Silica Nano tubes synthesised using *insitu* growth of DL Tartaric acid nanocrystals and concurrent sol-gel hydrolysis and condensation of silane.

POSS was mechanically dispersed in a functionalized polysiloxane gum using a speedimix (needs some details) and the mix cured using tin catalyzed condensation chemistry. Silica and Carbon nano fiber composites were produced by mixing the fiber into functionalized polysiloxane gum and the mix cured using tin catalyzed condensation chemistry.

Mechanical properties were assessed through Dynamic Mechanical Analysis (DMA), Proton NMR relaxation ( $T_2$ ) studies were used to assess segmental chain dynamics. X-ray micro tomography was used to characterize foam structure. Gamma irradiation was performed by exposure to a  $^{60}\text{Co}$  source.

## Results and Discussion

### Carborane Modified Materials

The plots in Figure 1 and Figure 2 display changes in the  $T_2$  relaxation time for a series of samples exposed to gamma radiation doses. The plots in Figure 1 were obtained using a conventionally silica filled PDMS material. The linear region of the plot where  $1/T_2$  increases after a dose of approximately 0.1 MGy is caused by radiation induced crosslinking resulting in a stiffening of the material. At low doses, between 0 and 0.1 MGy,  $1/T_2$  decreases, with dose. This is caused by radiation effects on the polymer filler interface, which reduce the extent of

interaction. The result is reduction in the effective crosslink density and a softening of the system.

The data for the plot in Figure 2 was obtained using a PDMS polymer modified with a carborane unit. A schematic of the system is given in Figure 3. For this material there is no radiation effect on an interface and the plot is linear over the entire dose range. The development of an ageing model that provided a predictive capability and high confidence is far easier in a system that displays a linear trend than on with a complex non linear relationship.

### Polyhedral Oligomeric Silsesquioxane (POSS) Modified Materials

A generic schematic of POSS is given in Figure 4, while Figure 5 displays compressive strain plots for a variety of PDMS materials. The POSS systems are functionalised with the different R groups indicated on the plot and are shown along with the virgin PDMS for comparison. The methyl and phenyl modified systems have a reinforcing effect on the resulting material whilst the hydroxyl functionalised system results in a softer material. This is caused by an overall reduction in crosslink density as the OH reacts during the curing process.

The plots in Figure 6 show stress strain curves for two optimised PDMS systems formulated with 6% dihydroxyhexamethyl- and octaphenyl- modified POSS. Although somewhat softer than the silica filled equivalent, also shown, plots indicate a far simpler behaviour with no obvious Mullins effect and little

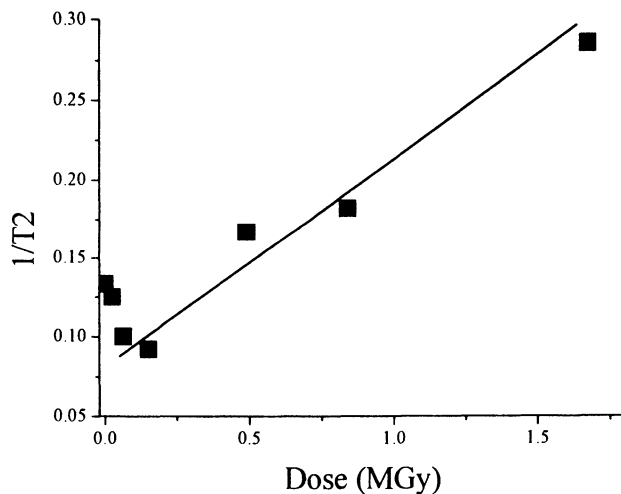


Figure 1. Plot showing the changes in  $T_2$  for a series of silica filled PDMS samples exposed to a variety of gamma radiation doses.

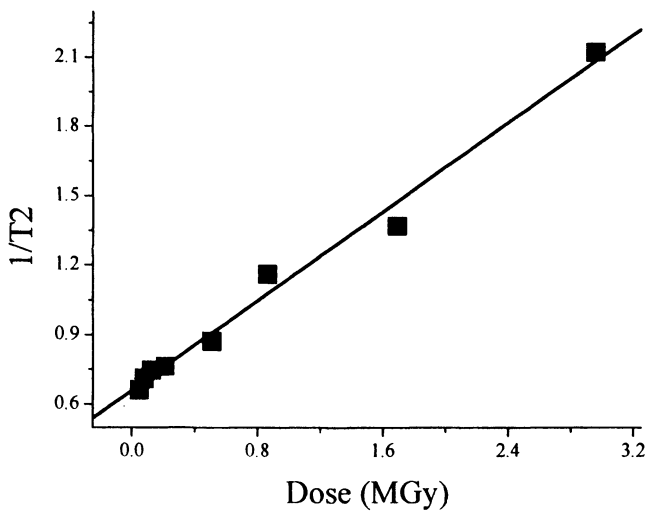


Figure 2. Plot showing the changes in  $T_2$  for a series of carborane modified PDMS samples exposed to a variety of gamma radiation doses.

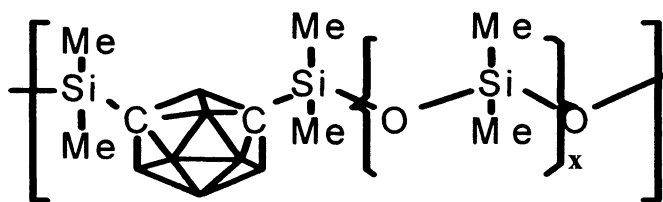


Figure 3. Schematic of the carborane modified PDMS system used for the radiation degradation study.

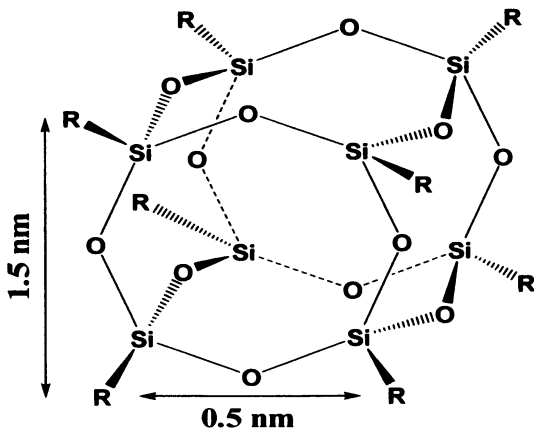


Figure 4. Schematic representation of POSS with an indication of the size of the molecule.

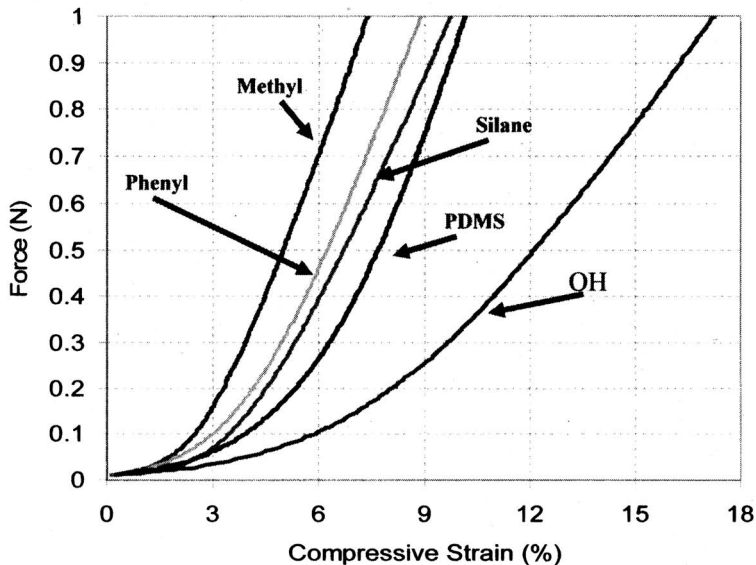


Figure 5. Compressive strain plots for a variety of PDMS materials functionalized as indicated.

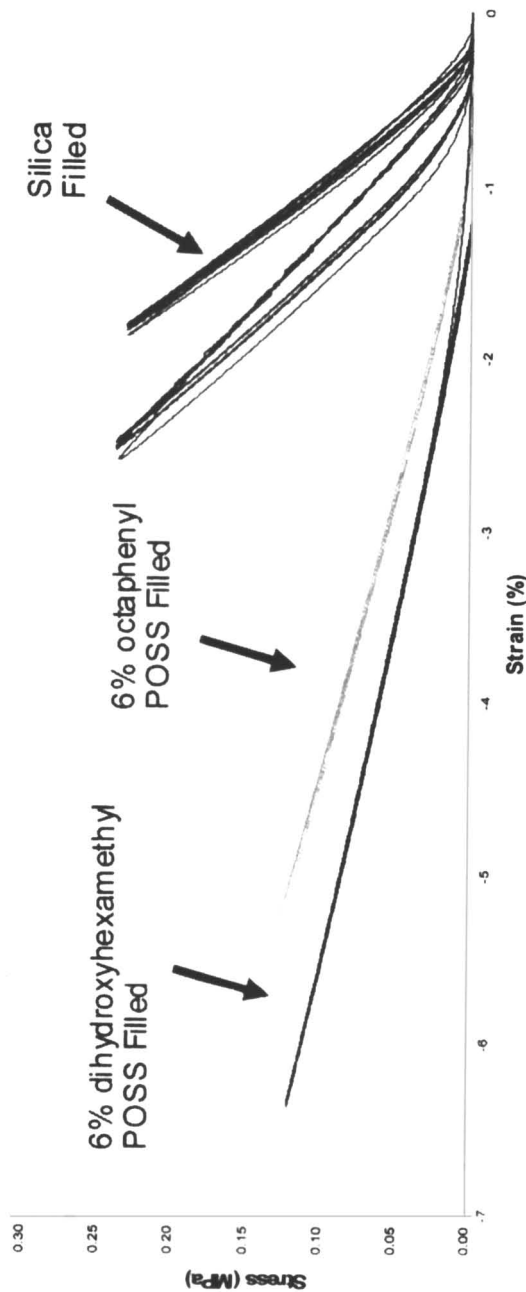


Figure 6. Stress strain hysteresis of conventional silica and POSS filled PDMS composites.

loss modulus. The softening effect of the nanoparticles is possibly related to the onset of plastisation effects at these loadings.

### **Silica and Carbon Nano Fibre Modified Systems**

The SEM picture in Figure 7 shows a cut surface from a PDMS modified with silica nano fibers. The picture shows two fibres protruding from the surface and two holes resulting from fibres being pulled free from the material shown. Clearly this is indicative of a weak interface between the PDMS matrix and silica nano fibers. It should be noted that the production process for the silica nano fibre results in a significant amount of small particulate material. However, the stress strain response obtained from the PDMS systems formulated with the nano fibre shows some interesting trends.

Figure 8 shows a series of stress strain cycles for a PDMS formulated with fumed silica, the ubiquitously large Mullins effect is evident. The plots for the compression and release phases are also very different indicating a significant loss modulus element to the compressive response, also a common feature of these materials. Figure 9 shows the equivalent plots for a PDMS modified with silica nano fibers. The stress strain response is almost identical and again the system displays a complex modulus. There is however, a significant difference as the Mullins effect, that is a common feature of fumed silica modified materials is greatly reduced. In this particular sample the effect has been completely removed.

The SEM pictures, shown in Figure 10, were obtained from a PDMS formulated with carbon nano fibre (CNF). The top micrograph shows the surface of a typical sample, indicating that fibres are evenly distributed through the material. The bottom micrograph shows the cut surface of a sample and the pull out of the reinforcing fibers. These materials offer a significant advantage over the silica systems as the fibres can be produced without significant amounts of non fibre particulate material. An SEM of the CNF is given in Figure 11, which shows the fibrous nature of the material and the lack of particulate contamination. Stress strain curves for silica nano fibre, CNF and materials formulated with more refined single and multi walled nano tubes were obtained and are discussed below.

Stress strain curves for silica nano fibre, CNF and systems formulated with more refined single and multi walled nano tubes are shown in Figure 12. The further simplification of the stress strain response over the PDMS formulated with fumed silica is apparent. There is no Mullins effect, in any of the tubular carbon modified systems, they all have a non complex modulus and a highly linear stress strain response.



*Figure 7. SEM of the cut surface from a PDMS modified with silica nano fibers. There are two fibers protruding from the surface and two holes resulting from fibers being pulled free.*

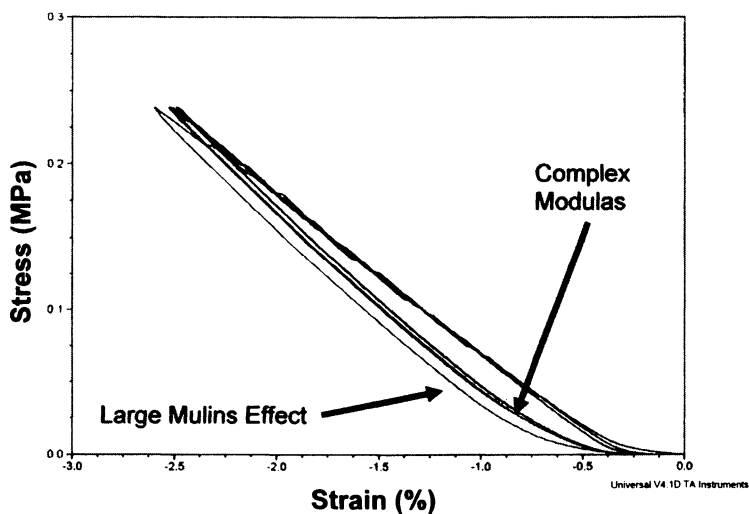


*Figure 8. Stress strain curves for a PDMS formulated with fumed silica. The plots show a large Mullins effect and complex modulus.*

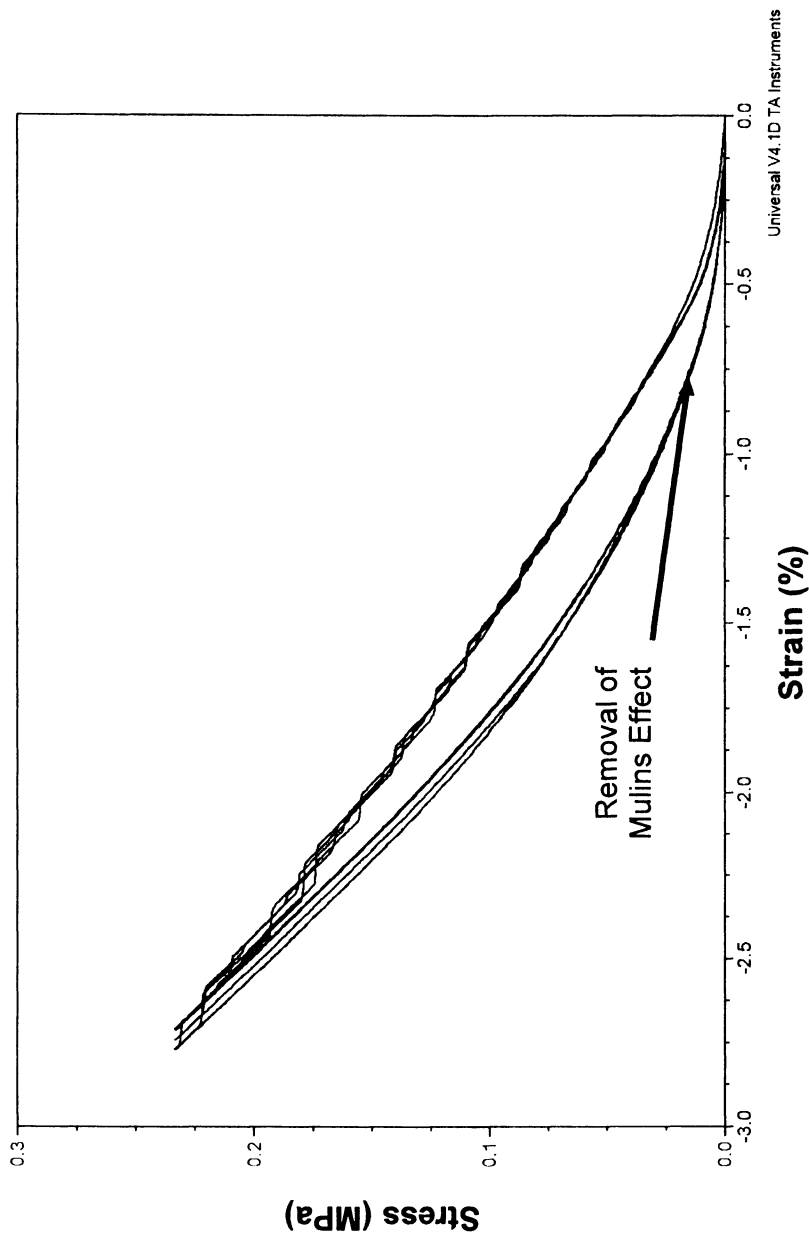
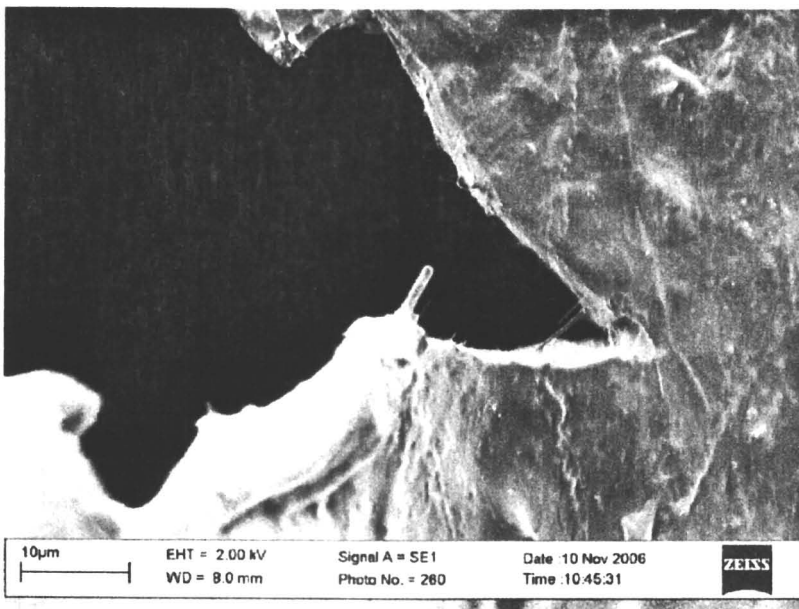
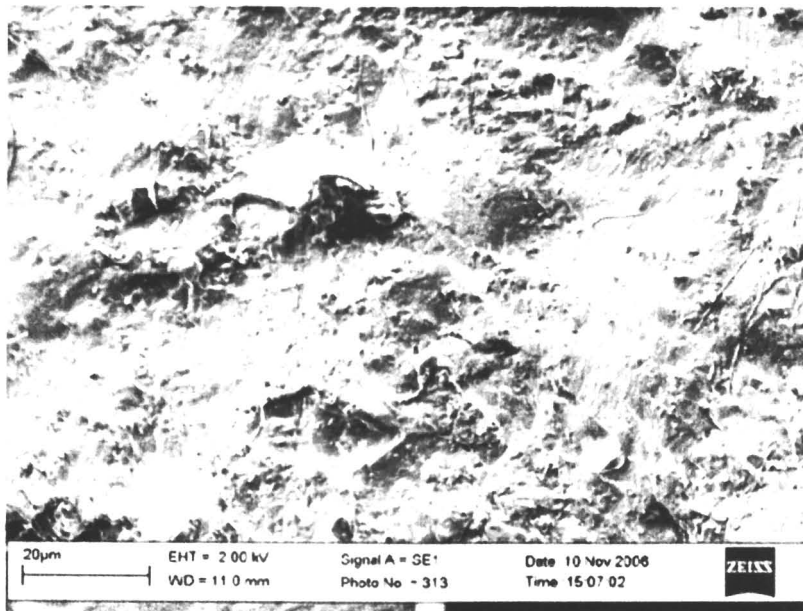
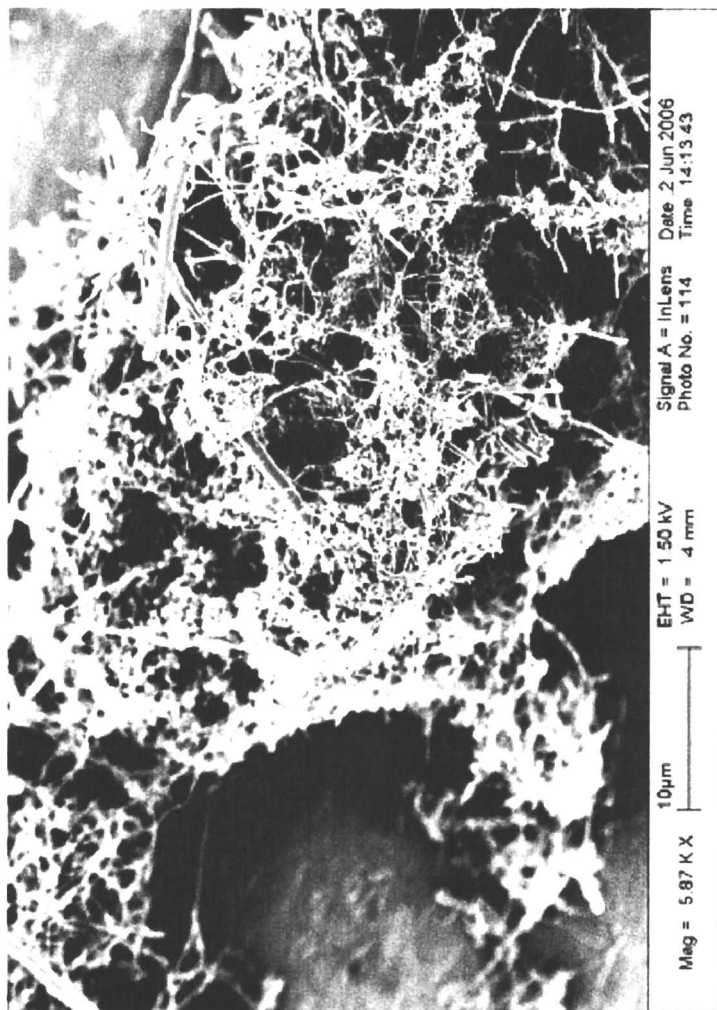


Figure 9. Stress strain curves for a PDMS formulated with silica nano fibers. The plots show no significant Mullins effect.





*Figure 10. SEM pictures obtained from a PDMS formulated with carbon nano fiber (CNF).*



*Figure 11. SEM showing the discrete fibrous nature of the carbon nano fibers.*

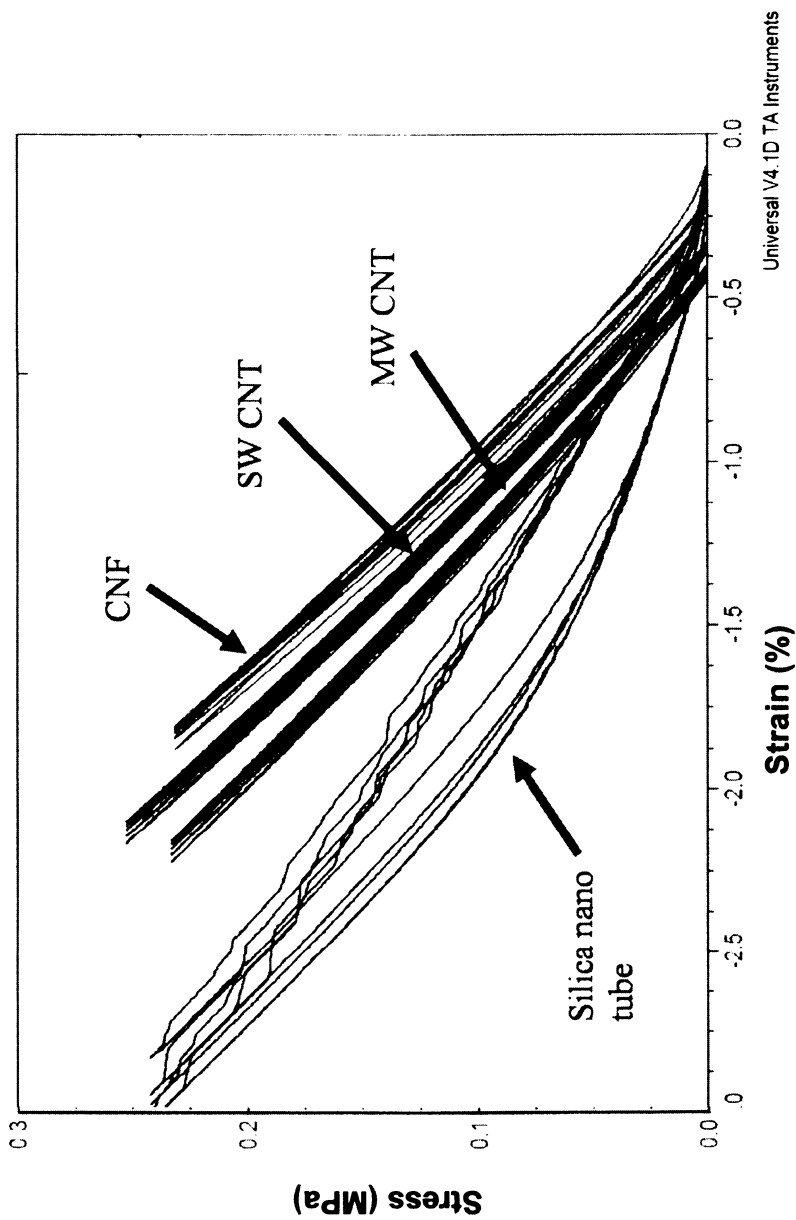


Figure 12. Stress strain curves for PDMS modified with 5% silica nano fibre, CNF and with more refined single and multi walled nano fiber.

## Development and Characterisation of Foams

Foamed PDMS elastomers generally play an important role in a number of specific stress absorbing applications. Reports on Polystyrene and Polyurethane foams have tended to dominate the literature in recent years. Such systems generally exhibit high stiffness to weight ratios and some unique mechanical properties that are dependent upon the microstructure of the foam and the properties of the polymer making up the cell walls (10). In general, the desirable material property requirements of foams may be summarised as shown below:

- Uniform pore size/distribution.
- Controlled load-deflection properties.
- Good batch to batch and sample reproducibility.
- Low compression set.

Understanding the link between microstructure in PDMS foams and the mechanical performance is crucially important for the development of ageing trends that allow long term qualification. The plots in Figure 13 show force decay curves for a series of siloxane foam samples with varying closed cell contents. The trend demonstrates the time dependent nature of the measurement of physical properties. This creates an additional source of variation and if possible then it should be eradicated by the production of 100% open cell structures.

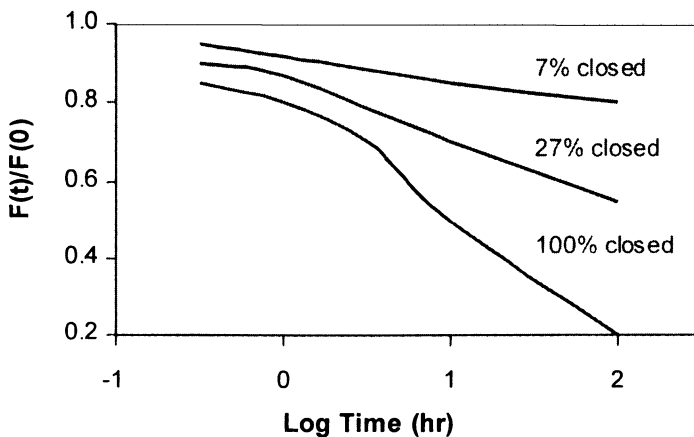


Figure 13. Force decay curves for a series of siloxane foam samples with varying closed cell contents demonstrating the time dependent nature of resulting physical properties measured.

The structure of a foam, which deforms in a specific manner also influences physical properties. Upon initial compression there is a deformation of the structure that requires an increase in the amount of force applied. Once the foam has been deformed significantly the sides of the cell walls buckle leading to cell collapse and the production of elliptically deformed structures. A picture of such cells deformed under extreme compression is shown in Figure 14. During this phase of the compression the rate of increase in the force applied is significantly decreased.



*Figure 14. Picture of elliptically deformed foam cell structures.*

Once the foam structure has been largely compressed the physical properties are dominated by the polymer itself and the rate of increase in the force applied goes up once again. The exaggerated S shaped stress strain curves observed siloxane foams are shown in Figure 15. The linear plots are typical of those observed for the polymers that have not been made into a foam.

An additional source of variation is added as the critical properties of a foam structure are highly dependent upon the extent of compression. For

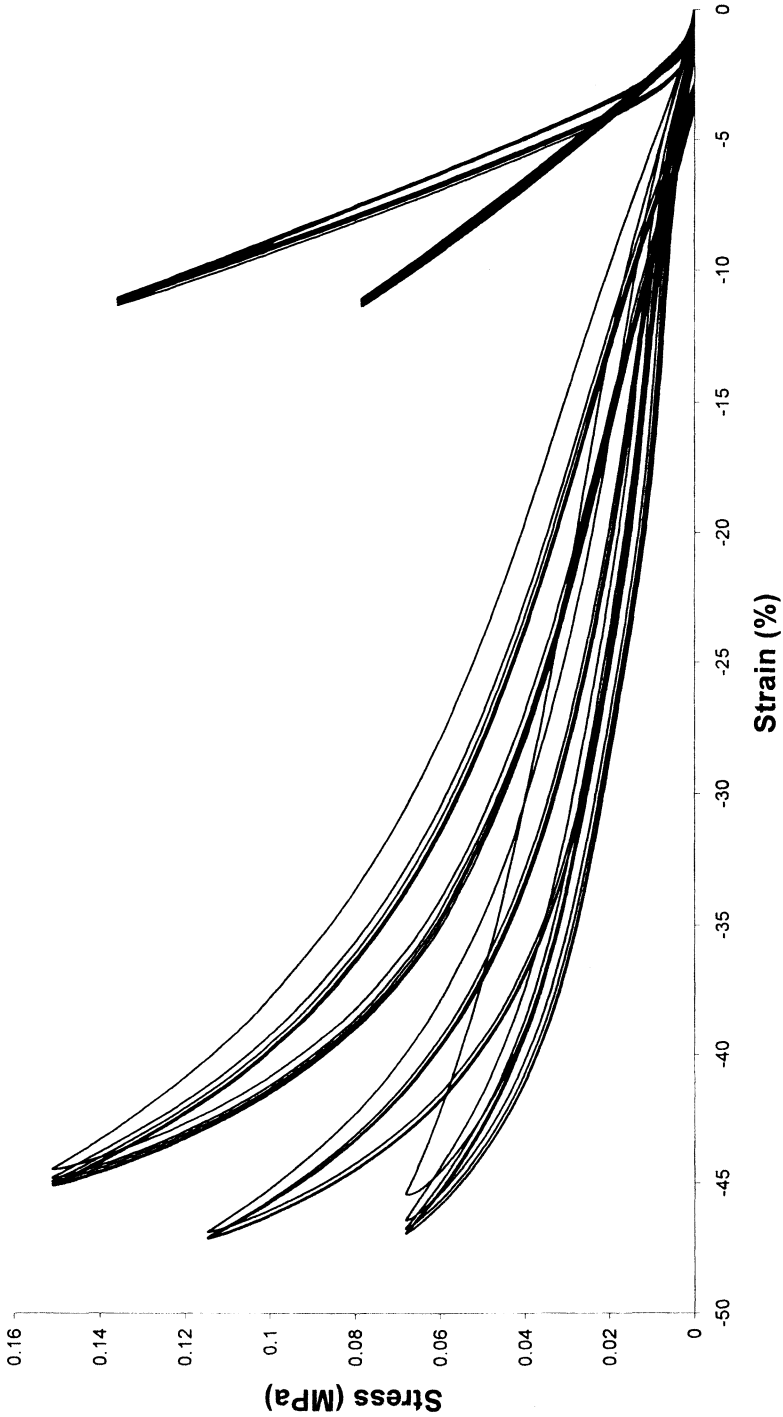


Figure 15. Stress strain curves for foamed and unfoamed PDMS systems.

systems that have undergone compression set, it is crucial to have original measurements as subjecting a foam to a % compression, could cause the property measurement to shift into a different region of the S curve.

Some of the problems associated with foams can be alleviated by the production of idealized structures. One such method is to incorporate a sacrificial particle that can be removed after curing leaving a void. The pictures in Figure 16 show a foam structure produced in such a way before and after removal of the sacrificial pore former.

To further enhance the understanding of microstructure in PDMS foams and the influences on mechanical performance 3D X-Ray Computer Tomography (3DCT) (11) can be applied. This technique allows an accurate 3 dimensional image of a foam to be generated, a typical structure with open cells and uniform size distribution is shown in Figure 17.

It is then possible to generate a Finite Element Mesh of the foam microstructure to enhance understanding of the physical properties and how they relate to the structure. A sample of a foam structure with an FE mesh is shown in Figure 18.

It is possible to compress a foam sample whilst obtaining Images using 3D X-Ray CT and Figure 19 shows a series of 2 dimensional slices through a foam obtained during deformation. The information obtained is a powerful tool to enable understanding of foams and their resulting physical properties.

## Conclusion

The nano modified PDMS systems discussed have properties that enable a more confident prediction of ageing trends. The properties of the carborane modified system change in a linear fashion with radiation dose as opposed to the nonlinear trend observed for conventional particulate filled PDMS. The silica and carbon nano tubular systems display simplified mechanical properties. The reduction in Mullins effect or move to a more linear, less complex stress strain behavior, allows increased accuracy in property measurements.

The production of foams was extensively discussed along with many of the unique difficulties that such systems present. Many advanced characterization techniques and methods for foam production were detailed. Used in conjunction with nano filled PDMS, the development of confident ageing predictions should be possible.

## References

1. Joshi, M.; Butola, B. S. *J. Macromol. Sci.* **2004**, *44*, (4) 389.
2. Bhowmick, A. K.; Stephens, H. L. *Handbook of Elastomers*; 2<sup>nd</sup> ed.; Marcel Dekker Inc.: 2001, ISBN 0-8247-0383-9.

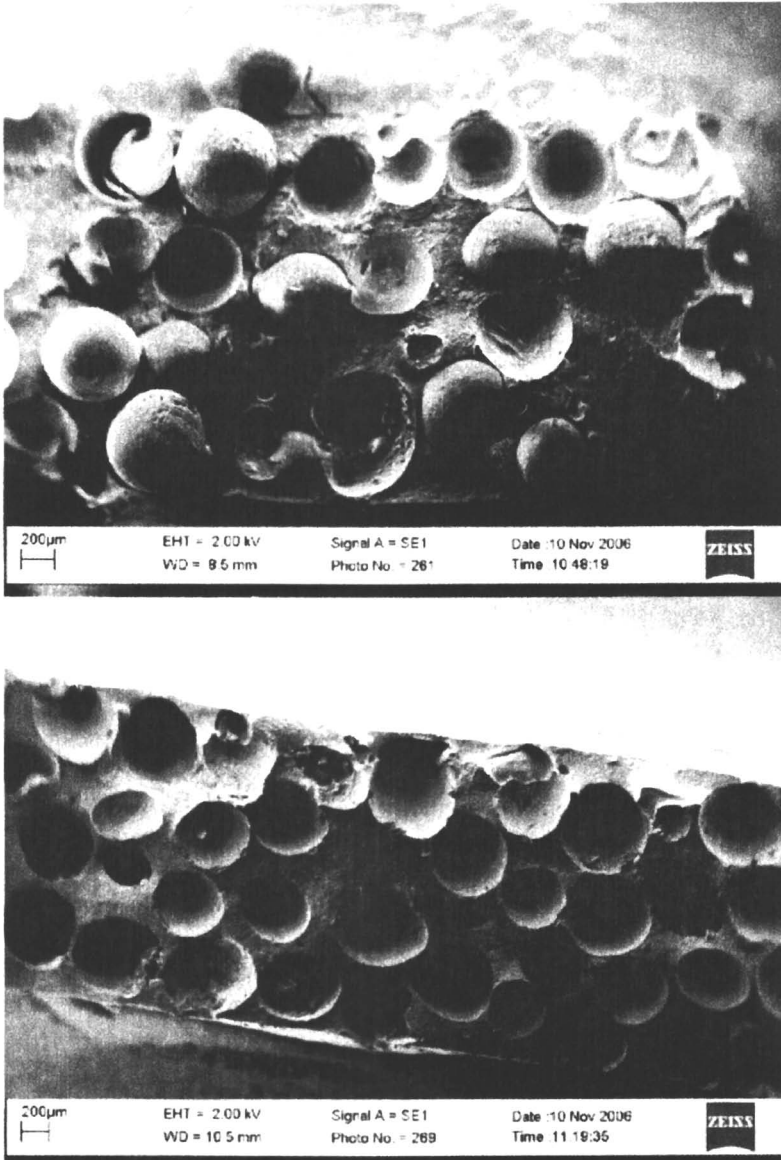


*Figure 16. Pictures of foam structures before and after removal of a sacrificial pore former.*



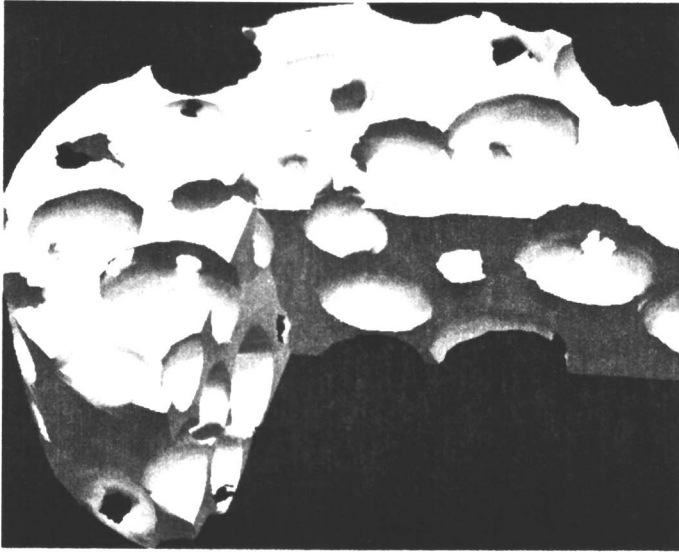


Figure 17. 3 dimensional image of a foam to be generated X-ray tomography.

LS-Dyna export from ScanFE

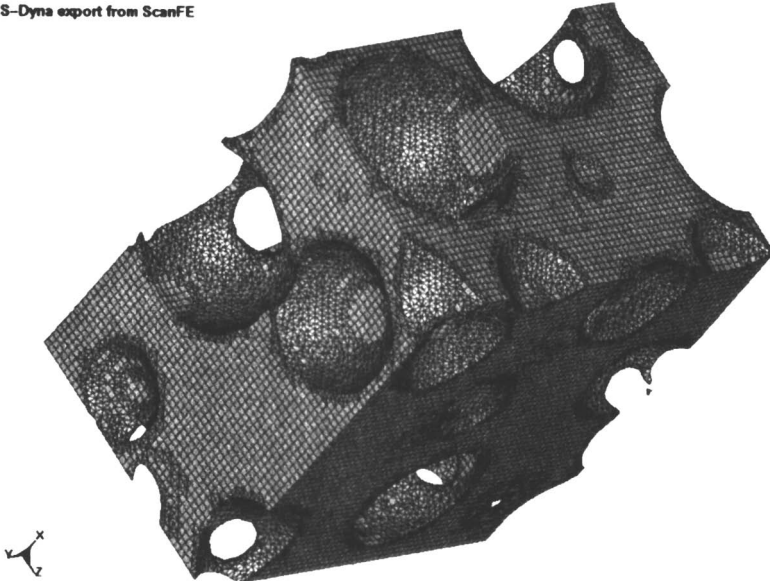
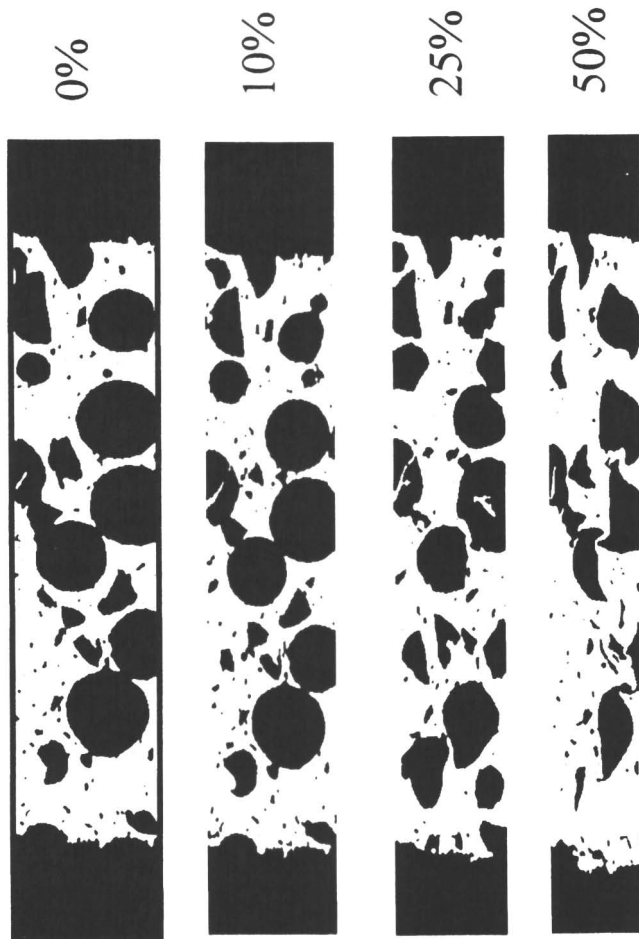


Figure 18. FE Mesh overlaid onto 3D X-Ray Computer Tomography generated image of a foam microstructure.



*Figure 19. 2 dimensional slices of a foam structure obtained using 3D X-Ray CT.  
The values on the right correspond to the % compression.*

3. Noll, W. *Chemistry and Tech. of Silicones*; 2<sup>nd</sup> ed.; Academic Press: 1968.
4. Patel, M.; et al. *Polym. Degrad. Stab.* **2006**, *91*, 406.
5. Chapiro, A. *Radiation Chemistry of Polymeric Systems*; John Wiley and Sons: 1962.
6. Hanson, D. E.; et al. *Polymer* **2005**, *46*, 10989.
7. Rodriguez, J. G -I.; et al. *J. Therm. Anal. Calor.* **2007**, *87*, 45.
8. Eisenberg, A.; Tsagaropolous, G. *Macromolecules* **1995**, *28*, 396.
9. Eisenberg, A.; Tsagaropolous, G. *Macromolecules* **1995**, *28*, 6067.
10. Lin, H. R. *Polym. Test.* **1997**, *16*, 429.
11. Kinney, J. H.; et al. *J. Appl. Polym. Sci.* **2001**, *80*, (10) 1746.

## Chapter 23

# Effect of Pigment Dispersion on Optical Properties and Durability of a TiO<sub>2</sub> Pigmented Epoxy Coating

Li-Piin Sung<sup>1</sup>, Xiaohong Gu<sup>1</sup>, Cyril Clerici<sup>1</sup>, Haiqing Hu<sup>1</sup>,  
Elena Loizou<sup>2</sup>, and Derek L. Ho<sup>3</sup>

<sup>1</sup>Polymeric Materials Group, Building and Fire Research Laboratory,  
<sup>2</sup>NIST Center for Neutron Research, and <sup>3</sup>Polymers Division, Materials  
and Engineering Laboratory, National Institute of Standards  
and Technology, 100 Bureau Boulevard, Gaithersburg, MD 20899

The effect of pigment dispersion on (i) surface morphology and appearance, and (ii) the weathering durability of a TiO<sub>2</sub> pigmented epoxy coating was investigated. The microstructure and dispersion of pigmented epoxy coatings were characterized using ultra small angle neutron scattering (USANS). Atomic force microscopy (AFM) and laser scanning confocal microscopy (LSCM) were used to characterize surface morphology of unexposed and weathered coatings. Surface optical scattering and commercial gloss measurements were carried out to study the corresponding optical properties of the coatings. Preliminary results of optical and surface morphological changes are presented and related to material properties as a function of outdoor weathering for two coatings of different dispersion states.

## Introduction

The overwhelming majority of commercial polymeric construction products have pigments dispersed throughout the polymeric matrix. Poor dispersion of these pigments is qualitatively known to adversely affect the appearance, service life, and mechanical properties of these products. The ability to accurately characterize pigment dispersion and relate the state of dispersion to performance properties will lead to polymeric products having improved appearance and greatly improved service life. The objectives of this study were to investigate the effect of pigment dispersion on (i) surface morphology and appearance, and (ii) the weathering durability of a TiO<sub>2</sub> pigmented epoxy coating. Various states of pigment dispersion were achieved through different mixing conditions. The microstructure and dispersion of pigmented epoxy coatings were characterized using ultra small angle neutron scattering (USANS). Atomic force microscopy (AFM) and laser scanning confocal microscopy (LSCM) were used to characterize surface morphology of unexposed and weathered coatings. Surface optical scattering and commercial gloss measurements were carried out to study the corresponding optical properties of the coatings. Preliminary results of optical and surface morphological changes are presented and related to material properties as a function of outdoor weathering time for two coatings of different dispersion states.

## Experimental\*

### Materials

An amine-cured TiO<sub>2</sub> pigmented epoxy was selected for this study. The epoxy resin was a pure diglycidyl ether of bisphenol A and the curing agent was 1,3-bis(aminomethyl)-cyclohexane. Commercial pigment grade TiO<sub>2</sub> (Dia. ≈ 230 nm) was used at 15 % pigment volume concentration (PVC). The solvent was n-butyl acetate and 1-methoxy-2-propanol acetate at a 4:1 ratio. To achieve a better dispersion, 6 % (by mass of pigment) of dispersant was added to the mixture.

---

\* Certain trade names and company products are mentioned in the text or identified in an illustration in order to adequately specify the experimental procedure and equipment used. In no case does such an identification imply recommendation or endorsement by the National Institute of Standards and Technology, nor does it imply that the products are necessarily the best available for the purpose.

## Sample Preparation

The samples were prepared by the following procedures: (i) epoxy resin was mixed with/without dispersant in the solvent using a mechanical mixer at 209.4 rad/s mixing speed for 20 min.; (ii) TiO<sub>2</sub> pigment was added during mixing while mixing at 366.5 rad/s for 60 min ; (iii) amine curing agent was then added at the stoichiometric ratio with respect to epoxy resin and mixed at 104.7 rad/s for 10 min.; (iv) the mixture was applied to release paper using a drawdown technique in a CO<sub>2</sub>-free, dry air glove box with a wet film thickness of 150 μm; (v) all samples were then cured at room temperature for 24 h in the same glove box, followed by heating at 130°C for 2 h in an air-circulation oven. The samples were denoted as “Clear” for un-pigmented epoxy; “Disp” and “NonDisp” for the pigmented epoxy coatings with and without dispersant added in the mixing processing, respectively.

## Outdoor UV Exposure

Outdoor exposures were conducted on the roof of a National Institute of Standards and Technology (NIST) research laboratory located in Gaithersburg, Maryland. Specimens were loaded in the multiple-window exposure cells and placed in an outdoor environmental chamber at 5 degrees from the horizontal plane facing south. The bottom of the chamber was made of black-anodized aluminum, the top of the chamber was covered with “borofloat” glass; all four sides of the chamber were perforated and these perforations were covered with a non-moisture absorbing fabric material that acted as a filter to prevent dust particles from entering the chamber. The exposure cell was equipped with a thermocouple and a relative humidity (RH) sensor. The temperature and the RH in the chamber were recorded every minute throughout the day.

## Microstructure and Pigment Dispersion Characterization

Ultra small angle neutron scattering (USANS) was carried out to characterize the microstructure and pigment dispersion of the coating. The USANS measurements were performed at the NIST Center for Neutron Research (NCNR) using a perfect crystal diffractometer (PCD) instrument (1). Details of instrumentation and scattering theory are given in Reference (2). The USANS data presented in this paper were a one-dimensional absolute scattered intensity curve as a function of the scattering wave vector  $q$  ( $q = 4\pi \sin(\theta/2)/\lambda$ , where  $\theta$  is the scattering angle and  $\lambda$  is the wavelength). The estimated extended uncertainties ( $k=2$ ) in the data are presented in this paper.

## Material Properties Measurements

Glass transition temperature,  $T_g$ , and storage modulus,  $E'$ , were measured to explore how the pigment dispersion affects the material (i.e. cross-link density) and mechanical properties. Both  $T_g$  and  $E'$  were determined from dynamic mechanical analysis method using a dynamic mechanical thermal analyzer (DMTA, TA Instruments RSA III) equipped with transient testing capability. A minimum of 3 to 4 specimens were analyzed from each sample. The estimated uncertainties of data are one-standard deviation.

## Surface Morphology Characterization

Atomic force microscopy (AFM, Veeco Metrology Dimension 3100) and laser scanning confocal microscopy (LSCM, Zeiss LSM510) were used to characterize surface morphology of the unexposed and weathered coatings. Details of instrumented specification and measurements are given in References (3-5). With the combination of these two microscopic techniques, a range of surface areas from ( $1 \mu\text{m} \times 1 \mu\text{m}$ ) to ( $2 \text{mm} \times 2 \text{mm}$ ) can be measured. The AFM images presented here are height images, while the LSCM images are 2D intensity projections. The 2D intensity projection image is effectively the sum of all the light back scattered by different planar layers of the coating. The pixel intensity level represents the total amount of backscattered light. Approximately 6 to 10 micrographs were obtained for each sample, with representative images reported here.

## Optical Properties Measurements

Optical scattering measurements using a newly constructed optical scattering instrument in the Building and Fire Research Laboratory at NIST (6) were conducted at various incident angles in the specular and off-specular configurations on surfaces of unexposed and weathered coatings. The optical results are presented in a two-dimensional scattering pattern or a one-dimensional circularly-averaged scattered intensity curve as a function of the scattering angle away from the specular angle. The estimated uncertainties in the optical scattering intensity data are around 4% from the mean value for 4 different locations. The specular gloss measurements were also carried out using a handheld commercial glossmeter (Minolta, Multi-Gloss model 268). Measurements conform to the ASTM D 523 standard measurement protocol. The data were expressed as gloss retention, which is defined as the percentage change in the gloss of a specimen relative to its initial gloss value. The estimated uncertainties in the gloss retention are at one standard deviation from the mean value for all 24 measurements from three replicas.

## Results and Discussion

Structure and pigment dispersion characterization of pigmented TiO<sub>2</sub> epoxy coatings were conducted using USANS and the results are shown in Figure 1. In the low  $q$  region (i.e. at larger size scale), the scattering intensity of the NonDisp coating is much higher than that of the Disp coating. This implies that larger clusters exist in the NonDisp coating than in the Disp coating. Additionally, there is a notable shape difference in the scattering curves between these two coatings. The scattering curve of the Disp coating can be fitted to a form factor of polydisperse spheres with a TiO<sub>2</sub> particle size equivalent to a sphere radius of  $(115.2 \pm 5.0)$  nm with a polydispersity of 19%. However, it is difficult to obtain a meaningful fit to the scattering curve of the NonDisp coating due to multiple sizes and shapes in the coating microstructure. As expected that USANS data indicates that the Disp coating (with dispersant added) had a better TiO<sub>2</sub> particle dispersion than the NonDisp coating in term of cluster size and its spatial distribution.

Figure 2 shows the surface morphology and optical properties of the Disp and NonDisp coatings. The bright spots come mostly from the backscattered light of the TiO<sub>2</sub> particle; therefore by analyzing the intensity distribution of the LSCM images, one can map the pigment distribution on/near the coating surface (7). There is a significant difference in terms of surface topographic features (i.e. surface roughness) and optical contrast in the 2D LSCM projection images as shown in Figure 2a. Moreover, the difference in the subsurface microstructure (3  $\mu$ m below the surface, Figure 2b) becomes greater. Many irregular domains are observed in the lower graph (NonDisp) of Figure 2b, while it appears to be uniformly spotted with TiO<sub>2</sub> particle throughout the image of Disp. The corresponding 2D optical scattering (OS) intensity profiles at an incident angle of 20° and 2D detector positioned at 23° are also displayed in Figure 2c. Note that optical scattering is a result of light scattered from each constituent/component (polymer, pigment) of a coating on the surface and subsurface. By studying optical scattering profiles, one may gain information for analyzing microstructure and pigment dispersion near the surfaces.

To obtain a quantitative comparison of optical properties between Disp and NonDisp coatings, 1D scattering curves were plotted as a function of angle from the specular angle. As shown in Figure 2d, the optical scattering (OS) intensity of the NonDisp displays a higher off-specular (diffuse) scattering than that of Disp. It is due to the higher surface roughness as well as the irregular subsurface microstructure as observed in Figure 2b. Clearly, poor pigment dispersion affects surface morphology and subsurface microstructure, and consequently affects the optical properties of a coating.

Effect of pigment dispersion on UV degradation was investigated via outdoor UV exposure experiments. Figures 3a and 3b present the glass transition temperature,  $T_g$ , and storage modulus,  $E'$ , measured from DMA for the



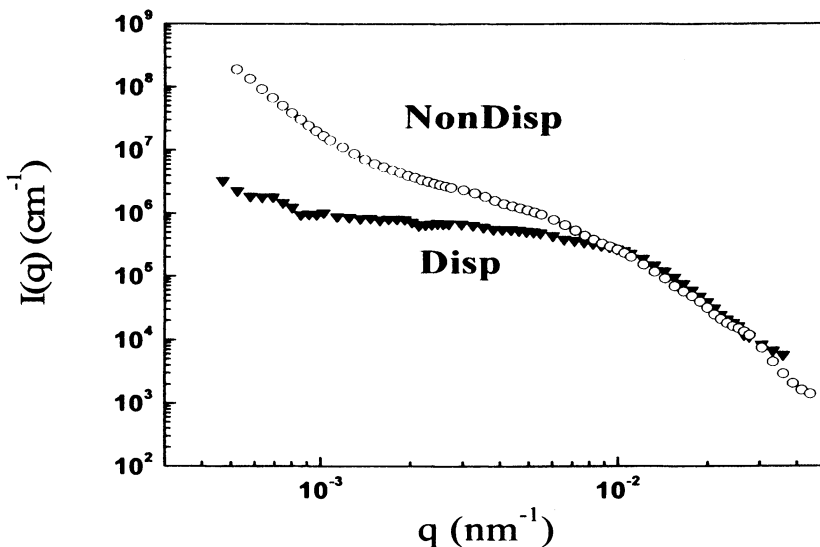


Figure 1. USANS scattering intensity of Disp and NonDisp coatings as function of scattering wave vector  $q$  in a log-log plot. The error bars are smaller than the size of symbols.

NonDisp and Disp coatings. The  $T_g$  values (Figure 3a) decrease with increasing exposure time for both coatings, but the decrease rate is higher for the NonDisp coating than for the Disp coating for the exposure time  $< 80$  d. There are no significant changes in the storage modulus data (Figure 3b) for exposure time  $< 80$  d, but a slow decrease is observed for both coatings after 80 d of exposure time. However, we have observed dramatic changes (Figure 3c) in the  $20^\circ$  gloss retention versus exposure time for the NonDisp coating with respect to the changes observed in the Disp coating. The big difference in the trend of gloss retention might be due to the different morphological changes among the coatings when exposed to outdoor UV radiation.

Figure 4 shows surface morphology of three coatings at different size scales along with their respective 2D optical scattering profile after 151 d exposure time. Apparently, the degradation evolution differed for each coating. For example, for the Disp coating, pigments emerge on the surface (as observed in the AFM study, images are not presented here) and exhibit chalking behavior at 151 d of exposure time. On the other hand, there are no pigments appearing but rough topographic features and cracks on the NonDisp coating. These changes in surface morphology directly impact appearance (i.e. optical properties) of the coatings. As a result, OS profiles (Figure 4d) reveal a strong increase in diffuse scattering and a specific scattering pattern from crack formation as shown in

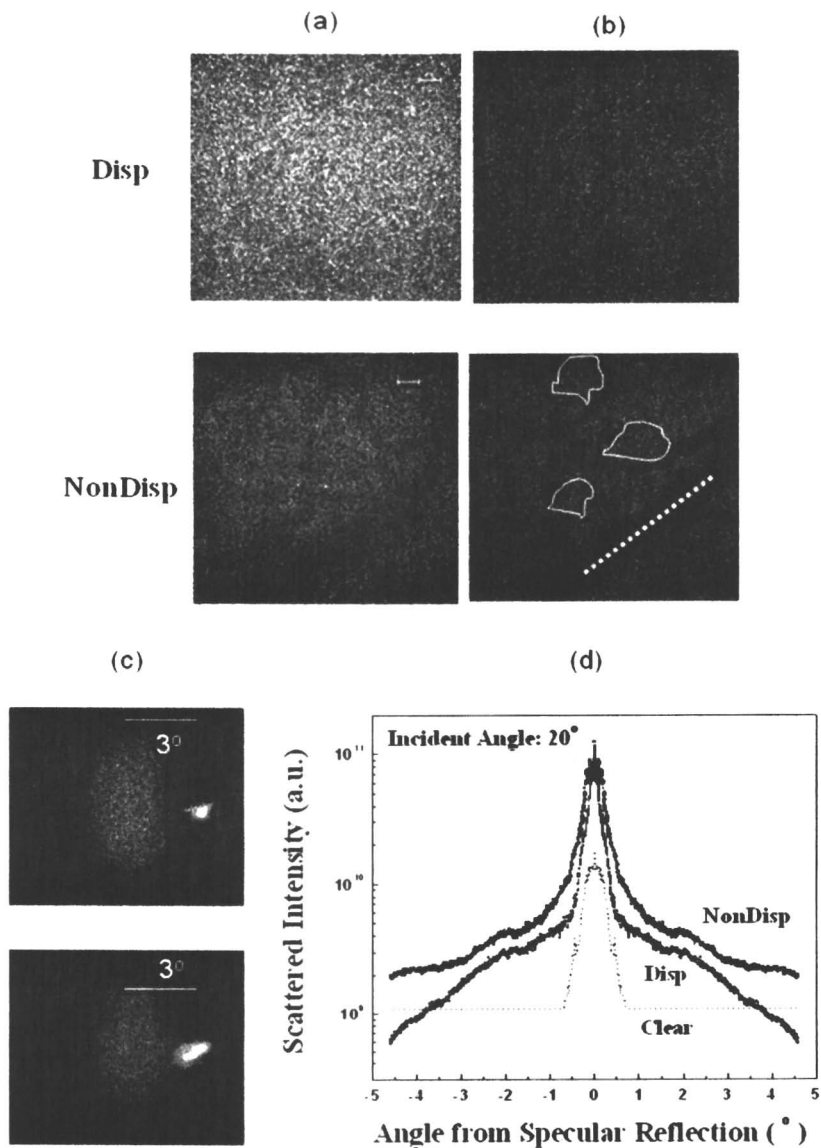


Figure 2. (a) 2D projection LSCM images, (b) images from 3  $\mu\text{m}$  below the polymer-air surface, (c) the corresponding 2D optical scattering (OS) profiles at 20° incident angle, and (d) 1D scattering curving as a function of angle from specular reflection for Disp and NonDisp coatings. The OS scattering curves of Clear coatings is also plotted in (d) for reference. All LSCM image sizes are 64  $\mu\text{m}$  x 64  $\mu\text{m}$ .

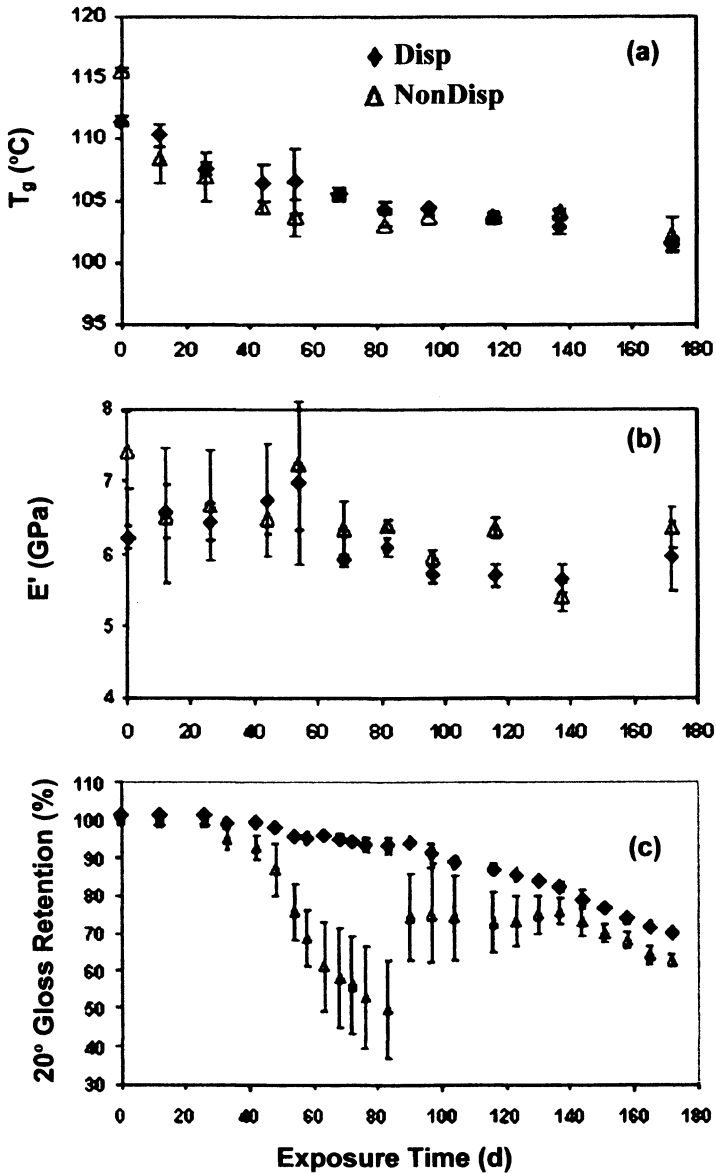
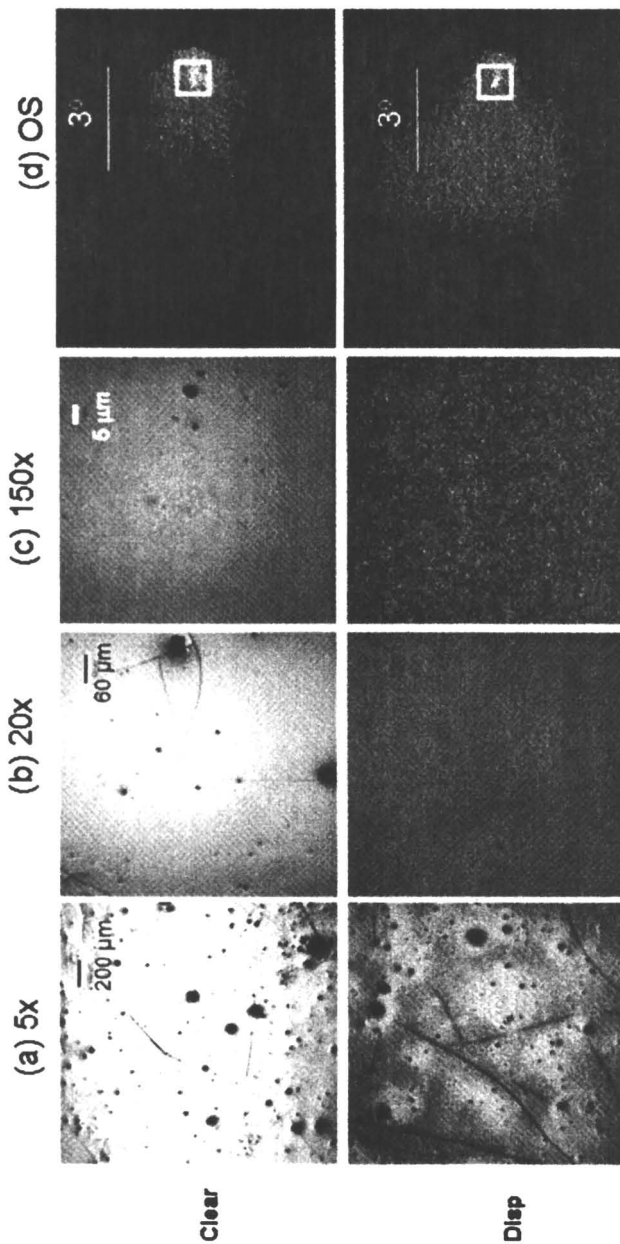
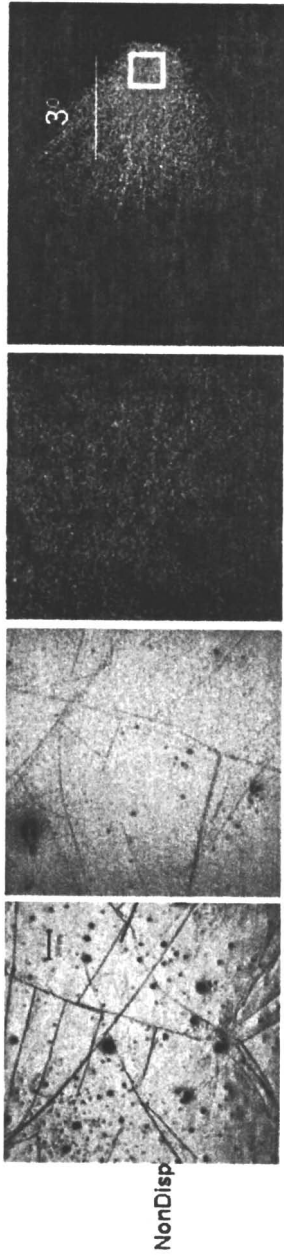


Figure 3. (a) Glass transition temperature,  $T_g$ , (b) Storage modulus,  $E'$ , and (c) 20° gloss retention for Disp and NonDisp coatings as function of outdoor exposure time. The error bars represent one-standard deviation.





*Figure 4. LSCM images at magnification of (a) 5x, (b) 20x, (c) 150x, and (d) OS profiles for Clear, Disp, and NonDisp coatings after 151 d outdoor exposure. The size scale bars in (a) to (d) represent 100  $\mu\text{m}$ , 50  $\mu\text{m}$ , 5  $\mu\text{m}$ , and 3 $^\circ$ , respectively. The  $\square$  areas in (d) are compatible to the measuring angular range of 20 $^\circ$  specular gloss measurements.*

Figure 4d. Note that the detecting angular range of a commercial specular glossmeter is equivalent to the yellow box areas illustrated in Figure 4d. Therefore, the commercial gloss measurements are not always adequate to capture the overall changes in optical properties of a pigmented coating as exposed to UV radiation. Extensive analyses of microscopy, optical scattering, and other results are ongoing to better correlate the pigment dispersion to performance properties.

### Acknowledgement

We acknowledge the support of the National Institute of Standards and Technology, U.S. Department of Commerce, in providing the neutron research facilities used in this work. The authors also thank Dr. Paul Butler of NIST for his help in conducting USANS experiments and insightful discussion in the data analyses.

### References

1. Barker, J. G.; Glinka, C. J.; Moyer, J. J.; Kim, M. H.; Drews, A. R.; Agamalian, M. *J. Appl. Cryst.* **2005**, *38*, 1004 -1011.
2. Higgins, J. S.; Benoit, H. C. *Polymers and Neutron Scattering*; Clarendon Press: Oxford, UK, 1994.
3. Corle, T. R.; Kino, G. S. *Confocal Scanning Optical Microscopy and Related Imaging Systems*; Academic Press: 1996.
4. VanLandingham, M. R.; Nguyen, T.; Byrd, W. E.; Martin, J. W. *J. Coat. Technol.* **2001**, *73*, 43-50.
5. Sung, L.; Jasmin, J.; Gu, X.; Nguyen, T.; Martin, J. W. *J. Coat. Technol. Res.* **2004**, *1*, 267-276.
6. Sung, L.; Drazl, P.; VanLandingham, M. R.; Wu, T. -Y.; Chang, S.-H. *J. Coat. Technol. Res.* **2005**, *2*, 583-589.
7. Faucheu, J.; Sung, L.; Martin, J. W.; Wood, K. A. *J. Coat. Technol. Res.* **2006**, *3*, 29-39.

## Chapter 24

# Photolysis and Photooxidation in Engineering Plastics

Pieter Gijsman<sup>1,2</sup> and Marjolein Diepens<sup>2</sup>

<sup>1</sup>DSM Research, P.O. Box 18, 6160 MD Geleen, The Netherlands

<sup>2</sup>Laboratory of Polymer Technology, Department of Chemical Engineering,  
Eindhoven University of Technology, P.O. Box 513,  
5600 MB Eindhoven, The Netherlands

The most important UV-degradation mechanisms for polymers are photolysis and photo-oxidation. For polyolefins it is well known that photo-oxidation is the dominating mechanism. These polymers do not have an inherent absorption at wavelengths present in terrestrial sunlight (>290 nm) so photolysis cannot play an important role. In contrast to polyolefins, the majority of engineering plastics do have absorptions at these wavelengths. As a result, for these polymers, besides photo-oxidation, photolysis can play an important role. For polyamide 6, poly(butylene terephthalate), two different copolyetheresters and bisphenol-A polycarbonate, the importance of photolysis as well as that of photo-oxidation in polymer light-induced degradation is discussed.

The most important mechanisms causing weathering of polymers are photolysis and photo-oxidation (1, 2). If the absorption of light leads directly to chemical reactions causing degradation, this is called photolysis. Photo-oxidation is a result of the absorption of light which leads to the formation of radicals that induce oxidation of the material. For polyolefins it is well known that photo-oxidation is the dominating mechanism (2); these polymers do not have an inherent absorption at wavelengths present in terrestrial sunlight (>290-300 nm), so that photolysis cannot play an important role. Nevertheless, irradiation of these polymers with terrestrial wavelengths results in accelerated degradation. This can be ascribed to impurities that are formed during storage and processing or to charge transfer complexes between the polymer and oxygen (2, 3). Due to photolytic reactions of these absorbing species, radicals are formed which initiate the photo-oxidation.

In contrast to polyolefins, the majority of engineering plastics do have absorptions at wavelengths present in terrestrial sunlight, so that for these polymers photolysis can also play an important role. For these polymers in principle there are three mechanisms that can describe their light induced degradation:

- Photolysis; absorption as a result of the inherent polymeric structure results in chemistry causing changes in the molecular weight distribution.
- Photo-oxidation initiated by photolysis reactions of the polymer itself as mentioned above.
- Photo-oxidation initiated by impurities not part of the inherent polymer structure.

For polyesters (e.g. poly(butylene terephthalate), PBT), polyamides (e.g. polyamide 6 (PA6) and polycarbonate (PC) it is known that they show photolysis as well as photo-oxidation (1, 4, 5). Figure 1 shows the UV absorption spectra of these polymers.

The lowest wavelength present on earth lies between 290 and 300 nm (somewhat dependent on the location). PBT shows a large absorption above 290 nm (see Figure 1), meaning that for this polymer photolysis can play an important role. PA6 only shows a limited absorption. PC shows a small absorption between 290 and 300 nm, which implies that for this polymer the value of the lowest wavelength present can play a significant role. For this polymer a difference in degradation mechanism can be anticipated when the smallest wavelength present changes from 290 to 300 nm.

In the case of polyamides and polyesters the most important photolytic reactions are the Norrish I and II reactions (see Scheme 1). The Norrish I reaction leads to chain cleavage and radicals that might initiate oxidation, the Norrish II reaction only leads to chain cleavage. The main question for these polymers is: What is the relative importance of photolysis and photo-oxidation?



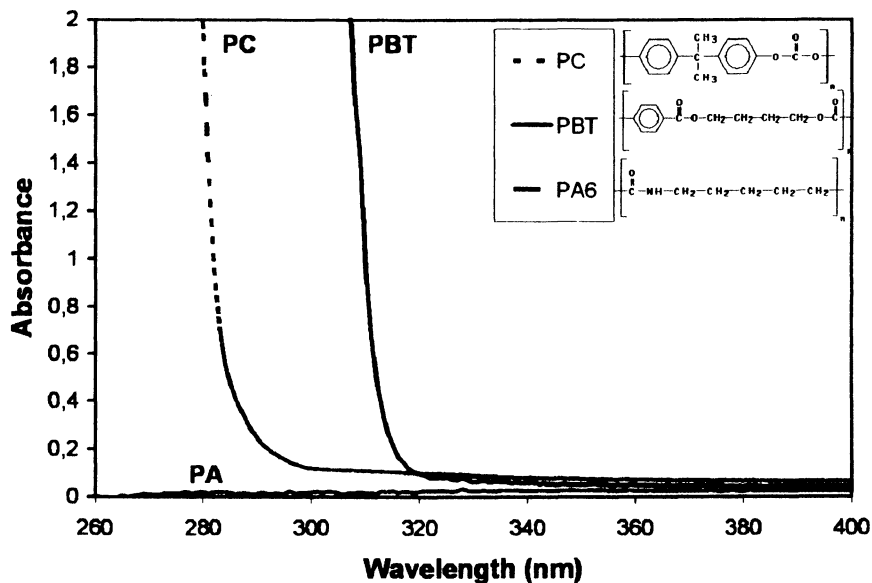
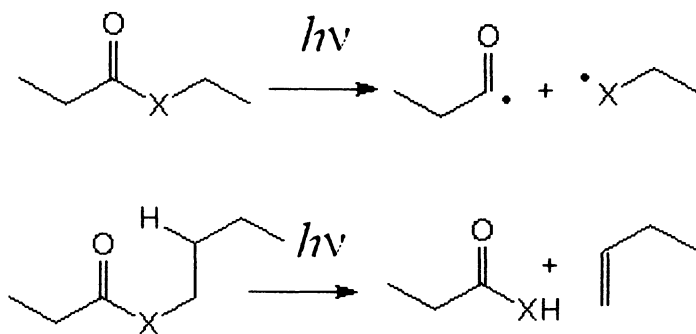


Figure 1. UV absorption spectrum of Polycarbonate, Polybutylene terephthalate and Polyamide 6.



Scheme 1. Norrish I (top) and Norrish II (bottom) reactions for polyamides ( $X=NH$ ) and polyesters ( $X=O$ ).

For polycarbonate the main photolytic reaction is the photo-Fries reaction (see *Scheme 2*). For this polymer the main questions are: How important is the photo-Fries reaction and if it plays a role does it form free radicals that initiate the oxidation of the polymer?

As mentioned above all of the discussed polymers can also undergo photo-oxidative reaction. The mechanism describing the photo-oxidation of polymers is shown in *Scheme 3*.

In this paper the relative importance of photolysis and photo-oxidation during weathering of the above mentioned engineering plastics as well as two polyetherester copolymers will be discussed.

## Experimental

### Materials

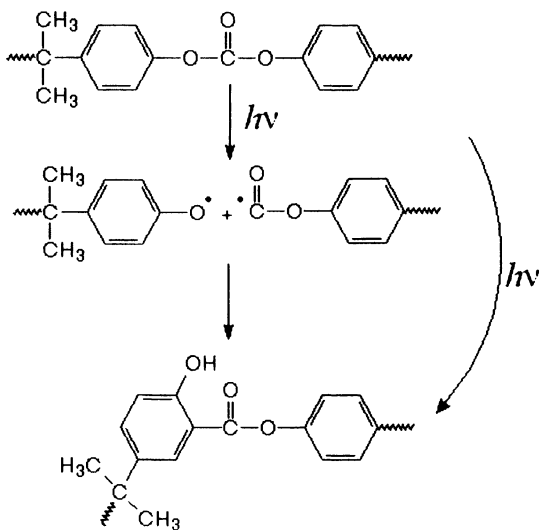
The polyamide 6 (PA6) used was a cast film of 50  $\mu\text{m}$  thickness made from an unstabilized PA6. The polybutylene terephthalate (PBT) used was a cast film of 25  $\mu\text{m}$  thickness made of an unstabilized PBT.

Two PBT based thermoplastic elastomers were studied. One was a PBT-polytetrahydrofuran (pTHF) copolymer (PECO-1) and the other one a PBT-poly(propylene glycol) (PPG) copolymer (PECO-2). In both cases the degradations were done on 30  $\mu\text{m}$  thick films. All of these polymers were supplied by DSM Engineering Plastics.

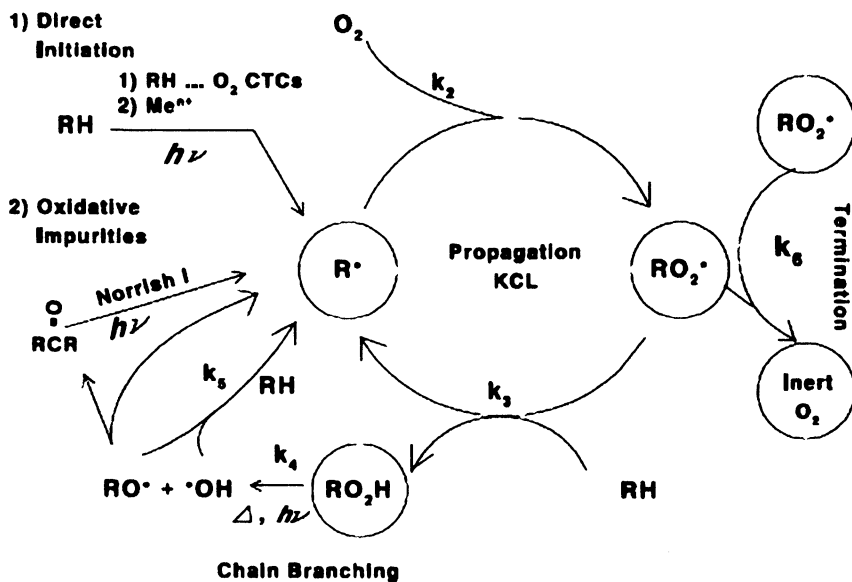
Extruded films of unstabilized bisphenol A polycarbonate (PC) were supplied by GE Plastics. The thickness of these films was approximately 0.2 mm.

### Weathering

Weathering tests were done in different types of Atlas apparatus (Atlas Material Testing Technology b.v.) a standard Suntest CPS (CPS), a Suntest XXL+ (XXL+) and a Weather-O-meter Ci 65 (WOM) all using filtered xenon lamps. The light intensity level in the Suntest was 0.3  $\text{W}/\text{m}^2/\text{nm}$  at 340 nm at a chamber temperature of 30-40°C. In the XXL+ the intensity was 0.4  $\text{W}/\text{m}^2/\text{nm}$  at 340 nm, the chamber temperature 35°C and a relative humidity of 40%. In the WOM the intensity at 340 nm was 0.35  $\text{W}/\text{m}^2/\text{nm}$ , the test chamber temperature 46°C and the relative humidity 55%. Due to the filters used there was a small difference in the wavelength cut off of both Suntesters (see *Figure 2*).



Scheme 2. Photo-Fries reaction of Bisphenol A Polycarbonate.



Scheme 3. Photo-oxidation mechanism of polymers  $RH$  is most labile hydrogen.

The PA6, PBT and the two polyetherester copolymers were aged in closed boro-silicate vessels filled with air or nitrogen. The PC was weathered as a free standing film.

## Analysis

Oxygen uptake, CO and CO<sub>2</sub> formation were determined by gas phase analysis after different oxidation times using gas chromatography (GC) (for details see ref 6).

A Shimadzu UV-3102PC UV-VIS-NIR scanning spectrophotometer was used to record the UV-VIS spectra. Infrared spectra were recorded using a BioRad FTS 6000 spectrometer in the attenuated total reflection (ATR) mode for 200 scans at a resolution of 4 cm<sup>-1</sup>. The BioRad Merlin software was used to analyze the spectra.

Fluorescence spectra were recorded on a Shimadzu RF-1501 spectrofluorimeter. The irradiated polycarbonate samples were dissolved in dichloromethane (0.001 wt% PC in DCM). Emission spectra were recorded using an excitation wavelength of 310 nm (7). The second-order Rayleigh scattering peak (located at 622 nm) was used to scale the recorded fluorescence spectra (8).

The elongation at break was measured in triplicate using a Zwick 1445 at an elongation speed of 50 mm/min.

## Results and Discussion

### PA6 and PBT

The rate of oxygen uptake of PA6 and PBT was determined in duplicate (Figure 3). Both polymers oxidize and show a linear relation between weathering time and oxygen uptake without an induction time. The oxygen uptake rate is a little higher for PBT than for PA6.

Oxygen uptake leads to several oxidation products. Two major gaseous products that are formed are CO and CO<sub>2</sub>. The relation between the oxygen uptake and the CO and CO<sub>2</sub> formed are shown in Figure 4 and Figure 5 respectively.

In the case of PBT the conversion of oxygen into CO and CO<sub>2</sub> is independent of the weathering time. For PA6, after an oxygen uptake of about 600 mmol/kg, which corresponds to a weathering time of 100-150 hours, an increase in the CO<sub>2</sub> formation rate was observed. The conversion of oxygen into CO is about 5% and into CO<sub>2</sub> about 10%. For both polymers CO can be formed by photolysis, but in the case of PA6, CO<sub>2</sub> can only be formed by oxidation.

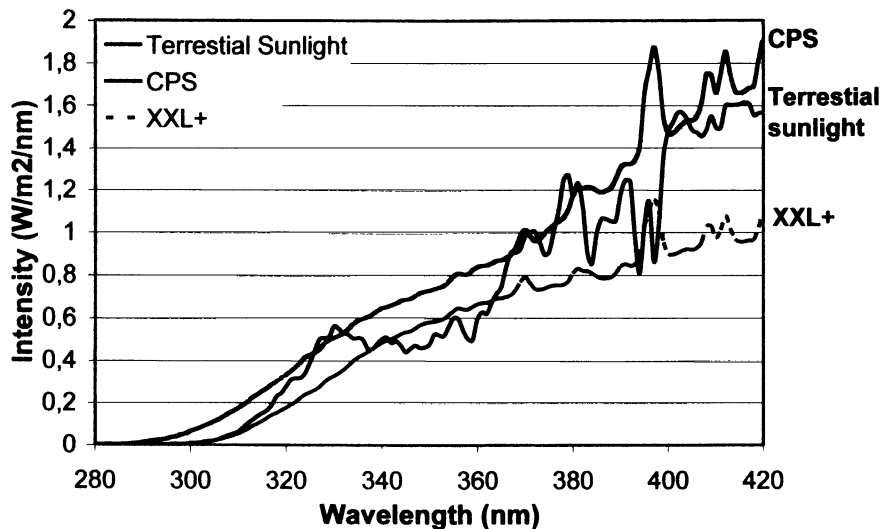


Figure 2. Irradiation wavelength spectra in Suntest CPS and XXL+ in comparison to the terrestrial solar spectrum.

However, the amounts formed by photolysis are limited as shown by weathering experiments in a nitrogen atmosphere (Figure 6). In this case for both polymers a constant formation rate of CO (PBT and PA6) and CO<sub>2</sub> (PBT only) was observed. Based on the comparison of the amount of CO formed in PBT and PA6, it can be calculated that the photolysis rate in PBT is 3 times higher than in PA6. However, for PBT, when the amount of CO<sub>2</sub> formed by photolysis is also taken into account, the difference in photolysis rate between PA6 and PBT becomes even more pronounced.

In PBT three possible Norrish 1 reactions can take place, two lead to CO<sub>2</sub> and one to CO (see Scheme 4). The ratio between the amount of CO and CO<sub>2</sub> formed in PBT is about 1:2, thus it seems that all three Norrish 1 reactions are of equal importance.

For applying engineering plastics in an outdoor environment, the change of the mechanical properties is one of the most important factors. During weathering in oxygen and nitrogen, the drop of the elongation at break (EAB) was determined. For PA6 the results are shown in Figure 7 and for PBT in Figure 8.

In the case of PA6 there is a large influence of the environment on the decline of the mechanical properties. In air the degradation is much faster than in nitrogen (Figure 7). In nitrogen PA6 shows some decrease in mechanical properties. This drop corresponds to the formation of CO (Figure 9) and is caused by photolysis. However, the decrease of the EAB in air is much faster,

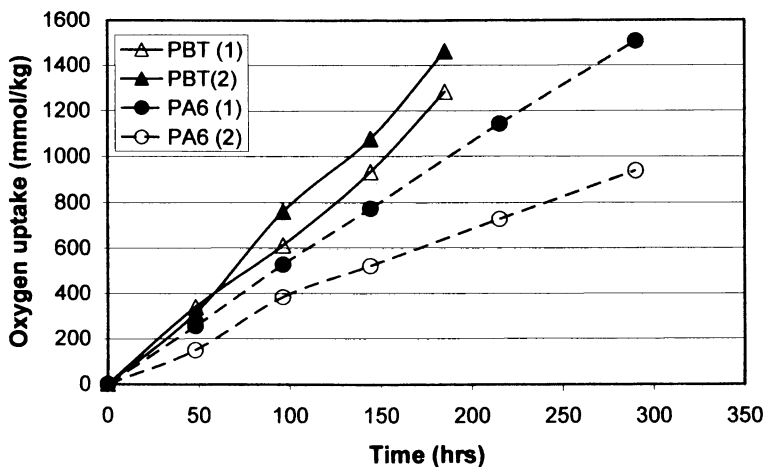


Figure 3. Oxygen uptake of PA6 and PBT (in duplicate) during weathering in borosilicate vessels filled with dry air in the WOM.

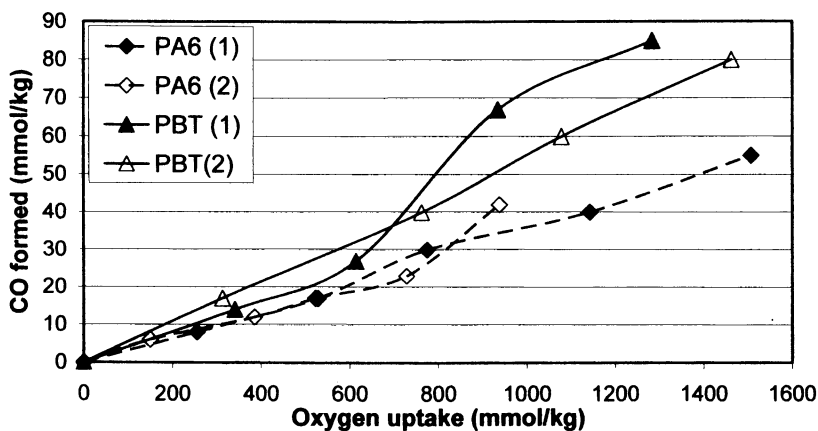


Figure 4. CO formed versus Oxygen uptake of PA6 and PBT (in duplicate) aged in borosilicate vessels filled with dry air in the WOM.

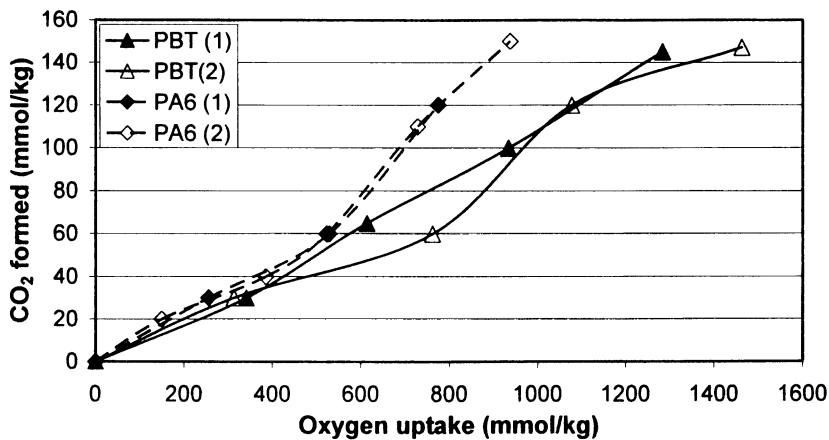


Figure 5. CO<sub>2</sub> formed versus Oxygen uptake of PA6 and PBT (in duplicate) aged in borosilicate vessels filled with dry air in the WOM.

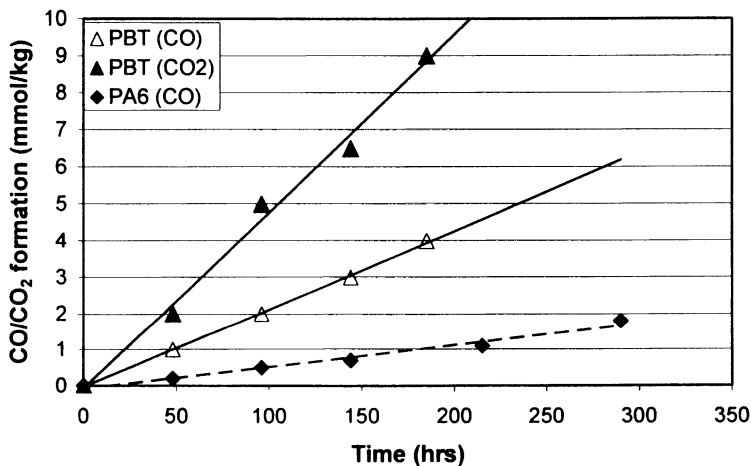
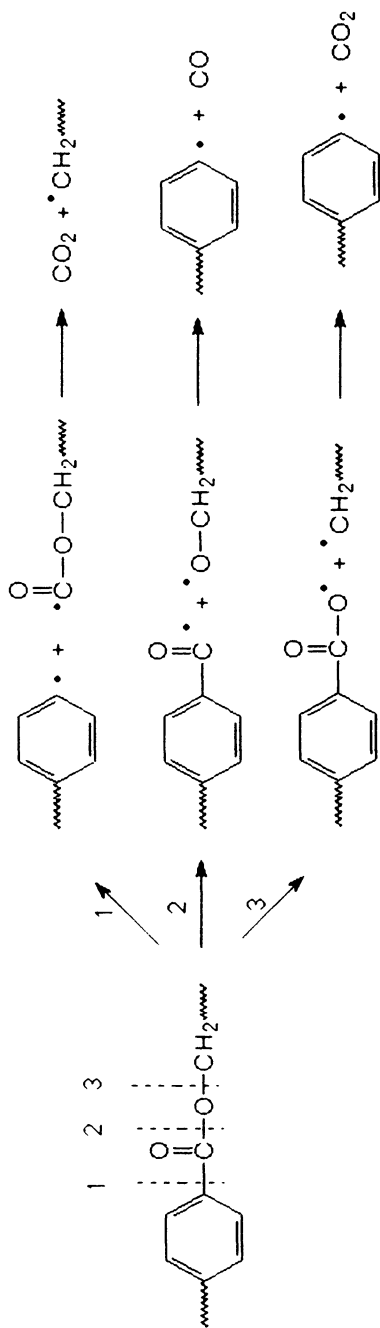


Figure 6. CO (PBT and PA6) and CO<sub>2</sub> (PBT) formed during weathering in borosilicate vessels filled with dry nitrogen as a function of time in a WOM.



Scheme 4. Possible Norrish 1 reactions in PBT.



which means that for PA6, photo-oxidation is much more important than photolysis.

For PBT the situation is different. In this case there is no large difference in decline in EAB in nitrogen and in air (*Figure 8*). This means that the loss of the mechanical properties is mainly due to photolysis. In this case the decrease in EAB corresponds to the formation of CO and CO<sub>2</sub> (*Figure 9*). It was shown that PBT oxidizes, but this oxidation does not lead to a faster decrease of the mechanical properties, which means that oxidation does not contribute to the breaking of chains and thus has to be a result of the oxidation of chains broken by photolysis.

### **PBT and its Polytetrahydrofuran (PECO-1) or Poly(propylene glycol) (PECO-2) Copolymer**

As was shown above the drop of the elongation at break of PBT is mainly due to photolysis. For polyether-ester copolymers containing pTHF or PPG this is different. In a nitrogen atmosphere a drop in the elongation at break was found, but for both copolymers the drop in the elongation at break in air is faster (*Figure 9*). As expected the PPG containing copolymer shows a faster decrease in the elongation at break in air than the pTHF containing copolymer (*Figure 9*), which can be ascribed to the higher oxidizability of PPG in comparison to pTHF, as is shown in *Figure 10*. In this graph the oxygen uptake of these polymers and PBT are shown during ageing in closed borosilicate vessels. The reproducibility of the oxygen uptake of both PECO is quite good. At the beginning the oxidation rate of all polymers is about comparable. After about 5 hours PECO-2 starts to deviate from the PBT curve and after 20 hours PECO-1. It seems that sufficient radicals have to be produced in the PBT before the polyether part starts to oxidize.

For PBT and its copolymers CO and CO<sub>2</sub> can be formed by photolysis as well as by oxidation. The CO and CO<sub>2</sub> formation rate of PBT and its copolymers in nitrogen is depicted in *Figure 11* and *Figure 12*. These gases can only be formed in the PBT part of the copolyetheresters. However, although the amount of PBT in both copolymers is lower than in the PBT homopolymer the formed amount of CO and CO<sub>2</sub> is not. It seems that the incorporation of polyether leads to a higher CO and CO<sub>2</sub> formation rate, especially for PPG. It is known that the incorporation of this polyether into PBT leads to a change in morphology of the amorphous PBT part, causing an increased mobility of this phase (9), which might be the reason for the higher CO and CO<sub>2</sub> formation rate for the PPG containing copolyetherester.

For PBT and its copolymers the formation rate of CO and CO<sub>2</sub> in air (*Figure 13* and *Figure 14*) is much larger than in nitrogen. Thus, in air the majority of the CO and CO<sub>2</sub> are formed by oxidation.

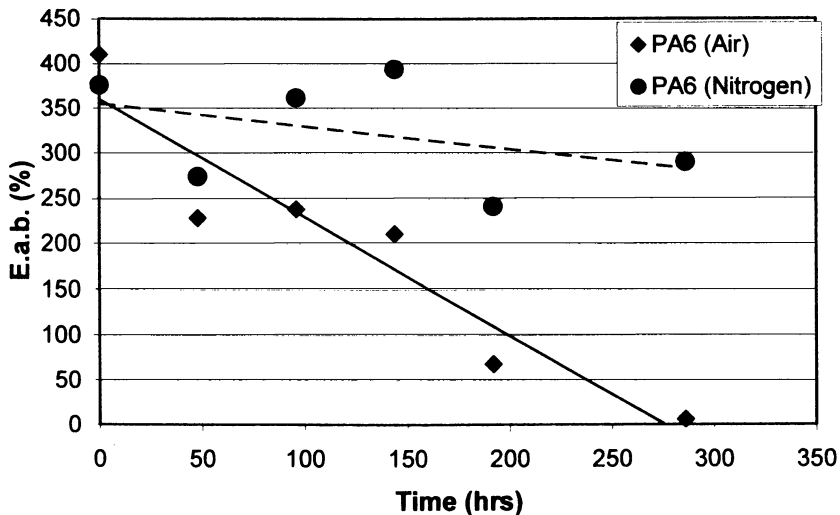


Figure 7. Relative drop of the elongation at break of PA6 weathered in borosilicate vessels filled with dry air or dry nitrogen as a function of time in a WOM.

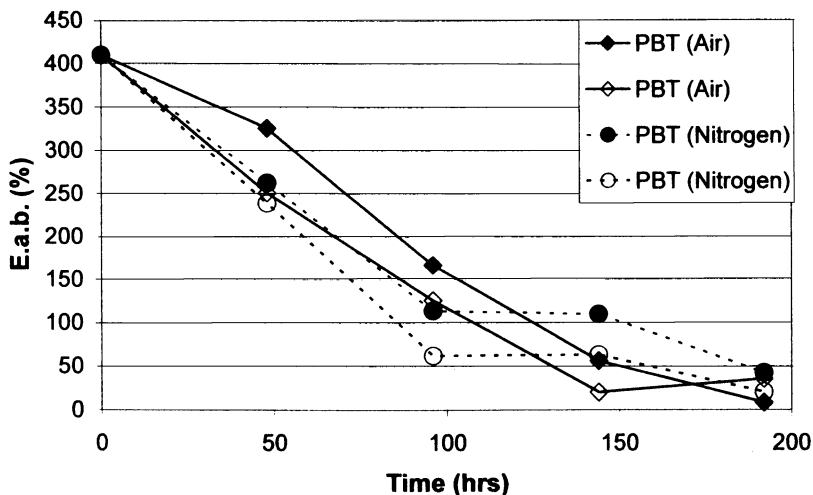


Figure 8. Relative drop of the elongation at break of PBT (in duplicate) weathered in borosilicate vessels filled with dry air or dry nitrogen as a function of time in a WOM.

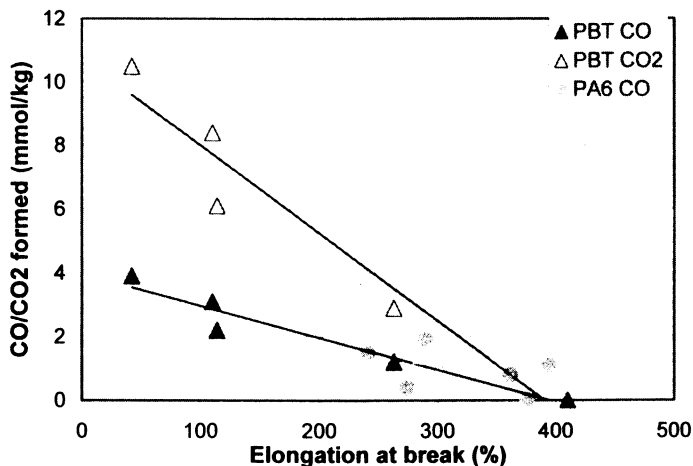


Figure 9. Amount of CO and CO<sub>2</sub> formed versus drop in elongation at break for PA6 and PBT weathered in borosilicate vessels filled with dry nitrogen in a WOM.

The oxygen uptake of PECO-2 starts to deviate from the PBT curve after about 5 hours and PECO-1 after about 20 hours. For the formation of CO and CO<sub>2</sub> this is different. For PECO-2, the formation of CO starts to deviate from the PBT line at about the same time as for the oxygen uptake, but for the amount of CO<sub>2</sub> this takes more than 20 hours. For PECO-1, the formation of CO<sub>2</sub> starts to deviate from the PBT line at around the same time as for the oxygen uptake, but for the formation of CO this deviation appears already earlier.

From the oxygen uptake and CO/CO<sub>2</sub> formation in nitrogen, it can be concluded that the main degradation mechanism of both PECOs is photo-oxidation, which is initiated by the photolysis of the PBT phase.

### Bisphenol A Polycarbonate

Another engineering plastic that can degrade by photolysis and photo-oxidation is polycarbonate. It was shown that the relative importance of these mechanisms depends on the irradiation wavelengths used; the photo-Fries rearrangement reaction is more likely to occur when light with wavelengths shorter than 300 nm is used, whereas photo-oxidation reactions are more important when light of longer wavelengths (> 340 nm) is used (4, 10, 11). It was also postulated that the photolytic reaction products can initiate the photo-oxidation (12), although other oxidation initiating reactions were postulated too (13). PC samples were irradiated with differently filtered xenon light (Figure 2).

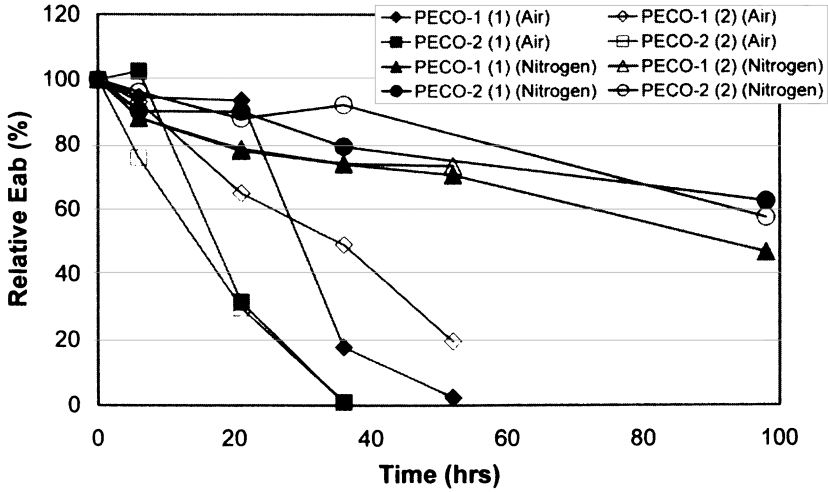


Figure 9. Relative drop of the elongation at break of PECO-1 and PECO-2 (in duplicate) aged in borosilicate vessels filled with dry air or dry nitrogen as a function of time in a WOM

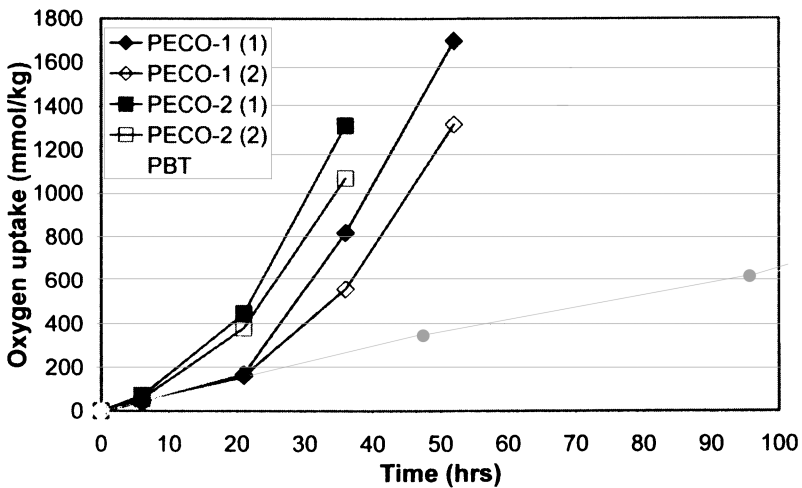


Figure 10. Oxygen uptake of PECO-1 and PECO-2 (in duplicate) and PBT in borosilicate vessels filled with dry air as a function of time in a WOM

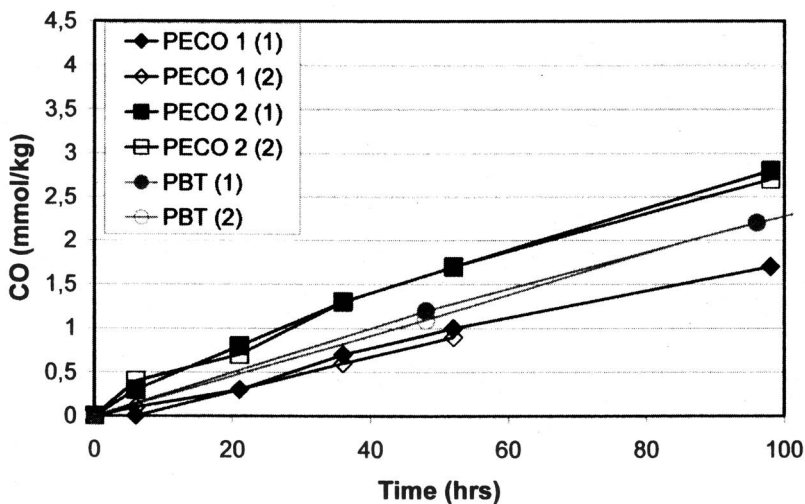


Figure 11. CO formed as a function of ageing time of PECO-1 and PECO-2 and PBT (in duplicate) aged in a borosilicate vessel filled with dry nitrogen in a WOM.

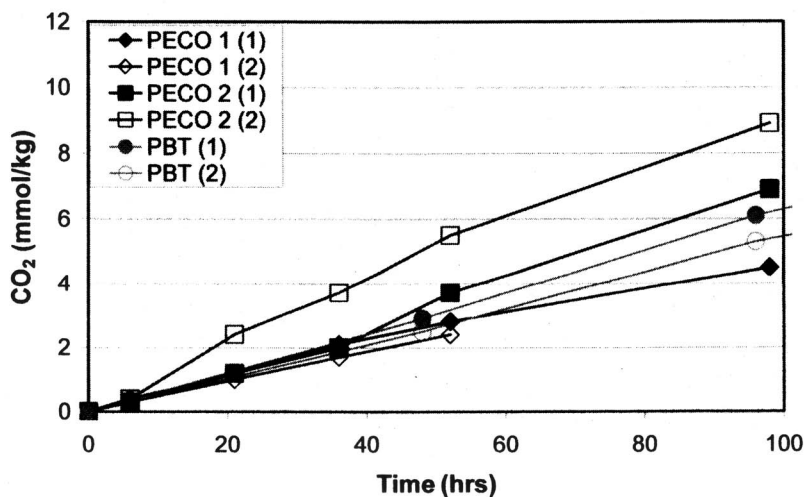


Figure 12. CO<sub>2</sub> formed as a function of time of PECO-1 and PECO-2 and PBT (in duplicate) aged in borosilicate vessels filled with dry nitrogen in a WOM.

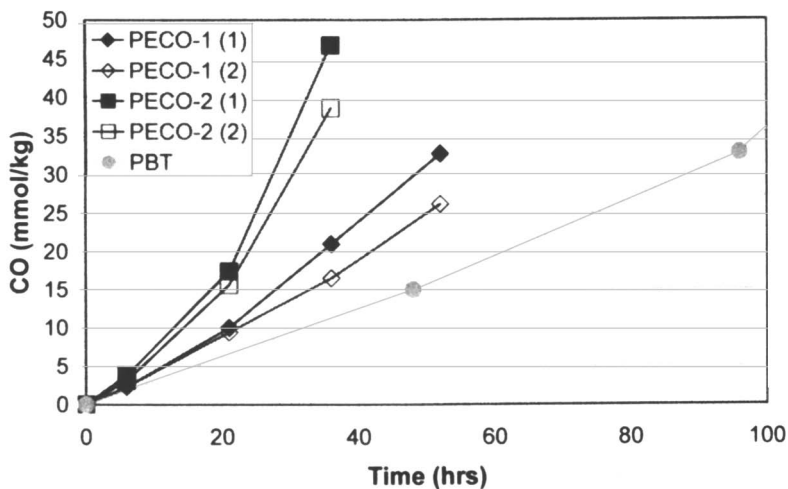


Figure 13. CO formed as a function of ageing time of PECO-1 and PECO-2 (in duplicate) and PBT aged in borosilicate vessels filled with dry air in a WOM.

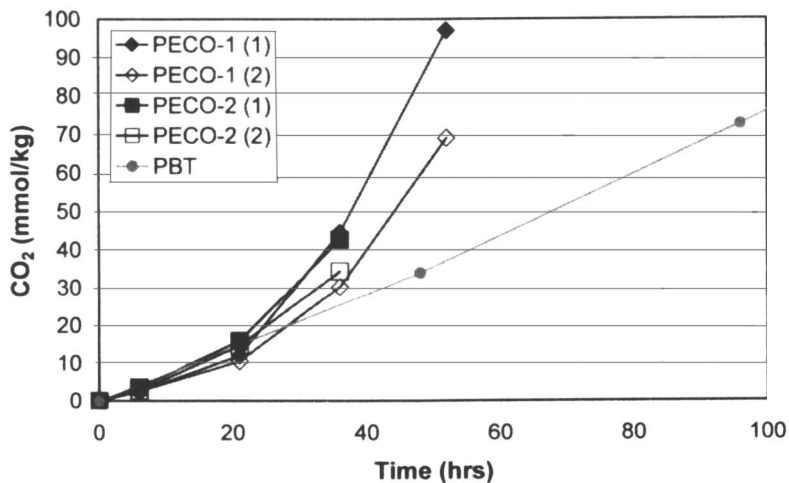


Figure 14. CO<sub>2</sub> formed as a function ageing time of PECO-1 and PECO-2 (in duplicate) and PBT aged in borosilicate vessels filled with dry air a WOM.

UV absorptions at 320 nm were measured as an indication for photo-Fries rearrangement reactions and IR absorptions at  $1713\text{ cm}^{-1}$  were used as an indication for photo-oxidation. Irradiation in the CPS leads to an increased absorption at 320 nm compared to irradiation in the XXL+ (Figure 15), which might be an indication for more photolytic reactions in the CPS. Fluorescence spectroscopy can also be used to detect photo-Fries rearrangement products in polycarbonates (14, 15). Emission spectra of solutions in DCM of polycarbonate films irradiated in the CPS and XXL+ were recorded and normalized to the second-order Rayleigh scattering peak at 622 nm. The normalized intensity at 480 nm increases with increasing irradiation times. The change in fluorescence intensity is shown in Figure 16. This figure shows that in the CPS this intensity increases more rapidly with increasing irradiation times than in the XXL+. This also means that the formation rate of photo-Fries products in the CPS is higher than in the XXL+. The increased amount of photo-Fries reactions can be attributed to the presence of shorter wavelengths in the CPS. The rate of carbonyl formation (absorption at  $1713\text{ cm}^{-1}$ ) is comparable in both cases (Figure 17), from which can be concluded that in both cases the photo-oxidation rate is similar. Thus, although in the CPS the photo-Fries reaction is more important, this does not lead to a faster oxidation. From this, it can be concluded that the initiation of the photo-oxidation results from reactions other than the photo-Fries reaction.

## Conclusions

Polymers that absorb terrestrial sunlight wavelengths can degrade under environmental conditions according to different mechanisms.

- Photolysis, light absorption as a result of the inherent polymer structure results in chemistry causing changes in the molecular weight distribution.
- Photo-oxidation initiated by photolysis reactions.
- Photo-oxidation initiated by impurities not being part of the inherent polymer structure.

For PBT it was demonstrated that loss of mechanical properties in an inert atmosphere occurs with a comparable rate as in air, from which it can be concluded that photolysis is the most important degradation mechanism. For polyether copolymers of PBT the situation changes. Due to the high oxidizability of the polyether moiety, the most important UV-degradation mechanism for these polymers is photo-oxidation, which is probably initiated by photolysis products of the PBT. The same mechanism is important for PA6; the

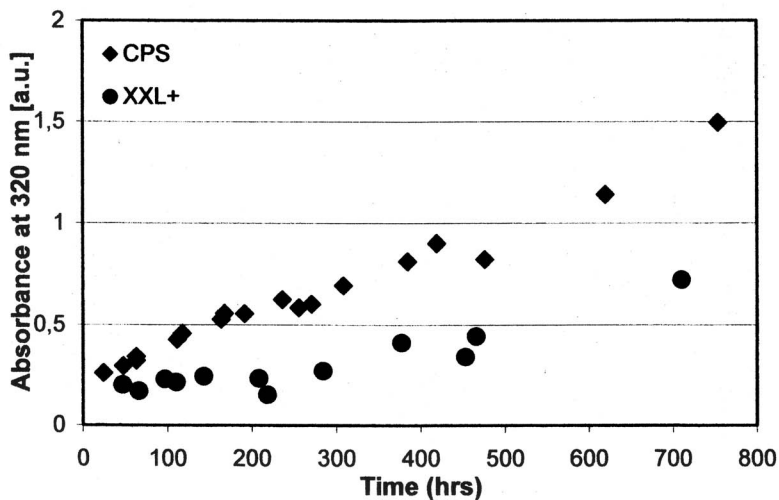


Figure 15. Absorbance at 320 nm as a function of irradiation time in the CPS and XXL+.

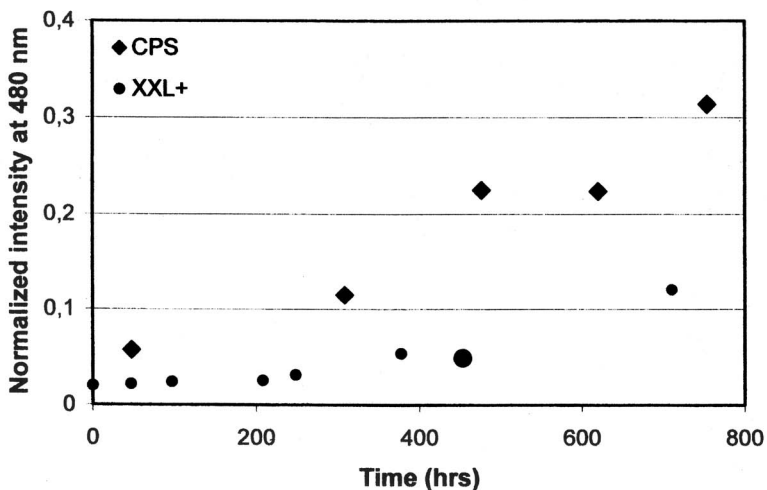


Figure 16. Fluorescence emission at 480 nm (excitation wavelength: 310 nm) as a function of irradiation time in the CPS and XXL+.



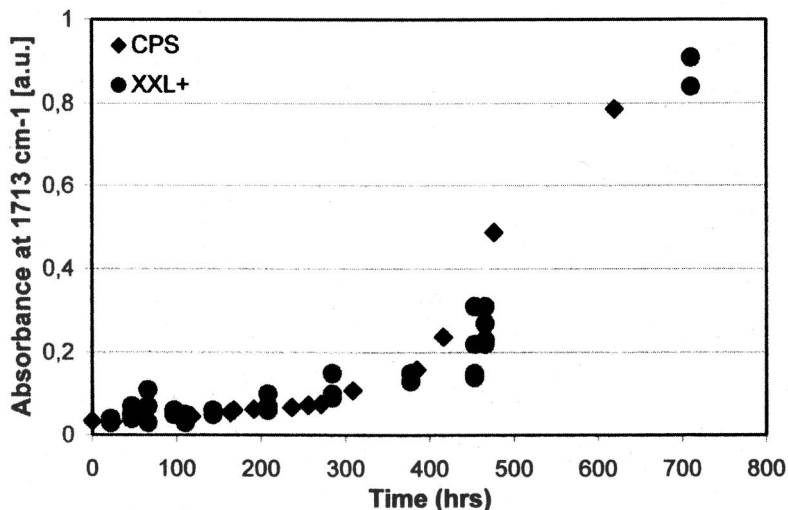


Figure 17. Absorbance at  $1713\text{ cm}^{-1}$  as a function of irradiation time in the CPS and XXL+.

main degradation mechanism is photo-oxidation, which is initiated by photolytic reactions.

PC also shows photolytic (in this case photo-Fries) and photo-oxidation reactions, but when PC is irradiated with wavelengths above 300 nm, photolysis only plays a minor role. Photo-oxidation is the major degradation mechanism; it was shown that the initiation of this photo-oxidation is not due to the photo-Fries rearrangement reaction.

## References

1. Gijsman, P.; Meijers, G.; Vitarelli, G. *Polym. Degrad. Stab.* **1999**, *65*, 433-441.
2. Rabek, J. F. *Polymer Photodegradation: Mechanisms and Experimental Methods*; Chapman and Hall: Cambridge, 1995.
3. Gijsman, P. *Polym. Degrad. Stab.* **1998**, *60*, 217-219.
4. Lemaire, J.; Gardette, J. L.; Rivaton, A.; Roger, A. *Polym. Degrad. Stab.* **1986**, *15*, 1-13.
5. Diepens, M.; Gijsman, P. *Polym. Degrad. Stab.* **2007**, *92*, 397-406.
6. Gijsman, P.; Hennekens, J.; Tummers, D. *Polym. Degrad. Stab.* **1993**, *39*, 225-233.
7. Hoyle, C. E.; Sha, H.; Nelson, G. L. *J. Polym. Sci. A: Polym. Chem* **1992**, *30*, 1525-33.

8. Potyrailo, R.; Lemmon, J. U. S. Patent 6,193,850 B1, 2001.
9. Lange, R. F. M.; Gabrielse, W. *e-Polymers* **2004**, no 064.
10. Rivaton, A.; Sallet, D.; Lemaire, J. *Polym. Photochem.* **1983**, *3*, 463-481.
11. Torikai, A.; Mitsuoka, T.; Fueki, K. *J. Polym. Sci. A: Polym. Chem.* **1993**, *31*, 2785-2788.
12. Factor, A.; Chu, M. L. *Polym. Degrad. Stab.* **1980**, *2*, 203-223.
13. Factor, A. *Handbook Polycarbonate Science and Technology*; Marcel Dekker: New York, 2000; pp 267-292
14. Hoyle, C. E.; Sha, H.; Nelson, G. L. *J. Polym. Sci. A: Polym. Chem.* **1992**, *30*, 1525-33.
15. Shah, H.; Rufus, I.; Hoyle, C. *Macromolecules* **1994**, *27*, 553-61.

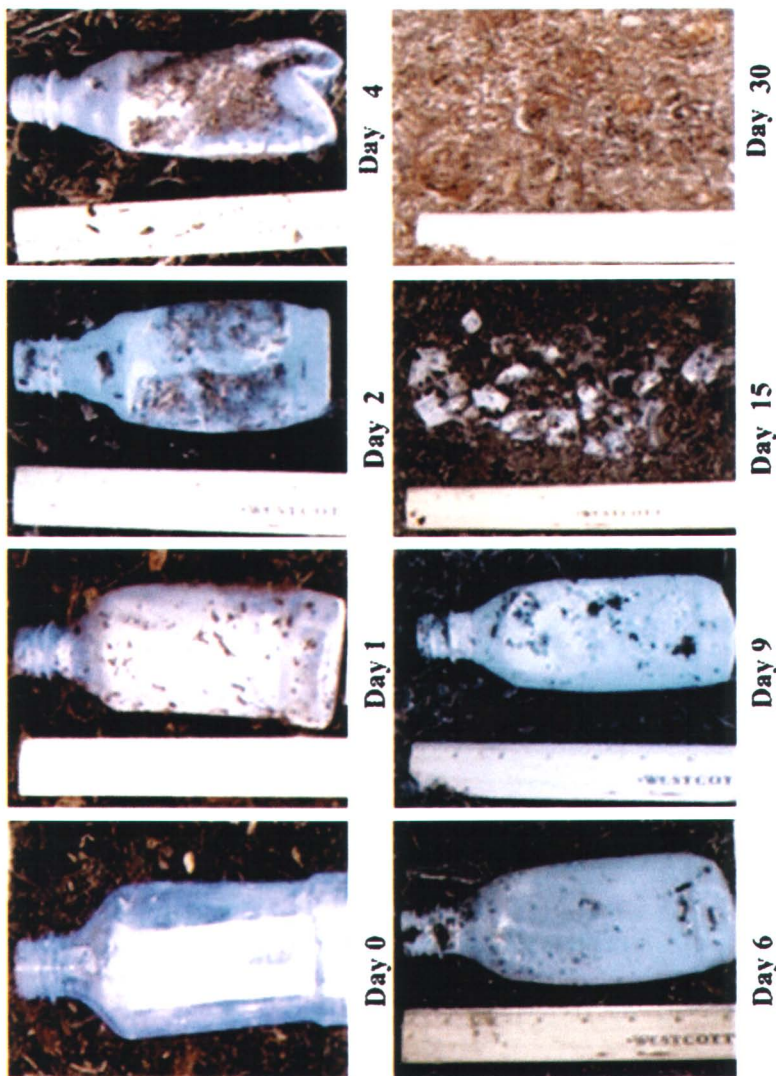


Figure 3. 4. Biodegradation of PLA bottles exposed to commercial composting (Reproduced with permission from reference 1. Copyright 2007 WILEY-VCH Verlag GmbH & Co. KGaA).

2 - Color insert

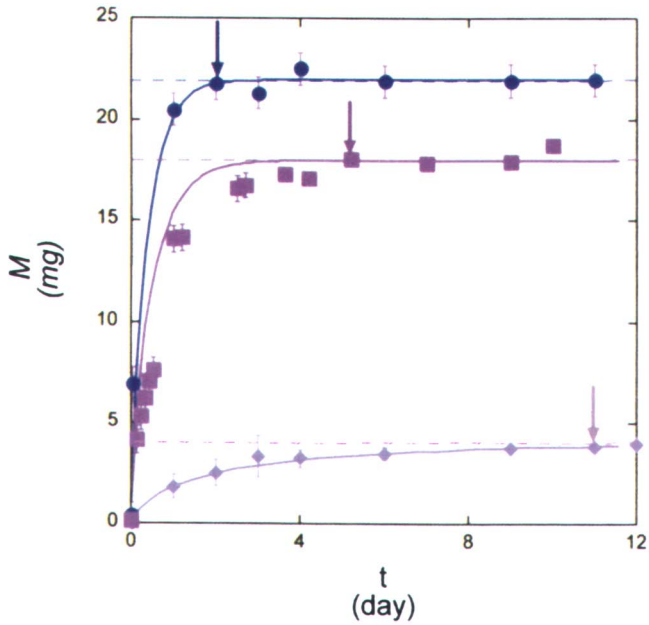


Figure 5.1. The mass of nicotine released from PCL,  $M$ , as a function of time. Diamonds denote 10% initial loading, Squares 40% initial loading, and circles 50% initial loading. The dashed lines show the maximal amount of drug in the system. Arrows mark the time at which 100% release was achieved. Solid lines are the result of a fit using equations (1-3).

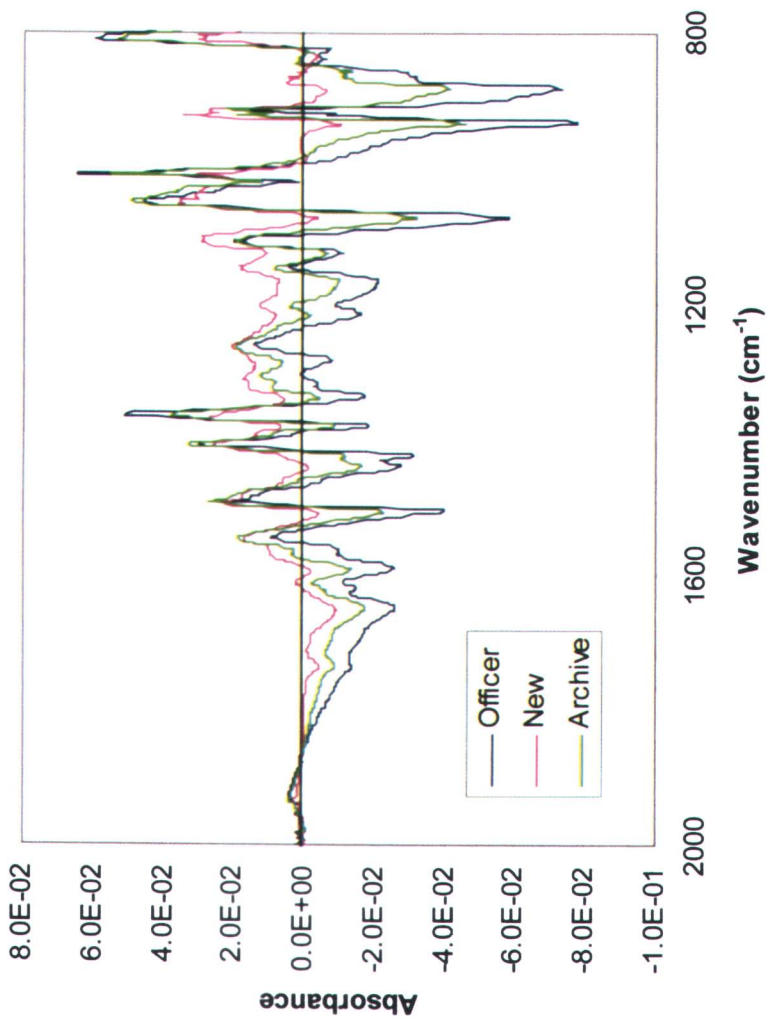


Figure 10.1. Difference spectra of the officer's, new and archive vest yarns, referenced to spectrum of virgin yarn.

4 - Color insert

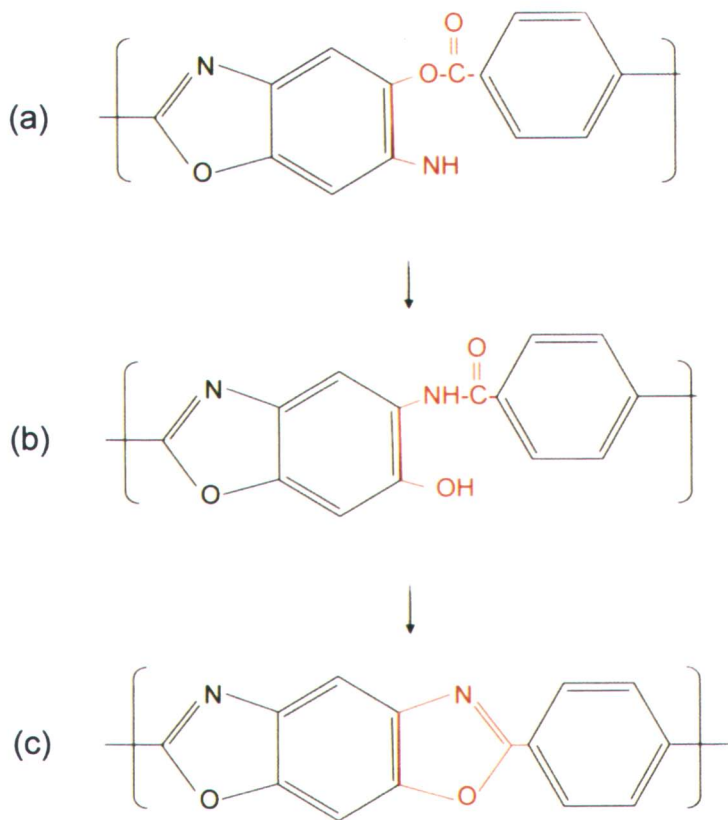


Figure 10.2. Proposed intermediate products in the synthesis of PBO, showing (a) aminophenylbenzoate, (b) hydroxyphenylbenzamide, and (c) benzoxazole.

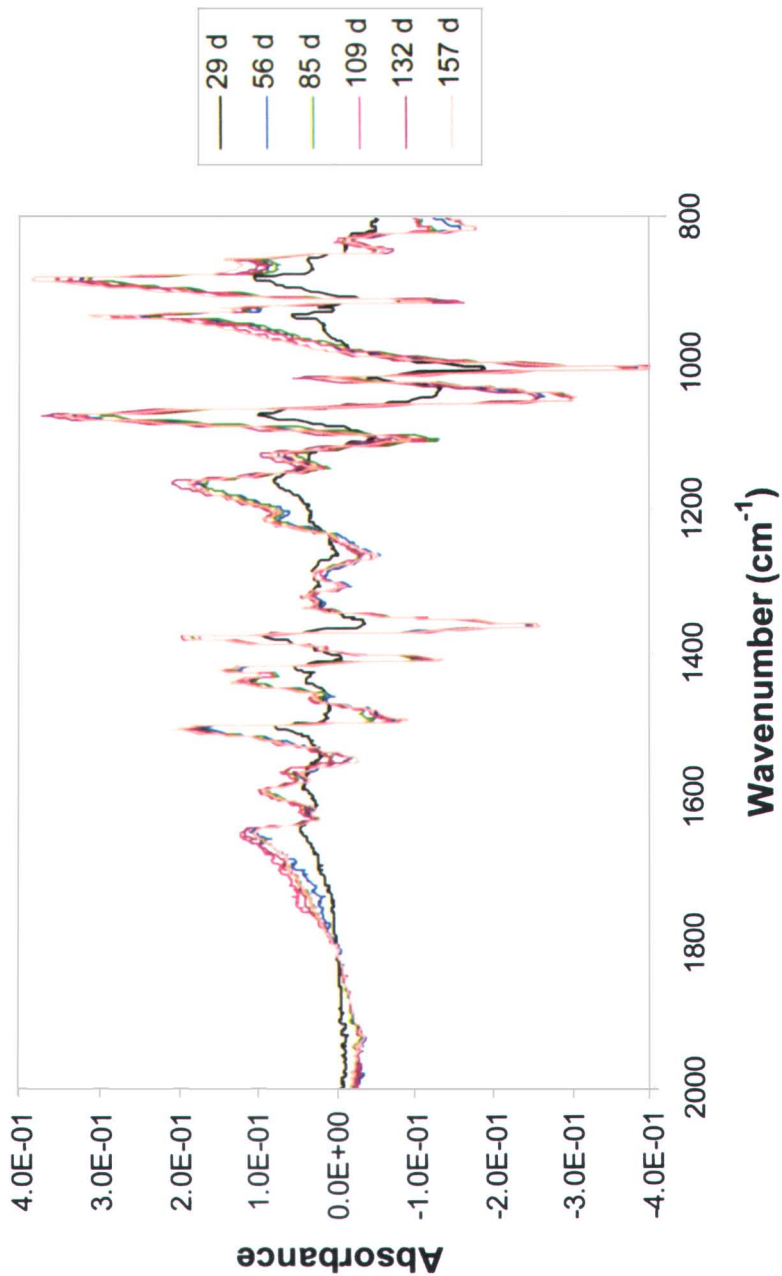


Figure 10.3. Difference spectra for PBO yarns extracted from aged vests, referred to spectrum of yarn taken at beginning of exposure.

6 - Color insert

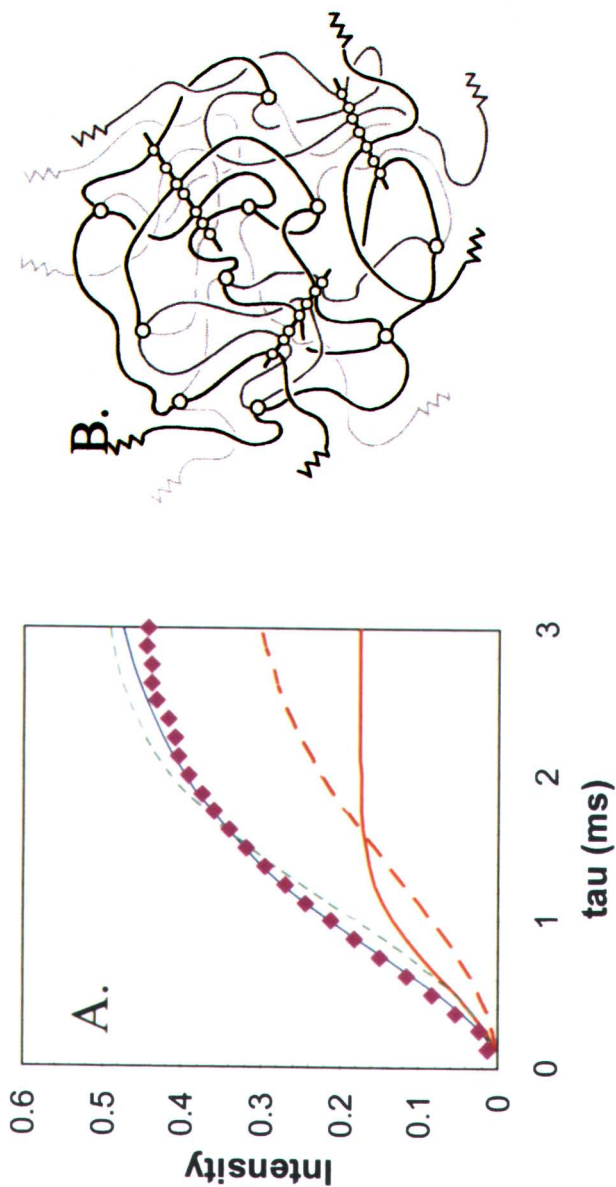


Figure 15.2. (A) Growth curve for pristine sample showing results of one site fit (dotted line) and two site fit (solid line) components are shown underneath curve in red; (B) Schematic of network structure of typical engineering silicone with both short and long chain constituents and standard four site crosslinking species and highly functional crosslinking sites. (Figure 2B is reproduced from reference 17. Copyright 2005 American Chemical Society.)



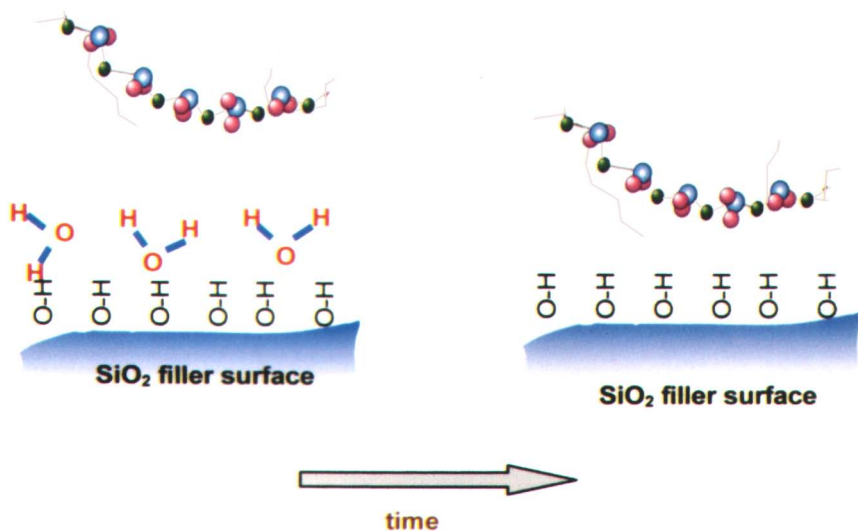


Figure 15.5. Illustration of speciation changes at polymer-filler interface that would be expected to alter the interaction strength and effect reinforcement.

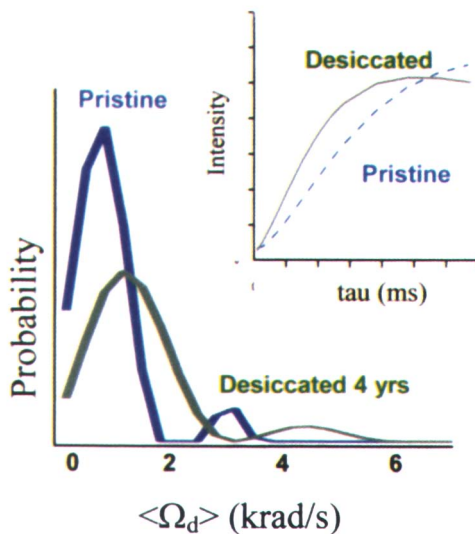


Figure 15.6. Results of MQ-NMR analysis of highly filled PDMS sample exposed to highly desiccating environment for 4 years. Inset: MQ growth curves.